USC
UNIVERSIDADE
DE SANTIAGO
DE COMPOSTELA

DEPARTAMENTO DE FÍSICA DA MATERIA
CONDENSADA

TESIS DOCTORAL

THEORETICAL AND COMPUTATIONAL STUDY OF STATIC AND DYNAMIC PROPERTIES OF HOMOGENEOUS AND INHOMOGENEOUS MIXTURES OF IONIC LIQUIDS

Trinidad Méndez Morales

Santiago de Compostela, 2015

USC
UNIVERSIDADE
DE SANTIAGO
DE COMPOSTELA

D. Luis Javier Gallego del Hoyo, Catedrático del Departamento de Física de la Materia Condensada de la Universidad de Santiago de Compostela, y **D. Luis Miguel Varela Cabo**, Profesor Titular del mismo Departamento,

INFORMAN:

Que el trabajo titulado *Theoretical and computational study of static and dynamic properties of homogeneous and inhomogeneous mixtures of ionic liquids* ha sido realizado bajo su dirección por **Dª. Trinidad Méndez Morales** en el Departamento de Física de la Materia Condensada de la Universidad de Santiago de Compostela, y constituye la memoria para optar al grado de Doctor en Ciencia de Materiales.

Santiago de Compostela, 9 de Marzo de 2015.

Prof. Luis Javier Gallego del Hoyo

Prof. Luis Miguel Varela Cabo

USC
UNIVERSIDADE
DE SANTIAGO
DE COMPOSTELA

Summary

Ionic liquids, defined as salts composed solely of ions that can be found in the liquid state under ambient conditions, have been known for about a century. However, although their discovery dates back to 1914 (when Walden described ethylammonium nitrate as an ionic liquid with a melting point of 287.6 K), it was not until the last decades that the interest and activity in the field of ionic liquids has experienced an exponential growth, far surpassing mere scientific or academic curiosity to become potential candidates to various industrial applications (in electrochemical devices, as thermal storage fluids, as lubricants or in the area of separation). Moreover, ionic liquids have many fascinating properties that characterize them as "green solvents", such as low vapor pressure, thermal stability up to high temperatures, high electrical and thermal conductivity and very good solvents properties for a wide variety of compounds. Thus, the possibility of customizing ionic liquids for many specific demands, making use of the nearly infinite combinations of suitable cations and anions, makes them to be termed "designer solvents".

This extent of tunability makes computational models to be of fundamental importance to systematically explain and predict the properties of ionic liquids. Due to the huge number of ionic liquids that can be produced, and also to the fact that small variations of the ions composing an ionic liquid lead to a substantial alteration of its characteristics, computer simulations can be used with the aim of knowing their properties *a priori* instead of through trial-and-error tests. Not only is this approach less time consuming but it also allows researchers to reduce a lot the money involved in the process. This can be observed in the increase in the number of computational works published along the last decades, as well as in the more and more numerous efforts devoted to the development of new potentials and more powerful computational tools. Concerning the computational methods that are more commonly employed for analyzing the properties of ionic liquids, the more accurate technique must be chosen taking into account the specific issues that we need to overcome (such as the high viscosity of the ionic liquids, the liquid state, the size of the ions or the description of the electronic structure) and trying to find a balance

between detail and efficiency. For example, *ab initio* quantum chemical methods include electronic effects such as polarization and charge transfer and are able of accurately describing the electronic structure. However, they are not suitable to study a great number of molecules due to their high computational cost. In the opposite corner are molecular dynamics and Monte Carlo methods, since although they are both useful for simulating a large number of ions interacting with each other and, thus, adequately describing the liquid phase, none of them can achieve a good model of the motion of the electrons within this type of systems. Halfway between the previous techniques, *ab initio* molecular dynamics methods provide reliable information about the electronic structure but are not capable of investigating a great number of molecules.

In the present thesis we present a computational study of structural and transport properties of ionic liquids. By means of molecular dynamics simulations we investigated the effect of several solutes (water, alcohols and salts of electrochemical interest) on the behaviour of these dense ionic solvents. Despite the increasing interest that ionic liquids have been generating, the solvation mechanism of diverse molecules and ions in these novel compounds is still scarcely comprehended. Additionally, the vast majority of the huge number of studies of ionic liquids and their mixtures reported up to now has been performed using experimental techniques, whereas the computational efforts have remained more little in spite of being an essential tool for getting a detailed knowledge of ionic liquids at the atomic level. By that means, the main goal of this research is to provide a deeper knowledge of how molecular level properties of ionic liquids are affected by the addition of the former solutes to the mixture. The whole set of simulations included in this thesis was carried out using the open source and free software Gromacs 4.5.4 package, whose features (extremely high performance and cost efficiency, massively parallel simulations, accuracy of compression and user friendly interface) make it one of the most used packages for molecular simulations. The potential energy functions of the force fields integrated in Gromacs include the non-bonded interactions (a repulsion term, a dispersion term and a Coulomb term), the bonded interactions (bond stretching, bond angle and dihedral angle interactions) and some restraints that can be necessary in some special cases. In addition, although the employed force fields were non-polarizable they provide very accurate structural predictions and qualitatively correct dynamic results.

Due to their high hygroscopic character, water is an omnipresent impurity in ionic liquids. The presence of water in these solvents can be a problem

or a benefit depending on the application, but in all cases its influence on the physicochemical properties of the ionic liquid should be well known. Chapter 2.1 contains the analysis of the structure and dynamics of bulk mixtures of water with 1-alkyl-3-methylimidazolium based ionic liquids. Several structural properties, such as, radial radial distribution functions, coordination numbers, hydrogen bonds, and also single-particle dynamics (self-diffusion coefficients, mean square displacements andvelocity autocorrelation functions) were studied under the influence of the length of the cation alkyl chain (ethyl, butyl, hexyl and octyl), of the hydrophobic nature of the anion (hexafluorophosphate, chloride and bromide) and of water concentration. We observed the formation of water clusters, whose size was strongly dependent on the hydrophobicity of the anion and nearly independent on the cation chain length. A notable clustering tendency at low amounts of water was found for both halogenated anions and, above all, for the hydrophobic one; which eventually leads to bigger water clusters the greater the water concentration up to a point where they form a percolating network. These clusters of water molecules are mainly located in the polar regions of the bulk mixtures, since they preferentially interact with the anions. The analysis of the velocity autocorrelation functions showed a rattling motion of water molecules in the polar nanoregions of the hydrophilic mixtures, whereas the presence of the more hydrophobic anion leads to a rapid cancellation of the correlations. Another evidence of water molecules being more strongly clusterized in the polar regions of the mixtures the more hydrophobic the anion was provided by the evolution of the three regimes of the mean-square displacements (a ballistic behavior of the ions that dominates at short times, a diffusive motion at long times and a long subdiffusive regime characteristic of glass formers in the supercooled region at intermediate times). In this case, the diffusive dynamics was sooner reached when the hexafluorophosphate anion was present in the system, due to a more similar water motion to that registered in pure water. Thus, all the results support the picture of water molecules being solvated in the polar nanodomains of bulk mixtures with aprotic ionic liquids, in which they form clusters whose size grows up until a percolating network is reached.

Since having a detailed knowledge on the properties of not only pure ionic liquids but also their mixtures is of fundamental importance for their potential use in a number of industrial applications, in Chapter 2.2 we tried to shed some light on the solvation process of molecular solvents when mixed with ionic liquids. More specifically, we investigated the structural properties of

bulk mixtures of two alcohols of different chain length (methanol and ethanol) with ionic liquids composed of the 1-hexyl-3-methylimidazolium cation and three anions with a different level of hydrophobicity (hexafluorophosphate, tetrafluoroborate and chloride). The solvation mechanism that takes place in these systems was compared to that found in mixtures with water by studying how densities, coordination numbers, radial distribution functions and number of hydrogen bonds change upon mixing. As a result, we found an structural picture that largely differs from the one reported for mixtures with water in Chapter 2.1. In particular, there is no cluster formation of alcohol molecules, which are, instead, almost homogeneously distributed in the bulk and are located at approximately the same distance from all other species in the mixture. It must be noted that in those mixtures with the more solvophobic anion the existence of some kind of network could be stated, but its size is not even comparable to that formed in mixtures with water. This different behaviour is due to the amphiphilic character of alcohol molecules, which allows them to be inserted in the polar and apolar regions of the bulk. This process in which the nanoseggregated structure of the ionic liquids accommodates the similar parts of the alcohols is named as nanotructured solvation.

In Chapter 2.3 we expanded the analysis started in Chapter 2.2 and confirmed that the differences found in structural properties of water and alcohols when mixed with ionic liquids have also a deep impact on the single-particle dynamics behaviour of these systems. Contrarily to what happens in aqueous mixtures, the rattling motion related to a caging effect was not seen for alcohol molecules due to their lack of cluster formation and their greater ability to diffuse in the bulk mixtures. This reinforces the picture of alcohol molecules being nearly homogeneously solvated in the polar and apolar areas of the mixture, as opposed to the greater lipophobicity of water molecules that constraints them to be placed in the polar domains of the mixture where they form clusters. The only aspect that alcohol molecules share with their water counterparts is the nanotructured solvation. That is, these solutes are not able to destroy the nanoseggregated structure of the ionic liquids, but rather adapt to it and place themselves in the most favorable areas of the mixture, which undoubtedly has a big effect on the structural and dynamic properties of the resultant systems. In addition, the anion nature was confirmed to have a dominant role on the structural and dynamic properties of mixtures of ionic liquids with molecular solvents.

The importance of ionic liquids in electrochemistry is such that the devel-

opment of efficient electrochemical devices involves the use of ionic liquids for improving the ion trasport properties. Many ionic liquids offer a range of properties (conductivity, viscosity, and wide electrochemical potential windows) that makes them very attractive to be used in various electrochemical devices, such as solar cells, fuel cells, lithium batteries and supercapacitors. With the aim of better understanding the role of ionic liquids in these devices, a detailed picture of the structural and ion transport properties of lithium salt-doped ionic liquids is included in Chapter 2.4. For this purpose, we considered ionic liquids based on the 1-butyl-3-methylimidazolium cation and three different anions (hexafluorophosphate, tetrafluoroborate and bis(trifluoromethylsulfonyl)imide) mixed with lithium and sodium salts with a common anion. As in mixtures with molecular solvents, the basis of nanotructured solvation were also found in mixtures with alkali salts. In this regard, salt cations are mainly restricted to be located in the polar regions of the mixtures, in which they are strongly coordinated with the anions adopting two possible conformations (monodentate and bidentate) in the first solvation layer that are sensitive to the amount of salt present in the mixture. This leads to the formation of long-lived aggregates that act as stable kinetics entities inside which a marked rattling motion of salt ions was registered. This structure was probed to be extraordinarily resilient and survive during tens of nanoseconds. The first solvation shell of anions is followed by a second layer of lithium/sodium molecules and a third shell of imidazolium cations, which resembles a pseudolattice structure according to the structural model on the basis of Bahe–Varela theory. The analysis of the self-diffusion coefficients allowed us to calculate the values of the ionic conductivity; however, the need of employing polarizable force fields for obtaining accurate dynamic properties provided us with slightly underestimated data.

Although lithium-battery research has been usually focused on the use of aprotic ionic liquids as electrolytes, protic ionic liquids must be also considered as an alternative to conventional electrolytes, since the cost and difficulty of synthesizing protic ionic liquids are lower than that of aprotic ionic liquids and they have been experimentally confirmed as usable electrolytes for these devices. Thus, in Chapter 2.5 we extended the study to the structural features of solutions of lithium nitrate in a protic ionic liquid, ethylammonium nitrate. The analysis of densities, radial distribution functions, spatial distribution functions, hydrogen bonds and coordination numbers showed the same structural picture as the one described in Chapter 2.4, in which cation

salts form anionic aggregates with the anions of their first coordination shell in pseudolattice-like ordered polar nanoregions. The study of the center-of-mass velocity autocorrelation functions of lithium cations confirmed the presence of surrounding cages formed by their nearest anions, as it was observed in solutions of lithium salt in aprotic ionic liquids. The well-known hydrogen bond network that takes place in protic ionic liquids is slightly disrupted by the addition of salt to the mixture, due to the presence of lithium cations in the polar regions of the bulk and their strong coordination with nitrate anions, which leads to the transference of nitrate anions to the inner regions of the polar nanodomains where lithium cations are mainly placed. Furthermore, even though this mixture could be expected to behave like a molten salt, its behaviour is more similar to a solid-like structure, with intermediate range ordering and double peaks in the lithium-anion radial distribution functions that mimic the calcite-type structure characteristic of solid lithium nitrate. This formation of solid-like aggregates leads to phase separation with increasing the amount of salt.

Chapter 2.6 includes an analysis of the influence of the chain length of the alkylammonium cation on the structural properties of protic ionic liquids when doped with lithium salts. On this occasion we studied mixtures of propylammonium nitrate and butylammonium nitrate with a salt with a common anion, lithium nitrate. Thus, the increase in the alkyl chain length causes an increase in the segregation of the mixtures, with better defined polar and apolar domains and less densely packed and less resilient structures. However, despite the better defined polar and apolar regions the longer the alkyl chains, the polar domains of propylammonium nitrate and butylammonium nitrate mixtures seem to be, on average, less ordered than those in ethylammonium nitrate mixtures. This increment of the orientational disorder in the nanoregions could be associated to the collapse of the directional hydrogen bond network inside the polar nanoregions. In addition, the disruption of the network of hydrogen bonds was found to be more pronounced the longer the alkyl chain of the cation, which is due to the lower degree of hydrogen bonding of these mixtures. It must be highlighted that the structure of both protic and aprotic ionic liquids is very resilient to the addition of any type of additive, including water, alcohols and salts. The polar regions were found to experience a compaction as the alkyl chain length of the ionic liquid cation was increased, associated to a decrease in their volume fraction via a "dilution effect". At the same time, this polar domains show an expansion as increasing

the amount of salt in the system, which is due to the increase in the number of ions in these regions associated to a decrease of the number of hydrogen bonds. In spite of everything, the polar and apolar domains of the bulk mixtures are only slightly eroded by the presence of the solutes, whose solvation takes place accommodating the molecular moieties of the solute molecules in the nanoregions of the amphiphilically nanostructured ionic liquids that are more similar to their molecular entities.

The simulation of more realist systems is a required step for a deeper comprehension of the potential use of ionic liquids in electrochemistry. Chapter 2.7 closes the research project of this thesis with the study of mixtures of ionic liquids with alkali salts confined between graphene walls. The studied systems were 1-butyl-3-methylimidazolium tetrafluoroborate mixed with lithium tetrafluoroborate and with potassium tetrafluoroborate between two charged and uncharged parallel graphene electrodes. These simulations were carried out at 450 K in order to avoid the system being "trapped" in a local minimum due to the well-known high viscosity of ionic liquids, but the results are expected to be representative of the behaviour of these systems at somewhat lower temperatures. The analysis of the structure confirmed that the ionic liquid adopts a highly inhomogeneous structure in the proximities of the surface, in which cation and anion layers whose ion densities are greater than in the bulk are formed due to overscreening in the charge distribution of ionic liquids. This behaviour was also obtained in the presence of uncharged graphene walls and leads to electroneutrality at long distances from the electrodes, where the values of the bulk densities are reached. When the charge of the walls increases the ions experienced a systematic rearrangement, in which anions are segregated towards the positive electrode and cations toward the negative one. In addition, the average orientation of imidazolium rings varied from an angle of 36° with respect to the normal vector of the surface to a more perpendicular fashion as the electrode potential increases. As seen in previous chapters, the addition of salt to the mixture has little effect on the organization of the ions of the ionic liquid near the graphene walls. Hence, the nanostructure solvation could be considered as a sort of universal solvation mechanism in these amphiphilically nanostructured dense ionic solvents. Although the distribution of lithium and potassium cations could be expected to be governed by the electrode potential, the truth is that it is mainly detemined by the structure that the ionic liquid adopts and by the formation of the ionic aggregates that salt cations arrange with the anions in their first coordination shell. Thus, lithium

and potassium cations are able to be adsorved on the negative surface only for high concentrations of salt due to the occurrence of very high free energy barriers that they must overcome for getting to the wall.

This thesis ends with a brief summary of the main conclusions.

Resumen

Los líquidos iónicos, los cuáles se definen como sales compuestas únicamente de iones y que se pueden encontrar en estado líquido bajo condiciones ambientales, se conocen desde hace aproximadamente un siglo. Sin embargo, aunque su descubrimiento data de 1914 (cuando Walden identificó el nitrato de etilamonio como un líquido iónico con un punto de fusión de 287,6 K), no fue hasta las últimas décadas que el interés y la actividad en el campo de los líquidos iónicos han experimentado un crecimiento exponencial, superando ampliamente el simple interés académico o científico para convertirse en candidatos potenciales para diversas aplicaciones industriales (en dispositivos electroquímicos, como fluidos de almacenamiento térmico, como lubricantes o en el área de separación). Además, los líquidos iónicos poseen muchas propiedades fascinantes que los convierten en "disolventes verdes", tales como baja presión de vapor, estabilidad térmica hasta temperaturas elevadas, alta conductividad térmica y eléctrica y muy buenas propiedades como disolventes para una amplia variedad de compuestos. De este modo, la posibilizar de crear líquidos iónicos para muchas demandas específicas utilizando las infinitas combinaciones de cationes y aniones disponibles hace que sean calificados como "disolventes de diseño".

Este grado de adaptación hace que los modelos computacionales tengan una gran importancia a la hora de explicar de manera sistemática y predecir las propiedades de los líquidos iónicos. Debido al enorme número de líquidos iónicos que se pueden obtener, y también al hecho de que pequeñas variaciones en los iones que componen un líquido iónico conducen a cambios sustanciales en sus características, las simulaciones por computadora pueden utilizarse con el objetivo de conocer sus propiedades *a priori* en lugar de usar métodos de prueba y error. Este enfoque no sólo es menos caro computacionalmente hablando, sino que también permite que los investigadores reduzcan ampliamente el dinero involucrado en el proceso. Esto se puede observar en el aumento del número de trabajos computacionales que se han publicado a lo largo de las últimas décadas, así como en los cada vez más numerosos esfuerzos dedicados al desarrollo de nuevos potenciales y herramientas computacionales

más potentes. Con respecto a los métodos computacionales que se emplean más comunmente para analizar las propiedades de los líquidos iónicos, la técnica más adecuada debe elegirse teniendo en cuenta los problemas específicos que debemos tratar (tales como la elevada viscosidad de los líquidos iónicos, la fase líquida, el tamaño de los iones o la descripción de la estructura electrónica) y tratando de encontrar un equilibrio entre eficiencia y detalle. Por ejemplo, los métodos de química cuántica *ab initio* includen efectos electrónicos como la polarización y la transferencia de carga y son capaces de describir adecuadamente la estructura electrónica. Sin embargo, dichos métodos no son adecuados para estudiar un número grande de moléculas debido a su elevado coste computacional. En el lado opuesto se encuentran las técnicas de dinámica molecular y monte carlo, ya que aunque ambas son útiles para simular un gran número de iones interaccionando entre ellos y, así, describir apropiadamente la fase líquida; ninguna de ellas puede alcanzar un buen modelo del movimiento de los electrones en este tipo de sistemas. A medio camino entre las técnicas anteriores, los métodos de dinámica molecular *ab initio* proporcionan información fiable acerca de la estructura electrónica pero no son capaces de investigar un gran número de moléculas.

En la presente tesis se presenta un estudio computacional de las propiedades estructurales y de transporte de los líquidos iónicos. Mediante simulaciones de dinámica molecular se investiga el efecto que tienen diversos solutos (agua, alcoholes y sales de interés electroquímico) en el comportamiento de estos densos disolventes iónicos. A pesar del interés creciente que los líquidos iónicos han generado, el mecanismo de solvatación de diversas moléculas e iones en estos nuevos compuestos se comprende aún de manera muy escasa. Además, la gran mayoría del enorme número de estudios de líquidos iónicos y sus mezclas que se han publicado hasta ahora han sido realizados utilizando técnicas experimentales, mientras que los esfuerzos computacionales han sido menores a pesar de ser una herramienta esencial para conseguir un conocimiento detallado de los líquidos iónicos a nivel atómico. De este modo, el objetivo principal de esta investigación es proporcionar un conocimiento más profundo acerca de cómo las propiedades de los líquidos iónicos a nivel molecular resultan afectadas por la agregación de los solutos anteriores a la mezcla. Todo el conjunto de simulaciones incluídas en esta tesis se ha llevado a cabo usando el paquete de código abierto Gromacs 4,5,4, cuyas características (rendimiento extremadamente alto, minimización del coste maximizando la eficiencia, simulaciones masivamente paralelizadas, compresión de datos

adecuada e interfaz amigable y sencilla) lo convierten en uno de los paquetes más utilizados en la simulación molecular. Las funciones de energía potencial integradas en Gromacs incluyen las interacciones no enlazantes (un término repulsivo, un término dispersivo y un término Coulombiano), las interacciones enlazantes (estiramiento de enlace, flexión de ángulo y ángulos diedros) y algunas restricciones que pueden ser necesarias en casos especiales. Además, aunque los campos de fuerzas empleados no son polarizables, proporcionan predicciones estructurales adecuadas y resultados dinámicos cualitativamente correctos.

Debido a su carácter higroscópico, el agua es una impureza omnipresente en los líquidos iónicos. La presencia de agua en estos disolventes puede ser un problema o un beneficio dependiendo de la aplicación, pero en todos los casos su influencia en las propiedades fisicoquimicas del líquido iónicos debería ser conocida. El Capítulo 2.1 contiene el análisis de la estructura y la dinámica del bulk de mezclas de agua con líquidos iónicos basados en el catión 1-alquil-3-metilimidazolio. Varias propiedades estructurales, tales como las funciones de distribución radial, los números de coordinación, los enlaces de hidrógeno, y también la dinámica de la partícula (coeficientes de autodifusión, desplazamientos cuadráticos medios y funciones de autocorrelación de velocidades) se estudiaron bajo la influencia de la longitud de la cadena del catión (etil, butil, hexil y octil), de la naturaleza hidrofóbica del anión (hexafluorofosfato, cloro y bromo) y de la concentración de agua. Observamos la formación de clusters de agua, cuyo tamaño era fuertemente dependiente de la hidrofobicidad del anión y prácticamente independiente de la longitud de la cadena catiónica. Se encontró una notable tendencia a la clusterización a bajas concentraciones de agua para ambos aniones halogenados y, sobretodo, para el hidrófobo; el cual eventualmente dio lugar a clusters de agua más grandes cuanto mayor era la concentración de agua hasta llegar al punto de formar una red percolante. Estos clusters de moléculas de agua están situados principalmente en las regiones polares del bulk de las mezclas, ya que interactúan principalmente con los aniones. El análisis de las funciones de autocorrelación de velocidades mostró un movimiento vibrante de las moléculas de agua en las nanoregiones polares de las mezclas hidrofílicas, mientras que la presencia del anión más hidrofóbico conduce a una cancelación rápida de las correlaciones. Otra evidencia de que las moléculas de agua están más clusterizadas en las regiones polares de las mezclas cuanto más hidrofóbico es el anión fue proporcionada por la evolución de los regímenes de los desplazamientos cuadráticos medios

(un comportamiento balístico de los iones que predomina a tiempos cortos, un movimiento difusivo a tiempos largos y un gran regimen subdifusivo característico de los formadores de vidrios en la región subenfriada a tiempos intermedios). En este caso, la dinámica difusiva se alcanzó antes cuando el anión hexafluorofosfato estaba presente en el sistema, debido a un movimiento más parecido al registrado en agua pura. De este modo, todos los resultados apoyan la imagen de las moléculas de agua siendo solvatadas en los nanodominios polares del bulk de las mezclas con líquidos iónicos apróticos, en las cuáles forman clusters cuyo tamaño crece hasta formar una red percolante.

Ya que tener un conocimiento detallado de las propiedades, no solo de líquidos iónicos, sino también de sus mezclas, es de fundamental importancia para su potencial uso en numerosas aplicaciones industriales, en el Capítulo 2.2 intentamos aclarar el proceso de solvatación de disolventes moleculares al ser mezclados con líquidos iónicos. De manera más específica, investigamos las propiedades estructurales del bulk de mezclas de dos alcoholes de diferente longitud de cadena (metanol y etanol) con líquidos iónicos compuestos por el catión 1-hexil-3-metilimidazolio y tres aniones con un nivel diferente de hidrofobicidad (hexafluorofosfato, tetrafluoroborato y cloro). El mecanismo de solvatación que tiene lugar en estos sistemas se comparó con el encontrado en mezclas con agua estudiando cómo las densidades, los números de coordinación, las funciones de distribución radial y el número de enlaces de hidrógeno cambia en la mezcla. Como resultado, encontramos una imagen estructural que difiere notablemente de la presentada para mezclas con agua en el Capítulo 2.1. En particular, no hay formación de clusters de moléculas de alcohol, las cuáles, en lugar de eso, están distribuidas de manera prácticamente homogénea en el bulk y están situadas aproximadamente a la misma distancia de todas las otras especies de la mezcla. Cabe destacar que en las mezclas con el anión más solvofóbico se puede afirmar que se forma una cierta red, pero su tamaño no es ni siquiera comparable al encontrado en mezclas con agua. Este comportamiento diferente es debido al carácter anfifílico de las moléculas de alcohol, lo cual permite que se inserten en las zonas polares y apolares del bulk. Este proceso en el cual la estructura nanosegregada de los líquidos iónicos acomoda las partes similares de los alcoholes se denomina solvatación nanoestructurada.

En el Capítulo 2.3 expandimos el análisis comenzado en el Capítulo 2.2 y confirmamos que las diferencias encontradas entre las propiedades estructurales entre agua y alcoholes en mezclas con líquidos iónicos también tiene un

profundo impacto en el comportamiento de la dinámica de partícula de estos sistemas. Al contrario de lo que sucedía en mezclas acuosas, el movimiento vibrante relacionado con un efecto de caja no se encontró para moléculas de alcohol debido a la ausencia de formación de clusters y a su mayor abilidad para difundir en el bulk de las mezclas. Esto refuerza la imagen de las moléculas de alcohol solvatadas casi de manera homogénea en las áreas polares y apolares de la mezcla, contrariamente a la mayor lipofobicidad de las moléculas de agua que las restringe a situarse en los dominios polares de la mezcla, en los cuáles forman clusters. El único aspecto que las moléculas de alcohol comparten con las de agua es la solvatación nanoestructurada. Es decir, estos solutos no son capaces de destruir la estructura nanosegregada de los líquidos iónicos, sino que se adaptan a ella y se sitúan en los lugares más favorables de la mezcla, lo cual indudablemente tiene un gran efecto las propiedades dinámicas y estructurales de los sistemas resultantes. Además, se confirma que la naturaleza del anión juega un papel dominante en las propiedades dinámicas y estructurales de las mezclas de líquidos iónicos con disolventes moleculares.

La importancia de los líquidos iónicos en electroquímica es tal que el desarrollo de dispositivos electroquímicos eficientes implica el uso de líquidos iónicos para mejorar las propiedades de transporte iónico. Muchos líquidos iónicos ofrecen una serie de propiedades (conductividad, viscosidad, y amplia ventana de potencial electroquímico) que los hace muy atractivos para ser utilizados en numerosos dispositivos electroquímicos, tales como celdas solares, celdas de combustible, baterías de litio y supercondensadores. Con el objetivo de comprender mejor el papel de los líquidos iónicos en estos dispositivos, en el Capítulo 2.4 se incluye una descripción detallada de las propiedades estructurales y de transporte iónico de líquidos iónicos dopados con sales de litio. Para este propósito, consideramos líquidos iónicos basados en el catión 1-butil-3-metilimidazolio y tres aniones distintos (hexafluorofosfato, tetrafluoroborato y bis(trifluorometilsulfonil)imida) mezclados con sales de litio y sodio con un anión común. Como en las mezclas con disolventes moleculares, las bases de la solvatación nanoestructurada también se encontraron en mezclas con sales alcalinas. En este aspecto, los cationes de la sal están principalmente restringidos a situarse en las regiones polares de las mezclas, en las cuales están fuertemente coordinados con los aniones adoptando dos posibles conformaciones (monodentada y bidentada) en la primera capa de solvatación que son sensibles a la cantidad de sal presente en la mezcla. Esto conduce a la formación de agregados longevos que actúan como entidades cinéticas estables

dentro de las cuáles se registra un movimiento vibrante de los iones de la sal. Esta estructura es extraordinariamente resistente y sobrevive durante decenas de nanosegundos. A la primera celda de solvatación de aniones le sigue una segunda capa de moléculas de litio/sodio y una tercera celda de cationes imidazolio, lo cual recuerda a la estructura de pseudored que se corresponde con el modelo estructural de la teoría de Bahe-Varela. El análisis de los coeficientes de autodifusión nos permitieron calcular los valores de la conductividad iónica; sin embargo, la necesidad de utilizar campos de fuerzas polarizables para obtener propiedades dinámicas adecuadas nos llevó a obtener datos ligeramente subestimados.

Aunque la investigación de las baterías de litio se ha centrado normalmente en el uso de líquidos iónicos apróticos como electrolitos, los líquidos iónicos próticos también deben ser considerados como una alternativa a los electrolitos convencionales, ya que el coste y la dificultad de sintetizar líquidos iónicos próticos son menores que en el caso de los líquidos iónicos apróticos y se ha confirmado experimentalmente que se pueden utilizar como electrolitos en este tipo de dispositivos. De este modo, en el Capítulo 2.5 extendemos el estudio a las características estructurales de disoluciones de nitrato de litio en un líquido iónico prótico, nitrato de etilamonio. El análisis de las densidades, las funciones de distribución radial, las funciones de distribución espacial, los enlaces de hidrógeno y los números de coordinación mostró la misma imagen estructural que la que describimos en el Capítulo 2.4, en la cual los cationes de la sal forman agregados aniónicos con los aniones de la primera capa de solvatación en las nanoregiones polares que se organizan como una pseudored. El estudio de la función de autocorrelación de velocidades de los cationes de litio confirmó la presencia de cajas que los rodeaban y que estaban formadas por los aniones más cercanos, tal y como se observó en disoluciones de sales de litio en líquidos iónicos apróticos. La famosa red de enlaces de hidrógeno que tiene lugar en líquidos iónicos próticos resulta ligeramente perturbada al añadir sal a la mezcla, debido a la presencia de cationes de litio en las regiones polares del bulk y su fuerte coordinación con los aniones nitrato, lo cual conduce a la transferencia de los aniones nitrato a las regiones internas de los nanodominios polares en los cuales se sitúan los cationes de litio. Además, incluso aunque podríamos esperar que esta mezcla se comportase como una sal fundida, su comportamiento es más similar al de una estructura de tipo sólido, con ordenamiento de medio alcance y picos dobles en las funciones de distribución radial litio-anion que imitan la estructura de tipo calcita característica

del nitrato de litio sólido. Esta formación de agregados de tipo sólido conduce a una separación de fases al aumentar la cantidad de sal.

El Capítulo 2.6 incluye un análisis de la influencia de la longitud de la cadena del catión alquilamonio en las propiedades estructurales de los líquidos iónicos próticos cuando se dopan con sales de litio. En esta ocasión estudiamos mezclas de nitrato de propilamonio y nitrato de butilamonio con una sal con anión común, nitrato de litio. De este modo, el aumento de la longitud de la cadena alquílica provoca un aumento de la segregación de la mezcla, dando lugar a dominos polares y apolares mejor definidos, menos empaquetados y con una estructura menos resistente. Sin embargo, a pesar de las regiones polares y apolares mejor definidas a mayores longitudes de cadena, los dominios polares de las mezclas con nitrato de propilamonio y nitrato de butilamonio parecen estar, en promedio, menos ordenados que en mezclas con nitrato de etilamonio. Este aumento del desorden de las orientaciones en las nanoregiones podría estar asociado con el colapso del enlace de hidrógeno direccional en el interior de las nanoregiones polares. Además, la perturbación de la red de enlaces de hidrógeno era más pronunciada a medida que aumentaba la longitud de la cadena del catión, lo cual es debido al menor grado de enlace de hidrógeno en estas mezclas. Cabe destacar que la estructura de los líquidos iónicos tanto próticos como apróticos es muy resistente a la incorporación de cualquier tipo de aditivo, incluyendo agua, alcoholes y sales. Se encontró que las regiones polares experimentaron una compresión a medida que aumentaba la longitud de la cadena catiónica, lo cual se asocia a una disminución de su fracción volúmica mediante un "efecto de dilución". Al mismo tiempo, estos dominios polares mostraron una expansión al aumentar la cantidad de sal en el sistema, lo cual se debe al aumento del número de iones en estas regiones asociado a la disminución del número de enlaces de hidrógeno. A pesar de todo, los dominios polar y apolares del bulk de las mezclas se erosionaron solo ligeramente por la presencia de solutos, cuya solvatación tiene lugar acomodando las fracciones de las moléculas de soluto en las regiones de los líquidos iónicos nanoestructurados anfifílicamente que son más parecidas a sus entidades moleculares.

La simulación de sistemas más realistas es un paso necesario para una comprensión más profunda del uso potencial de los líquidos iónicos en electroquímica. El Capítulo 2.7 cierra el proyecto de investigación de esta tesis con el estudio de mezclas de líquidos iónicos con sales alcalinas confinadas entre dos paredes de grafeno. Los sistemas estudiados fueron tetrafluoroborato de

1-butil-3-metilimidazolio mezclado con tetrafluoroborato de litio y con tetrafluoroborato de potasio entre dos electrodos de grafeno paralelos cargados y descargados. Estas simulaciones se llevaron a cabo a 450 K para evitar que el sistema quedase "atrapado" en un mínimo local debido a la elevada viscosidad de los líquidos iónicos, pero es de esperar que los resultados sean representativos del comportamiento de estos sistemas a temperaturas ligeramente menores. El análisis de la estructura confirmó que el líquido iónico adopta una estructura altamente inhomogénea en las proximidades de la superficie, en las cuáles se forman capas de cationes y aniones cuyas densidades iónicas son más elevadas que en el bulk debido al sobre apantallamiento en la distribución de la carga de los líquidos iónicos. Este comportamiento también se obtuvo en presencia de paredes de grafeno sin carga y conduce a la electroneutralidad a distancias largas desde los electrodos, donde se alcanzan los valores de la densidad del bulk. Cuando la carga de las paredes aumenta los iones experimentan una reorganización sistemática, en la cual los aniones se segregan hacia el electrodo positivo y los cationes hacia el negativo. Además, la orientación media de los anillos del catión imidazolio varía desde un ángulo de 36° con respecto al vector normal de la superficia a una configuración más perpendicular a medida que aumenta el potencial del electrodo. Como hemos visto en capítulos anteriores, la inclusión de sal en la mezcla no tiene demasiado impacto en la organización de los iones del líquido iónico cerca de las paredes de grafeno. Así, la solvatación nanoestructurada podría considerarse como un mecanismo universal de solvatación en estos disolventes iónicos nanoestructurados anfifílicamente. Aunque podría esperarse que la distribución de los cationes de litio y potasio estuviese gobernada por el potencial del electrodo, lo cierto es que está determinada principalmente por la estructura que adopta el líquido iónico y por la formación de los agregados iónicos que los cationes de sal organizan con los aniones de su primera capa de solvatación. De este modo, los cationes de litio y potasio son capaces de adsorverse en la superficie negativa solo a altas concentraciones de sal debido a la aparición de barreras de energía libre muy elevadas que deben superar para poder alcanzar la pared.

Esta tesis termina con un breve resumen de las conclusiones principales.

Agradecimientos

Me gustaría utilizar estas líneas para expresar mi más profundo y sincero agradecimiento a todas aquellas personas que, de una manera u otra, han colaborado en la realización de la presente tesis. Espero no olvidarme de nadie.

- A mis directores de tesis, D. Luis Miguel Varela Cabo y D. Luis Javier Gallego del Hoyo, por vuestra inestimable ayuda y vuestros consejos, sin los cuales esta tesis no hubiera sido posible; pero sobre todo por vuestro apoyo y confianza a lo largo de estos años.
- A mis compañeros del grupo de Nanomateriales y Materia Blanda, especialmente a Jesús Carrete Montaña; parte de esta tesis es tan tuya como mía.
- A Dª. Ruth M. Lynden Bell y a D. Jonathan Doye, por vuestra colaboración y ayuda durante mis meses de estancia en vuestros departamentos de las Universidades de Cambridge y Oxford, respectivamente.
- A mis amigos, por vuestra compañía y por los buenos momentos que hemos pasado juntos.
- A Ismael, por tu apoyo incondicional, tu paciencia y tu comprensión tanto en las buenas como en las malas.
- A mi familia, por vuestro apoyo y estímulo no sólo durante la realización de esta tesis, sino a lo largo de toda mi vida. Especialmente doy las gracias a mis padres, por haberme convertido en la persona que soy ahora, por vuestro cariño, vuestra ayuda y porque siempre habéis creído en mí. No hay palabras suficientes para dejar en estas páginas un agradecimiento como el que os merecéis.

También deseo agradecer al Centro de Supercomputación de Galicia las numerosas horas de procesador puestas a mi disposición, y al Ministerio de Educación su financiación de esta tesis mediante una beca del programa de Formación de Profesorado Universitario (FPU). La tesis fue realizada con las ayudas de los proyectos 10-PXI-103-294 PR, 10-PXIB-206-294 PR y GPC2013-043

(Xunta de Galicia), y del proyecto FIS2012- 33126 (Ministerio de Ciencia e Innovación); todos estos proyectos fueron financiados parciamente con fondos FEDER. Deseo, asimismo, agradecer a la red Gallega de Líquidos Iónicos, REGALIs, CN 2012/120.

A mis padres

Contents

USC
UNIVERSIDADE
DE SANTIAGO
DE COMPOSTELA

1 Introduction

In the end, scientists are lucky people: we play what we want for life.

Lee Smolin

1.1. Motivation and purpose

Due to the search of more secure, cleaner and more efficient energy sources and storage systems that we are experiencing nowadays, energy harvesting and storage are considered to be among the most important scientific and technological challenges of our time. The transition to a more sustainable energy system is unavoidable, which makes researchers devote significant efforts to the development of new, more efficient and greener electrochemical devices. A lot of new energy technologies and solutions rest upon devices such as batteries, supercapacitors, fuel cells, thermoelectrochemical cells, actuators, solar panels, superconductors (ionic liquid gating), electrodeposition and so on. In order to increase the efficiency of these devices, fundamental knowledge of all the physical processes involved in charge transport in the electrolyte, interaction with the device walls and electron transfer in the electrodes is needed. However, despite many efforts done in the last decades, this is far from being attained in general. More specifically, these processes are mostly unknown when the electrolytes are ionic liquids (ILs), nanostructured room-temperature molten salts forming a new class of "designer solvents" whose tunable properties and green reputation make them the most promising candidates nowadays for many electrochemical and thermoelectrochemical applications. A huge number of theoretical, experimental and simulation results are published each year concerning the properties of these systems, but many aspects of ionic solvation, charge transport in ILs, and of IL interaction with surfaces remain

largely unknown, limiting their effective applicability in electrochemical technology.

The beginning of the history of ILs dates back to the early twentieth century, when P. Walden studied ethylammonium nitrate (EAN) in 1914 [1], which is considered to be the first published example of an IL. However, it was not until approximately the year 2000 that the interest and activity in ILs began to expand at an exponential rate, with an annual number of publications going from 100 in that same year to well above 2000 in 2011 (seen by a search performed on SciFinder using "ionic liquids").

During the wide spread of these systems over the last 20 years, they have found many applications in a variety of research areas. For example, a few years ago ILs were mainly used to replace conventional molecular solvents for catalytic and organic reactions [2–5]. Nowadays, even though this interest undoubtedly continues, they are also being explored in many other fields. For example, many ILs are expected to be suitable for application in electrochemical devices including batteries, fuel cells, solar cells and supercapacitors [6, 7]. Much of the scientific effort is also directed towards employing ILs as thermal storage and heat transfer fluids [8, 9]. In addition to this, they are also being used as lubricants and fuel additives [10, 11]. There is also a number of ways to employ ILs in the area of separation: in gas separation, membrane separation processes, distillation and chromatography [12, 13]; and relatively recently in biomass processing and drug delivery [14, 15].

Due to the vast number of cations and anions that can be combined with each other, the amount of theoretically possible ILs is estimated to be as high as 10^6 binary or 10^{18} ternary systems [16] and the full potential of these solvents still remains unexplored. Thus, trying to increase their general understanding, one of the main focal points in IL research is the development of methods and techniques suitable to correlate properties and structure, not only in order to save experimental laboratory time and funds, but also to design and optimize ILs for many potential applications. For this purpose, computer simulations are currently considered as an esential tool to shed some light on various aspects of ILs at a level that can not be reached experimentally.

So, this thesis falls in this general framework and tries to get some insight into several structural and dynamic properties of pure ILs and their mixtures with organic solvents (water and alcohols) and salts of electrochemical interest, at the level of classical MD simulations, implemented by means of the Gromacs package. More specifically, the differences between water and

alcohols when mixed with AILs is discussed through the analysis of various properties such as density, radial distribution functions, coordination numbers, hydrogen bonds, mean-square displacements, ballistic and diffusive times and velocity autocorrelation functions. Mainly, it could be pointed out that, whereas water molecules tend to clusterize in the polar domains of the mixtures, alcohol molecules tend to be homogeneously distributed in both polar and apolar regions. Following the same path, the solvation process of alkali salts in PILs and AILs is compared and reported. For this purpose, radial distribution functions, coordination numbers, hydrogen bonds, spatial distribution functions and velocity autocorrelation functions have been analized. In both cases, the results clearly show how salt cations tend to place themselves in the polar regions of the bulk and to form aggregates with the anions of their first coordination shell. The main difference between these two types of systems is the well-known network of hydrogen bonds that takes place in PILs, which is gradually disrupted by the addition of salt to the mixture. Finally, the potential applications of ILs as electrolytes in electrochemical systems led us to simulate mixtures of AILs with lithium and potassium salts confined between two charged and uncharged graphene walls. In this case, the analysis of number density, free energy profiles and orientational distributions shows a clear layering behaviour of the IL in the proximities of the walls (even when they are uncharged) and salt ions are forced to adapt to this inhomogeneous structure. In addition, the distribution of both lithium and potassium cations is not mainly governed by the electrode potential but by the formation of anionic clusters that takes place as it happens in the bulk. All the studies carried out in this thesis clearly reveal that, regardless of the solute with which the IL is doped, the solvation of the solute molecules takes place by means of a nanostructured solvation; in which a resilient IL structure forces the additives to adapt to its configuration.

The rest of this chapter deals with the main characteristics of this new class of low-melting-point solvents and the methodology employed for the simulations. Right afterwards, the results obtained are analized and discussed and, finally, we summarize the main conclusions of this thesis.

1.2. Ionic liquids

Scientific literature uses the concept of IL to refer to compounds that are composed exclusively of ions. However, this specification includes an ad-

ditional characteristic that differentiates them from the classic definition of a molten salt. Whereas the term "molten salt" is attributed to a highly viscous medium that can reach the liquid phase at elevated temperatures, ILs are found in liquid state at moderate temperatures (they usually display a melting point lower than 100 ℃) and its viscosity is relatively low. This apparently arbitrary separation line between molten salts and ILs can be justified by taking into account the enormous amount of industrial applications in this range of temperatures.

As it has been mentioned in the previous section, this type of new dense ionic solvents has been known since 1914, due to the synthesis of EAN carried out by P. Walden [1]. Nevertheless, his study did not receive great attention at that time and it was not until 1948 that further activity was registered in the field, when the first detailed experimental description of an IL with chloroaluminate ions was reported [17]. This discovery remained a mere curiosity for several decades until the groups of Seddon and Hussey, in the 80's, started to use ILs as polar solvents to investigate transition metal complexes [18–20]. At about the same time, Evans *et al.* [21] investigated the aggregation of surfactants to form micelles in EAN by means of classical and quasi-elastic light scattering. As researchers performed studies about many chemical reactions in ILs, it was highlighted that their behaviour was different from that observed in traditional media, either polar or apolar. After almost 80 years of existence, the concept of IL became of fundamental importance due to the work of Wilkes and coworkers in 1992, when they described the synthesis of air and water stable ILs based on the 1-ethyl-3-methylimidazolium ($[Emim]^+$) cation [22]. Since then a huge number of publications has been reported and the vast majority of them are focused on the synthesis of new ILs [23, 24], the systematic research of their chemical properties [25–29] and their applications as solvents [2, 3, 30–35].

Concerning the chemical composition of ILs, it can be generally stated that they consist of large organic cations and small organic or inorganic anions (either monoatomic or polyatomic anions) [2, 36]. Among the most well-known ILs we can find organic cations such as N-alkyl-pyridinium ($[APyr]^+$) and 1-alkyl-3-methylimidazolium ($[Amim]^+$) combined with inorganic anions (see Figure 1.1) such as chloride ($[Cl]^-$), nitrate ($[NO_3]^-$), bis(trifluoromethanesulfonyl)imide ($[NTf_2]^-$), hexafluorophosphate ($[PF_6]^-$) and tetrafluoroborate ($[BF_4]^-$). ILs are believed to be found in liquid state due to the big size and shape asymmetry of their ions, which lead to weaker attractive forces and

Figure 1.1 Structures of the most common cations and anions of ILs (from http://www.sigmaaldrich.com/technical-documents/articles/chemfiles/ionic-liquids1.html).

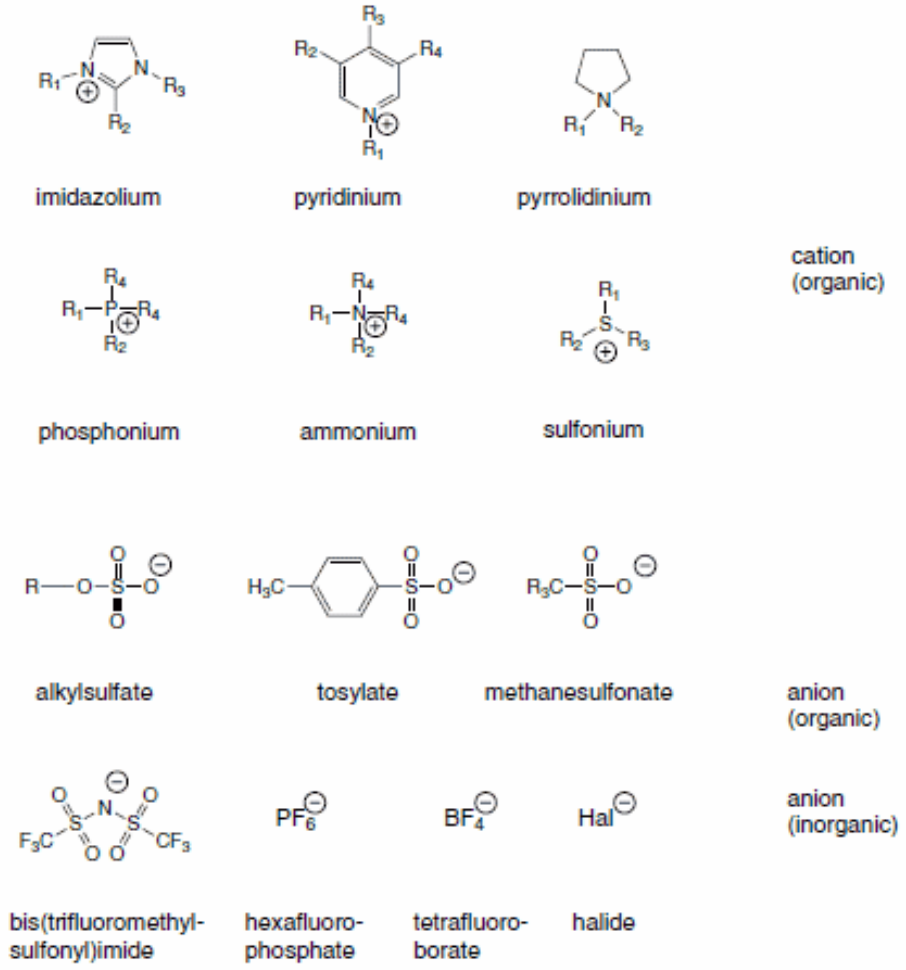

smaller lattice energies between cations and anions than in the case of molten salts preventing the formation of the compact lattice structure. Hence, even a small energy input, like the thermal energy at temperatures close to room temperature, can break the ionic bonds, whereas molten salts must be heated at much higher temperatures (e.g. around 800 °C for NaCl) to be melted.

As we mentioned in the previous section, Due to the great amount of available cations and anions, there is a wide range of possibilities when it comes to

select the most suitable IL for a specific application. That is the reason why ILs are also known as "designer solvents" [37]. Thus, synthesizing a new IL can be relatively easy, but determining its usefulness requires deep knowledge of its physicochemical properties. This is of fundamental importance for their industrial application, but the ideal situation of predicting the properties of a given IL by analyzing its chemical composition has not be reached yet. however, computational simulations are an essential tool for gaining insight into the relationship between the properties of ILs and their structure. In general, the cation can be considered responsible for the IL chemical behaviour, whereas the anion contributes to most of its physical properties [38].

Curiously, until recently ILs were thought to possess a homogeneous microstructure. However, in 2006 Canongia-Lopes and Pádua [39] observed, using molecular dynamics simulations, the aggregation of the alkyl chains of ILs that belong to the 1-alkyl-3-methylimidazolium family and whose length is longer that or equal to C_4 (1-butyl-3-methylimidazolium) to form non polar domains. This existence of nanoscale heterogeneities in ILs was experimentally confirmed by Triolo *et al.* [40] in 2007 by means of X-ray diffraction. To find nanoscale segregation in ILs whose alkyl chain is shorter than C_4 we must move to PILs, as pointed out by Atkin *et al.* [41] in 2008, when they reported the first experimental evidence of the formation of polar and apolar domains in EAN and propylammonoum nitrate (PAN).

Thereby, ILs are characterized by several special and unique physicochemical properties that make them very attractive for being used in different areas of research and industry. Among these characteristics, probably the most important are [42]:

- **Low vapor pressure:** The strong Coulombic interactions between ions within an IL results in negligible vapor pressure (almost undetectable) at temperatures up to their thermal decomposition temperatures. This is one of the most notorious properties of ILs, since it makes them easy to handle, excluding overpressures and air pollution in their applications.

- **High viscosity:** ILs are, in general, more viscous than conventional molecular solvents. As an example, their viscosities at room temperature usually vary between 10 and 1000 cP, while that of water is 0.890 cP. In addition, the temperature, as well as the presence of impurities, has a dramactic impact on the viscosity of ILs. Weakly coordinating anions

are found to lead to lower viscosities, whereas this magnitude generally increases with increasing the cation size.

- **High ionic conductivity and high electrochemical stability:** These two features make ILs very appealing for being used in electrochemical processes. Their intrinsic ionic conductivity, which is due to the fact that they are composed solely of ions, depends on the number of mobile charge carriers available in the system and on their mobilities. Since the number of charge carriers that can be found in ILs is greater than in electrolyte solutions and other ionic fluids, this somehow compensates their lower mobilities, due to higher viscosity. However, the conductivity of these liquids is usually of the order of 10^{-1} S/m, lower than that of conventional electrolytes [43, 44]. However, their electrochemical windows, whose size is affected by the presence of impurities, show values between 2.0 and 6.0 V and a great stability [45–47], far above that of aqueous electrolytes or those with organic solvents.

- **Wide liquid range and high thermal stability:** ILs can be found in liquid state in a range of temperatures far wider than molecular solvents. Many ILs employed as solvents are so stable that their short-term thermal decomposition temperature can reach values close to 350 °C, whereas their long-term thermal decomposition temperature can be close to 250 °C [48]. This means that there are no obtacles for using ILs in many high-temperature applications without significant solvent degradation. In addition, as they tipically show glass transition temperatures close to −80 °C, they have liquid ranges of over 350 °C.

- **High density:** Density values of most currently known ILs have been measured, since it must be known for many applications. In general, they are denser than water and, in contrast to other properties such as viscosity, density of ILs is not very sensitive to changes in temperature (e.g. Thermal expansion coefficients of ILs range between $5 - 7 \cdot 10^{-4}$ K^{-1} [49, 50], whereas water or ethanol show values of $2.1 \cdot 10^{-4}$ K^{-1} and $2.5 \cdot 10^{-4}$ K^{-1}, respectively).

- **Solubility and miscibility:** Polarity is usually considered the essential parameter that determines the ability of a solvent to dissolve a solute. ILs are generally considered as polar solvents as a consequence of their inherent ionic nature, but, as previously mentioned, they also usually

have apolar parts on their molecular structures. This dual nature gives rise to a peculiar amphiphilically induced nanostructure made of polar and apolar nanodomains, which makes them highly versatile solvents able to dissolve both polar and apolar substances. On the other hand, the miscibility of ILs with other solvents depends on the dielectric constant of the latter, so ILs are miscible with compounds with medium or high dielectric constants and inmiscible with liquids with low dielectric constant liquids.

- **Colour and variable pH:** ILs are usually colourless in their pure state. Sometimes they present certain colours due to the presence of impurities. Aditionally, the acidity of ILs varies widely depending on the nature of the anions and the cations.

- **Toxicity/biodegradability:** Thanks to the low volatility of ILs, they scarcely contribute to air pollution, being direct contact with the skin or ingestion the only possible ways of contamination. Although ILs are irritating, it is possible to design nontoxic ILs by the appropriate selection of the cation and the anion. It can not be stated that ILs or their synthesis processes are completely green, but it is true that they show several environmental benefits when used in chemical processes.

- **Protic or aprotic in character:** PILs are formed by the transfer of a proton between a Brønsted acid and a base, whereas AILs contain other substituents at the position of the labile proton. Thus, the synthesis of AILs needs strategies different from the acid-base reactions proper to PILs. The presence of proton-donor and proton-acceptor sites in PILs leads to the formation of a hydrogen-bonded network that highly resembles the three dimensional network of hydrogen bonds of water [51].

- **ILs as self-assembly media:** Aggregation behaviour of surfactants in ILs has attracted considerable attention due to their potential applications. The solvophobic interaction between the surfactant and the IL leads to the formation of micelles, which is similar to the self-assembly of amphiphilic molecules observed in aqueous solutions [52]. This formation of nanostructured aggregates can be controlled by the choice of the cation and anion of the IL. PILs are considered to be more appealing to support amphiphilic self-assembly due to their ability to form networks

of hydrogen bonds, but self-assembly nanostructures have also been reported in AILs.

1.3. Methods and models

The experimental analysis of the properties of ILs at a microscopic level can be complicated at times and, because of this reason, computer simulations are considered as a fundamental tool for understanding the properties and behaviour of this new class of solvents at this level. Even though the slow dynamics of ILs makes them not very easy to be investigated using computational techniques, the truth is that these methods play an increasingly important role in getting a deep knowledge of the fundamental nature of these compounds. The physical characterization of ILs by means of simulations has been significantly developed over the last decades and enormous progress has been achieved in the design of new potentials and more powerful computational tools, which was reflected in the increasing number of published computational studies in this field [53–55].

Several are the computational techniques employed for studying the characteristics of ILs, such as *ab initio* quantum chemical (AIQC), *ab initio* molecular dynamics (AIMD), Monte Carlo (MC) and molecular dynamics (MD) (see Figure 1.2). Each of them can pose specific problems when dealing with ILs. For example, whereas AIQC methods include polarization and charge transfer and are very suitable to accurately describe the electronic structure, they are computationally expensive and therefore not useful when it comes to analize a great number of molecules. On the other hand, MC and MD methods are appropriate for describing the liquid state, since they are capable of simulating a great number of ions interacting with each other. However, they can not be expected to adequately model the motion of the electrons within this kind of systems. AIMD methods fall somewhere in between, since they provide information about the electronic structure but can not be used to investigate a large number of molecules. Thus, in order to obtain a reasonably good analysis of ILs, it is of fundamental importance to deeply understand both the advantages and disadvantages of each and every technique and choose the most appropriate one depending on the size and time scales of the problem.

The doors opened for the study of ILs by means of computer modelling during the 2000*s* decade. Whereas the first MD simulation of ILs was reported in 2001 by Hanke *et al.* [56], quantum computer simulations

Figure 1.2 Modelling of ILs scheme (from B. Kirchner http://wet.kuleuven.be/english/summerschools/ionicliquids/lectures/kirchner.pdf).

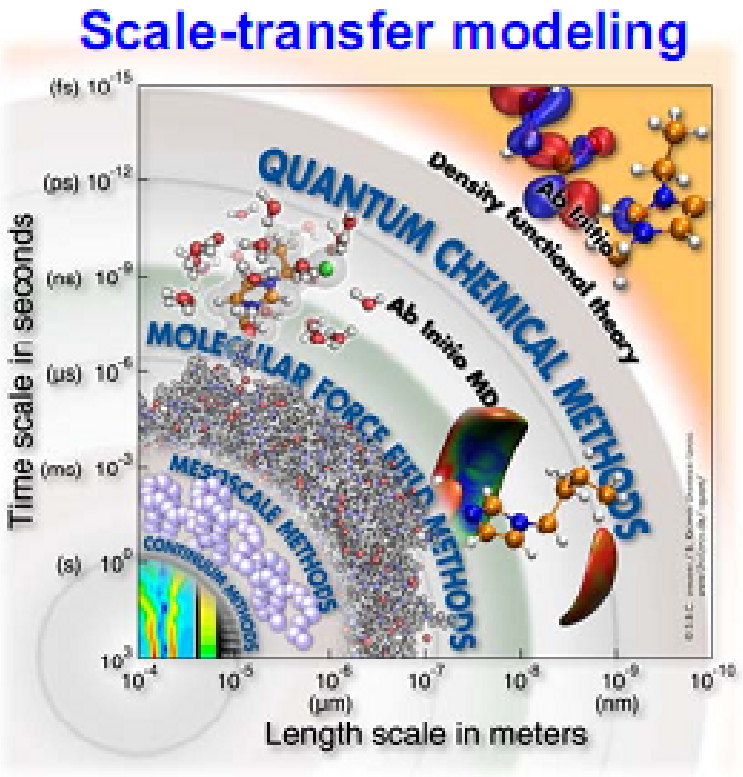

had to wait a couple of years more [57, 58]. In the first case, Lynden-Bell and coworkers [56] reported the development of intermolecular potentials for 1,3-dimethylimidazolium chloride ([dmim][Cl]), 1-ethyl-3-methylimidazolium chloride ([Emim][Cl]), 1,3-dimethylimidazolium hexafluorophosphate ([dmim][PF_6]) and 1-ethyl-3-methylimidazolium hexafluorophosphate ([Emim][PF_6]), and included results for the structure and dynamics of these four ILs. Only a year later, Maginn and coworkers [59] carried out for the first time MC simulations of 1-butyl-3-methylimidazolium hexafluorophosphate ([Bmim][PF_6]) to calculate several properties such as molar volume, isothermal compressibility, volumetric expansion coefficient and cohesive energy density. Again on the question of quantum methods, in 2003 Turner

et al. [57] investigated ILs based on 1-alkyl-3-methylimidazolium halides by means of AIQC calculations. They analyzed the correlations between interaction energy and melting point, as well as between interaction energy and alkyl chain length. Two years later the first AIMD simulations arrived to the field of ILs, when del Pópolo *et al.* [58] compared the local liquid structure of [dmim][Cl] from density functional theory with that obtained from two classical force fields and from neutron scattering experiments.

Next we go deeper into the theory of MD simulations [60–62], since all the studies concerning ILs that are presented in this thesis were performed using this methodology. Without claiming to be exhaustive, since more details will be provided in each of the specific sections of the next chapter, we would like to highlight the most remarkable contributions reported up to date in this field. The first MD simulations applied to the comprehension of ILs were devoted to pure ILs. As an example, Urahata and Ribeiro [63] performed in 2004 a detailed study of the structure of ten different ILs (the anion size as well as the length of the alkyl chain were systematically varied) and they showed that large anions tend to place themselves in the regions above and below the imidazolium ring of the cation. A year later they expanded their analysis with the investigation of single-particle dynamics of the same systems [64] and found that ionic displacement of cations was larger than that of anions. A moment with a before and an after in the study of pure ILs was undoubtedly the publication of the aggregation of alkyl chains larger than C_4 in apolar domains by Canongia-Lopes and Pádua [39] using MD simulations. Furthermore, the knowledge of the interaction between water and ILs has been considered to be of fundamental importance and has attracted considerable interest. The first MD simulations of mixtures of 1,3-dialkylimidazolium ionic liquids ([dmim][Cl] and [dmim][PF_6]) with water were performed by Hanke and Lynden-Bell in 2003 [65], when they reported the formation of a continous water network at high water concentrations. Even though they are also very relevant for industrial applications, mixtures of ILs with alcohols have attracted much less attention than those with water. Among the former we can find the analysis carried out by Jahangiri *et al.* [66], in which they implemented MD simulations of [Emim][Cl], [Emim][PF_6], 1-propyl-3-methylimidazolium hexafluorophosphate ([Pmim][PF_6]) and [Bmim][PF_6] mixed with methanol and ethanol with the aim of analyzing structural and physical properties of the resulting mixtures. Another challenging topic in the field of ILs is their use as electrolytes in electrochemical applications; however, despite the considerable

amount of experimental results, the behaviour of ILs between electrodes has remained much less explored by molecular simulations. As an example, Fedorov and coworkers [67, 68] studied the interfacial layer formation provided by [dmim][Cl] in the proximities of a charged and uncharged graphite wall. They also investigated the free energy profiles for probes of different sizes as a function of the distance from the wall. In order to improve the modelling of these systems, porous electrodes have also been analized by Merlet *et al.* [69] with simulations of [Bmim][PF_6] confined between realistically modelled microporous carbon electrodes.

Concerning this modelling technique, MD simulations generate information at the microscopic level by solving Newton's equations of motion for a system of N interacting atoms:

$$m_i \frac{\partial^2 \vec{r}_i}{\partial t^2} = \vec{F}_i, \; i = 1...N. \tag{1.1}$$

The forces are also expressed as the gradient of the potential energy of the system:

$$\vec{F}_i = -\frac{\partial V}{\partial \vec{r}_i} \tag{1.2}$$

Integration of the equations of motion provide us with a trajectory that describes the positions, velocities and acelerations of the particles as a function of time. After some time, the system reaches an equilibrium state from which the average values of several properties can be determined.

All the simulations of this thesis were carried out using the open source Gromacs 4.5.4 package [70, 71], which is one of the most popular software packages available; not only for being one of the fastest programs but also due to its ease of use. The velocity Verlet algorithm is implemented in Gromacs [72], but the *leap-frog* algorithm [73] is used by default when it comes to integrate the equations of motion. The positions and velocities are updated employing the forces $\vec{F}(t)$ by means of these relations:

$$\vec{v}(t + \frac{1}{2}\Delta t) = \vec{v}(t - \frac{1}{2}\Delta t) + \frac{\Delta t}{m}\vec{F}(t)$$

$$\vec{r}(t + \Delta t) = \vec{r} + \vec{v}(t + \frac{1}{2}\Delta t)\Delta t \tag{1.3}$$

On the other hand, Gromacs includes the potential functions of the most popular force fields (AMBER, CHARMM, GROMOS and OPLS). The potential energy functions are of the form:

$$V = V_{non-bonded} + V_{bonded} + V_{restraints} \tag{1.4}$$

Non-bonded interactions, $V_{non-bonded}$, include a repulsion term, a dispersion term, and a Coulomb term. Bonded interactions,V_{bonded} , contain the bond stretching, bond angle and dihedral angle interactions. Finally, in some special cases (due to the need of avoiding disastrous deviations or to include some experimental data) it is necessary to impose restraints on the motion of the system, but they are not really part of the force field.

In our case, among the force fields implemented in Gromacs we chose GROMOS-96 [74] so as to perform the simulations reported in 2.1. This is a united atom force field, that is to say, it does not include explicitely a representation of nonpolar hydrogen atoms. However, from paper 2.2 on, we chose an all-atom force field, OPLS-AA [75], to carry out the simulations with the aim of obtaining more realistic results. The explicit form of these potentials are reported in the corresponding sections of the next chapter. It must be noted that despite both being non-polarizable potentials they lead to very accurate structural predictions and qualitatively correct dynamic results.

Initial arrangements of the molecules were built using PACKMOL [76]. The molecules were randomly distributed in such a way to let atoms from different molecules to keep safe pairwise distances of 2.5 Å, and the sides of the cubic box were a 10% larger than those corresponding to the experimental density.

In order to avoid problems related to edge effects caused by the finite size of our systems, we applied periodic boundary conditions, i.e. to mimic an infinite system the simulation box was surrounded by translated copies of itself, which means that if any atom leaves the box by the right-hand face, it enters the box by the left-hand face. This artifact was combined with the minimum image convention, with which short-range non-bonded interactions only takes into account the nearest image of each particle. Additionally, in order to get accurate long-range electrostatic interactions we employed lattice sum methods such as Particle Mesh Ewald [77].

Simulations of ILs confined between walls were slightly different from the rest of the studies and they needed several specific requirements. The graphene electrodes, whose carbon atoms were frozen in all three spatial

directions, were built with the help of the Visual Molecular Dynamics (VMD) package [78]. Due to the use of periodic boundary conditions, a slab of vacuum must be included outside the walls in order to avoid artificial influence of the images. In addition, Yeh–Berkowitz corrections [79, 80] were needed for calculating long range interacions in this kind of 3D systems periodic in 2D.

Further details of each simulation are given in the specific sections of the next chapter.

References

1. Walden, P. *Bull. Russian Acad. Sci.* **1800,** 405–422 (1914).
2. Wasserscheid, P. & Keim, M. *Angew. Chem. Int. Ed. Engl.* **39,** 3772–3789 (2000).
3. Welton, T. *Chem. Rev.* **99,** 2071–2084 (1999).
4. Hallett, J. P. & Welton, T. *Chem. Rev.* **111,** 3508–3576 (2011).
5. Yue, C., Fang, D., Liu, L. & Yi, T. *J. Mol. Liq.* **163,** 99–121 (2011).
6. MacFarlane, D. R., Forsyth, M., Howlett, P. C., Pringle, J. M., Sun, J., Annat, G., Neil, W. & Izdorodina, E. *Acc. Chem. Res.* **40,** 1165–1173 (2007).
7. Armand, M., Endres, F., MacFarlane, D. R., Ohno, H. & Scrosati, B. *Nat. Mat.* **8,** 621–629 (2009).
8. Valkenburg, M. E. V., Vaughn, R. L., Williams, M. & Wilkes, J. S. *Thermochim. Acta* **425,** 181–188 (2005).
9. Reddy, R. G., Zhang, Z., Arenas, M. F. & Blake, D. M. *High Temp. Mat. Proc.* **22,** 87–94 (2003).
10. Ye, C., Liu, W., Chen, Y. & Yu, L. *Chem. Commun.* **2001,** 2244–2245 (2001).
11. Bermúdez, M., Jiménez, A., Sanes, J. & Carrión, F. *Molecules* **14,** 2888–2908 (2009).
12. Han, X. & Armstrong, D. W. *Acc. Chem. Res.* **40,** 1079–1086 (2007).
13. Berthod, A., Ruiz-Angel, M. J. & Carda-Broch, S. *J. Chromatogr. A* **1184,** 6–18 (2008).
14. Hough, W. L., Smiglak, M., Rodríguez, H., Swatloski, R. P., Spear, S. K., Daly, D. T., Pernak, J., Grisel, J. E., Carliss, R. D., Soutullo, M. D., Davis, J. H. & Rogers, R. D. *New J. Chem.* **31,** 1429–1436 (2007).

15. Tadesse, H. & Luque, R. *Energy Environ. Sci.* **4,** 3913–3929 (2011).

16. Carmichael, A. J. & Seddon, K. R. *J. Phys. Org. Chem.* **13,** 591–595 (2000).

17. Hurley, F. H. & Wier, T. P. *J. Electrochem. Soc.* **98,** 207–212 (1951).

18. Scheffler, T. B., Hussey, C. L., Seddon, K. R., Kear, C. M. & Armitage, P. D. *Inorg. Chem.* **22,** 2099–2100 (1983).

19. Laher, T. M. & Hussey, C. L. *Inorg. Chem.* **22,** 3247–3251 (1983).

20. Scheffler, T. B. & Hussey, C. L. *Inorg. Chem.* **23,** 1926–1932 (1984).

21. Evans, D. F., Yamauchi, A. & Wei, G. J. *J. Phys. Chem.* **87,** 3537–3541 (1983).

22. Wilkes, J. S. & Zaworotko, M. J. *J. Chem. Soc., Chem. Commun.* **1992,** 965–967 (1992).

23. Dzyuba, S. V., Kollar, K. D. & Sabnis, S. S. *J. Chem. Educ.* **86,** 856–858 (2009).

24. Kim, D. J., Oh, K. H. & Park, J. K. *Green Chem.* **16,** 4098–4101 (2014).

25. Suarez, P. A. Z., Einloft, S., Dullius, J. E. L., de Souza, R. F. & Dupont, J. *J. Chim. Phys.* **95,** 1626–1639 (1998).

26. Tokuda, H., Hayamizu, K., Ishii, K., Susan, M. A. B. H. & Watanabe, M. *J. Phys. Chem. B* **108,** 16593–16600 (2004).

27. Tokuda, H., Hayamizu, K., Ishii, K., Susan, M. A. B. H. & Watanabe, M. *J. Phys. Chem. B* **109,** 6103–6110 (2005).

28. Tokuda, H., Ishii, K., Susan, M. A. B. H., Tsuzuki, S., Hayamizu, K. & Watanabe, M. *J. Phys. Chem. B* **110,** 2833–2839 (2006).

29. Marsh, K. N., Boxall, J. A. & Lichtenhaler, R. *Fluid Phase Equilib.* **10,** 93–98 (2004).

30. Wilkes, J. S. *J. Mol. Catal. A: Chem.* **214,** 11–17 (2004).

31. Olivier-Bourbigou, H. & Magna, L. *J. Mol. Catal. A: Chem.* **182–183,** 419–437 (2002).

32. Keskin, S., Kayrak-Talay, D., Akman, U. & Hortaçsu, O. *J. Sup. Fluids* **43,** 150–180 (2007).

33. Andreani, L. & Rocha, J. D. *Braz. J. Chem. Eng.* **29,** 1–13 (2012).

34. Ghandi, K. *Green and Sustainable Chemistry* **4,** 44–53 (2014).

35. Pandey, S. *Anal. Chim. Acta* **556,** 38–45 (2006).

36. Wasserscheid, P. & Welton, T. *Ionic liquids in synthesis* (Wiley Online Library, 2003).

37. Plechkova, N. V. & Seddon, K. R. in *Methods and Reagents for Green Chemistry* 103–130 (John Wiley & Sons, Inc., 2007).

38. Mohammad, A. & Inamuddin. *Green solvents II. Properties and applications of ionic liquids* (Springer, 2012).

39. Canongia-Lopes, J. N. & Pádua, A. A. H. *J. Phys. Chem. B* **110,** 3330–3335 (2006).

40. Triolo, A., Russina, O., Bleif, H.-J. & Di Cola, E. *J. Phys. Chem. B* **111,** 4641–4644 (2007).

41. Atkin, R. & Warr, G. G. *J. Phys. Chem. B* **112,** 4164–4166 (2008).

42. Freemantle, M. *An Introduction to Ionic Liquids* (RSC Publishing, 2009).

43. Sato, T., Maruo, T., Marukane, S. & Takagi, K. *J. Power Sources* **138,** 253–261 (2004).

44. Lee, J. S., Bae, J. Y., Lee, H., Quan, N. D. & Kim, H. S. *J. Ind. Eng. Chem.* **10,** 1086–1089 (2004).

45. Buzzeo, M. C., Evans, R. G. & Compton, R. G. *Chem. Phys. Chem.* **5,** 1106–1120 (2004).

46. Endres, F. & Abedin, S. Z. E. *Phys. Chem. Chem. Phys.* **8,** 2101–2116 (2006).

47. Galiński, M., Lewandowski, A. & Stepniak, I. *Electrochim. Acta* **51,** 5567–5580 (2006).

48. Cao, Y. & Mu, T. *Ind. Eng. Chem. Res.* **53,** 8651–8664 (2014).

49. Rocha, M. A. A., Ribeiro, F. M. S., Lobo-Ferreira, A. I. M. C., Coutinho, J. A. P. & Santos, L. M. N. B. F. *J. Mol. Liq.* **108,** 196–202 (2013).

50. Capelo, S. B., Méndez-Morales, T., Carrete, J., Lago, E. L., Vila, J., Rodríguez, O. C. J. R., Turmine, M. & Varela, L. M. *J. Phys. Chem. B* **116,** 11302–11312 (2012).

51. K. Fumino, A. W. & Ludwig, R. *Angew. Chem. Int. Ed.* **48,** 3184–3186 (2009).

52. Fernández-Castro, B., Méndez-Morales, T., Carrete, J., Fazer, E., Cabeza, O., Rodríguez, J. R., Turmine, M. & Varela, L. M. *J. Phys. Chem. B* **115,** 8145–8154 (2011).

53. Hunt, P. A. *Mol. Sim.* **32,** 1–10 (2006).

54. Bhargava, B. L., Balasubramanian, S. & Klein, M. L. *Chem. Commun.* 3339–3351 (2008).

55. Maginn, E. J. *J. Phys.: Condens. Matter* **21,** 373101(1)–373101(17) (2009).

56. Hanke, C. G., Price, S. L. & Lynden-Bell, R. M. *Mol. Phys.* **99,** 801–809 (2001).

57. Turner, E. A., Pye, C. C. & Singer, R. D. *J. Phys. Chem. A* **107,** 2277–2288 (2003).

58. Pópolo, M. G. D., Lynden-Bell, R. M. & Kohanoff, J. *J. Phys. Chem. B* **109,** 5895–5902 (2005).

59. Shah, J. K., Brennecke, J. F. & Maginn, E. J. *Green Chem.* **4,** 112–118 (2002).

60. Frenkel, D. & Smit, B. *Understanding molecular simulation: From algorithms to applications* (Academic Press: New York., 1996).

61. Hansen, J. P. & McDonald, I. R. *Theory of simple liquids* (Academic press: Oxford, 1986).

62. Allen, M. P. & Tildesley, D. J. *Computer Simulations of Liquids* (Oxford University Press, 1987).

63. Urahata, S. M. & Ribeiro, M. C. C. *J. Chem. Phys.* **120,** 1855–1863 (2004).

64. Urahata, S. M. & Ribeiro, M. C. C. *J. Chem. Phys.* **122,** 024511(1)–024511(9) (2005).

65. Hanke, C. G. & Lynden-Bell, R. M. *J. Phys. Chem. B* **107,** 10873–10878 (2003).

66. Jahangiri, S., Taghikhani, M., Behnejad, H. & Ahmadi, S. J. *Mol. Phys.* **106,** 1015–1023 (2008).

67. Lynden-Bell, R. M., Frolov, A. I. & Fedorov, M. V. *Phys. Chem. Chem. Phys.* **14,** 2693–2701 (2012).

68. Fedorov, M. V. & Lynden-Bell, R. M. *Phys. Chem. Chem. Phys.* **14,** 2552–2556 (2012).

69. Merlet, C., Rotenberg, B., Madden, P. A., Taberna, P.-L., Simon, P., Gogotsi, Y. & Salanne, M. *Nat. Mater.* **11,** 306–310 (2012).

70. Spoel, D. V. D., Lindahl, E., Hess, B., Buuren, A. R. V., Apol, E., Meulenhoff, P. J., Tieleman, D. P., Sijbers, A. L. T. M., Feenstra, K. A., Drunen, R. V. & Berendsen, H. J. C. *Gromacs User Manual version 4.0* (http://www.Gromacs.org, 2005).

71. Hess, B., Kutzner, C., Spoel, D. V. D. & Lindahl, E. *J. Chem. Theory Comput.* **4,** 435–447 (2008).

72. Swope, W. C., Andersen, H. C., Berens, P. H. & Wilson, K. R. *J. Chem. Phys.* **76,** 637–649 (1982).

73. Hockney, R. W., Goel, S. P. & Eastwood, J. W. *J. Comp. Phys.* **14** (1974).

74. Scott, W. R. P., Hünenberger, P. H., Tironi, I. G., Mark, A. E., Billeter, S. R., Fennen, J., Torda, A. E., Huber, T., Krüger, P. & Gunsteren, W. F. V. *J. Phys. Chem. A* **103,** 3596–3607 (1999).

75. Jorgensen, W. L., Maxwell, D. S. & Tirado-Rives, J. *J. Am. Chem. Soc.* **118,** 11225–11236 (1996).

76. Martínez, L., Andrade, R., Birgin, E. G. & Martínez, J. M. *J. Comput. Chem.* **30,** 2157–2164 (2009).

77. Darden, T., York, D. & Pedersen, L. *J. Chem. Phys.* **98,** 10089–10094 (1993).

78. Humphrey, W., Dalke, A. & Schulten, K. *J. Mol. Graphics* **14,** 33–38 (1996).

79. Yeh, I. & Berkowitz, M. L. *J. Chem. Phys.* **111,** 3155–3162 (1999).

80. Yeh, I. & Berkowitz, M. L. *J. Chem. Phys.* **112,** 10491–10495 (2000).

2 Results and discussion

> There is only one science, physics: everything else is social work.
>
> James D. Watson

This chapter includes the full description of the results obtained in the thesis work. The common goal of all of them was to get a detailed picture of solvation and transport mechanism in these dense ionic solvents. For that we analyzed the structure and single-particle dynamics of mixtures of ILs (protic and aprotic) with molecular cosolvents (water and alcohols) and with salts in homogeneous (bulk) and inhomogeneous (interface) conditions. For all these systems we studied the influence of the nature of the anions, of the cationic chain length and of the solvent concentration on the behaviour of the solutions. For this purpose, not only structural properties such as hydrogen bonds, radial distribution functions or coordination numbers were investigated, but also single-particle dynamics (self-diffusion coefficients, velocity autocorrelation functions, mean square displacements or ballistic and diffusive times). The main difference between the two types of cosolvent analyzed when mixed with ILs is the fact that, whereas water molecules are solvated forming clusters in the polar nanoregions of the bulk, alcohol molecules are homogeneusly solvated between apolar and polar nanoregions of the mixture. Another step forward in the research of ILs was given with the studies of both protic and aprotic ILs doped with inorganic salts. Once again, the solvation process that takes place in the bulk mixtures was evaluated as a function of the length of the IL cation, of the nature of the anions as well as of the cations of the added salt and of the amount of salt present in the system. The analysis of radial distribution functions, hydrogen bonds, coordination numbers and spatial distribution functions revealed that, in all cases, lithium and sodium cations of the salt are strongly coordinated with the anions present in the polar regions of the

bulk, which gives rise to the formation of stable anionic clusters that diffuse in a bonded-like state. Interestingly, our evidences shown that these bonded-like structures, formed by a central lithium cation and the anions within its first coordination shell, lead to a solid-like short ranged-order different from the expected molten salt-like behaviour. In addition, in mixtures with PILs we found a progressive disruption of the PIL network of hydrogen bonds due to the lithium cations placing themselves in the apolar nanodomains of the system, this effect being more pronounced for PILs whose cations have longer alkyl chains due to the lower degree of hydrogen bonding among their constituents. Finally, we moved to simulations of ILs near the electrodes of electrochemical devices, for which we investigated mixtures of aprotic ILs with lithium and potasium salts confined between two charged and uncharged graphene walls. The study of the molecular density profiles, free energy profiles and the orientational distributions of imidazolium cations as a function of the salt concentration and electrode potential proved the formation of a layered structure in the proximities of the surface even when they are uncharged. Salt cations adapted themselves to this layered structured resulting from overscreening and crowding mechanisms near walls. Moreover, imidazolium cations were found to show a distribution of angles with respect to the electrode surface, whose average increases with the electrode charge. On the other hand, free energy profiles for taking a lithium or potassium cation from the bulk to the graphene electrode revealed high free energy barries that let the salt cations to reach the negative electrode only at high concentrations of salt. All evidence seems to indicate that the IL structure is highly resilient to the addition of any of these solutes, which leads to the solute molecules being accommodated in the nanodomains of the amphiphilically nanostructured IL that are more similar to their molecular entities. This solvation mechanism, which has been called nanostructured solvation, seems to be an universal solvation mechanism in these dense ionic solvents.

All these studies that were carried out are presented below in a detailed way. For each of them we include a brief summary and the corresponding published paper. It must be noted that the reference indicators, as well of those of figures and tables, are integrated with the text; due to which it is possible that the numbers do not correspond to those indicated in the papers.

2.1. Molecular Dynamics Simulation of the Structure and Dynamics of Water/1-Alkyl-3-methylimidazolium Ionic Liquid Mixtures.

The presence of water in ILs is almost inevitable and plays a critical role in many applications for which these compounds are being employed. Thus, the analysis of IL/water interactions and of the detailed properties of their mixtures becomes of fundamental importance for an adequate choice or design of ILs. In Ref.[81] we reported one of the first studies that focus on the properties of ILs mixed with water.

In this work the influence of cation and anion natures, as well as of water concentration, on the structure and dynamics of bulk mixtures of water with 1-alkyl-3-methylimidazolium ($[Amim]^+$) based ILs was analyzed by means of MD simulations. All the possible combinations between three anions of different hydrophobicities and sizes ($[PF_6]^-$, $[Cl]^-$ and $[Br]^-$) and four different lengths of the cation alkyl chain ($[Emim]^+$, $[Bmim]^+$, $[Hmim]^+$ and $[Omim]^+$) were mixed with water in order to determine the water concentration dependende of numerous structural properties, such as radial distribution functions, coordination numbers, hydrogen bonds, and also on the single-particle dynamics (self-diffusion coefficients, mean square displacements and velocity autocorrelation functions). The formation of water clusters, whose size strongly depends on the hydrophobicity of the anion, was observed. In addition, water molecules showed a rattling motion in the cavities of the halogenated ILs, whereas in hydrophobic ILs correlations were rapidly cancelled out. Mean-square displacements revealed three different regimes: a ballistic motion of the molecules at short times, a long-time diffusive regime characterized by a Brownian motion and complex non-Markovian dynamics at intermediate times. The transition times to a diffusive dynamics was found to be shorter the more hydrophobic the anion, since water motion is then more similar to that in pure water.

2.1.1. Paper I: Molecular Dynamics Simulation of the Structure and Dynamics of Water/1-Alkyl-3-methylimidazolium Ionic Liquid Mixtures; *J. Phys. Chem. B 115 (2011) 6995-7008.*

Trinidad Méndez-Morales,[1] Jesús Carrete,[1] Óscar Cabeza,[2] Luis J. Gallego[1] and Luis M. Varela[1]

We have performed extensive molecular dynamic simulations to analyze the influence of cation and anion natures, and of water concentration, on the structure and dynamics of water/1-alkyl-3-methylimidazolium ionic liquid mixtures. The dependence on water concentration of the radial distribution functions, coordination numbers, and hydrogen bonding degree between the different species has been systematically analyzed for different lengths of the cation alkyl chain (alkyl = ethyl, butyl, hexyl, and octyl) and several counterions. These include two halogens of different sizes and positions in Hoffmeister series, Cl^- and Br^-, and the highly hydrophobic inorganic anion PF_6^- throughout its whole solubility regime. The formation of water clusters in the mixture has been verified, and the influences of both anion hydrophobicity and cation chain length on the structure and size of these clusters have been analyzed. The water cluster size is shown to be relatively independent of the cation chain length, but strongly dependent on the hydrophobicity of the anion, which also determines critically the network formation of water and therefore the miscibility of the ionic liquid. The greater influence of the anion relative to the cation one is seen to be reflected in all the analyzed physical properties. Finally, single-particle dynamics in IL-water mixtures is considered, obtaining the self-diffusion coefficients and the velocity autocorrelation functions of water molecules in the mixture, and analyzing the effect of cation, anion, and water concentration on the duration of the ballistic regime and on the time of transition to the diffusive regime. Complex non-Markovian behavior was detected at intermediate times within an interval progressively shorter as water concentration increases.

[1]*Grupo de Nanomateriales y Materia Blanda, Departamento de Física de la Materia Condensada, Universidad de Santiago de Compostela, E-15782 Santiago de Compostela, Spain*

[2]*Facultad de Ciencias, Universidade de A Coruña, Campus A Zapateira s/n, E-15008, A Coruña, Spain*

2.1.2. Introduction

Pure ionic liquids (ILs) are nonaqueous but polar solvents that have attracted enormous research effort for both theoretical reasons and with a view to their potential applications. Many are the properties which confer ILs their unique character as alternative green solvents: high cohesive energy densities combined with melting points often below 100 °C [3, 82], nonvolatility, nonflammability, high thermal and electrochemical stability, ability to dissolve an enormous range of inorganic, organic, and polymeric materials at very high concentrations, noncorrosiveness, low viscosity, negligible vapor pressure, and so forth [22, 83–86]. These systems (whose number has been evaluated to be around 10^{18}) are considered to be tunable "designer" solvents, since a wide variation in physicochemical properties such as viscosity, catalytic activity, or solvation can be obtained by changing the anion or the lateral chains attached to the heterocyclic unit.

The mixing of ILs with both inorganic and organic compounds, particularly water, is extremely important in many of their applications. For example, the immiscibility of ILs with organic compounds is used in biphasic catalysis, and in some reactions IL/water mixtures are employed as biphasic systems. The presence of water in ILs is almost inevitable [87, 88], and its well-known influence on the nanostructural organization of room-temperature molten salts is a central topic in synthetic chemistry and catalysis. Many experimental studies have been performed to adequately characterize the influence of water on IL nanostructure, ranging from small angle neutron scattering (SANS) [89] to surface properties [90]. Turmine *et al.* [90] verified the existence of a surface transition for aqueous solutions of imidazolium-based ionic liquids associated to the nanoaggregation of electrolytes. Moreover, the spontaneous self-organization and the formation of a liquid-crystalline gel were shown by Firestone and co-workers [91] adding water to 1-decyl-3-methylimidazolium bromide, and Antonietti and co-workers [92] showed that, with the addition of water, ILs exhibit classical surfactant self-organization with high order.

Despite all of these studies, our knowledge of the interaction between water and ILs remains somewhat empirical, as it has been pointed out by Jiang *et al.* [93]. Particularly, the role of cation and anion is not yet fully understood, and its impact on magnitudes such as the hydrogen bonding degree in bulk mixtures or the velocity autocorrelation functions has not been previously considered in literature. Since it is normally very difficult to experimentally

probe the properties of ILs at the atomic level, particularly the environment experienced by a solute in an IL, and the theoretical studies reported so far on these systems are somehow scarce, computer simulations may play an essential role for understanding their behavior. In fact, several computational studies of the properties of both pure ILs and IL/water mixtures have been reported in the last years, dealing mainly with thermodynamic and structural properties and single particle dynamics (for a recent review, see ref.[94] and references therein). However, mixtures have attracted less attention. In what the aqueous mixtures are concerned, Hanke and Lynden-Bell [65] reported a seminal molecular dynamics (MD) study of the structure and physicochemical properties of water/1,3-dialkyl-imidazolium mixtures, providing the first molecular picture for the water structure and water-enhanced ion dynamics in mixtures. Canongia-Lopes *et al.* [95] contributed to a new understanding of the solvation mechanisms of nonpolar and polar molecules in ILs reporting the existence of microphase separation of polar and nonpolar domains. Jiang *et al.* [93] analyzed the effect of varying water concentrations on the nanostructural organization of IL-water mixtures. These authors considered the relative role of hydrophobic and electrostatic interactions in the evolution of the polar and water networks with water content, as well as on the turnover point where ordered micelle (cation-cation) structure and water network are formed. Moreover, Spickermann *et al.* [96] performed Carr-Parrinello simulations in which they considered the structure of the hydration shells around ion pairs, proving that water-water radial distribution functions (RDFs) differ significantly from bulk water and that no ion pair dissociation takes place since the solvation of both cation and anion is not complete. Recently, Porter *et al.* [97] considered the size of water clusters in aqueous IL mixtures and proved that they are hydrogen bonded to two anions with the cation playing a minor role.

As it is well-known, the nanostructures of pure ILs and their mixtures are highly dependent on the choice of the cation and anion. Particularly, the length of the chains attached to the heterocyclic unit is conventionally thought to be the main responsible for the hydrophobicity of ILs, and therefore of the properties of their mixtures with water, and the role of the anion is not yet well-understood. An adequate microscopic understanding of the role of both species in the solvation of water and the rest of physicochemical properties in IL-water mixtures is of fundamental importance. However, the role of both cation and anion in the structure and dynamics of ILs and their mixtures has

not received attention until recently. For pure ILs, Urahata and Ribeiro [63] reported a systematic analysis of the matter simulating 10 different systems at 323 K using united atom force fields, in which different anion sizes (F^-, Cl^-, Br^-, and PF_6^-) and alkyl chain lengths of 1-alkyl-3-methylimidazolium cations (alkyl = methyl, ethyl, butyl, and octyl) were considered. For what mixtures are concerned, Feng and Voth [98] reported very recently the first (to our knowledge) MD analysis of the role of alkyl size chain of both cation and anion on the structure and dynamics of IL/water mixtures. The authors considered three IL/water mixtures at various water mole fractions: 1-butyl-3-methylimidazolium $BMIMBF_4$, 1-octyl-3-methylimidazolium $OMIMBF_4$, and OMIMCl, and they found significant influence of the alkyl chain length on the aggregation behavior of the cation, since the longer the chain the more extensive is micelle formation at large water proportions. On the other hand, water-anion interactions seem to be responsible for the water structure at low water contents. However, to the best of our knowledge, no results have been reported for 1-ethyl-3-methylimidazolium ($EMIM^+$) or 1-hexyl-3-methylimidazolium ($HMIM^+$), and no attention seems to have been devoted to the strongly hydrophobic anion PF_6^-, probably due to its very low solubility in water (from $w = 0$ to $w \approx 26\%$ and from $w \approx 99.84\%$ to $w = 100\%$ in $BMIMPF_6$; from $w = 0$ to $w \approx 22\%$ and from $w \approx 99.95\%$ to $w = 100\%$ in $HMIMPF_6$; from $w = 0$ to $w \approx 20\%$ and from $w \approx 99.99\%$ to $w = 100\%$ in $OMIMPF_6$) [99–102]. Moreover, the systematic analysis of the influence of both ionic species on the degree of hydrogen bond in the bulk—crucial for understanding the nanostructure of these systems—or in the velocity autocorrelation functions in IL/water mixtures have not been explicitly considered up to now, although they are essential for understanding the solvation mechanisms and dynamics of these systems.

Although MD simulations of transport properties of pure ILs were reported for the first time in the literature at the beginning of this century [63, 65, 103], only recently single-particle dynamics in IL-water mixtures has begun to be considered. In particular, Porter *et al.* [97] performed MD calculations to obtain the diffusion coefficients and the mean square displacement (MSD) of different species in mixtures of a water miscible ($EMIMBF_4$) and a water immiscible ($EMIMNTf_2$, NTf_2^- bis(trifluoromethylsulfonyl)imide) IL containing very small amounts of water. These authors reported a wide range of thermodynamic and transport properties of mixtures of $EMIMEtSO_4$ ($EtSO_4^-$, ethyl sulfate), including rotational relaxation times, self-diffusivity, shear viscosity,

and thermal conductivity. More recently, Feng and Voth [98] investigated the concentration dependence of the self-diffusion coefficients of water mixtures of EMIM, BMIM, and OMIM tetrafluoroborates and chlorides, together with the water rotational correlation time in these systems. However, systematic calculations of the velocity autocorrelation functions (VACF) of aqueous mixtures of the first members of the imidazolium family have not been reported yet, nor they have the roles of both ionic species and of water content in the times of transition to both ballistic and diffusive regimes and in the duration of the subdiffusive regime at intermediate times.

In the work described here we performed extensive MD simulations to investigate the structure and some dynamic properties of aqueous mixtures of four members of the family of the 1-alkyl-3-methylimidazolium (alkyl = ethyl, butyl, hexyl, octyl) (AMIM) for three counterions, with different positions in the Hoffmeister series (Br^- and Cl^-) and one hydrophobic (PF_6^-) with low miscibility with water throughout its entire solubility region (see schemes in Figure 2.1). We analyze the influence of the chemical structure of the IL and of the water concentration on the evolution of the microstructure of the mixtures (radial distribution functions, hydrogen bonding degree, coordination numbers) and on several transport properties like the self-diffusion coefficients and MSDs of water molecules in the mixtures, with an analysis of the ballistic and diffusive regimes, and water-water VACFs.

The remainder of this paper is organized as follows. In section 2.1.3 we describe the computational methods employed in this paper; in section 2.1.4 we present and discuss the obtained results, and in section 2.1.5 we summarize our main conclusions.

2.1.3. Simulation details

MD simulations for pure AMIM ILs and their mixtures with water were performed using Gromacs package [70, 104]. All of the simulations except those for $EMIMPF_6$ were carried out at 298.15 K, and the water molar percentages in the water-IL mixtures were those of the set w = {0, 0.50, 0.95, 5.00, 10.60, 25.00, 50.00, 75.00, 80.00, 85.00, 90.00, 95.00, 99.50, 100.00%} for which the different ILs are miscible with water. These percentages were calculated fixing the number of ion pairs at 210 (except with 99.50 and 100.00%, which had 50 and none, respectively) and adjusting the number of water molecules in each situation, so they are equivalent to

Figure 2.1 Molecular structures of 1-octyl-3-methylimidazolium, and hexafluorophosphate ions.

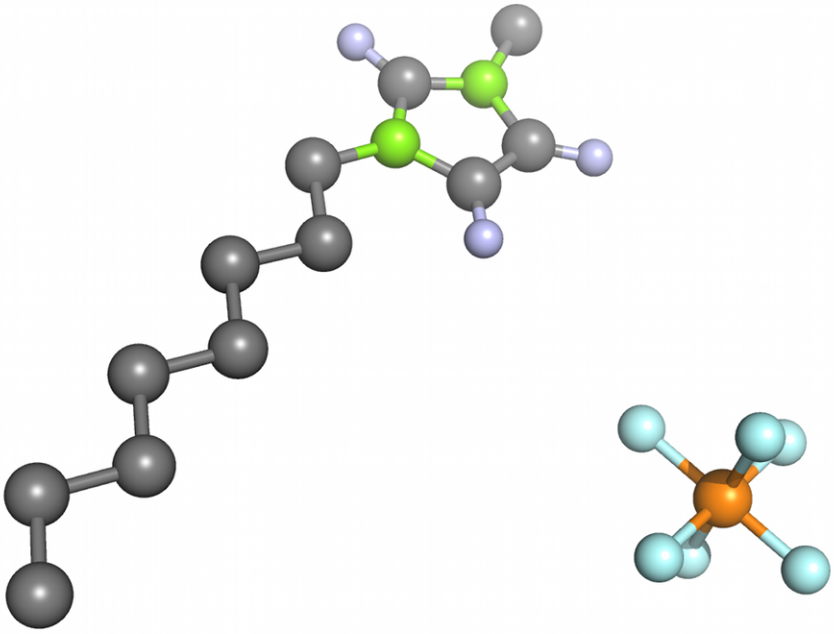

the mole fractions. $EMIMPF_6$ is solid at ambient temperature, and to our knowledge, the highest melting temperature reported in the literature for $EMIMPF_6$ is $T = 333.15$ K [102], so we chose $T = 340.15$ K as the simulation temperature to ensure the substance is in its liquid phase. The simulations for AMIMCl and AMIMBr were carried out only for the two cations with the longest chain, hexyl and octyl, since the other compounds are solid at ambient temperature.

The parametrization of the ions was made in the framework of the GROMOS96 43A1 FF force field [74]:

$$V(\vec{r};s) = \sum_{n=1}^{N_b} \frac{1}{4} K_{b_n} \left[b_n^2 - b_{0_n}^2 \right]^2 + \sum_{n=1}^{N_\theta} \frac{1}{2} K_{\theta_n} \left[\cos\theta_n - \cos\theta_{0_n} \right]^2 + \sum_{n=1}^{N_\xi} \frac{1}{2} K_{\xi_n} \left[\xi_n - \xi_{0_n} \right]^2 + \\ + \sum_{n=1}^{N_\varphi} K_{\varphi_n} \left[1 + \cos(\delta_n) \cos(m_n \delta_n) \right] + \sum_{i,j} \left(\frac{C12_{ij}}{r_{ij}^{12}} - \frac{C6_{ij}}{r_{ij}^{6}} \right) + \sum_{i,j} \frac{q_i q_j}{4\pi\varepsilon_0 \varepsilon_1} \frac{1}{r_{ij}} \qquad (2.1)$$

The first four terms represent the bonded interactions, that is, bonds, angles, and torsions, and the nonbonded interactions are described in the last two terms, including van der Waals and Coulombic interactions. b_n and θ_n are the actual bond between atoms i and j and the actual angle between atoms i, j, and k, respectively. Equilibrium bond lengths, r_0, and angles, θ_0, were obtained from X-ray diffraction, while force constants (K_r, K_θ) were taken from experimental spectroscopic data. In the improper and torsional dihedral-angle interaction terms, ξ_n and φ_n are the actual values of a dihedral angle defined by atoms i, j, k, and l, δ_n is the phase shift (restricted to 0 or π), and m_n is the multiplicity of the torsional dihedral angle. $C12_{ij}$ and $C6_{ij}$ parameters in the Lennard-Jones (LJ) interactions depend on the atoms involved in the interaction, and they are obtained from parameters for each type of atom using geometric combination rules, $C12_{ij} = (C12_{ii} \cdot C12_{jj})^{1/2}$ and $C6_{ij} = (C6_{ii} \cdot C6_{jj})^{1/2}$. For these values we used $C6_{ii} = 4\varepsilon_i\sigma_i^6$ ($\mathrm{kJ \cdot nm^6 \cdot mol^{-1}}$) and $C12_{ii} = 4\varepsilon_i\sigma_i^{12}$ ($\mathrm{kJ \cdot nm^{12} \cdot mol^{-1}}$), where σ_i is the distance at which the LJ potential vanishes for species i. The electrostatic interactions include parameters defined as the charges on the atoms, q_i, the dielectric permittivity of vacuum (ε_0), and the relative permittivity of the medium in which the atoms are embedded (ε_1). The value of ε_1 is conventionally set to 1.

The cations were modeled using a united-atom representation of the CH_2 and CH_3 groups in the alkyl chain, as well as of the methyl group attached to the imidazolium ring. Partial charges were calculated by the *ab initio* restrained electrostatic potential (RESP) fitting method [105]. In what the anions are concerned, both Br^- and Cl^- were modeled by single sites of charge $-e$, while PF_6^- was modeled as a set of seven sites with partial charges of 1.100 for the phosphorus atom and −0.350 for the fluorine atoms. On the other hand, water molecules were described by means of the conventional Berendsen's SPC water model [106], and the electrostatic interactions were treated using particle-mesh Ewald (PME) method [77, 107] with a grid spacing of 0.12 nm and a cubic interpolation. The search for neighbors was made up to a distance of 0.9 nm from the central ion and was actualized every five simulation steps.

The SPC water model is developed in the GROMOS force field. This model considers water as a rigid molecule with an ideal tetrahedral shape which consists of a LJ interaction site with a negative partial charge (−0.82) placed on the oxygen atom and two positive partial charges (+0.41) located at the positions of the hydrogen atoms. Many other models for water were proposed over the years, such as TIP3P [108] or TIP5P [109]. The former model is implemented

in the AMBER force field [110], and it has three interaction points; this model, as the SPC model, shows a stronger interaction of water and ions because of the larger partial charges on the atoms compared to TIP5P water. The TIP5P model was made for the OPLS-AA force field [75], and in addition to the LJ center placed on the oxygen and the charges located at the hydrogen atoms, it places two partial charges representing the lone pairs of the oxygen atom. However, this latter water model overestimates the density more than a 5% and does not describe some structural properties in the best manner, the SPC model giving more accurate results [111].

None of these models is able to reproduce the immiscibility of $AMIMPF_6$ with water, having to use some special techniques to achieve this result [99, 112]. As no water model available is able to reproduce all the water properties with good accuracy, our justification for the choice of the SPC water model is that this popular model describes the global structural properties of pure liquid water in a good manner with a low computational cost.

As a check of the computational method employed, Figure 2.2.a shows the comparison between the RDFs of $BMIMPF_6$ mixed with a 25% of water provided by GROMOS96 and the OPLS-AA force fields, for which the main difference is that the former one is a united-atom representation and the latter one is an all-atom force field. Only the anion-anion RDF exhibits significant differences, showing a double peak in the GROMOS force field and a single peak in the OPLS-AA one. Figure 2.2.b compares the RDF of pure water for the SPC and TIP5P models with the experimental radial distribution function at 298 K [113]. As can be seen, both the SPC and TIP5P models provide a good description of the experimental RDF.

Initial configurations were energy-minimized for 1000000 steps using the steepest descent method to remove bad contacts resulting from the initial random configuration of cations and anions. The maximum step size and the tolerance were 0.01 nm and 0.1 $kJ \cdot nm^{-1} \cdot mol^{-1}$, respectively. The equilibration phase was performed in the isothermal-isobaric ensemble during 100 steps to ensure the full equilibration of all the properties of the system. The results of an additional 2000 ps simulation in the isothermal-isobaric ensemble were used for analysis. Temperature control was implemented using a Berendsen thermostat [114]. Cations and anions (and water in cases where we include the solvent) were separated in two (three) baths with temperature coupling constants of 0.1 ps. Pressure control was set by means of a Berendsen barostat [114] with a reference pressure of 1 atm, an isothermal compressibility of

Figure 2.2 (a) Comparison between RDFs of $BMIMPF_6$ at 25% water concentration calculated using GROMOS and OPLS-AA force fields, and (b) comparison between experimental RDF of pure water with the predictions of SPC and TIP5P models of water, used with the GROMOS and the OPLS-AA force fields, respectively.

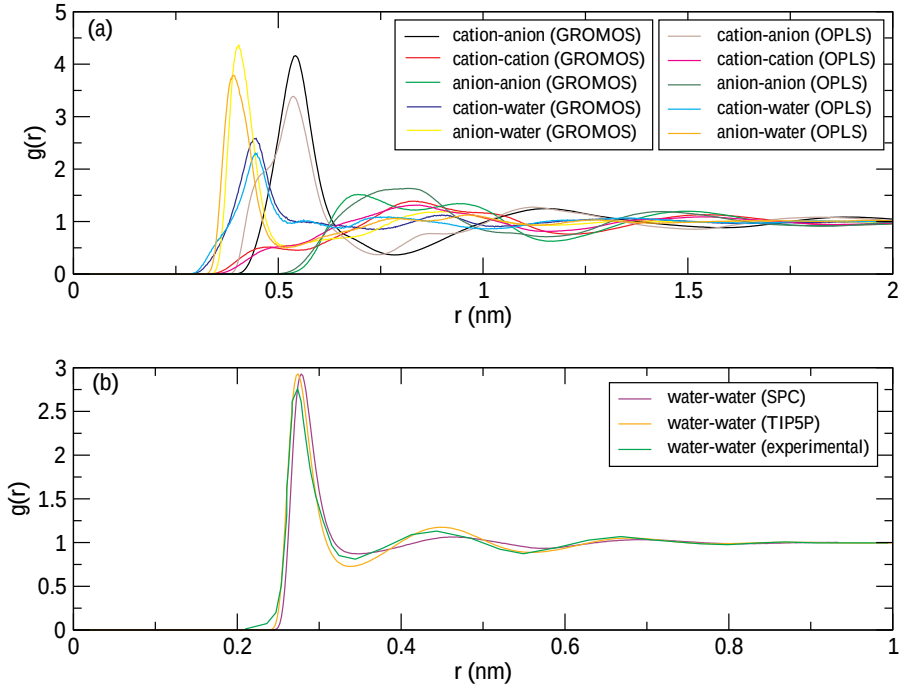

$4.5 \times 10^{-5} \cdot \text{bar}^{-1}$, and a relaxation time of 1.0 ps.

These simulations provide us a sequence of configurations, that is, positions and instantaneous velocities of all atoms of the system, which were analyzed to obtain structural, thermodynamic, and dynamical information of the mixed IL-water systems mentioned above.

2.1.4. Results and discussion

The structure of dense fluids is usually characterized by means of the RDF defined as

$$g(r) = \frac{1}{V} \left\langle \sum_{ij} \delta(r - r_{ij}) \right\rangle \tag{2.2}$$

where V stands for the system volume, i and j run over all the particles, and brackets indicate the ensemble average. Calculated ion-ion RDFs of the pure ILs analyzed in this paper are shown in Figures 2.3 and 2.4. All RDFs were calculated using the geometric center of the anions and the geometric center of the imidazole ring of the cations. It is noteworthy that, to the best of our knowledge, this is the first time that the RDFs of pure $HMIMPF_6$ and $OMIMPF_6$ are reported at ambient temperature, while the RDF of pure $BMIMPF_6$ was showed for the first time by Morrow and Maginn [115]. Figure 2.3 shows the influence of the cationic chain length on the RDFs of the analyzed pure AMIMs, and Figure 2.4 presents the influence of the anion on the structure of the system for the ILs with a melting temperature below room temperature. As can be seen in these representations, the calculated RDFs exhibit some of the characteristic features previously reported in literature: (i) cation-cation and cation-anion distances around 0.7 and 0.5 nm, respectively, in coincidence with previously reported results (see ref.[116] and references therein), (ii) considerably long-ranged out-of-phase distribution of one ion around the other one as is the case for other imidazolium-based ionic liquids containing halides and PF_6^- anions. This order is preserved typically for at least three interionic distances, thus confirming the so-called pseudolattice arrangement in the liquids, on the basis of the Bahe-Varela model [117, 118], and (iii) very limited presence of like-ions in the first coordination shell of ions of the other type. However, we did not obtain the shoulders in the cation-cation RDFs recently reported by Bowron *et al.* [116] representative of ring stacking; our simulations are more in agreement with those reported by Urahata and Ribeiro [63], who did not found such a feature. Particularly, it is visible in Figure 2.3 that the RDFs show considerable clustering of PF_6^- anions around the imidazolium cation (at an average distance of 0.54 nm) and ordering up to 2 nm. The most significant effects of the increment of the chain length of the cation on the anion-cation RDF is the increase of the height of the first peak in the cation-anion RDF. Given this peak, we evaluated the coordination numbers integrating numerically the radial distribution function $4\pi r2g(r)$ up to its first minimum. Our calculated coordination number for the cation-anion first peak in pure $BMIMPF_6$, 5.4, differs from another simulation values near 7 reported in the literature [115], but one must recall that this property is very sensitive to the choice of the position of the minimum. It is also noteworthy that the first peak of the cation-anion RDF exhibits a shoulder around 0.67 nm (see arrows in Figure 2.3), a feature which has also been observed in some liquids such as Ga, Si, Sn, or Bi (see

ref.[119] and references therein), and it has been interpreted as a signature of a short-lived diatomic molecular unit. Contrarily to what happens with this first peak, the impact of the variation of the cationic chain length in the distribution of higher order neighbors seems to be relatively limited. On the other hand, a more complex structure is observed in the case of cations, with a weak first peak at 0.48 nm and a double second peak centered at 0.95 nm. This structure is probably associated to the different lengths of the cation alkyl side chains of the $AMIM^+$ cations [97]. As can be seen in the representation, a cation-cation RDF is very resilient to the change of the alkyl chain length. Probably, the most notable effect of the modification of the number of carbon atoms in the alkyl side chain of the cation one is the smoothing out of the shoulder appearing in the second peak of the cation-cation RDF at 0.95 nm, what could indicate a more difficult ring-stacking of the cations as their chain length is increased. Concerning the anion network structure, once again we see that considerable long-range ordering is observed in the anion-anion RDFs and that a double first peak centered at 0.84 nm is obtained for PF_6^- anions. The influence of the chain length of the cation is registered mainly on the first peak of the anion-anion RDF. This peak suffers a progressive reduction of its height and an overlapping with the second peak, which is even dominant for $OMIMPF_6$, reflecting a reduction of the ability of PF_6^- to coordinate with the cations as the chain length of the latter is increased. In fact, the calculated numbers of anions coordinating our studied cations were 6.87 for $EMIMPF_6$, 5.40 for $BMIMPF_6$, 5.37 for $HMIMPF_6$, and 3.48 for $OMIMPF_6$. Similar trends were observed for the halogenated ILs analyzed in this paper.

The effect of the anion in the RDFs of the different species in our studied ILs can be seen in Figure 2.4. A first notable effect is that the calculated first peak of the anion-cation RDFs for the PF_6^- anion is lower and broader than those obtained for the halogen anions (Figure 2.4.a,d), and it is a little bit displaced to higher distances with respect to its halogen counterparts, probably due to the greater hard sphere radius of the PF_6^- anion. The shoulder in the first peak mentioned above is more visible for the halogen anions than for PF_6^- (see arrows in Figure 2.4.a,d). Moreover, a first peak around 0.4 nm is registered in the cation-cation RDF for the halogen ions, but it is almost completely smeared out in $HMIMPF_6$ and also $OMIMPF_6$ (see arrows in Figure 2.4.b,e). The results obtained with this force field are clearly comparable to both experimental and calculated RDFs previously reported in the literature for the same or related ILs (see for example refs.[63, 120–124]).

Figure 2.3 RDFs of EMIMPF6 at 340.15 K (a), $BMIMPF_6$ (b), $HMIMPF_6$ (c), and $OMIMPF_6$ (d) at 298.15 K and 1 atm. The arrows indicate the shoulder in the first peak of the RDF mentioned in the text.

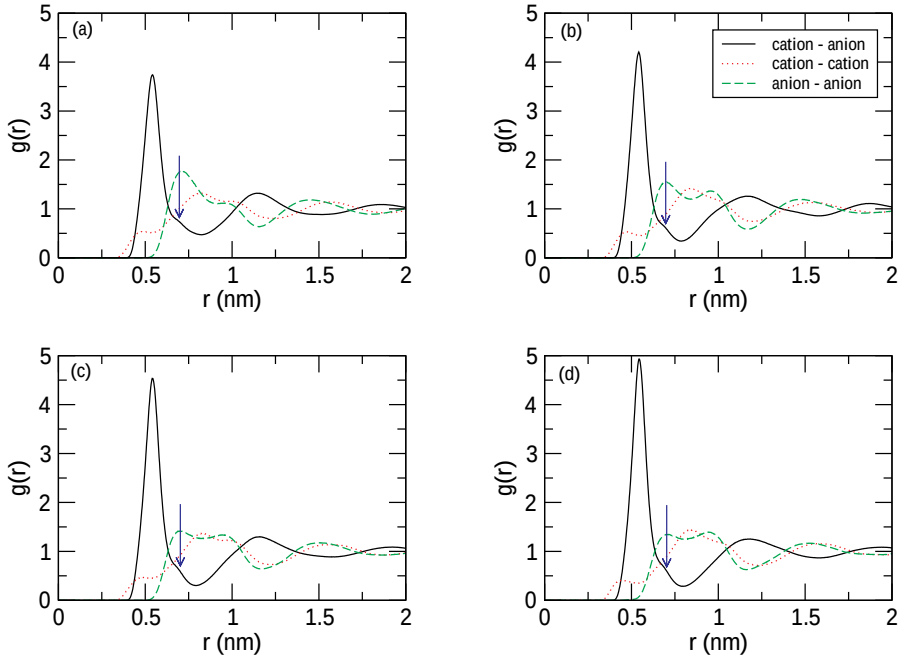

Water-water (w/w), water-cation, and water-anion RDFs in mixed systems are represented in Figures 2.5, 2.6, and 2.7, respectively. In the first of these representations, w/w RDF is seen to exhibit a very strong clusterization at the lowest water concentration, as indicated by the height of its first peak. The position of this peak (ca. 0.27 nm) indicates that the water molecules in the first coordination shell are hydrogen bonded according to the criteria given below for this kind of bond to exist ($r < 0.35$ nm, angle acceptor-H-donor below 35°). As expected, this clusterization is much more notable in the case of the hydrophobic anion PF_6^- (Figure 2.5.a-c), for which the height of the peaks is seen to monotonically decrease with water concentration throughout the entire miscibility regions of the different cationic chain length. This is to be attributed to the fact that the number of water contacts increases slower than the number of water molecules in the bulk itself [98]. Moreover, the height of this first peak of the RDF notably increases with alkyl chain length of the cation, a similar behavior to that reported for $BMIMBF_4$ and $OMIMBF_4$ by Feng and Voth in ref.[98].

Figure 2.4 RDFs for cation-anion (a, d), cation-cation (b, e), and anion-anion (c, f) of $HMIM^+$ and $OMIM^+$ for three different counterions (PF_6^-, Cl^-, and Br^-) at 298.15 K and 1 atm. The arrows indicate the features of the RDFs mentioned in the text.

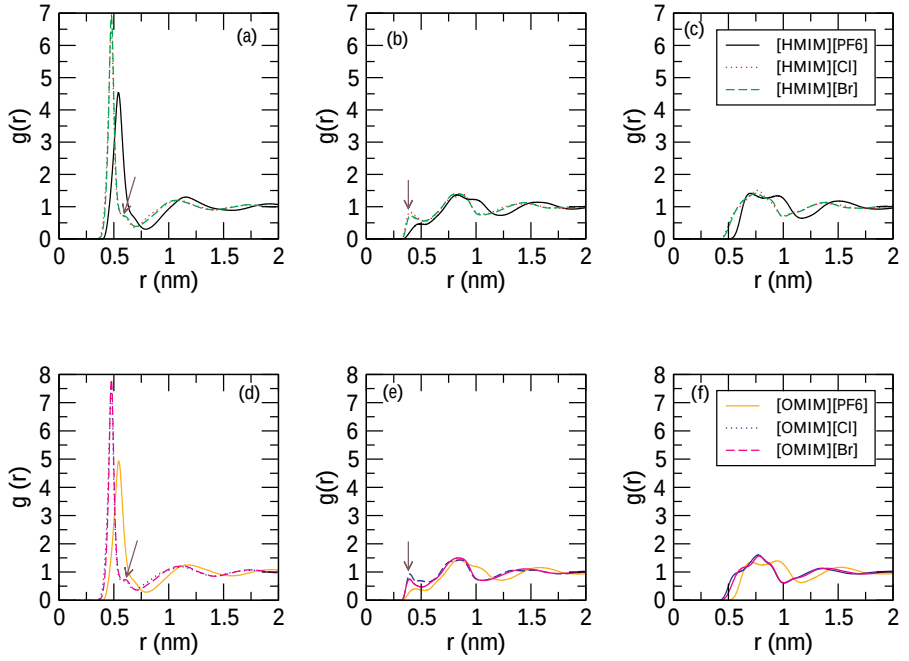

The first peaks of the ILs with the hydrophobic PF_6^- are much higher than those of their halogenated homologues with the same cationic chain length (Figure 2.5.d-g), confirming the role of the hydrophobicity of the cation in the spatial correlation of water in bulk IL mixtures. It is also interesting to compare our results for $OMIMPF_6$ with that for $OMIMBF_4$ reported by Feng and Voth in the Figure 2b of ref.[98]. The height of the first peak of the RDF for $OMIMBF_4$ at a water concentration of w = 20% is roughly 15, while in our case it is around 33 for w = 20%, as expected given the stronger hydrophobicity of the PF_6^- anion as compared to BF_4^-. Consequently, we can conclude that water is strongly clusterized in $AMIMPF_6$ ILs in the very narrow miscibility regions of these hydrophobic compounds and that the increase in the number of cations in the alkyl side chain dramatically affects the structuring of water in the bulk.

The situation is somehow different for the mixtures with halogenated compounds (Figure 2.5.d-g). While in $AMIMPF_6$ water seems to exhibit no remark-

Figure 2.5 Concentration dependence of water-water RDFs of $BMIMPF_6$ (a), $HMIMPF_6$ (b), $OMIMPF_6$ (c), HMIMCl (d), OMIMCl (e), HMIMBr (f), and OMIMBr (g) at 298.15 K and 1 atm.

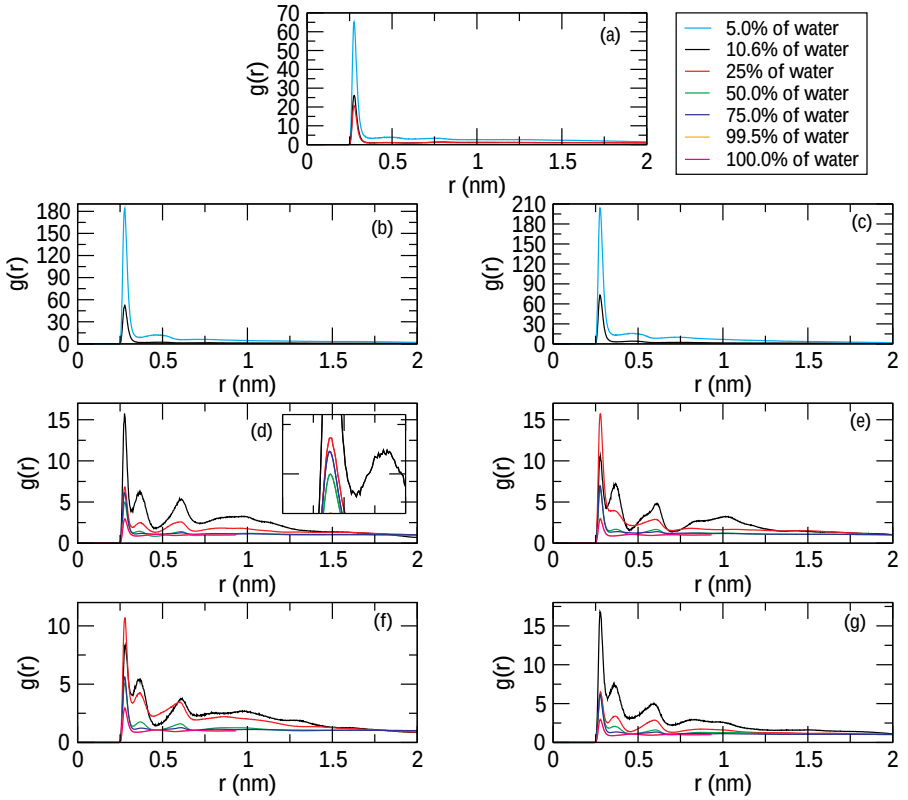

able long-ranged order (no secondary peaks important enough relatively to the first peaks are observed), this is not the case for the ILs with halogen anions. In these cases, we can observe the existence of more marked long-ranged order, particularly visible in the less studied low water concentration region. The crucial role of the anion in water structure is strongly suggested by these observations, and it is further reinforced comparing the RDFs of $HMIMPF_6$ and $OMIMPF_6$ with their hydrophilic homologues with halogenated anions in Figure 2.5.d-g. The heights of the first peaks in the latter cases are less than half their values for the hydrophobic compound. Moreover, as we mentioned previously, while the intensity of the first peak of the w/w RDF for $AMIMPF_6$ monotonically decreases as the concentration of water increases, until it finally

Figure 2.6 Concentration dependence of cation-water RDFs of $BMIMPF_6$ (a), $HMIMPF_6$ (b), $OMIMPF_6$ (c), HMIMCl (d), OMIMCl (e), HMIMBr (f), and OMIMBr (g) at 298.15 K and 1 atm.

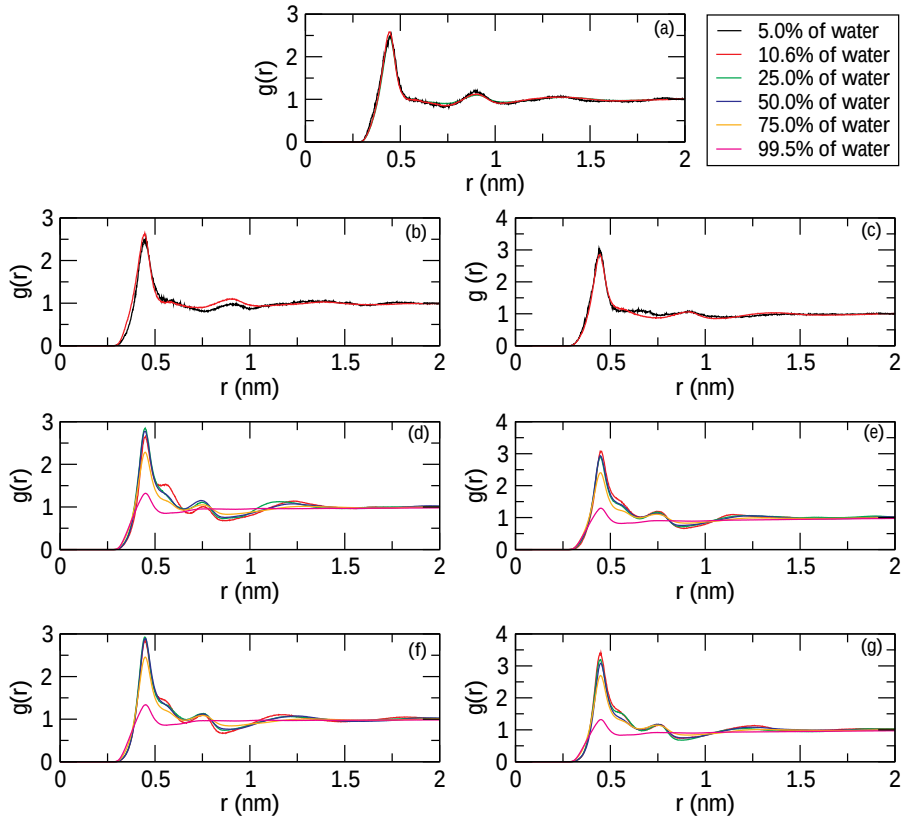

recovers the RDF of pure water, the situation is much richer in the case of the hydrophilic halogen anions. As can be seen in the inset of Figure 2.5.d, an inversion is registered between the heights of this peak for 50% water concentration and 75% water concentration in all the considered ILs, which is indicative of a stronger spatial correlation of water molecules at this percentage of water. This behavior is in agreement with the behavior reported for $OMIMBF_4$ and OMIMCl by Feng and Voth [98]. This behavior was also reported by Hanke and Lynden-Bell for dMIMCl-water mixtures [65] and by Jiang *et al.* [93] for $OMIMNO_3$, and the latter authors also associated this enhancement of the water-water spatial correlation to the formation of heterogeneous water networks. Moreover, we detected a previously unreported inversion of

Figure 2.7 Concentration dependence of anion-water RDFs of $BMIMPF_6$ (a), $HMIMPF_6$ (b), $OMIMPF_6$ (c), HMIMCl (d), OMIMCl (e), HMIMBr (f), and OMIMBr (g) at 298.15 K and 1 atm.

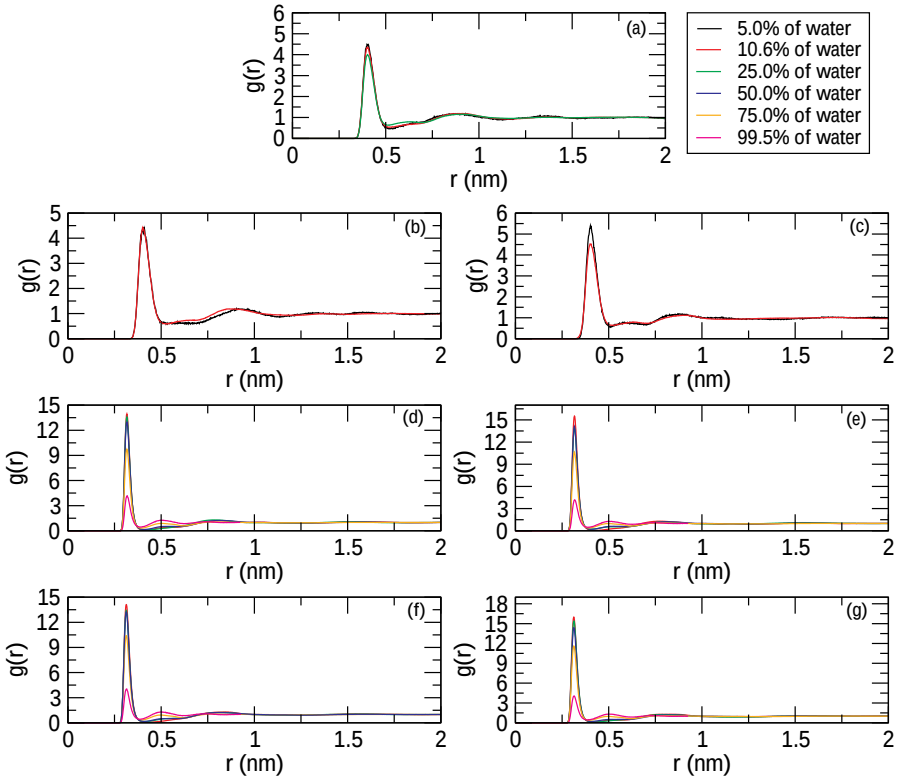

the first peak of the RDF, which exhibits an inversion at the lowest concentrations analyzed, w = 10% and w = 25%, highly dependent on the cation and anion nature. Interestingly enough, the inversion is detected in mixtures of the IL with the longest cation chain length (OMIM) for Cl^- and in HMIM for Br^-. This behavior suggests some kind of interplay between cation chain length and anion size, but the actual origin of this correlation needs further study.

As stated above, a detailed analysis of the highly diluted water regime was not previously reported for IL-water mixtures, to our knowledge. Thus, we extended our simulations down to a water concentration of w = 10% corresponding to 25 molecules of water in our ensemble, and as can be seen in Figures 2.5.d-g, two very interesting features concerning the structure of the water network in the mixture are observed in this regime. First, we observe in Fig-

ures 2.5.a-c that relatively weak peaks associated to the second neighbors of the central water molecule are registered around 0.5 nm in $AMIMPF_6$ for all water concentrations and that the peaks of the third neighbors can be neglected in practice relative to the first ones of these compounds. However, strongly marked second and third peaks are registered at 0.37 and 0.6 nm, respectively, for aqueous mixtures of the halogenated salts of $HMIM^+$ and $OMIM^+$ in the low to intermediate water concentration regime (up to $w = 50\%$). Even a fourth peak is registered for the lowest concentration. This reflects once more that water in hydrophilic ILs adopt a less densely packed, more dispersed arrangement of small water clusters coordinated with hydrophilic anions, while in hydrophobic ILs water tends to adopt a highly organized network of large water clusters even at very low concentrations. This effect will also be reflected in the number of w/w hydrogen bonds, as it will be seen. Water molecules tend to be strongly clusterized in dispersed clusters at the lowest concentrations coordinated with hydrophilic anions, and only at high enough concentrations continuous water regions are formed in the bulk mixture. Hence, at the lowest analyzed concentrations, the addition of water molecules reinforces local water clusters leading to an increase of the first peak together with a weakening of longer range spatial correlations between water clusters associated to higher order peaks of the RDF. Moreover, Cl^- anions seem to perturb more strongly the structure of added water than Br^-, in agreement with the positions of these anions in the Hoffmeister series, in which Br^- is two positions above Cl^-, and so the latter tends to be more strongly hydrated than Br^- due to the highly localized point charge of the former. In both cases three strongly marked peaks (once again, relatively to the height of the first ones), and a more diffuse fourth one, are visible in the w/w RDF for the lowest water concentrations (10%, 25%), and these peaks are still visible at concentrations as high as 50% (Figures 2.5.d-g). However, in the case of Cl^- (Figures 2.5.d and 2.5.e), the heights of the peaks and the depth of the valleys are higher than those for Br^- (Figures 2.5.f and 2.5.g). Moreover, the close proximity of the first and second peaks (less than 0.1 nm) suggests again the effect of the different lengths of the alkyl side chains of the cation on the water shell surrounding it.

Figures 2.6 and 2.7 show, respectively, the RDFs of cation-water and anion-water in the studied mixtures. In all the cases shown in Figure 2.6 one can observe a first peak around 0.45 nm which slightly increases with cationic chain length. Moreover, it is apparent in Figures 2.6 and 2.7 that the presence of halogen ions induces a more oscillatory behavior in the RDFs, reflecting once

more the more long-ranged order in these cases when compared to those of ILs with the PF_6^- anion. Particularly, in this latter case, the first and second peaks in the RDFs in Figures 2.6a-c and 2.7.a-c are separated a distance of ca. 0.5 nm, indicating that throughout the whole miscibility region water weakly hydrates the cationic chain, probably due to the presence of a hydrophobic anion, and prefers to form its own clusters in agreement with our previous interpretation of w/w RDFs. This is certainly not the case for the halogen anions, for which water molecules are less clusterized and more in contact with the cations, as reflected by the positions and heights of the RDFs in Figures 2.6.d-g. The situation is similar for the anion, being the strongly hydrophobic PF_6^- (Figures 2.7a-c) much less hydrated than their halogens counterparts (Figures 2.7.d-g), as reflected both by the height of the first peaks of the RDFs of the halogenated IL-water mixtures, essentially three times higher than in PF_6^- based water-IL mixtures, and also by the oscillations around the anion at the origin. Water around the hydrophobic PF_6^- is structured in two hydration layers separated by 0.5 nm, while for the halogens this distance is only about 0.2 nm. Moreover, as can be seen in these representations, this structuring is weakened in all the studied cases as water concentration increases. Besides, the distance from the central anion to the first hydration layer (position of the first peak) is greater for PF_6^- than for the halogen ions, as expected due to the greater size of the former and its more hydrophobic character.

Thus, from the analysis of the RDFs we can conclude that water tends to clusterize in the cavities of the IL liquids, the distributions of water in the bulk being strongly dependent on the hydrophobicity degree of the cation and, even more strongly, of the anion. The more hydrophobic the anion, the more clusterized water is in the bulk mixture. Very limited hydration is detected for both cations and hydrophobic PF_6^-, and water interacts more strongly with the halogen anions. The influence of the cation is much weaker. These conclusions are reinforced with the results shown in Figure 2.8 in which the average number of hydrogen bonds per water molecule is shown for all the analyzed IL-water mixtures. As mentioned previously, according to ref.[71] a hydrogen bond is considered to exist if the distance between the tagged hydrogen and the acceptor is smaller than 0.35 nm and the angle of the donor-hydrogen-acceptor bond is below 30°(according to Gromacs criterion, OH and NH groups are regarded as donors, and O and N are considered to be acceptors). Moreover, we have organized the calculated information in the figure to show the effect of the anions on the number of hydrogen bonds, since it is well-known that wa-

Figure 2.8 Concentration dependence of the average number of water-water hydrogen bonds per water molecule in the mixture.

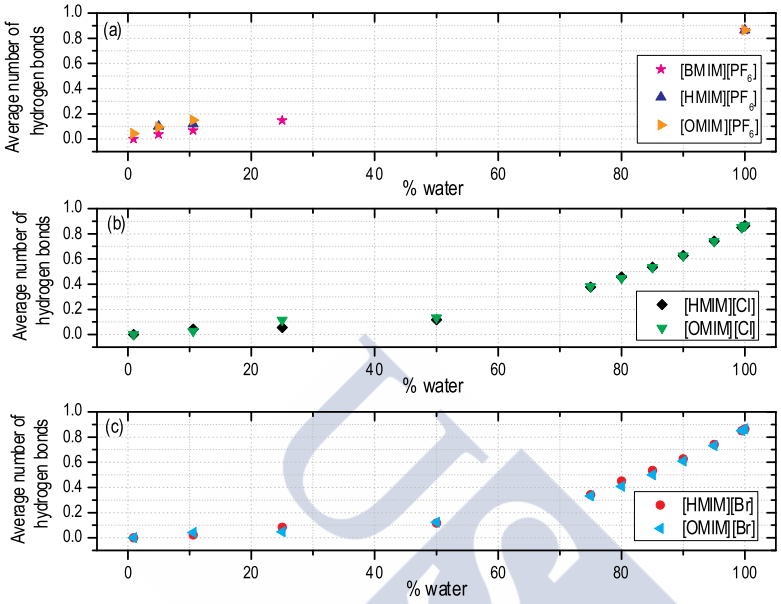

ter molecules are mainly hydrogen-bonded to anions [96, 125]. As can be seen, the number of hydrogen bonds per molecule monotonically increases with the amount of water in all of the studied cases, although for the halogenated ILs this increase is notably smaller than for the PF_6^- throughout all the miscibility region of this IL. In fact, the average number of hydrogen bonds per water molecule in $AMIMPF_6$-water mixtures is already 0.15 at 25% water content, while that value is not reached in the halogenated compounds until a concentration ca. 50%. This fact reinforces the picture of a dispersed network formed by small clusters in the case of ILs with hydrophilic anions, and larger clusters in the case of ILs with more hydrophobic ones. These clusters are more similar to bulk water than their homologous in ILs with hydrophilic anions, thus confirming our interpretation of the results for the RDFs mentioned above. No significant difference is detected in w/w hydrogen bonding degree between the two studied halogen ions.

On the other hand, Figure 2.9 represents the water-cation hydrogen bonding degree for all of the studied cases. As one can see there, the average num-

Figure 2.9 Concentration dependence of the average number of cation-water hydrogen bonds per water molecule in the mixture.

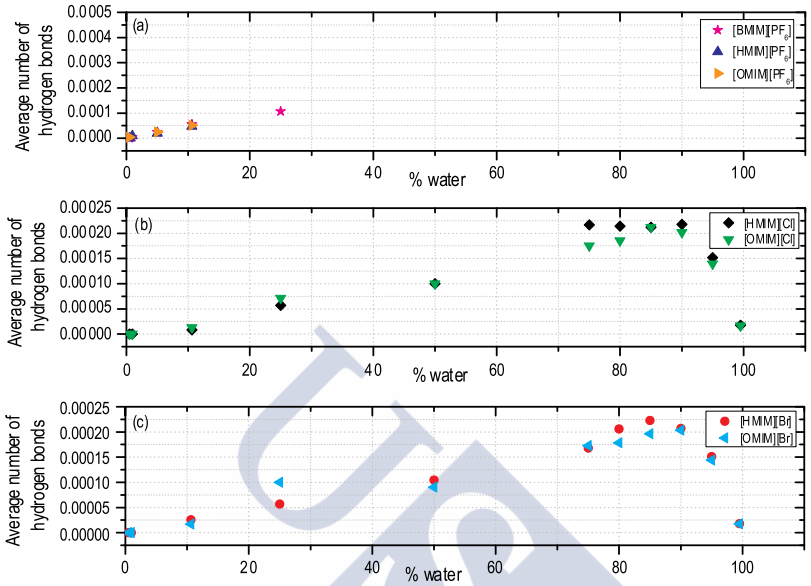

ber of hydrogen bonds per molecule is greater by almost 1 order of magnitude for AMIMPF$_6$-water mixtures than for its halogenated counterparts, probably due to repulsive interactions between water molecules and the hydrophobic anion. The value 10^{-4} is reached at 25% water content in AMIMPF$_6$-water mixtures, while this value is not reached until a water concentration of 50% for the halogenated anions. Once again, no relevant difference is observed between the two halogens, and only slight differences are observed between alkyl chain lengths, leading the compounds with longer chains to the formation of less hydrogen bonds of cations with water in the high water concentration, as should be expected due to its more hydrophobic nature.

On the other hand, where anion-water is concerned, the hydration numbers of water molecules around the anions were calculated by direct integration of the first peak of the corresponding RDFs up to their first minimum. They show monotonous increases in all cases up to a calculated limiting value of 7.4 for Cl^- and 7.2 for Br^-. This value must be compared to an experimental value of 6.54 [126]. This overestimation is registered in many other MD force

Figure 2.10 Snaphots of (a) $BMIMPF_6$-water mixtures at 25% water concentration (limit of miscibility) and (b) HMIMCl-water mixtures at 75% water concentration. Red and gray spheres correspond to oxygen and hydrogen atoms respectively, and for clarity they are augmented.

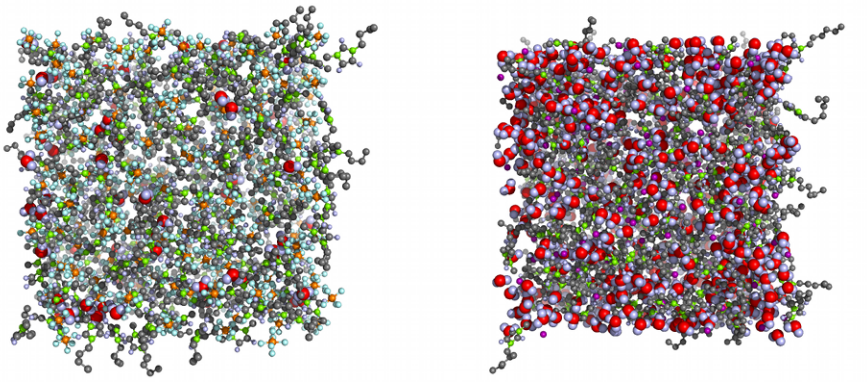

fields, for which values of 7 or even higher have been reported, and similar deviations are reported in the literature [127].

A pictorial representation of water clustering in these compounds can be observed in Figure 2.10, where we present a snapshot of the water clusters formed in $HMIMPF_6$ and HMIMCl at water concentrations of 25% and 75%, respectively. In the former case it is apparent that water molecules present in the mixture are already clusterized even at so low concentrations (it must be taken into account that a small number of water molecules is included in the simulation), announcing immiscibility by the formation of quasi-continuous aqueous regions inside the mixture. However, in HMIMCl small clusters dispersed throughout the mixture are still observed even at such a high water concentration.

We now discuss the results for the dynamical properties of IL-water mixtures, of considerable importance in many processes. In Figure 2.11 we represent the water VACF, defined as

$$C(t) = \langle \vec{v}(t) \cdot \vec{v}(0) \rangle \tag{2.3}$$

where $\vec{v}(t) = \sum_j m_j \vec{v}_j / \sum_j m_j$ is the velocity of the center of mass of the molecule and the scalar product is calculated in the laboratory frame. As far as we know, these are the first reported simulations for this magnitude in water-IL mixtures. As one can see, the mean collision time of water molecules, as

indicated by the first zero of the function, is a little bit greater in the case of $AMIMPF_6$ (around 0.1 ps due to the "cage effect") than those in the halogenated compounds. As we know, water molecules are highly clusterized in these compounds when compared to their halogenated counterparts, and thus water motion in bulk cavities of the mixture is more similar to that in pure water (collision time ca. 0.2 ps). On the other hand, a very limited effect of the chain length on this collision time is registered in all of the studied cases. The correlations are rapidly but nonmonotonically weakened in all mixtures, so within 0.5 ps correlations are no longer present for PF_6^- and within 1 ps they are canceled out even for the halogenated ILs with the shortest studied chain length ($HMIM^+$). However, in the case of the halogenated compound, considerable oscillatory behavior of the VACF is registered up to this latter time in all of the studied compounds, in marked contrast with the monotonic weakening registered in pure ILs [128]. This indicates a "rattling" motion of water molecules inside the cages formed by its heavier neighbors [61] that is more marked and relatively more long-lived for the ILs with the shortest chain lengths. Interestingly, this rattling motion is more markedly observed for Br^- than for the lightest Cl^-, something to be attributable to the fact that this latter anion is more strongly hydrated than the former. Besides, the main effect of water addition is a progressive smoothing out of the VACF until the pure water value is recovered—in agreement to previously reported results [129, 130]. Contrarily to what happened with the collision time, an increase in the chain length leads to a less oscillatory behavior of the VACF in the case of the first compounds.

Another important magnitude for the characterization of the single-particle dynamics in dense fluids is the diffusion coefficient. We evaluated this magnitude with the procedure already implemented in the Gromacs package. In Figure 2.12 we represent the dependence of the self-diffusion coefficients of a water molecule in all the analyzed water-IL mixtures. As it is well-known, two different regimes can be observed for this magnitude: (i) a slow increase in the diffusion coefficients associated to glassy states at low water concentrations, and (ii) a rapid increase at low IL concentrations associated to the formation of the water network. However, as expected, a faster diffusion is observed for $AMIMPF_6$ than for the halogenated ILs due to the more hydrophobic character of the PF_6^- anion [97]. It is also noteworthy that the diffusion coefficients of water molecules in pure ILs are typically 2 orders of magnitude lower than in pure water, in agreement with results previously reported in the literature for imidazolium-based ILs [97, 131].

Figure 2.11 Concentration dependence of the water molecules VACF in water mixtures with $BMIMPF_6$ (a), $HMIMPF_6$ (b), $OMIMPF_6$ (c), HMIMCl (d), OMIMCl (e), HMIMBr (f), and OMIMBr (g).

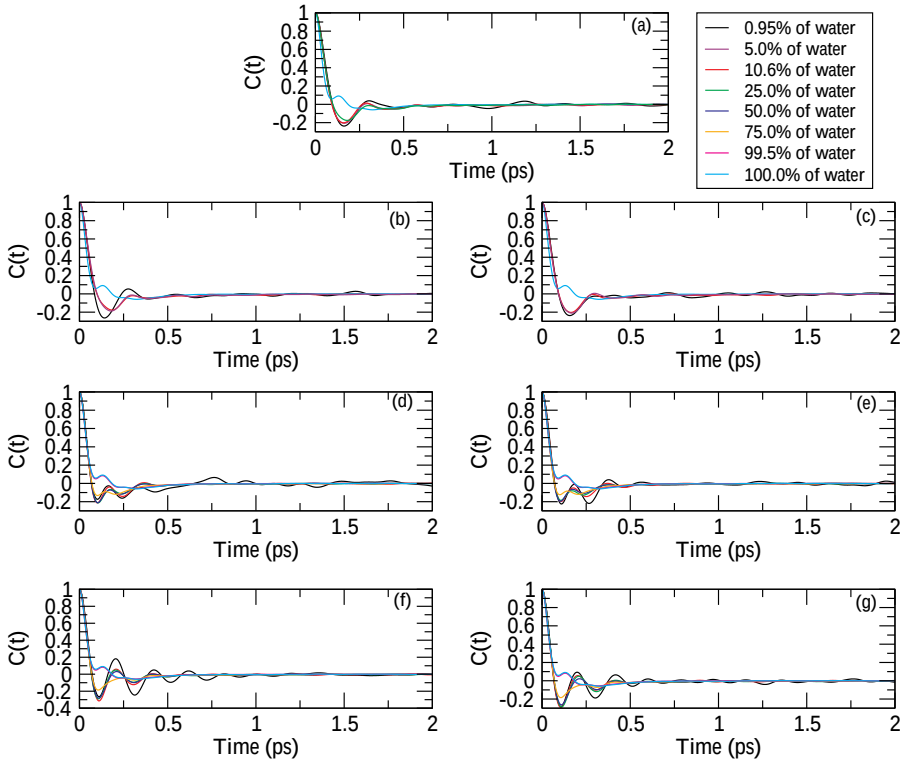

Finally, no significant effects of chain length of the IL cation are detected on the diffusion coefficient of water molecules.

In Figure 2.13 we represent the MSDs of water molecules and of cation and anion in $BMIMPF_6$-water mixtures at 25% water concentration. This magnitude is defined as

$$\left\langle \Delta|\vec{r}(t)|^2 \right\rangle = \frac{1}{N}\left\langle \sum_{i=1}^{N} |\vec{r}_i(t) - \vec{r}_i(0)|^2 \right\rangle \tag{2.4}$$

where the sum extends over all the molecules present, and the positions of the molecules have been calculated from their centers of mass. Two different regimes can be observed in Figure 2.13 corresponding to the ballistic motion of the molecules at short times, $\langle \Delta|\vec{r}(t)|^2 \rangle \propto t^2$, and a long-time diffusive regime

Figure 2.12 Concentration dependence of the diffusion coefficients of water molecules in several mixtures.

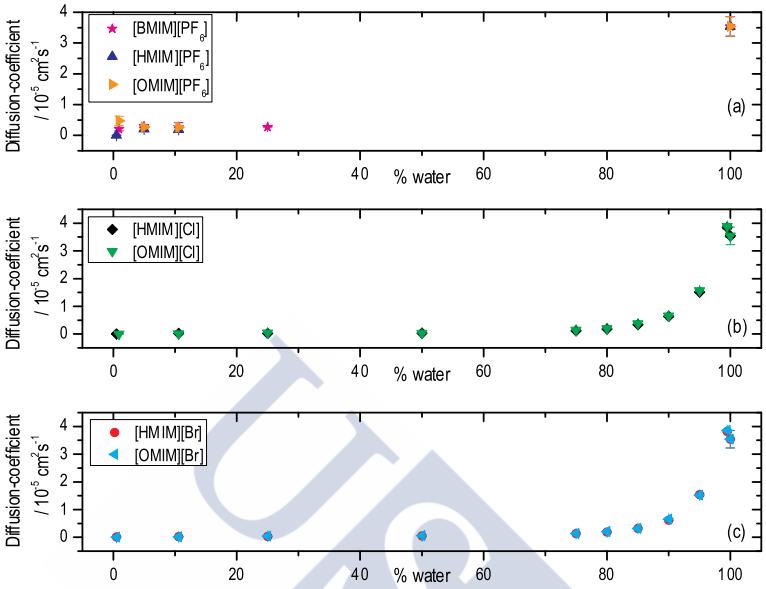

characterized by a Brownian motion, $\langle \Delta|\vec{r}(t)|^2 \rangle \propto t$. The intermediate subdiffusive plateaus can be compared to those reported for supercooled liquids near the glass transition (see ref.[128] and references therein). We can define the characteristic times of ballistic (τ_b) and diffusive (τ_d) times as the times corresponding to the beginning and the end of the intermediate plateau, that can be estimated as the intersection of the two straight lines corresponding to the plateau and the two lines defining the ballistic and diffusive regimes themselves (see Figure 2.13). We have calculated in this fashion the evolution of τ_b and τ_d with water concentration in our mixtures, and the results are represented in Figure 2.14. As can be seen in this representation, both ballistic and diffusive times decrease with water concentration, so the addition of water provokes a faster transition to the diffusive regime. Moreover, it is noteworthy that τ_b is approximately 100 to 1000 times greater than τ_d, so the subdiffusive regime extends over hundreds of ps, in accordance with previously reported results [128]. According to del Popolo and Voth [128], this is indicative of long cage escape times for the water molecules during the intermediate stage, being this

Figure 2.13 Log-log plot of the MSDs of (a) water and (b) cation and anion in a mixture with $BMIMPF_6$ at 25% water concentration. Dotted lines of slope 1 and 2 have been included to identify the ballistic and diffusive regimes.

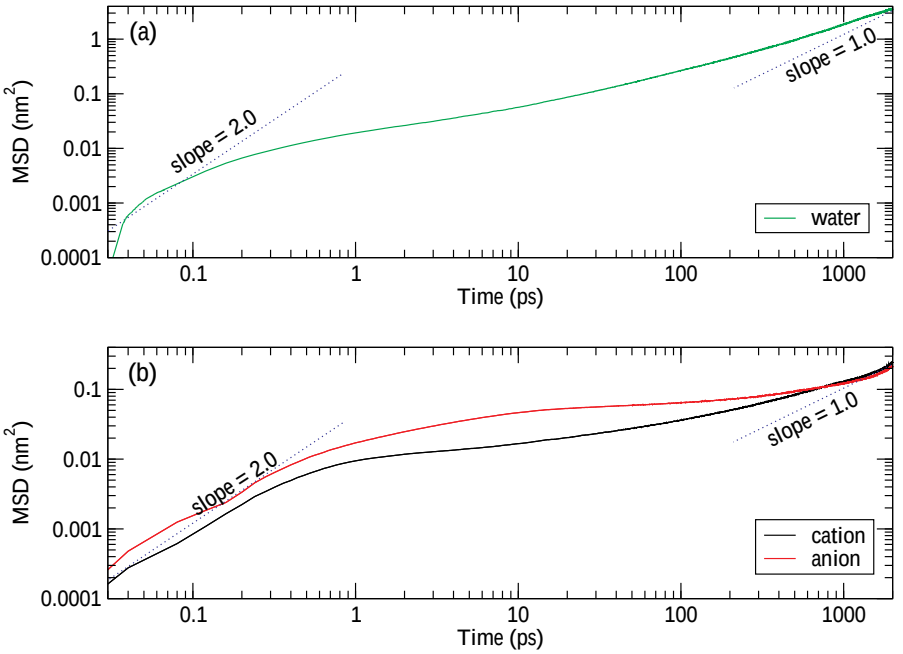

subdiffusive dynamics (for which $\langle \Delta|\vec{r}(t)|^2 \rangle \propto t^\beta$ with $\beta < 1$) characteristic of glass formers. This complex non-Markovian dynamics at intermediate times, which indicates a slow structural relaxation of these liquids, is progressively weakened by the addition of water. We must also mention that these times are shorter for the more hydrophobic cation, and for the Cl^- anion in the case of the halogenated ILs, in agreement with our previous observations for the clusterization of water in mixtures with these ILs. According to the exposed above, water is more strongly clusterized following the series $PF_6^- > Cl^- > Br^-$, so the opposite behavior is expected for the transition time to diffusive motion typical of pure water. Finally, let us point out that these times seem to be maximized for $HMIM^+$ in all of the studied cases, but the precision of our estimations does not allow a more accurate prediction at this stage.

Figure 2.14 Evolution of the ballistic (triangles) and diffusive (circles) characteristic times with water concentration in water-IL mixtures. Lines are guides to the eye.

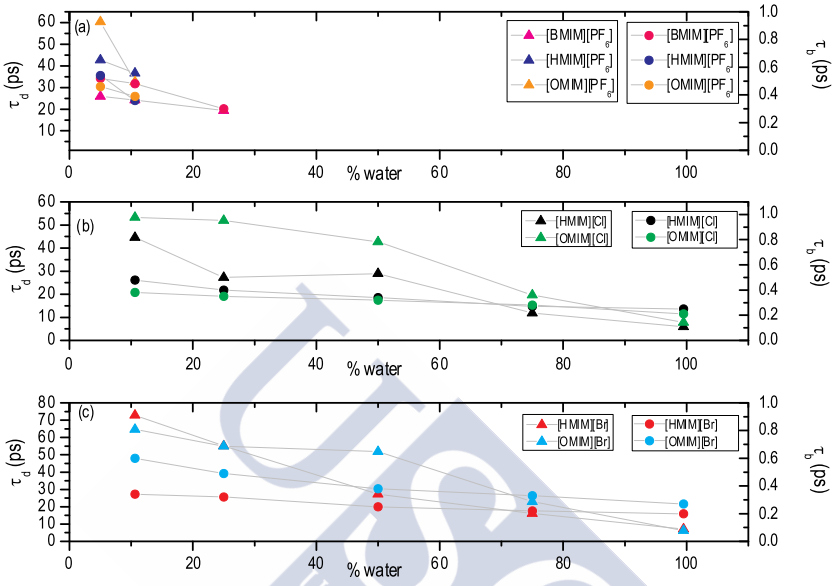

2.1.5. Conclusions

We have presented systematic computer simulations of the structure and dynamics of water mixtures with imidazolium-based ILs of different hydrophobicities (including the highly hydrophobic anion PF_6^- throughout its entire miscibility regime), and we have analyzed the influence of both anion and cation hydrophobicity degrees, and of water concentration on the structural and dynamic properties. Particularly, we have analyzed RDFs, coordination numbers, and average degree of hydrogen bonding of the ionic and molecular species present in the bulk mixtures. We have seen that water tends to clusterize in the cavities of the IL, being the water structuring in the bulk strongly dependent on the hydrophobicity degree of the cation and, even more strongly, of the anion, that leads to greater clusterization of water molecules in the bulk mixtures as its hydrophobic character increases. The average number of hydrogen bonds per molecule is greater by almost 1 order of magnitude for AMIMPF_6-water mixtures than for its halogenated counterparts, probably

due to repulsive interactions between water molecules and the hydrophobic anion. On the other hand, the analysis of the velocity autocorrelation function of water molecules revealed that the correlations cancel out faster for water-IL mixtures with more hydrophobic anions, and that rattling motion of water molecules is registered in the cavities of the halogenated ILs, this motion being more intense when the anion is less hydrated. Two different regimes were observed for the diffusion coefficients of water molecules in IL-water mixtures: (i) a slow increase in the diffusion coefficients associated to glassy states at low water concentrations, and (ii) a rapid increase at low IL concentrations associated to the formation of the water network. Faster diffusion was observed for $AMIMPF_6$ than for the halogenated ILs due to the more hydrophobic character of the PF_6^- anion. Finally, complex non-Markovian dynamics at intermediate times associated to slow structural relaxation of the mixtures are observed. Ballistic and diffusive times were respectively defined as the upper and lower bounds of the ballistic region at short times and the diffusive regime at long times, after the molecule has undergone many collisions in the bulk. These times were shown to be shorter for more hydrophobic cation, and for the Cl^- anion in the case of the halogenated ILs, as determined by the degree of clusterization of water in mixtures with these ILs. A comprehensive study of both single-particle and collective dynamics of IL-water mixtures and of mixtures of ILs with other molecular liquids are now in progress and will be presented in a forthcoming paper.

2.2. Molecular Dynamics Simulations of the Structural and Thermodynamic Properties of Imidazolium-Based Ionic Liquid Mixtures.

In order to further analyze the solvation of molecular liquids in ILs, we performed MD simulations for binary mixtures of ILs composed of the $[Hmim]^+$ cation and three anions of different hydrophobicity degrees ($[Cl]^-$, $[BF_4]^-$ and $[PF_6]^-$), with two alcohols with different chain lengths (methanol and ethanol) [132]. Due to the importance of having a detailed knowledge of the physicochemical properties of this kind of mixtures for the further development of applications of ILs as solvents, we performed a systematic study of how several thermodynamic and structural properties change upon mixing, as well as of the solvation of alcohols in ILs.

The analysis of densities, excess molar volumes, total and partial radial distribution functions, coordination numbers, and hydrogen bonds degrees revealed that the solvation process largely differs from that found in mixtures with water. Particularly, our results reveal that no clusters are formed that disrupt the IL polar network and, instead, the alcohol molecules are almost homogeneously distributed in the bulk IL. This behaviour arises mainly in mixtures with chloride-based ILs, whereas in the more solvophobic ILs the results seem to probe the existence of some kind of network, but its size is not comparable at all to the network found in 2.1. In this case, alcohol molecules also adapt to the nanoseggregated structure of the ILs, whose regions (polar and apolar) accommodate the similar parts of the alcohols, giving rise to a solvation process that could be identified as nanostructural solvation.

2.2.1. Paper II: Molecular Dynamics Simulations of the Structural and Thermodynamic Properties of Imidazolium-Based Ionic Liquid Mixtures; *J. Phys. Chem. B 115 (2011) 11170-11182.*

Trinidad Méndez-Morales,[1] Jesús Carrete,[1] Óscar Cabeza,[2] Luis J. Gallego[1] and Luis M. Varela[1]

In this work, extensive molecular dynamics simulations of mixtures of alcohols of several chain lengths (methanol and ethanol) with the ionic liquids (ILs) composed of the cation 1-hexyl-3-methylimidazolium and several anions of different hydrophobicity degrees (Cl^-, BF_4^-, PF_6^-) are reported. We analyze the influence of the nature of the anion, the length of the molecular chain of the alcohol, and the alcohol concentration on the thermodynamic and structural properties of the mixtures. Densities, excess molar volumes, total and partial radial distribution functions, coordination numbers, and hydrogen bond degrees are reported and analyzed for mixtures of the ILs with methanol and ethanol. The aggregation process is shown to be highly dependent on the nature of the anion and the size of the alcohol, since alcohol molecules tend to interact predominantly with the anionic part of the IL, especially in mixtures of the halogenated IL with methanol. Particularly, our results suggest that the formation of an apolar network similar to that previously reported in mixtures of ILs with water does not take place in mixtures with alcohol when the chloride anion is present, the alcohol molecules being instead homogeneously distributed in the polar network of IL. Moreover, the alcohol clusters formed in mixtures of [HMIM][PF6] with alcohol were found to have a smaller size than in mixtures with water. Additionally, we provide a semiquantitative analysis of the dependence of the hydrogen bonding degree of the mixtures on the alcohol concentration.

2.2.2. Introduction

Room temperature ionic liquids (ILs) are novel compounds that have been widely analyzed in the last two decades. Because of some unique properties, such as low vapor pressure, stability of their liquid state over a large temperature interval (around 300 ˚C), nonflammability, nonvolatility, or solubility in

[1]*Grupo de Nanomateriales y Materia Blanda, Departamento de Física de la Materia Condensada, Universidad de Santiago de Compostela, Campus Vida, s/n E-15782, Santiago de Compostela, Spain*
[2]*Facultad de Ciencias, Universidade de A Coruña, Campus A Zapateira s/n, E-15008, A Coruña, Spain*

a wide range of organic solvents [10, 82, 85, 86, 133], they have many applications as "green solvents" and have been considered as an alternative to common organic solvents [3, 134, 135]. These systems are, in general, composed of an organic cation and a monatomic or polyatomic inorganic or organic anion such as PF_6^-, BF_4^-, Cl^-, Br^-, NTf_2^-, and so forth. Physicochemical properties (viscosity, hydrophobicity, toxicity, catalytic activity, etc.) of ILs can be made to vary broadly by an appropriate selection of cations and anions; for this reason, and taking into account their huge estimated [16] number (10^{18}), they are considered "designer" solvents [83].

For the further development of applications of ILs as solvents, knowledge of their physicochemical properties, and those of their mixtures with both inorganic and organic compounds (mainly water and alcohols) is of crucial importance. For this purpose, it is particularly relevant to understand how the structure and properties of IL mixtures change upon mixing, as well as the dependence of the properties of the resulting mixtures on their composition.

The interaction between ILs and polar or apolar solvents has been investigated by means of molecular simulation and experimental studies before. However, contrarily to the case of IL/water mixtures, for which the number of reported contributions has greatly increased over the last years (see, for example, refs.[81] and [136] and references therein), studies of mixtures with alcohol are still scarce. In this latter case, some experimental results [137–147] have been reported during the past decade. Particularly, several works have been done studying the factors that govern the phase behavior of imidazolium based ILs in different systems [137–139]. For instance, Crosthwaite *et al.* [139] carried out a systematic study of the effect of different characteristics of the components on the liquid equilibrium of IL/alcohol mixtures. They reported results similar to those of Pereiro and Rodríguez [140], whose solubility studies show that the immiscibility range of IL/alcohol binary systems decreases with an increase in the IL alkyl chain length. These results are compatible with those of Domańska *et al.* [141], who determined that the solubility of ILs in alcohols decreases with an increase in the length of the molecular chain of the alcohol. Moreover, Pereiro and Rodríguez's results suggest that a replacement of the hydrogen at the *C*2 position of the imidazolium ring with a methyl group causes an increase in the upper critical solution temperature, whereas the choice of the anion has a great impact on this property, and its effect is related to the ability of the anion to form a hydrogen bond. Several experimental studies have also been performed with the aim of studying thermody-

namic properties of mixtures of imidazolium-based ILs with alcohols, such as densities and excess molar volumes, refractive indices, speed of sound, or surface tension [142–147]. As an example, Cabeza and co-workers [147] studied the influence on surface tension and density of the alkyl chain length of the IL family 1-alkyl-3-methylimidazolium tetrafluoroborate ([AMIM][BF_4]) with water and ethanol. The results obtained show a monotonic decrease of the density of the mixtures with increasing ethanol (or water) molar fraction, and a decrease of the surface tension with the increase of the alkyl chain length of the IL cation.

As it is usually very complicated to experimentally investigate the behavior of ILs at the atomic level, molecular dynamics (MD) simulations are usually the best way to probe the properties of the mixtures. In fact, a great number of simulation studies have been dedicated over the past years to investigate the thermodynamic and structural properties of both pure ILs and of IL/solvent mixtures. However, the truth is that mixtures have received much less attention. Up to now, the most studied among IL mixtures have been those with water. In 2003, Hanke and Lynden-Bell [65] reported the first, as far as we know, MD study of both the local structure and dynamics of mixtures of water with two ILs, 1,3-dimethylimidazolium chloride ([DMIM][Cl]) and 1,3-dimethylimidazolium hexafluorophosphate ([DMIM][PF_6]). Jiang *et al.* [93] investigated the influence of water concentration on the nanostructural organization in mixtures of 1-octyl-3-methylimidazolium nitrate ([OMIM][NO_3]) with water. Feng and Voth [98] reported very recently the first (to our knowledge) MD study of the effect of both alkyl chain length and anion on the structure and dynamics of IL/water mixtures. They analyzed three IL/water mixtures at several water mole fractions: 1-butyl-3-methylimidazolium tetrafluoroborate ([BMIM][BF_4]), 1-octyl-3-methylimidazolium tetrafluoroborate ([OMIM][BF_4]) and 1-octyl-3-methylimidazolium chloride ([OMIM][Cl]). We have also recently reported systematic MD simulations of the structure and dynamics of mixtures of water with several imidazolium-based ILs [81]. In particular, we analyzed radial distribution functions, coordination numbers, hydrogen bonding degrees, mean squared displacements, self-diffusion coefficients, and, for the first time, the velocity autocorrelation function of water molecules in the mixture.

In what IL/alcohol mixtures are concerned, the reported results are much scarcer. Hanke *et al.* [148] reported a computational study of mixtures of [DMIM][Cl] with water, methanol, dimethyl ether, and propane. They found

that the strongest solute-solvent interactions in water and methanol mixtures are hydrogen bonding of water and methanol with the IL anion, whereas for dimethyl ether and propane, interactions with the imidazolium cations are more important. In 2006, Canongia-Lopes *et al.* [95] analyzed the solvation of nonpolar, polar and associating solutes in 1-butyl-3-methylimidazolium hexafluorophosphate ([BMIM][PF_6]) in mixtures with n-hexane, acetonitrile, methanol, and water. These authors confirmed the presence of segregated polar and nonpolar domains in the bulk mixtures. Additionally, Raabe and Köhler [149] reported a computational study of binary mixtures of ILs of the 1-alkyl-3-methylimidazolium chloride ([AMIM][Cl]) IL family with ethanol and 1-propanol to calculate their densities, excess energies of mixing, and structural properties such as radial and spatial distribution functions. On the other hand, Jahangiri *et al.* [66] performed MD simulations of the mixture of 1-ethyl-3-methylimidazolium chloride ([EMIM][Cl]) and 1-ethyl-3-methylimidazolium hexafluorophosphate ([EMIM][PF_6]) with both methanol and ethanol in order to investigate excess properties and some physical and structural properties of the mixture, such as excess enthalpies, excess volumes, radial distribution functions, cohesive energy density, and diffusion coefficients. More recently, Heintz *et al.* [150] reported MD simulations to calculate tracer diffusion coefficients of the IL ions in mixtures of 1-ethyl-3-methylimidazolium bis(trifluoromethanesulfonyl)imide ([EMIM][NTf_2]) and 1-butyl-3-methylimidazolium bis(trifluoromethanesulfonyl)imide ([BMIM][NTf_2]), both with water and methanol.

A detailed knowledge and understanding of the physicochemical properties of alcohol/IL mixtures is of fundamental importance to further explore the great number of potential academic, industrial, and biomedical applications of ILs. However, a systematic study of the relation between the structure and the properties of the mixture, including the role of different parameters such as cation length, anion, composition and alcohol chain size, is not available at this point. As it is well-known [151, 152], the length of the imidazolium cation chain is directly related to the hydrophobicity of ILs, (the longer the chain, the more hydrophobic the IL), and consequently it is expected to have a deep impact on the properties of their mixtures. However, the role of the anion is not completely understood, although the expected tendency is an increase of the solvophobicity with the presence of larger anions (such as PF_6^-) instead of monatomic anions (such as Cl^-). In IL-water mixtures, the anion is known to be the most influential entity on the properties of the polar net-

Figure 2.15 Molecular structures of $HMIM^+$, PF_6^+, and BF_4^+ ions.

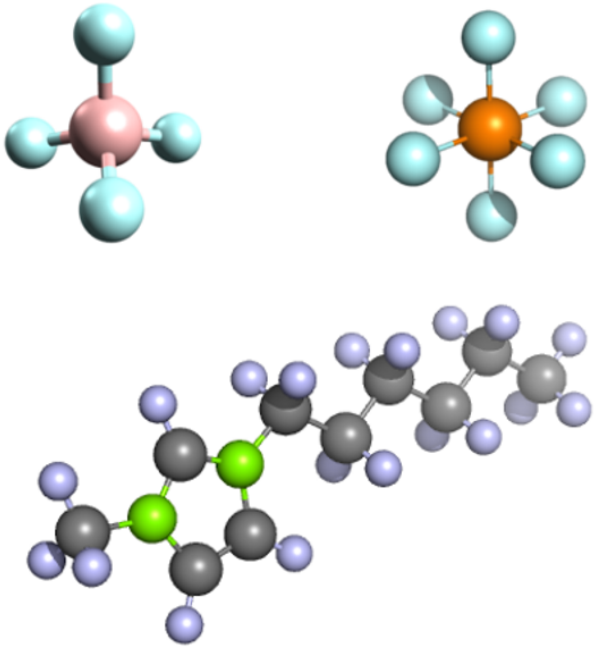

work in the bulk mixture, and it is also known to be an important factor in determining ILs solubility in water and alcohols. Moreover, in order to rationalize the behavior of IL-alcohol mixtures it is of fundamental importance to know how the latter compound takes part in the solvation process of ILs. In this work we performed extensive MD simulations to investigate several thermodynamic and structural properties of mixtures of alcohols and 1-hexyl-3-methylimidazolium ($HMIM^+$) with three different anions of various solvophilic degrees: Cl^-, the one with the larger effect on water structure according to the Hoffmeister series; the highly hydrophobic PF_6^-, with low miscibility with water; and BF_4^-, with intermediate characteristics (see Figure 2.15). The chosen alcohols were methanol and ethanol, in order to investigate and compare the influence of the length of the molecular chain of the alcohol in the properties of the mixtures. Moreover, we analyzed the impact of the anion nature and alcohol concentration on the microstructure of the mixtures by analyzing their densities, excess molar volumes, radial distribution functions, coordination numbers, and degrees of hydrogen bonding.

The remainder of this paper is organized as follows. In section 2.2.3 we give details of the computational procedure used in our study; in section 2.2.4 we present and discuss the obtained results, and, in section 2.2.5 we summarize our main conclusions.

2.2.3. Simulation details

The MD simulations for pure ILs and their mixtures with alcohols were performed using the Gromacs package [70]. All the simulations were run at 298.15 K, and the analyzed mole fractions of alcohol in the IL/alcohol mixtures were $x_{alcohol}$ = {0.00, 0.10, 0.20, 0.30, 0.40, 0.50, 0.60, 0.70, 0.80, 0.90, 0.95, 0.98, and 1.00}, as both ethanol and methanol are miscible with all the selected ILs ([HMIM][PF_6], [HMIM][BF_4] and [HMIM][Cl]) throughout the whole concentration range [140, 146, 147]. The number of IL molecules in the cubic box was set to 300, except for $x_{alcohol}$ = 0.10, where we considered 450 IL molecules in order to have enough alcohol to yield statistically significant trajectories, $x_{alcohol}$ = 0.95 – 0.98, where just 50 ionic pairs were introduced so as to keep the system size small enough, and $x_{alcohol}$ = 1.00, a case in which only alcohol molecules are present. The number of alcohol molecules was adjusted in each situation counting each ionic pair as a single molecule in the calculation of mole fractions.

The parametrization of the ions was carried out in the framework of the OPLS force field developed by Jorgensen and coworkers [153] for different organic fluids. In the functional form of the OPLS force field in eq 2.5, the first three terms represent the bonded interactions, *i.e.*, bonds, angles, and torsions, while the nonbonded interactions are described by the last two terms, and include van der Waals and Coulombic interactions:

$$\begin{aligned} E = & \sum_i K_{b,i}\left[r_i - r_{0,i}\right]^2 + \sum_i K_{b,i}\left[\theta_i - \theta_{0,i}\right]^2 + \\ & + \sum_i \left[\frac{1}{2}V_{1,i}(1+\cos(\varphi_i)) + \frac{1}{2}V_{2,i}(1+\cos(2\varphi_i)) + \right. \\ & \left. + \frac{1}{2}V_{3,i}(1+\cos(3\varphi_i)) + \frac{1}{2}V_{4,i}(1+\cos(4\varphi_i))\right] + \\ & + \sum_i \sum_{j<i} \left\{ \frac{1}{4\pi\varepsilon_0}\frac{q_i q_j e^2}{r_{ij}} + 4\varepsilon_{ij}\left[\left(\frac{\sigma_{ij}}{r_{ij}}\right)^{12} - \left(\frac{\sigma_{ij}}{r_{ij}}\right)^{6}\right]\right\}, \end{aligned} \tag{2.5}$$

The parameters used in the above equation are the force constants K, the reference values r_0 and θ_0, the Fourier coefficients V, and the partial atomic charges q. σ_{ij} and ε_{ij} represent the Lennard-Jones radii and potential well depths, respectively, which are obtained from parameters for each type of atom using geometric combination rules $\sigma_{ij} = (\sigma_{ii}\sigma_{jj})^{1/2}$ and $\varepsilon_{ij} = (\varepsilon_{ii}\varepsilon_{jj})^{1/2}$. As it is known, there are both united atom (OPLS-UA) and all-atom (OPLS-AA) versions of the OPLS force field. The former includes hydrogen atoms bonded to carbon implicitly in the carbon parameters, and in the latter every hydrogen atom is modeled explicitly. The cations were modeled using the all-atom representation of the CH_2 and CH_3 groups in the alkyl chain, as well as that of the methyl group attached to the imidazolium ring. As for the anions, PF_6^- was modeled as a set of seven sites with partial charges of 1.34 for the phosphorus atom and −0.39 for the fluorine atoms [154]. BF_4^- was modeled as a set of five sites with partial charges of 1.176 for the boron atom and −0.544 for the fluorine atoms [155], while Cl^- was modeled by a single site of charge −1 [156]. Among the partial charges used, those taken from the work by Acevedo and Canongia-Lopes *et al.* (refs.[154] and [156], respectively) come from application of the restrained electrostatic potential (RESP) fitting method [105], while the ones reported by Prado and Freitas in ref.[155] were computed by MP2/6-31 g(d) using the ChelpG methodology [157] implemented in the GAUSSIAN 94 package [158]. The force field parameters of $HMIM^+$, including partial charges, were taken from the development of OPLS-AA parameters for 68 combinations of ILs reported in ref.[154]. On the other hand, ethanol and methanol molecules were represented by the molecular model proposed by Jorgensen [75]. Long-range electrostatic interactions were processed using the particle-mesh Ewald (PME) [77] method with a grid spacing of 0.12 nm and cubic interpolation. The cutoff distance for Lennard-Jones interactions was set to 1.1 nm, and a search of neighbors was made up to this same distance from the central ion and was updated every five simulation steps. The Linear Constraint Solver (LINCS) algorithm [159, 160] with a fourth-order expansion of the constraint coupling matrix was used to constrain the bonds, and long-range dispersion corrections were used for energy and pressure.

Initial configurations were energy-minimized for 10^6 steps using a conjugated gradients algorithm in order to remove bad contacts resulting from the initial random configuration of ions. The maximum step size and the tolerance were set to 0.01 nm and 0.1 $kJ \cdot nm^{-1} \cdot mol^{-1}$, respectively. The equilibration phase was performed in the isothermal-isobaric (N,p,T) ensemble during

100 ps to ensure the full equilibration of all the properties of the system. For any given system, an appropriate choice of equilibration time depends on the complexity of the simulated molecules, their relative masses and the parameters of the thermostat and barostat, as well as on the temperature and density at equilibrium. In particular, our experience shows that, in contrast with other cases where several more conformationally complex molecules (such as proteins) are involved, for imidazolium-based ILs, 100 ps is usually considered to be enough [123]. In our simulations, as a criterion for equilibration we checked that all thermodynamic properties (except for pressure, which shows the expected very large short-term fluctuations usually present in this kind of simulations) were stable. The results of an additional 2000 − ps simulation in the isothermal-isobaric ensemble were used for analysis. The temperature control was implemented using the V-rescale thermostat [161]. Cations and anions (and alcohols in those cases where we include a solvent) were separated into two (three) baths with temperature coupling constants of 0.1 ps. The pressure control was set using a Parrinello-Rahman barostat [162] with a reference pressure of 1 atm, an isothermal compressibility of $4.5\times10^{-5}bar^{-1}$, and a relaxation time of 1.0 ps.

Each of these simulations provided us with a sequence of configurations, *i.e.*, positions and instantaneous velocities of all atoms of the system, which was analyzed to obtain structural and thermodynamic information about the aforementioned mixtures.

2.2.4. Results and discussion

Density of ILs is one of the most reliable sources of experimental data, therefore comparisons between experimental and computational results for liquid densities are usually used to estimate the accuracy of the force field employed in MD simulations [98, 149]. Densities of pure ILs and alcohols obtained from MD simulations, as well as their comparison with experimental data and the respective deviations, are shown in Table 2.1. The reported MD simulations of pure ILs at 298.15 K show underestimations of experimental densities [140, 146, 147] ranging from 0.6% to 1.8%. Moreover, the comparison of our simulated densities of pure alcohols with the experimental data [75, 146] exhibits an underestimation of 1.2% for methanol and an overestimation of 1.4% for ethanol, both at 298.15 K. Thus, we could say that our presently reported MD density results for pure ILs and pure alcohols are in good agreement

Table 2.1 Simulated and Experimental Densities and Experimental Molar Volumes for Pure ILs and Alcohols at 298.15 K, and Deviations from Experimental Data

compound	ρ_{sim} (kg/m^3)	ρ_{exp} (kg/m^3)	$\Delta\rho$ (%)	V_m (cm^3/mol)
[HMIM][PF_6]	1270.5 ± 4.9	1293.7	1.79	241.32
[HMIM][BF_4]	1128.6 ± 4.6	1145.4	1.47	221.83
[HMIM][Cl]	1034.4 ± 3.9	1040.4	0.57	194.86
Methanol	776.7 ± 5.9	786.0	1.19	40.76
Ethanol	796.6 ± 9.5	785.4	1.42	58.66

with the experimental ones. These results allow us to be reasonably confident in our simulation model and, consequently, in the calculated densities of the IL/alcohol mixtures, for which (to our knowledge) no MD results have been reported so far.

Our computational results for the density over the whole composition range of the binary mixture [HMIM][PF_6]/ethanol at 298.15 K are shown in Figure 2.16.a together with the experimental results reported by Pereiro and Rodríguez [140]. As can be seen there, the predictions for the density of [HMIM][PF_6]/ethanol mixtures are in excellent agreement with the experimental values. All the other mixtures showed the same tendency as this one, a monotonic decrease from the density of pure IL to that of pure alcohol with an increase of alcohol concentration, and their predicted densities were also in excellent agreement with the experimental values. It is noteworthy that this behavior is in marked contrast to that previously reported on mixtures of our halogenated IL with water, for which Gómez *et al.* [146, 163] reported that its binary mixtures with water present a maximum value of the density at $x_{water} \approx 0.5$. In this sense, one must recall that water is known to be the only molecular compound in which the existence of thermodynamic anomalies such as density maxima and a liquid-liquid phase transition is firmly established [164]. Thus, the density maximum in [HMIM][Cl]/water mixtures can be due to some structural transition in the associated to the formation of continuous networks of water during the transition from the ionic to the polar network, which does not take place in the case of mixtures with alcohol.

Additionally, the excess molar volumes of the mixtures were calculated from their density values through the well-known eq 2.6:

Figure 2.16 (a) Comparison between simulated (black dots) and experimental (red dots) densities of a [HMIM][PF_6]/ethanol mixture at 298.15 K, and (b) comparison between simulated (black dots) and experimental (red dots) excess molar volumes calculated from densities data of a [HMIM][PF_6]/ethanol mixture at 298.15 K; both as a function of the ethanol mole fraction. Experimental results were reported by Pereiro and Rodríguez [140].

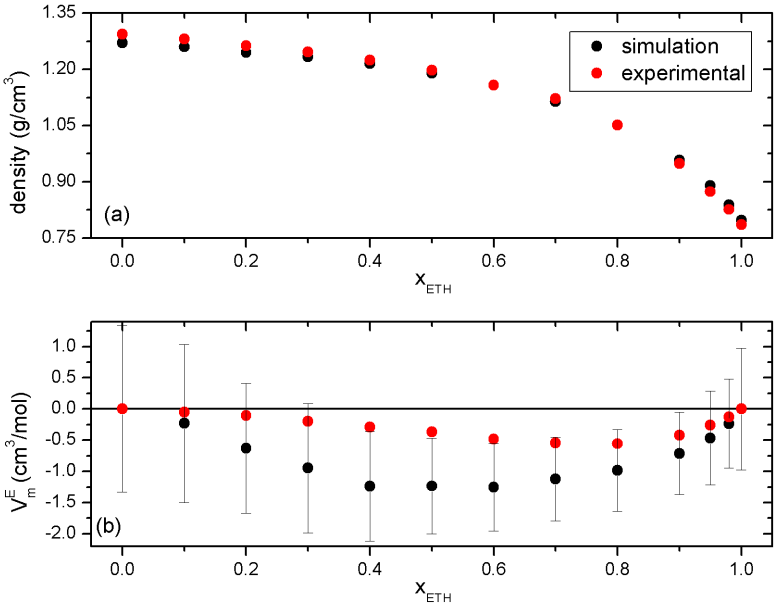

$$V_m^E = \sum_{i=1}^{2} x_i M_i (\rho^{-1} - \rho_i^{-1}) \tag{2.6}$$

where F and F_i stand for the density of the mixture and the density of the pure components, respectively, x_i represents the mole fraction of the ith component of the mixture, and M_i is its molar mass. Figure 2.16.b shows a comparison between the calculated excess molar volumes and the experimental ones reported by Pereiro and Rodríguez in ref.[140] for the binary mixture of [HMIM][PF_6] with ethanol at 298.15 K as a function of ethanol mole fraction. It is noteworthy that the relative reported experimental excess molar volumes for IL/alcohol mixtures are less than 0.5% of the molar volumes of the pure components (see Table 2.1), indicating the quasi ideal behavior of these systems [147]. It can be seen there that our simulations overestimate the excess molar

volume by $\sim$ 1 cm^3/mol, but the experimental values lie within the uncertainty intervals as represented by the error bars calculated by propagating the uncertainties of the stochastic series of simulated densities, whose uncertainties are given by Gromacs by calculating the dispersion of the density around its average value. As a matter of fact, it is extremely difficult to obtain V^E with accuracy from a simulation, given that very small differences in density can induce large differences in excess molar volume. Indeed, the same behavior was reported by Kelkar *et al.* [94], who concluded that the simple point charge (SPC) model of water overestimates excess molar volumes by $\sim$ 1 cm^3/mol in mixtures of 1-ethyl-3-methylimidazolium ethylsulfate ([EMIM][$EtSO_4$]) with water. Moreover, it can be seen in Figure 2.17 that the excess molar volumes are negative over the entire composition range for the binary mixtures, both in mixtures with ethanol and in those with methanol, in good agreement with experimental and computational results previously reported in the literature for IL/alcohol mixtures [140, 142, 143, 146]. Hence, all the studied compounds show a contractive tendency upon mixing, and all of them reach a minimum at $x_{alcohol}$ between 0.4 and 0.7. As it is well-known, the association trend on mixtures depends on the intermolecular forces between the components of the mixture, and the packing effect due to the different shapes and sizes of the molecules. In this case, the ion-dipole interactions between alcohol molecules and the IL ions are stronger than the interactions between the molecules in the pure components, so the excess molar volumes become slightly negative. Our calculated absolute values of V^E are larger in the case of mixtures of [HMIM][Cl] with both alcohols (Figure 2.17.c), reaching values twice as large as those obtained for PF_6^- and BF_4^- (Figure 2.17.a,b, respectively), which were similar to each other. This indicates that more alcohol molecules fit into the free volume between the ions of ILs in the case of mixtures with chloride than in the mixtures with the biggest anions. Thus, anions exert a deep impact on mixing, and hydrophilic ILs seem to have greater miscibility with methanol and ethanol than the hydrophobic ones. Moreover, the minimum of our calculated excess molar volume is more negative in mixtures with methanol than in mixtures with ethanol, showing a better packing for smaller molecular chain of the alcohol. Considering the predictions for the densities and excess molar volumes of the studied mixtures, we can conclude that the simulation model predicts reasonably well the thermodynamic properties of the system. In the following, we will apply it to the study of the microscopic structure of these mixtures.

Figure 2.17 Excess molar volumes calculated from our computational results for the densities of (a) [HMIM][PF_6]/alcohol, (b) [HMIM][BF_4]/alcohol, and (c) [HMIM][Cl] /alcohol (green dots correspond to methanol, and black dots correspond to ethanol) mixtures at 298.15 K as a function of the alcohol mole fraction.

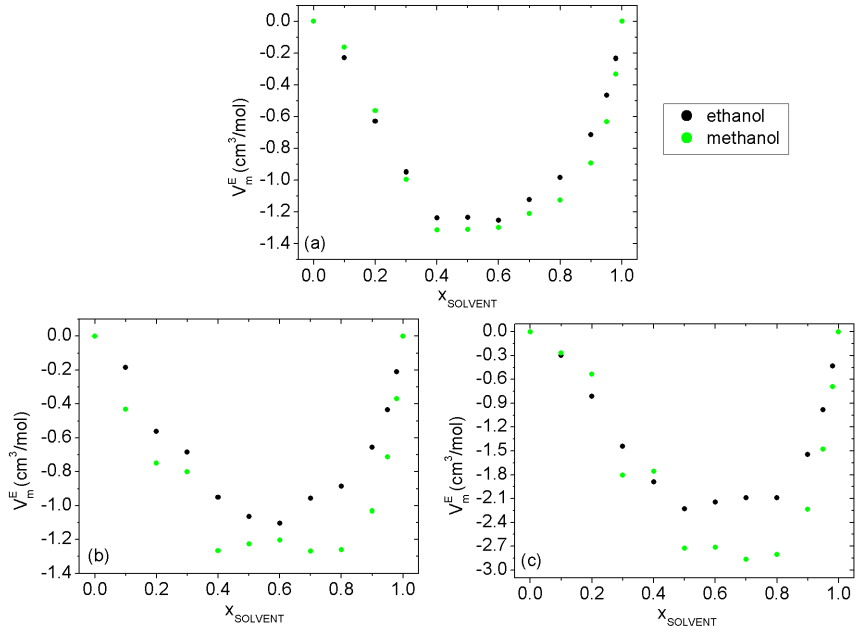

The structure of dense fluids is usually characterized by means of the radial distribution function (RDF) defined as

$$g(r) = \frac{1}{\rho N}\left\langle \sum_{ij} \delta(r - r_{ij}) \right\rangle \tag{2.7}$$

where N is the number of particles in the system, F stands for its number density, i and j run over all system particles, and brackets indicate ensemble average. All RDFs presented in this paper (unless otherwise noted) were calculated using the center of mass of the anions and the center of mass of the imidazolium ring of the cation. Our computational ion-ion RDFs for pure ILs are shown in Figure 2.18, where the influence of the anion on the structure of the system is analyzed. Most remarkably, the first peak of the cation-anion RDF for the halogen anion is notably higher than those obtained for the PF_6^- and BF_4^- anions (Figure 2.18.a), and it is placed at smaller distances (0.45 nm)

with respect to the polyatomic anions (0.53 nm for PF_6^- and 0.50 nm for BF_4^-), probably due to the bigger size of the fluorinated anions. For the same reason, the maximum of the first peak of the cation-anion BF_4^- RDF is registered at a slightly lower distance than that for the PF_6^- anion. Moreover, all cation-anion RDFs show a shoulder at the end of their first peaks of the cation-anion RDF, which is more prominent in the presence of the chloride ion (at 0.57 nm), and much more imperceptible for the more hydrophobic anions. These features have also been observed in some liquids such as Ga, Si, Sn, or Bi (see ref.[119] and references therein), where it has been interpreted as a signature of a short-lived diatomic molecular unit, and also in IL/water mixtures [81]. Contrary to what happens with this first peak, the impact of the variation of the anion in the distribution of higher order neighbors seems to be relatively limited. On the other hand, the cation-cation RDF (Figure 2.18.b) for the halogen anion shows a first peak around 0.40 nm, but similar features are almost invisible in [HMIM][PF_6] and [HMIM][BF_4]. Regarding the anion network structure, we see that a double first peak is obtained for PF_6^- and BF_4^- anions, centered at 0.80 and 0.75 nm, respectively; while the anion-anion RDF of [HMIM][Cl] exhibits a single peak around 0.70 nm. These results are in agreement with the features reported in our previous work about IL/water mixtures [81], in which the GROMOS96 43A1 force field was used.

In order to analyze the alcohol distribution in bulk mixtures, we calculated alcohol-alcohol, cation-alcohol, and anion-alcohol RDFs in IL/alcohol mixtures, and they are shown in Figures 2.19, 2.20, and 2.21, respectively. In the first one, ethanol-ethanol RDFs (Figure 2.19.a,c,e) exhibit a first peak at approximately 0.47 nm, with a maximum height of approximately 2.3 in the [HMIM][PF_6] and [HMIM][Cl] mixtures (Figure 2.19.a,e), at the lowest concentration of ethanol. However, the smallest quantity of ethanol in mixtures with [HMIM][BF_4] (Figure 2.19.c) shows the lowest peak of the whole concentration range of that mixture, its value being less than 1.4. In general, the first peak of ethanol-ethanol RDFs decreases with increasing ethanol mole fraction, indicating that spatial correlation between ethanol molecules decreases when ethanol concentration increases, but there are some exceptions that show an inversion, such as $x_{ethanol} = 0.2$ in the [HMIM][PF_6]/ethanol mixture, $x_{ethanol} = 0.3$ in the [HMIM][BF_4]/ethanol one, or $x_{ethanol} = 0.2$ and $x_{ethanol} = 0.4$ in the [HMIM][Cl]/ethanol mixture. On the other hand, methanol-methanol RDFs (Figure 2.19.b,d,f) show a double first peak, the first one (sharper in the case of [HMIM][PF_6] in Figure 2.19.b) at 0.33 nm, and the second one (sharper

Figure 2.18 RDFs for cation-anion (a), cation-cation (b), and anion-anion (c) of $HMIM^+$ with three different counterions (PF_6^-, BF_4^-, and Cl^-) at 298.15 K and 1 atm.

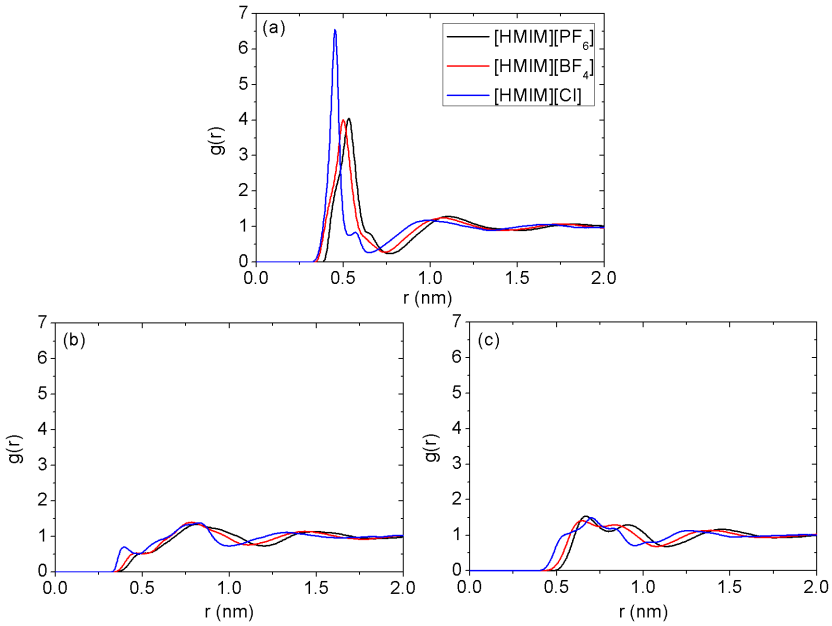

in the cases of [HMIM][BF_4] and [HMIM][Cl] in Figure 2.19.d,f, respectively) at 0.44 nm in all cases. It can be deduced that methanol molecules are distributed in two nearby shells around other methanol molecules, whereas ethanol molecules are distributed in two further shells (the center of the second shell is placed at 0.88 nm in mixtures with ethanol) and the peaks corresponding to third neighbors can be neglected. Moreover, it can be seen that RDFs of the methanol/[HMIM][Cl] mixture only show the first peak when $x_{methanol} = 0.9$ is reached, showing that the halogen anion prevents the formation of the first methanol layer. Furthermore, the second peak decreases with increasing methanol mole fraction, showing exceptions at $x_{methanol} = 0.1$ and $x_{methanol} = 0.4$. For methanol/[HMIM][BF_4] mixtures, the spatial correlation of methanol molecules increases with an increase of the mole fraction of alcohol, with an inversion at $x_{methanol} = 0.3$. The RDFs in Figure 2.19.b reach the highest maximum for the lower concentration of methanol in [HMIM][PF_6], with a value of approximately 5. From this representation we can infer that methanol molecules are more clusterized than ethanol ones when the hydro-

Figure 2.19 Alcohol mole fraction dependence of ethanol-ethanol (a,c,e) and methanol-methanol (b,d,f) RDFs for [HMIM][PF_6] (a,b), [HMIM][BF_4] (c,d), and [HMIM][Cl] (e,f) at 298.15 K and 1 atm.

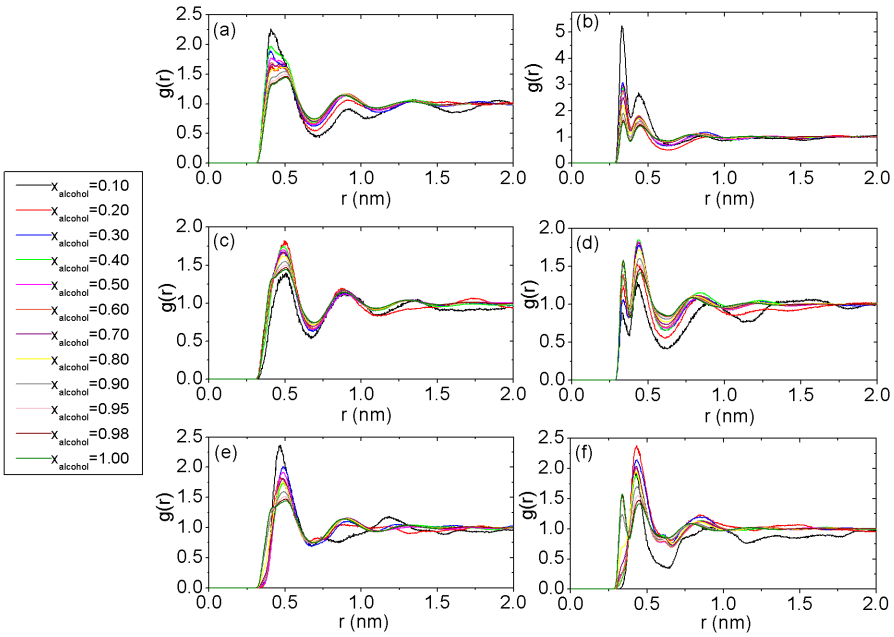

phobic anion is present, and that the height of this first peak decreases with increasing methanol mole fraction. However, the fact that highest peaks reach much lower values than those reported in our previous work for mixtures of [HMIM][PF_6] with water [81] allows us to deduce that the clusterization degree of methanol in mixtures with [HMIM][PF_6] is much lower than the clusterization degree of water in mixtures with the same IL. However, it is still higher than in mixtures of methanol with [HMIM][BF_4] or [HMIM][Cl]. In this same way, Raabe and Köhler [149] concluded that in binary mixtures of [AMIM][Cl] with ethanol and propanol, a continuous solvent network similar to that found in water/IL mixtures (see refs.[81] and [65, 93, 98]) is not present, and that the alcohol seems to be homogeneously distributed in the cation-anion network of the IL.

Figure 2.20 illustrates the cation-alcohol RDFs in the studied mixtures. For clarity, only a few of all the analyzed mole fractions are shown. In all the cases shown in Figure 2.20, one can observe a first peak around 0.48 nm, which

Figure 2.20 Alcohol mole fraction dependence of cation-ethanol (a,c,e) and cation-methanol (b,d,f) RDFs for [HMIM][PF_6] (a,b), [HMIM][BF_4] (c,d), and [HMIM][Cl] (e,f) at 298.15 K and 1 atm.

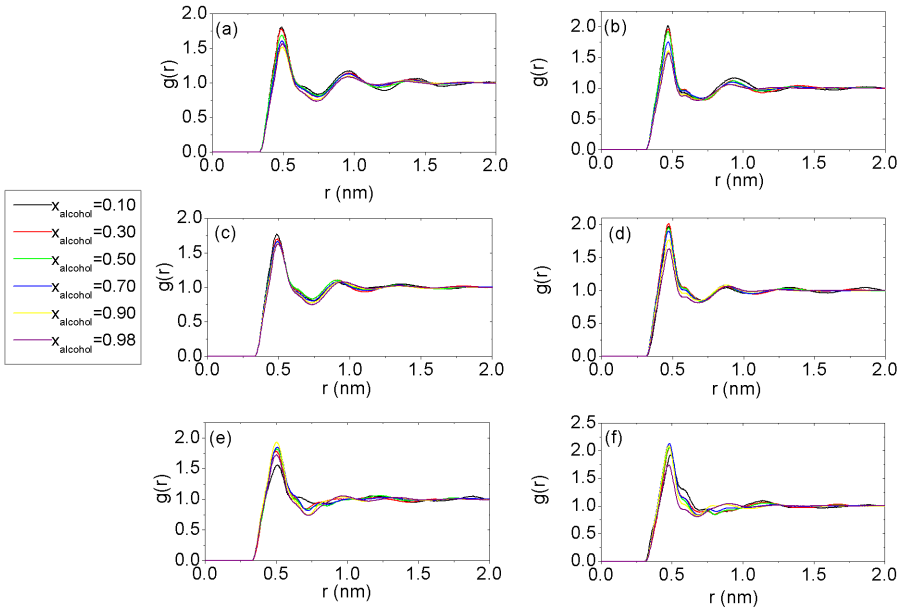

slightly decreases with an increase of the mole fraction of alcohol (except in [HMIM][Cl]/ethanol mixtures, where it shows the opposite tendency). In mixtures with both polyatomic anions (Figure 2.20.a-d), a second peak can be identified around 0.90 nm, whereas when chloride is present, cation-alcohol RDFs quickly converge to the ideal value for both alcohols. The fact that the first peak height is lower than 2 and that the RDFs are quickly smoothed out implies that there is no aggregation of alcohol molecules around the cations of ILs. This behavior was also reported by Jahangiri *et al.* [66] in mixtures of methanol with [EMIM][PF_6] and [EMIM][Cl].

The situation is completely different for the anion-alcohol RDFs shown in Figure 2.21. For the ethanol molecules around PF_6^- (Figure 2.21.a) there is a peak at 0.47 nm, whereas, in the case of methanol (Figure 2.21.b) there are two peaks, the first one at 0.42 nm being sharper and the second one around 0.50 nm broader. In both mixtures with [HMIM][BF_4] (Figure 2.21.c,d) the first peak of anion-alcohol RDFs is placed at shorter distances than in the case with PF_6^-, at 0.43 nm for the mixture with ethanol and at 0.40 nm for the system

with methanol. In the case of methanol/[HMIM][BF_4] mixtures, the second peak found in the presence of the PF_6^- anion is absent. Regarding mixtures of alcohols with [HMIM][Cl] (Figure 2.21.e,f), both RDFs show a high and sharp first peak, around 0.37 nm in mixtures with ethanol and at 0.33 nm in those with methanol. The height of these two peaks is higher in the case of the shorter alcohol, which implies that there is a stronger interaction of Cl^- with methanol than with ethanol. Moreover, it can be seen from Figure 2.21.e,f that this first peak of the anion-alcohol RDFs remains at the same position, but the height of the peaks increases with the increase of the mole fraction of alcohol, as was also reported in refs.[149] and [66]. However, this behavior is in contrast to our previous results for [HMIM][Cl]/water mixtures [81], in which we reported that the structuring was weakened as water concentration increased. Moreover, the height of the highest peak in methanol/[HMIM]-[Cl] mixtures (corresponding to $x_{methanol} = 0.8$) is lower than the highest peak in water/[HMIM][Cl] mixtures (corresponding to $x_{water} = 0.1$), their values being around 10 and 15, respectively. In [HMIM][Cl]/methanol mixtures (Figure 2.21.f), a melt second peak appears around 0.43 nm illustrating the establishment of a second solvation shell of methanol molecules placed around the halogen anion. This peak of second neighbors around the anion was also observed by Raabe and Köhler [149]. The maximum height of this second peak belongs to the lowest concentration of methanol ($x_{methanol} = 0.1$). An analogous behavior was reported by Hanke and Lynden-Bell [148] in their simulation studies of mixtures of [DMIM][Cl] with water. In our computational simulations of IL/water mixtures [81], we also found this second peak when the halogen anions were present, but its maximum height was registered for the highest water concentration. The different heights of the first peaks shown in Figure 2.21 imply that the interaction between alcohol molecules and anions is stronger in the case of the halogen anion than for the polyatomic ones, reproducing the same behavior that we previously detected in mixtures with water [81].

Thus, from analysis of the RDFs we can conclude that the alcohols interact preferentially with the IL anion, in agreement with previous computational studies of methanol/[BMIM][PF_6] mixtures performed by Canongia-Lopes *et al.* [95]. The above figures show that hydrogen bonding between the alcohol molecules and the anions, responsible for the first peaks in the corresponding RDF, is stronger than the hydrogen bonding between alcohol molecules when the anion that is present in the mixture is the halogen one. Moreover, these

Figure 2.21 Alcohol mole fraction dependence of anion-ethanol (a,c,e) and anion-methanol (b,d,f) RDFs for [HMIM][PF_6] (a,b), [HMIM][BF_4] (c,d), and [HMIM][Cl] (e,f) at 298.15 K and 1 atm.

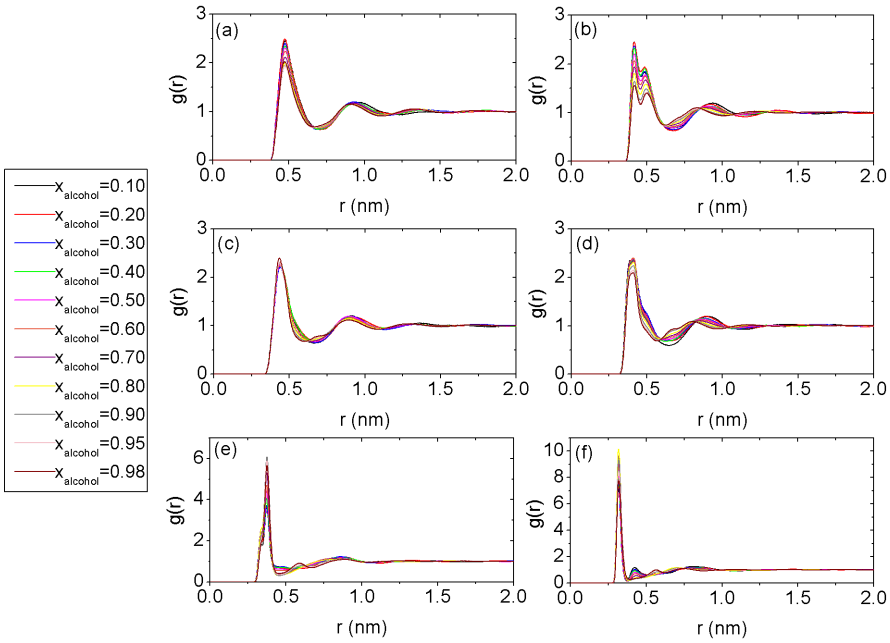

hydrogen-bond interactions between the chloride and the alcohol are more pronounced for the shorter alcohol chain. Although in mixtures of ILs with water we reported the formation of a continuous water network that breaks the ionic network, in the mixtures with alcohols of the present paper the hydrogen bonding between the alcohol molecules does not seem to be relevant enough until very high alcohol molar fractions, whereas the strong interaction between alcohols and chloride anions suggests once again that alcohol molecules are homogeneously distributed in the IL network. These conclusions are reinforced by the analysis of the coordination numbers and average number of hydrogen bonds per alcohol molecule shown in the following.

The above conclusions can be reinforced analyzing the coordination numbers of alcohol molecules in the mixtures. The most usual way for evaluating coordination numbers in the literature is by numerical integration of the RDF $4\pi r2g(r)$ up to the first minimum. In order to test our results, we computed the oxygen-hydrogen and oxygen-oxygen RDFs for liquid methanol and ethanol,

and compared the obtained curves and the corresponding coordination numbers with those reported in previous computational simulations [165]. These curves are shown in Figure 2.22. The coordination numbers calculated by integration of the corresponding first peak were for pure methanol and ethanol 2.61 and 2.08, respectively, in the case of O-O pairs and 1.13 and 0.82 when using O-H pairs. Our calculated coordination numbers differ only slightly from the ones reported by Saiz *et al.* [165], which are 2 and 1 for O-O and O-H pairs, respectively, but this property is known to be extremely sensitive to the choice of the position of the minimum. As one can see in this representation, sharp first peaks are registered for both alcohols both for O-H pairs and O-O pairs, followed by second broader peaks. Any appreciable correlation vanishes for $r > 0.6$ nm in both cases. Moreover, for O-O pairs, the first peaks are registered at 0.3 nm, 0.1 nm farther than for the former, reflecting the formation of hydrogen bonding in these systems (recall that a hydrogen bond is formed when the donor-acceptor distance is less than 0.35 nm, according to Gromacs criterion). It is also apparent in Figure 2.23 that our calculations predict slightly lower first peaks centered at larger distances of the central O atom for O-H pairs for both ethanol and methanol, and the same happens for the second peaks. This is also the case for O-O pairs, but in this case the maxima of our calculated second peaks are greater than those of Saiz *et al.* in ref.[165], and the second neighbors are placed at slightly smaller distances.

In Figure 2.23 we represent the coordination numbers of alcohol/IL mixtures over the whole range of alcohol concentrations, obtained by integration of the first peak of the RDFs of the center of mass of the molecules, a less biased choice of distribution function. On the other hand, the number of methanol molecules surrounding another molecule of methanol is higher in mixtures with the PF_6^--based IL than in mixtures with [HMIM][Cl] up to high concentrations of alcohol ($x_{methanol} \approx 0.7$). This is in agreement with our previous statement that methanol molecules have a greater ability to coordinate with the halogen anion than with the more solvophobic one. Furthermore, Figure 2.23 shows that the number of ethanol molecules around another molecule of ethanol in a mixture is higher than the methanol-methanol coordination number in the analogous mixture up to a high molefraction of alcohol, which implies that methanol has a stronger interaction with anions than ethanol, as we concluded from our previous analysis of Figure 2.21. Moreover, we can compare our limiting Cl^--alcohol coordination numbers (4.2 and 3.4 for ethanol and methanol, respectively) with the value of 7.4 reported for water in

Figure 2.22 RDFs for ethanol (red lines) and methanol (black lines) at 298.15 K, and comparison with the curves reported by Saiz *et al.* (dashes) [165].

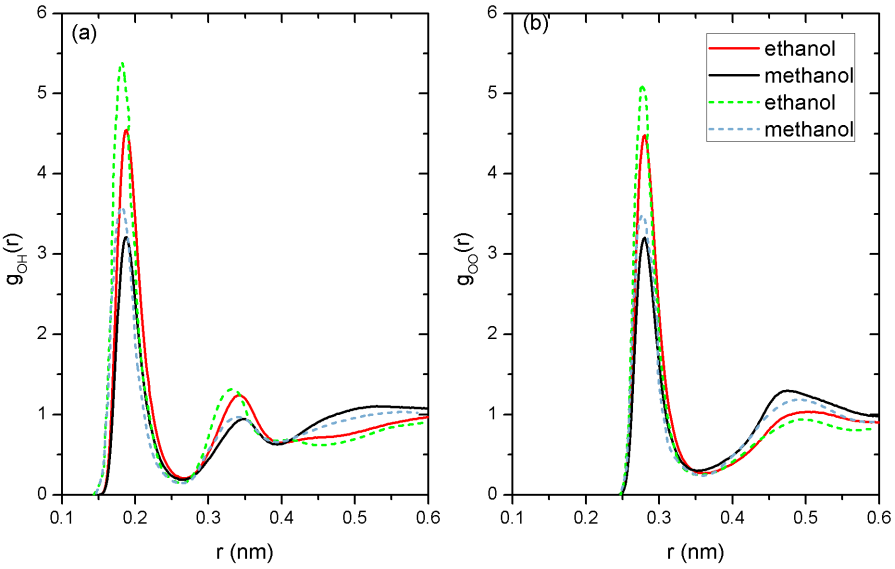

our previous work for IL/water mixtures [81] (by way of comparison, 6 is the experimental value of aqueous chloride) [166]. The limiting PF_6^--alcohol coordination number is 11.9 and 13.2 in mixtures with ethanol and methanol, respectively, while the value reported in our previous work in mixtures with water is 10.3.

The above discussion shows that calculation of coordination numbers by the usual method of integration under the first peak of an RDF involves a number of arbitrary choices. Furthermore, the information provided by the RDFs is limited by the fact that they lump together all the particles, so a certain degree of arbitrariness probably cannot be avoided unless a more detailed description is used. This issue has been discussed previously in the literature by McGreevy *et al.* [167]. They calculated the coordination numbers of molten RbCl and LiI using a method based on a deconvolution of the RDFs obtained from simulations in terms of the partial RDFs $G(n, r)$ ($n = 1, 2, ...$) defined as the probability density functions of finding the nth nearest neighbor of a particle at a distance r. Many parameters of these functions, such as peak position, height,

Figure 2.23 Coordination numbers of ethanol (a,c,e) and methanol (b,d,f) in mixtures with [HMIM][PF_6] (a,b), [HMIM][BF_4] (c,d), and [HMIM][Cl] (e,f) at 298.15 K.

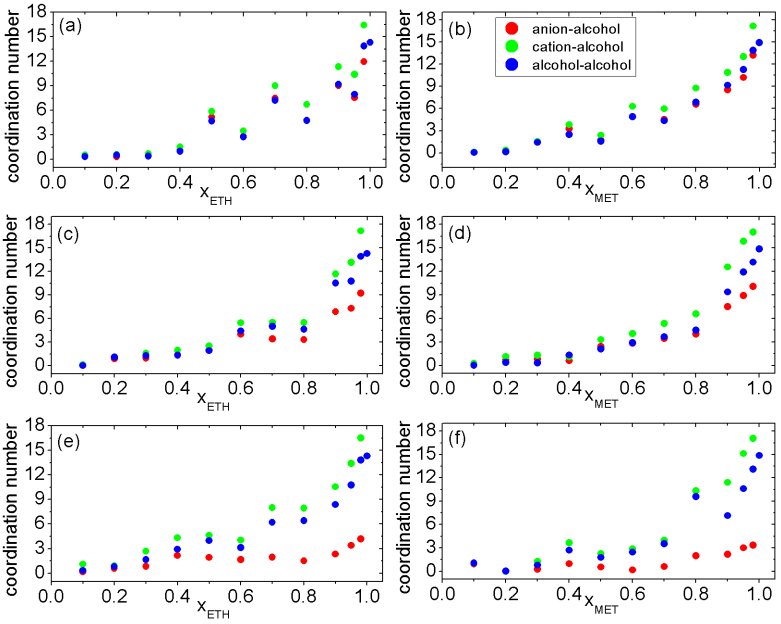

width at half-height, and so forth can be used in order to determine whether a particular radial distribution curve is the last one of an inner coordination sphere, an intermediate one, or the first one of an outer sphere. However, McGreevy *et al.* showed that the best way to determine the boundary between two coordination spheres is as the distance where the ratio of the half-widths measured to either limit of the curves from their peak position is equal to unity. This technique has been used by subsequent authors to gain additional insight into the neighborhood relations present in systems with complex spatial correlations, such as in the study of liquid Bi by Souto *et al.* [119]. Accordingly, we also analyzed the partial RDFs of nearest neighbors up to a distance of around 0.63 nm, which is the distance of the first and second minimum of pure ethanol and methanol, respectively. From the computed $G(n, r)$, some of them plotted in Figure 2.24, we found that pure ethanol has 12 first neighbors, while pure methanol has two neighbors in the first shell and 13 neighbors in the second one, which is in agreement which the values previously plotted in Figure 2.23. Moreover, interestingly enough, these two shells of liquid meth-

Figure 2.24 Deconvolution of the RDFs g(r) in terms of the partial RDFs $G(n,r)$ ($n = 1, 2, ..., 40$), corresponding to the first, second, third, etc., nearest neighbors in pure ethanol (a) and pure methanol (b), and in mixtures of ethanol (c) and methanol (d) with [HMIM][BF_4] at an alcohol content of $x_{alcohol} = 0.50$.

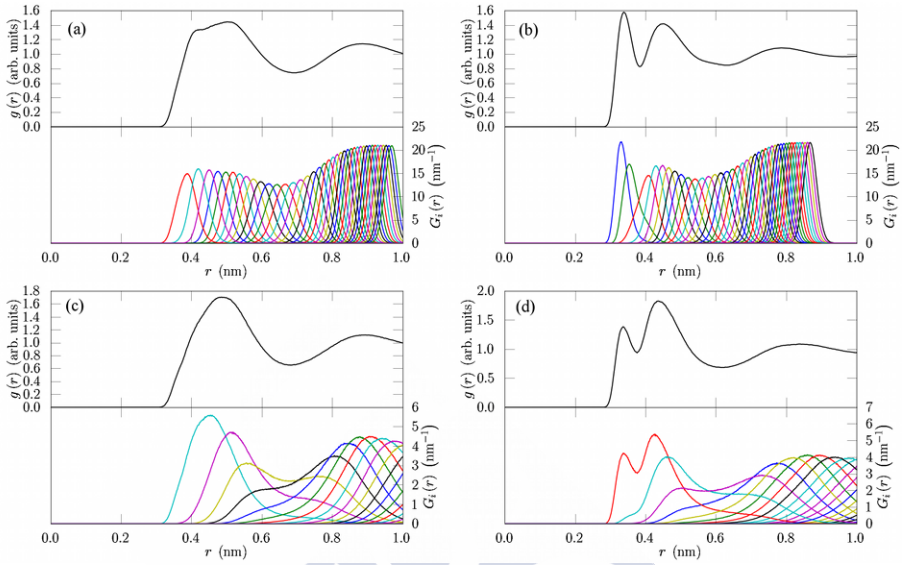

anol extend up to the same distance as the first shell of liquid ethanol. Some additional results for mixtures are shown in Table 2.2; it is noteworthy that [HMIM][Cl] in mixtures with methanol produces the disappearance of one of the two shells found in pure methanol, which is in agreement with the fact that RDFs of methanol/[HMIM][Cl] plotted in Figure 2.19 only show the first peak when high amounts of methanol are reached. It is also interesting to see the resonance of the first neighbor between the first two shells in mixtures of methanol/[HMIM][BF_4].

The criterion for defining a "hydrogen bond" in the context of computational simulations can be geometrical or energetic [168]. However, in the case of methanol, the choice is not as crucial as in other liquids such as water, and both criteria lead to almost identical results. According to ref.[168], a pair of molecules are considered H-bonded if the distance between the hydrogen and the acceptor is smaller than 0.35 nm and the angle of the donor-hydrogen-acceptor is less than 30°. (According to the criterion implemented in Gromacs, OH and NH groups are regarded as donors, and O and N are considered to be acceptors.) Figure 2.25 represents the cation-alcohol hydrogen bonding de-

Table 2.2 Alcohol-Alcohol Coordination Numbers in Mixtures with [HMIM][PF_6], [HMIM][BF_4], and [HMIM][Cl] Derived from $G(n, r)$.

	ethanol		
	$x_{eth} = 0.1$	$x_{eth} = 0.5$	$x_{eth} = 1.0$
	1^{st} *shell*	1^{st} *shell*	1^{st} *shell*
[HMIM][PF_6]	1	3.5	12
[HMIM][BF_4]	1	3.5	12
[HMIM][Cl]	1	3.5	12

	methanol					
	$x_{met} = 0.1$		$x_{met} = 0.5$		$x_{met} = 1.0$	
	1^{st} *shell*	2^{nd} *shell*	1^{st} *shell*	2^{nd} *shell*	1^{st} *shell*	2^{nd} *shell*
[HMIM][PF_6]	1	1	2	3	2	13
[HMIM][BF_4]	1	1	1	3	2	13
[HMIM][Cl]	1	–	2.5	–	2	13

gree for all the analyzed mixtures together with their uncertainties calculated as the standard deviations of the mean of the stochastic series of hydrogen bonds in the time series of configurations. It can be seen there that the average number of hydrogen bonds per alcohol molecule is approximately 1 order of magnitude greater in mixtures with [HMIM][PF_6] and with [HMIM][BF_4] than with the halogen anion, probably due to the greater interaction between alcohol molecules and the chloride anion. On the other hand, maxima in the number of hydrogen bonds are observed in the case of mixtures of [HMIM][Cl] with both alcohols (Figure 2.25.c). Although at very high concentration of alcohol ($x_{solvent} > 0.9$) the behavior of this magnitude is similar for all the studied compounds, below this concentration this number exhibits a relatively fast decrease in the case of the chlorinated IL, reflecting that most of the alcohol molecules in the bulk are bound to the other species in the mixture (anions or other alcohol molecules). Taking into account the results above, we can conclude that they are preferentially bound to chloride anions, what reflects once more that the affinity of Cl^- to hydrogen bonded to both methanol and ethanol molecules is much greater than those of more hydrophobic anions such as PF_6^- or BF_4^-.

Figure 2.26 shows the variable

$$\xi = \frac{n_{alc-alc}^{mixture}}{n_{alc-alc}^{pure}} \tag{2.8}$$

that is, the average number of alcohol-alcohol hydrogen bonds per alcohol molecule normalized to its value in pure alcohol for all the studied IL/alcohol mixtures in order to analyze the effect of the anion on the number of alco-

Figure 2.25 Concentration dependence of the average number of cation-alcohol hydrogen bonds per alcohol molecule for mixtures with [HMIM][PF_6] (a), [HMIM][BF_4] (b), and [HMIM][Cl] (c) at 298.15 K.

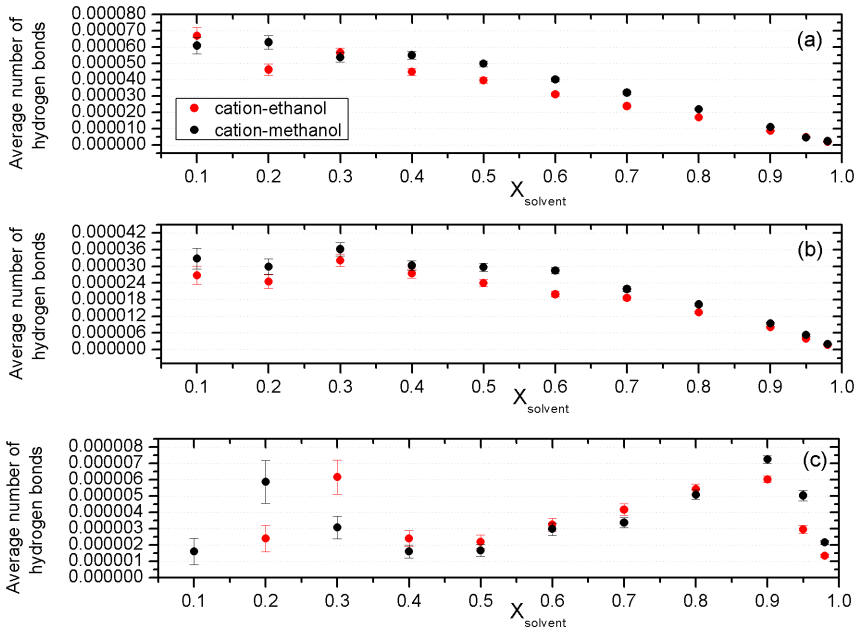

holÀalcohol hydrogen bonds. The average number of alcohol-alcohol hydrogen bonds in the pure system that appears as the denominator of eq.2.8 was computed to be 1.82 for both ethanol and methanol, in good agreement with the experimental value of approximately two hydrogen bonds per ethanol and methanol molecule [169]. This suggests the existence of linear chains of hydrogen bonded molecules of alcohol, a structure also reported in computational studies of liquid alcohols [153, 165, 168, 170]. As can be seen in Figure 2.26, the number of hydrogen bonds per alcohol molecule monotonically increases with the amount of alcohol. In the case of mixtures with water we reported in ref 11 a value of approximately 3.5 hydrogen bonds per water molecule in pure water, which is similar to the four hydrogen bonds of most water molecules in the liquid phase [171–173]. On the other hand, the increase of the average number of alcohol-alcohol hydrogen bonds per alcohol molecule is notably slower for the chlorinated IL than for the other compounds throughout the whole range of concentrations. In fact, in [HMIM][Cl]/alcohol mixtures, ξ does not reach

a value of 0.2 up to a content of alcohol around $x_{alcohol} \approx 0.8$, whereas that value is reached in [HMIM][BF_4]/alcohol mixtures at $x_{alcohol} \approx 0.6$, and in the most solvophobic compound at $x_{alcohol} \approx 0.4$. This fact reinforces the notion of the existence of strong hydrogen bonding between alcohol molecules and the chloride anion. Hydrogen bonding between alcohol molecules is not relevant until high alcohol mole fractions in mixtures with hydrophilic anions, while in mixtures where the solvophobic anions are present the interaction between alcohol molecules themselves seems to be stronger than that between alcohol molecules and the polyatomic anions. The results in Figure 2.26.c can be compared to those we previously reported for mixtures with water (Figure 8.b of ref.[81]). This comparison shows that the increase of average hydrogen bonding between solvent molecules is notably greater in mixtures of [HMIM][Cl] with water than in its mixtures with any of the alcohols. In mixtures with water the normalized average numberof water-water hydrogen bonds is greater than 0.1 at $x_{water} \approx 0.5$, and greater than 0.4 at a mole fraction of water of approximately $x_{water} \approx 0.75$, whereas in mixtures of [HMIM][Cl] with alcohols these values of the alcohol-alcohol hydrogen bonding degree are not reached up to $x_{alcohol} \approx 0.75$ and $x_{alcohol} \approx 0.9$, respectively. This reflects once again that no alcohol network similar to the water network formed with increasing water concentration in IL/water mixtures occurs in mixtures of alcohol with [HMIM][Cl], where the alcohol molecules seem to be homogeneously placed in the polar network of IL. However, in mixtures where polyatomic anions are present, alcohol molecules tend to form bigger clusters that increase in size with increasing mole fraction of alcohol, until they percolate to form a network of large alcohol clusters at high amounts of alcohol.

The behavior of $\xi(x_{solvent})$ at both extremes of the concentration range can be explained in a semiquantitative fashion using simple models. At very low solvent concentrations, solvent molecules can be thought of as acting like in an ideal gas with $g(r) \approx 1$. Thus, the frequency of two of these molecules being close enough to form an hydrogen bond in this limit is roughly proportional to the density of the system (which in turn can be approximated by the density of the pure IL) and therefore linear in the mole fraction of solvent. This linear behavior is clearly observed in Figure 2.26, and in fact extends reasonably well up to intermediate concentrations. As expected, the slope of the corresponding linear fit is higher for denser ILs, and proportional to the density of the pure IL. At the other end of the concentration spectrum, the action of adding an ionic pair to pure solvent is followed by a solvation process involving a

Figure 2.26 Concentration dependence of the average number of alcohol-alcohol hydrogen bonds per alcohol molecule normalized to its value in pure alcohol for mixtures with [HMIM][PF_6] (a), [HMIM][BF_4] (b), and [HMIM][Cl] (c) at 298.15 K. Also shown are linear (exponential) fits in the low (high) concentration range; see the text for details.

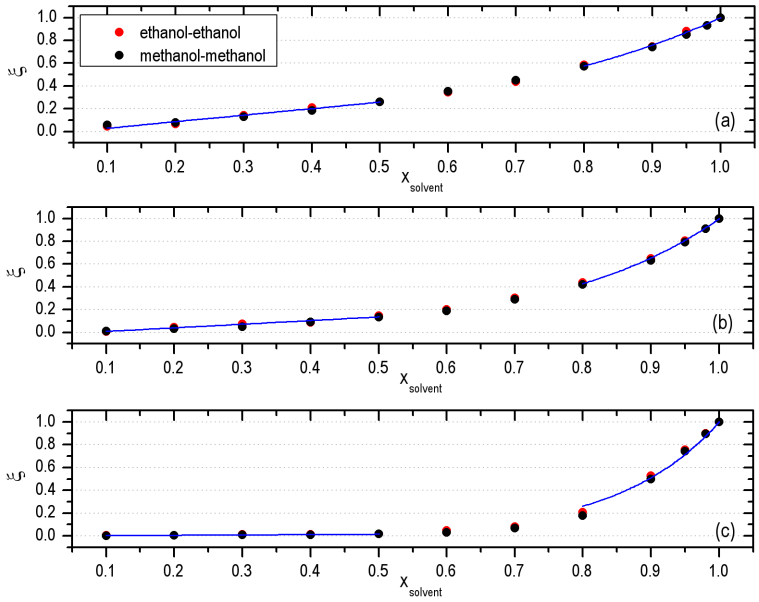

number of solvent molecules that are thus prevented from forming hydrogen bonds. The reduction in the total number of solvent-solvent hydrogen bonds is therefore proportional to the number of IL molecules introduced and to ξ. Using very simple approximations, this can be shown to yield a result of the form $\xi = e^{\gamma(x_{solvent}-1)}$ valid for $x_{solvent} \approx 1$, with a parameter γ, which should be larger in those systems in which solvent-IL interactions are stronger. The corresponding exponential fits are also shown in Figure 2.26, and the values of γ (2.8 for [HMIM][PF_6], 4.2 for [HMIM][BF_4], and 6.7 for [HMIM][Cl]) follow the expected trend. The mismatch between the slopes of the linear and exponential regions is barely noticeable for [HMIM][PF_6], somewhat more marked for [HMIM][BF_4], and fairly accused for [HMIM][Cl], where two clearly different regimes can be observed. Interesting conclusions for the degree of clusterization can be drawn from this contrast: the fact that the linear regime is valid in such a wide range for [HMIM][Cl] /alcohol mixtures indicates that

solvent molecules can be considered disaggregated up to very high concentrations, whereas the much earlier onset of bulk-like behavior in alcohol mixed with [HMIM][PF_6] points to the existence of large alcohol clusters (probably forming a network, which breaks the polar IL network) already at intermediate concentrations.

2.2.5. Conclusions

We performed MD simulations for binary mixtures of the imidazolium-based ILs [HMIM][PF_6], [HMIM][BF_4], and [HMIM][Cl] with methanol and ethanol, and we analyzed several thermodynamic and structural properties of the system. Moreover, we studied the influence of the anion hydrophobicity degree, the length of the molecular chain of the alcohol, and of the concentration of alcohol on the evolution of the microstructure of the mixtures. In particular, we have analyzed densities, excess molar volumes, total and partial RDFs, coordination numbers, and average degrees of hydrogen bonding of the species present in the mixtures.

To check the reliability of the force field employed, we calculated the densities of pure ILs and alcohols and compared them to experimental values. Our simulated densities show a maximum deviation from the experimental ones of 1.79%. Additionally, the densities of the mixtures were in good agreement with the experimental data available in the literature. In order to quantify the nonideality of the mixtures, we determined the excess molar volumes of mixing, which were negative for all the mixtures over the whole range of concentrations due to the intermolecular forces between the components of the mixture and the packing effect due to the different shapes and sizes of the molecules. We observed that alcohol molecules are more densely packed in mixtures with Cl^- than in mixtures with PF_6^- and BF_4^-, and that methanol molecules show a better packing than ethanol ones.

The RDFs of the mixtures showed that the interaction between anions and alcohols increases in the order $Cl^- > BF_4^- > PF_6^-$. Moreover, this interaction is more significant for methanol than for ethanol. Additionally, there is no aggregation of alcohol molecules around the cationic part of ILs. Significant hydrogen bonding between alcohol molecules does not come up until high concentrations of alcohols in the presence of the chloride anion. Thus, whereas in mixtures with water we reported the formation of a water network that breaks the polar network, in mixtures with alcohols the alcohol molecules are homo-

geneously distributed in the structure of the chloride-based IL. However, in the more solvophobic mixtures with fluorinated anions our results seem to be compatible with the formation of some kind of network. This aggregation trend was confirmed by the analysis of the evolution of the coordination number and the average number of hydrogen bonds per alcohol molecule with the mole fraction of alcohols. Moreover, the study of these two properties show that [HMIM][PF_6]/alcohol mixtures form clusters of alcohol molecules whose size increases with increasing mole fraction of alcohol and it is bigger than in [HMIM][Cl] /alcohol mixtures but smaller than in mixtures of [HMIM][PF_6] with water.

A systematic study of the dynamic properties of these mixtures, including their diffusion coefficients and the velocity autocorrelation functions, is now in progress.

2.3. Dynamical Properties of Alcohol + 1-Hexyl-3-methylimidazolium Ionic Liquid Mixtures: A Computer Simulation Study.

With the aim of extending the structural work in 2.2, we systematically evaluated the role of several parameters (anion nature, length of the molecular chain of the alcohol, and alcohol concentration) on the single-particle dynamics of the species in IL/alcohol mixtures. Specifically, we analized self-diffusion coefficients, mean square displacements (including ballistic and diffusive regimes) and velocity autocorrelation functions [174].

The study of the self-diffusion coefficients revealed that $[PF_6]^-$ anions had a faster diffusion than $[Cl]^-$ ones due to its higher hydrophobicity degree and the weaker interactions between alcohol molecules and hexafluorophosphate. Additionally, velocity autocorrelation functions of alcohol molecules were rapidly weakned and smaller collision times were found in mixtures with halogenated ILs, as determined by the clusterization degree of alcohols in these ILs. Contrarily to what happens in aqueous mixtures, no evidence of a rattling motion associated to a caging effect was found, which is due to the absence of clusters of alcohol molecules and the greater abiity of alcohols to diffuse in the apolar regions of the bulk.

The results obtained in 2.1, 2.2 and 2.3 allow to state that the anion has the dominant role on the structural and dynamic properties of ILs mixed with molecular cosolvents.

2.3.1. Paper III: Dynamical Properties of Alcohol + 1-Hexyl-3-methylimidazolium Ionic Liquid Mixtures: A Computer Simulation Study; *J. Phys. Chem. B 115 (2011) 15313-15322.*

Trinidad Méndez-Morales,[1] Jesús Carrete,[1] Manuel García,[1] Óscar Cabeza,[2] Luis J. Gallego[1] and Luis M. Varela[1]

In this work, extensive molecular dynamics simulations of the dynamics of mixtures of ionic liquids (ILs) composed of the cation 1-hexyl-3-methylimidazolium and several anions of different hydrophobicity degrees (Cl^-, BF_4^-, PF_6^-) with alcohols of different chain lengths (methanol and ethanol) are reported. We evaluated the influence of the nature of the anion, the length of the molecular chain of the alcohol, and the alcohol concentration on some dynamical properties of the mixtures, such as self-diffusion coefficients of all the species, mean square displacements (with an analysis of both ballistic and diffusive regimes), and velocity autocorrelation functions of alcohol molecules. The diffusivity of the mixtures was found to be highly dependent on the nature of the anion since the interaction between chloride and alcohols is greater than that with fluorinated anions and leads to slower dynamics. Additionally, our results show that self-diffusion coefficients increase with alcohol concentration. On the other hand, a subdiffusive regime over thousands of picoseconds was detected at intermediate times through analysis of the center-of-mass mean square displacements of alcohol molecules, a region that becomes narrower as alcohol concentration increases. Finally, the study of the role of the anion and of solvent concentration on velocity autocorrelation functions reflects an increase in mean collision times as the amount of alcohol increases until the value of pure alcohols is reached. These collision times are smaller in mixtures with halogenated ILs.

2.3.2. Introduction

Room temperature ionic liquids (ILs) have attracted increasing attention in recent years [36, 82, 83, 151, 175] from both academia and industry due to their interesting properties and potential applications. ILs exhibit some

[1]*Grupo de Nanomateriales y Materia Blanda, Departamento de Física de la Materia Condensada, Universidad de Santiago de Compostela, E-15782, Santiago de Compostela, Spain*

[2]*Facultad de Ciencias, Universidade da Coruña, Campus A Zapateira s/n E-15008, A Coruña, Spain*

unique characteristics, such as negligible vapor pressure, high thermal and electrochemical stability, nonvolatility, nonflammability, low viscosity, high ionic conductivity, and miscibility, with a wide range of organic and inorganic compounds [82–86, 133, 176–178], which confer them their reputation as "green solvents" and make them a good alternative to traditional organic solvents [2, 3, 84, 133–135, 179, 180]. Because of these properties, ILs have been investigated for many applications in different fields of chemistry: catalysis, synthesis, lubrication, thermal separation processes, and electrochemistry [3, 12, 36, 181–186].

As with any salt, these systems are formed entirely by ions: an organic cation such as those based on imidazolium, pyridium, pyrrolidinium, ammonium, phosphonium, or guanidinium and an anion like PF_6^-, BF_4^-, Cl^-, Br^-, NTf_2^-, NO_3^-, etc [178, 179, 187, 188]. The physicochemical properties of ILs can be easily modified simply by a proper choice of ions [3, 179]. Because of this potential tunability for any particular application [2, 16, 30, 36], ILs are usually called "designer solvents" [83, 180]. In practice, however, the design and development of ILs for a specific role requires a detailed understanding of their molecular and thermodynamic behavior. In particular, a systematic understanding of the correlation between the composition of mixtures of ILs with (organic or inorganic) solvents, their dynamical features, and their bulk physicochemical properties is of extreme importance for both theoretical and practical reasons. Accordingly, extensive computational and experimental research of the properties of ILs has been carried out during the last years (see, for example, refs.[189] and [190] and references therein). However, the understanding of the dynamical properties of ILs and their mixtures, even with water, is still very limited, and studies devoted to quantifying the relationship between the structure of the mixture and the dynamics of the molecules (which has a direct influence on the physicochemical properties) have as of yet been scarce, especially if we compare the number of ILs whose dynamical properties have been broadly studied and the immense number of ILs synthesized so far.

As regards experimental studies of dynamical magnitudes, a number of reports of mutual and self-diffusion coefficients of pure ILs can be found in the literature [26–28, 36, 191–199], as well as some measurements dealing with the diffusion of solid, liquid, and gaseous solvents in ILs [200–212]. Among the latter, however, papers concerned with IL + alcohol mixtures have not been abundant. As far as we know, the first measurements of mutual diffusion coefficients of mixtures between 1-butyl-3-methylimidazolium hexafluoro-

phosphate ([BMIM][PF_6]) and methanol, using digital image holography, were published by Ritcher *et al.* in 2003 [211]. Another example is the study, by Sarraute *et al.* [206], of the diffusion coefficients of several ILs based on the 1-alkyl-3-methylimidazolium cation ($AMIM^+$) in methanol, for temperatures ranging from 283 to 333 K, using the Taylor dispersion method.

Unfortunately, it is usually very complicated to experimentally or theoretically achieve a detailed knowledge of the correlation between structure and molecular mobility of ILs. To overcome this lack of information, computer simulations are often used to improve the understanding about the behavior of ILs at the molecular level. Due to the high computational cost of ab initio techniques, the best simulation method to probe the dynamical behavior of these systems is classical molecular dynamics (MD) [36, 64–66, 81, 93, 94, 98, 103, 115, 121–123, 128, 155, 189, 213–222]. So far, MD studies have concerned themselves mainly with pure components [64, 103, 115, 122, 123, 128, 155, 189, 216–220], while IL + solvent mixtures have received much less attention. A notable example of the former is the study, by del Pópolo and Voth [128], of the structure and dynamics of 1-ethyl-3-methylimidazolium nitrate ([EMIM]-[NO_3]), including dynamical magnitudes such as the center-of-mass velocity autocorrelation functions (VACFs) and the mean square displacements (MSDs) of the ions. Although the most studied among IL mixtures have been those with water [65, 81, 93, 94, 98, 215, 221, 222], a few instances of computational research about mixtures with other compounds such as acetonitrile [121] or supercritical carbon dioxide [213] can also be found. Like for experimental studies, the number of reported MD results regarding the dynamical properties of IL + alcohol mixtures is much lower. In 2008, Raabe and Köhler [149] performed MD simulations of mixtures of 1-alkyl-3-methylimidazolium chloride ([AMIM][Cl]) with ethanol and 1-propanol to calculate the diffusion coefficients and some structural properties of those systems. That same year, Jahangiri *et al.* [66] reported results of excess, dynamical, and structural properties of mixtures of 1-ethyl-3-methylimidazolium chloride ([EMIM][Cl]) and 1-ethyl-3-methylimidazolium hexafluorophosphate ([EMIM][PF_6]) with both methanol and ethanol obtained by MD simulations. A larger computational study of dynamical properties was carried out by Heintz *et al.* [210], who performed MD simulations with the aim to investigate tracer diffusion coefficients of the IL ions in mixtures of [EMIM][NTf_2] and [BMIM][NTf_2] with water or methanol at different temperatures between 288 and 313 K.

Even though a molecular understanding of the dynamical properties of al-

cohol + IL mixtures is of fundamental importance from both a fundamental and a practical standpoint, a systematic study of the role of different parameters such as alkyl chain length, anion nature, concentration of solvent, and alcohol chain size on the dynamical properties of this kind of mixtures is, as far as we know, still missing. As we reported in our previous work [132], the length of the chain of the alcohol and, above all, the nature of the anion have a direct influence on the solvation process of ILs and on the mixture structure, and consequently they are expected to have a deep impact on the transport properties.

Using previously reported simulation models [132], in this work we performed extensive MD simulations of mixtures of alcohols and 1-hexyl-3-methylimidazolium ($HMIM^+$) with three different anions of various solvophobicity degrees to investigate several dynamical properties of the systems: PF_6^-, the one with the higher level of hydrophobicity; Cl^-, with a great effect on water structure according to the Hoffmeister series; and BF_4^-, with intermediate characteristics. Moreover, the impact of the length of the chain in the chosen alcohols (methanol and ethanol) on the dynamic behavior was studied and compared. Additionally, we analyzed the influence of the anionic species and alcohol concentration on the single-particle dynamics of the mixtures by analyzing the self-diffusion coefficients of the involved species, MSDs (with an analysis of the ballistic and diffusive regimes), and VACFs of alcohol molecules.

This paper is organized as follows. We begin by giving a detailed description of the computational procedure used in our study. In the next section we present and discuss the obtained results, and in the final part we summarize our main conclusions.

2.3.3. Simulation details

The MD simulations for pure ILs and their mixtures with alcohols were performed using the Gromacs package [70]. All the simulations were run at 298.15 K, and the analyzed mole fractions of alcohol in the IL + alcohol mixtures were $x_{alcohol}$ = {0.00, 0.10, 0.20, 0.30, 0.40, 0.50, 0.60, 0.70, 0.80, 0.90, 0.95, 0.98, and 1.00} since both ethanol and methanol are miscible with all the selected ILs ([HMIM][PF_6], [HMIM][BF_4], and [HMIM][Cl]) over the whole concentration range [140, 146, 147]. The number of IL molecules in the cubic box was set to 300, except for $x_{alcohol}$ = 1.00, a case in which only alcohol

molecules are present, $x_{alcohol} = 0.95 - 0.98$, where just 50 ionic pairs were introduced to keep the system size small enough, and $x_{alcohol} = 0.10$, where we considered 450 IL molecules to have enough alcohol to yield statistically significant trajectories. The number of alcohol molecules was adjusted in each situation counting each ionic pair as a single molecule in the calculation of mole fractions.

The parametrization of the ions was carried out in the framework of the all-atom version of the fully flexible OPLS force field developed by Jorgensen and co-workers [153] for different organic fluids. The details of the parametrization used have been reported elsewhere [132], but it is important to remark, with regard to our description of the ions, that we used a nonpolarizable model with static partial charges adding up to +1 and −1 for the cation and anion, respectively; *i.e.*, full (nonreduced) charges were used. Our all-atom representation of 1-hexyl-3-methylimidazolium is shown in Figure 2.27. Other relevant details of the simulation include the fact that a neighbor search was made up to 1.1 nm from the central ion and updated every five simulation steps and that the cutoff distance for Lennard-Jones interactions was set to this same distance. Long-range electrostatic interactions were computed using the Particle-Mesh Ewald (PME) [77] method with a grid spacing of 0.12 nm and cubic interpolation. When needed, the Linear Constraint Solver (LINCS) algorithm [159, 160] with a fourth-order expansion of the constraint coupling matrix was used to constrain the bonds, and long-range dispersion corrections were used for energy and pressure.

To remove bad contacts resulting from the initial random configuration of ions, initial configurations were energy-minimized for 10^6 steps using a conjugated gradients algorithm. The maximum step size and the tolerance were set to 0.01 nm and 0.1 $kJ \cdot nm^{-1} \cdot mol^{-1}$, respectively. The equilibration phase was performed in the isothermal-isobaric (N, p, T) ensemble during 100 ps to ensure the full equilibration of all the properties of the system. The analysis was carried out using the results of an additional 2 ns simulation in the isothermal-isobaric ensemble. This very long simulation time is in keeping with the findings of recent MD studies, which remark that the simulation time used for analysis must be in the order of nanoseconds to ensure that the particles of the ILs have reached a diffusive behavior during the simulation since trajectories that seem to be in the linear diffusive regime are often still subdiffusive [36, 66, 94, 189, 213–216]. The temperature control was implemented using a velocity rescaling thermostat [161]. Cations and anions (and alco-

Figure 2.27 Molecular structure of 1-hexyl-3-methylimidazolium, modeled using an all-atom representation.

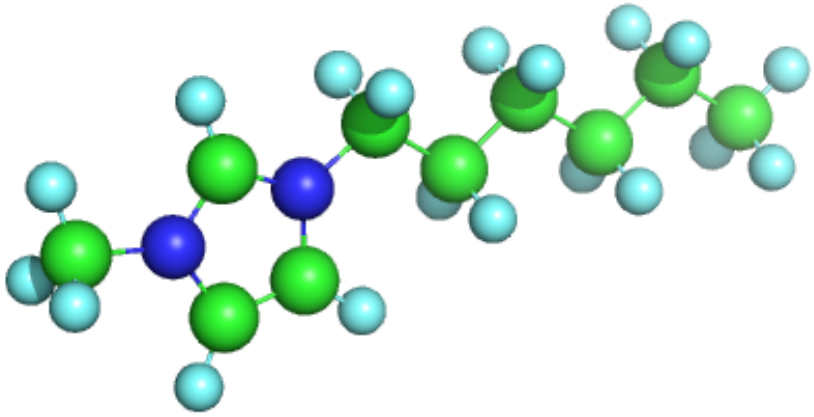

hols in those cases where we include a solvent) were separated in two (three) baths with temperature coupling constants of 0.1 ps. The pressure control was set using the Parrinello-Rahman barostat [162] with a reference pressure of 1 atm, an isothermal compressibility of 4.5×10^{-5}bar^{-1}, and a relaxation time of 1.0 ps. Tests performed prior to the simulation revealed that our results are largely insensitive to the choice of time scales of the thermostat and barostat.

Each of these simulations provided us with a sequence of configurations, *i.e.*, positions and instantaneous velocities of all atoms of the system, which was analyzed to obtain dynamical information about the mixtures previously mentioned.

2.3.4. Results and discussion

In addition to thermodynamical or structural properties, MD simulations are an efficient method to get a molecular understanding of the dynamical behavior of pure ILs and their mixtures. As it is well-known, the reliability of the properties obtained by computational studies depends on the accuracy of the employed force field, and density is usually the magnitude used to estimate the precision of this force-field-based simulation [98, 149]. This precision was tested for IL + alcohol mixtures in our previous work [132], where the compar-

ison between our simulated densities of both pure ILs and alcohols with the experimental data showed deviations smaller than 2.0%.

Single-particle dynamics of these systems can be described by means of the self-diffusion coefficient of species i, which is particularly amenable for calculation with MD simulations as it can be obtained from the well-known Einstein equation [60, 223]

$$D_i = \frac{1}{6} \lim_{t \to \infty} \frac{d}{dt} \left\langle \left[\vec{r}_i(t) - \vec{r}_i(0) \right]^2 \right\rangle \tag{2.9}$$

where $\langle [\vec{r}_i(t) - \vec{r}_i(0)]^2 \rangle$ is the ensemble-averaged MSD of component i and positions of molecules have been calculated from their center of mass at time t. The above equation is valid only at long simulation times, when the MSD exhibits a linear behavior with time and a truly diffusive regime is reached, since too short MD trajectories usually lead to overestimations of self-diffusion coefficients [189, 216]. In particular, for this work the data between 200 and 1800 ps were fitted to a straight line to apply eq. 2.9.

An additional validation of the accuracy of our force field, and therefore of the dynamical and transport properties of our model, can be made by calculating the self-diffusion coefficients of pure ILs and alcohols and contrasting them with some available experimental and computational values. Table 2.3 shows the simulated self-diffusion coefficients for cation (D_{cation}) and anion (D_{anion}) species in each pure IL and for pure methanol and ethanol, together with their respective uncertainties, provided bythe Gromacs package. The computed self-diffusion coefficients for both pure methanol and ethanol are very similar to the ones reported by Karger *et al.* [224] using NMR techniques, whose measured self-diffusivities were 2.3×10^{-5} cm^2/s for pure methanol at 292 K and 0.946×10^{-5} cm^2/s for pure ethanol at 290 K, both with a pressure of 0.1 MPa. These are largely due to the fact that the experimental studies of Karger *et al.* were done at lower temperatures than the present simulations. Our computational results for pure alcohols are also in good agreement with some previous values obtained by Martí *et al.* [225], Haughney *et al.* [168], and Guevara-Carrión *et al.* [226] using MD simulations. Concerning the obtained values of pure ILs, self-diffusion coefficients for $HMIM^+$ and PF_6^- are comparable to those reported by Iacob *et al.* [204] from their NMR measurements and the ones calculated by Liu *et al.* [121] from MD simulations. The values corresponding to $HMIM^+$ and BF_4^- are slightly smaller than the experimental results measured by Jin *et al.* [198] for [BMIM][BF_4] and those simulated by Liu *et al.*

Table 2.3 Simulated Self-Diffusion Coefficients and Uncertainties for Pure IL and Alcohols at 298.15 K and 1 atm.

	D (10^{-5} cm^2/s)	
compound	D_{cation}	D_{anion}
[HMIM][PF$_6$]	0.00463 ± 0.00035	0.00319 ± 0.00026
[HMIM][BF$_4$]	0.00600 ± 0.00067	0.00521 ± 0.00011
[HMIM][Cl]	0.00258 ± 0.00067	0.00202 ± 0.00014
methanol	2.57 ± 0.20	
ethanol	1.207 ± 0.033	

[121], Andrade *et al.* [220], and Prado *et al.* [155] for the same IL, all of them at room temperature. This is not surprising if we take into account that the self-diffusion coefficient decreases with increasing alkyl chain length as reflected in the increase of the viscosity [199]. Finally, our self-diffusion coefficients for $HMIM^+$ and Cl^- agree reasonably well with the ones computed by Jahangiri *et al.* [66] for [BMIM][Cl]. Interestingly, cation and anion were found to exhibit similar diffusion behavior for each IL, but self-diffusion coefficients of the cations are slightly greater than those of the anions in all cases, despite their larger volumes and masses, in agreement with previous results reported in the literature [28, 189, 217]. Moreover, all the self-diffusion coefficients of pure ILs reported in this work are around 2 orders of magnitude lower than that of pure water at 298.15 K and 1 atm, 2.6×10^{-9} m^2/s [81, 115, 121], and pure alcohols.

Figures 2.28-2.30 provide some further insight into the effect of the anion nature, the size of the alcohols, and solvent concentration on self-diffusion coefficients of the mixtures of imidazolium-based ILs with alcohols. In Figure 2.28 we represent self-diffusion coefficients of an alcohol molecule in all the analyzed IL + alcohol mixtures as a function of alcohol molar fraction. In all cases, self-diffusion coefficients of alcohol molecules increase with an increasing amount of alcohol, this increase being more gradual in mixtures with [HMIM][PF_6] and [HMIM][BF_4] over alcohol molar fractions of $x_{alcohol} = 0.7$ and of $x_{alcohol} = 0.9$ in mixtures with [HMIM][Cl]. Moreover, diffusion of methanol molecules in all the studied mixtures is higher than diffusion of ethanol molecules in IL + ethanol mixtures at the same concentration, probably due to their smaller sizes and weights. Figure 2.28 also illustrates that the diffusion of both alcohols is faster in mixtures of IL with polyatomic anions than in mixtures of the chlorinated IL over the whole concentration range, which

shows that alcohol molecules interact more strongly with chloride than with polyatomic ions, as we reported in our previous work [132]. These results are in good agreement with the ones previously published by Jahangiri *et al.* [66] for mixtures of methanol with [EMIM][PF_6] and [EMIM][Cl] and by Raabe and Köhler [149] for mixtures of ethanol and 1-propanol with [AMIM][Cl]. In addition, the self-diffusion coefficients for both ethanol and methanol molecules follow the same trend as those found in our previous work [81] for water molecules; however, their values are smaller than those of water over the entire miscibility range studied since significant interactions similar to the ones observed between water molecules were not found between alcohol molecules [132]. Furthermore, two different regimes can be distinguished: (i) at low alcohol concentrations self-diffusion coefficients of alcohol molecules increase slowly, pointing to a possible glassy state of the system and showing that no continuous solvent region is formed in the bulk mixture up to very high alcohol concentrations, and (ii) at low IL concentrations self-diffusion coefficients of alcohol molecules increase rapidly due to the percolation of alcohol regions in the mixture. Similar behavior was reported in previous experimental [209] and computational studies with water and alcohols [65, 66, 81, 93, 98, 149].

Figures 2.29 and 2.30 illustrate the self-diffusion coefficients of anions and cations, respectively, as a function of alcohol concentration. In general, the trend of these components is the same as the one observed for alcohol molecules, the diffusion of ions being very slow until the molar fraction of alcohol is greater than $x_{alcohol} = 0.8$, a concentration after which the diffusion of both species increases considerably. However, the values of the self-diffusion coefficients of anions and cations are very similar, with the diffusion of cations slightly faster than that of anions in the corresponding mixture, in spite of the smaller size of the latter ones. This supports the notion that, in these systems, the interaction between alcohol molecules and anions (above all with chloride) is stronger than that with cations [132]. Figure 2.29 shows that, although chloride is smaller than hexafluorophosphate, the former anion has a slower diffusion than the polyatomic one, which is due to the highly solvophobic character of PF_6^- and the existence of a stronger interaction between alcohol molecules and Cl^- [132]. Finally, it can be seen that the effect of solvent concentration and of anion nature on the self-diffusion coefficient is more notable for alcohol molecules than for any of the ions.

Thus, from the analysis of self-diffusion coefficients we can conclude that self-diffusivities of all components of the mixtures decrease rapidly with in-

Figure 2.28 Concentration dependence of the self-diffusion coefficients of alcohol molecules in (a) [HMIM][PF_6] + alcohol, (b) [HMIM][BF_4] + alcohol, and (c) [HMIM][Cl] + alcohol mixtures, calculated by the Einstein relation.

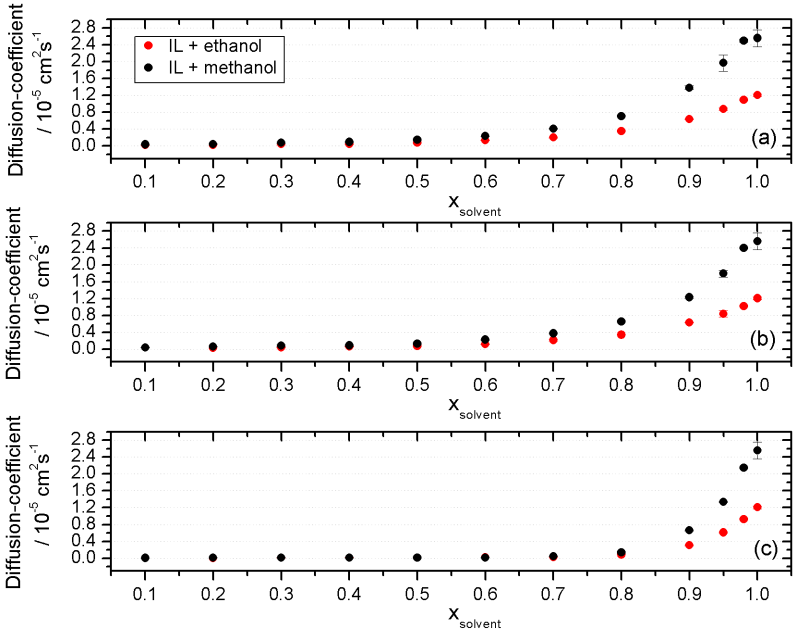

creasing amounts of IL. Moreover, both alcohols interact strongly with the anion of the IL, which has an important role in the structural and dynamical properties, and this interaction is stronger with the halogen anion than with the polyatomic ones, confirming previously reported results [132].

With the aim of getting further insight into the influence of the amount of alcohol on the dynamics of ILs, Figure 2.31.(a) shows the MSD of both cation and anion as a function of time in pure [HMIM][PF_6] and the MSD of PF_6^- in mixtures with an alcohol concentration of $x_{alcohol} = 0.5$. Likewise, in Figure 2.31.(b) we represent the MSD of pure alcohols and both methanol and ethanol in mixtures with [HMIM][PF_6] at a solvent concentration of $x_{alcohol} = 0.5$. The results for $HMIM^+$ and PF_6^- included in Figure 2.31.(a) are very similar to each other, with a faster diffusion of the anion at short times. However, after a few picoseconds both species diffuse approximately in the same proportion, which shows that the diffusion of these molecules is correlated and that they do not move separately.

Figure 2.29 Concentration dependence of the self-diffusion coefficients of anions in (a) [HMIM][PF_6] + alcohol, (b) [HMIM][BF_4] + alcohol, and (c) [HMIM][Cl] + alcohol mixtures, calculated by the Einstein relation.

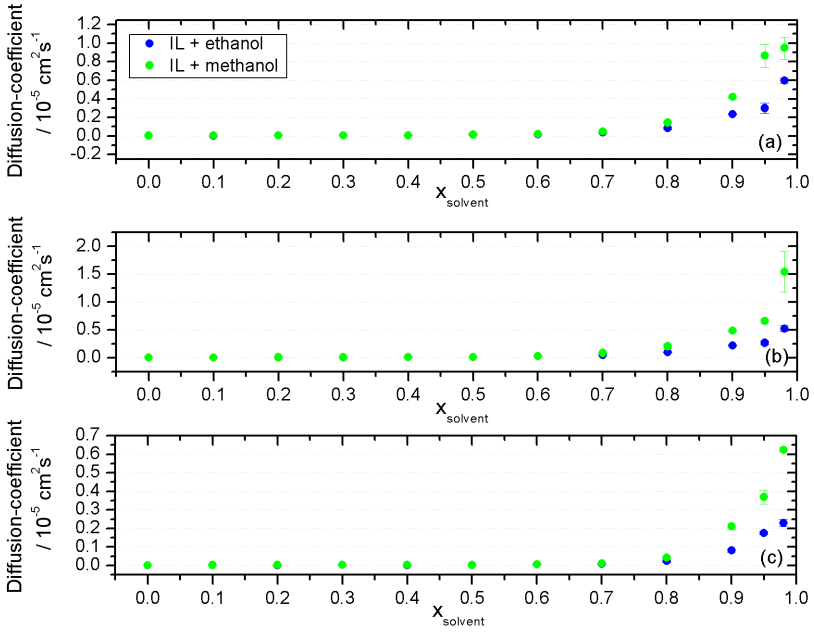

Figures 2.31.(c) and 2.31.(d) show the logarithmic plots of Figures 2.31.(a) and 2.31.(b), respectively. If we compare the MSDs of pure ILs with those of pure alcohols or pure water [227], it can be seen that ILs exhibit complex and slow dynamics, as we expected from the fact that the self-diffusion coefficients reported in Table 2.3 for pure ILs are around 2 orders of magnitude smaller than those of pure water or alcohols at the same temperature. In Figures 2.31.(a) and (b) it seems that the dynamics reaches a diffusive regime after a few picoseconds, since then MSDs appear to have a linear dependence with time. However, Figures 2.31.(c) and (d) prove that the situation is somehow more complex, and we can observe the existence of three different regimes that can be characterized by means of the dependence of the MSD with time. This can be measured as

$$\langle \Delta|\vec{r}(t)|^2\rangle = \frac{1}{N}\langle \sum_{i=1}^{N} |\vec{r}_i(t) - \vec{r}_i(0)|^2\rangle \propto t^{\beta} \tag{2.10}$$

where the sum extends over all the molecules present and β describes the

Figure 2.30 Concentration dependence of the self-diffusion coefficients of cations in (a) [HMIM][PF_6] + alcohol, (b) [HMIM][BF_4] + alcohol, and (c) [HMIM][Cl] + alcohol mixtures, calculated by the Einstein relation.

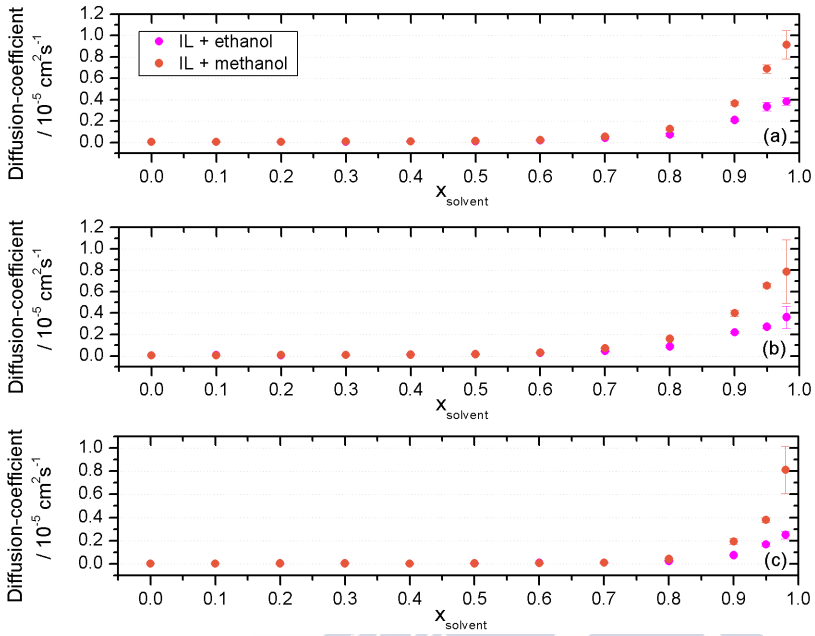

type of motion of the molecules of the system. As we have seen, self-diffusion coefficients of pure ILs are on the order of 10^{-11} m^2/s, which implies that ILs have very slow dynamics. For this reason, it is of fundamental importance to ensure that the system has reached the diffusive regime during the simulations to get correct values of the self-diffusion coefficient, which as can be seen is a long-time quantity. For this purpose

$$\beta(t) = \frac{d\log(\Delta|\vec{r}(t)|^2)}{d\log(t)} \tag{2.11}$$

can be used to analyze the regime in which the system is. First, a ballistic behavior of the ions dominates at short times, so that $\beta = 2$. Then, at long times the molecules of the system exhibit a diffusive motion, and this Gaussian diffusion implies $\beta = 1$. Finally, a very long subdiffusive regime is found at intermediate times, this non-Gaussian dynamics (for which $\beta < 1$) being characteristic of glass formers in the supercooled region [128]. Many research groups have reported that, in these systems, true diffusive motion only ap-

Figure 2.31 Concentration dependence of the self-diffusion coefficients of cations in (a) [HMIM][PF_6] + alcohol, (b) [HMIM][BF_4] + alcohol, and (c) [HMIM][Cl] + alcohol mixtures, calculated by the Einstein relation.

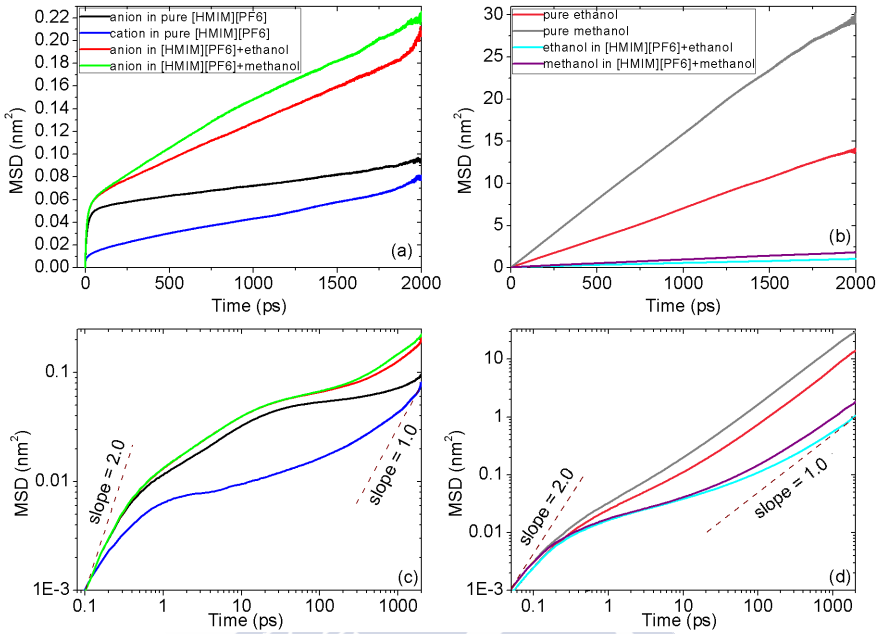

pears over large time scales, which are usually on the order of nanoseconds [94, 128, 189, 215, 216]. Looking at the log-log plot of the MSD of PF_6^- represented in Figure 2.31.(c), it can be seen that the transition from a ballistic regime to the subdiffusive one takes place at similar times in pure [HMIM][PF_6] and in its mixtures with alcohols. However, the diffusive regime is reached at lower times when alcohol is added to the system. Thus, the subdiffusive regime at intermediate times is progressively narrowed by the addition of alcohol to the mixture, as also detected in water [81]. On the other hand, as can be seen in Figure 2.31.(d), motion of alcohol molecules in mixtures with ILs is very different from that in pure alcohols at room temperature. In this latter case, the subdiffusive regime at intermediate times is almost absent, while in mixtures with IL it extends from about 0.2 ps up to hundreds or thousands of picoseconds.

This behavior can be further described by defining the characteristic times of ballistic (τ_b) and diffusive (τ_d) regimes defined as the times corresponding to the beginning and the end of the intermediate subdiffusive plateau that can

be approximated as the intersection of the straight line defining the plateau and the two lines corresponding to the ballistic and diffusive regime themselves, in the same way that we reported in our previous work for IL + water mixtures [81]. The end of the ballistic regime essentially coincides with the collision time. The calculated collision times increase monotonically with increasing alcohol concentration, much more rapidly above a solvent concentration of 80%. This behavior is due to the fact that the interactions present in an IL are stronger than the ones that exist in alcohols, so the greater the number of alcohol molecules in the mixture, the longer collision times are. In addition, diffusive times gradually decrease with increasing the amount of alcohol in all cases, so the addition of alcohol causes a faster transition to the diffusive regime. Moreover, it must be noticed that the subdiffusive regime at intermediate times extends over thousands of picoseconds, since τ_d is around 4 orders of magnitude greater than τ_b. Finally, let us point out that collision and diffusive times are shorter and larger, respectively, for the halogen anion than for the polyatomic ones, in agreement with our previous observations for the interaction between anions and alcohol molecules and therefore for the clusterization of alcohols in mixtures with ILs. These observations show a greater clusterization of alcohol molecules in the presence of hexafluorophosphate, which implies that the motion of alcohol molecules is more similar to that in pure alcohol.

A different way of characterizing single-particle dynamics in this kind of system is through the center-of-mass VACFs. In general, a VACF can be defined as

$$C(t) = \langle \vec{v}(t)\vec{v}(0) \rangle \tag{2.12}$$

where the vector $\vec{v}(t) = \sum_j m_j \vec{v}_j / \sum_j m_j$ is the velocity of the center-of-mass of the molecule and the scalar product is calculated in the laboratory frame. As far as we know, this is the first time that computational results are reported for this magnitude in alcohol + IL mixtures. In Figures 2.32 and 2.33, concentration dependence of normalized VACFs of ethanol and methanol molecules, respectively, are shown. The VACFs of both pure ethanol and methanol are in good agreement with the MD results reported previously by Saiz *et al.* [165] for liquid ethanol and by Haughney *et al.* [168] for liquid methanol. The $C(t)$ functions of both pure alcohols exhibit a secondary maximum at approximately 0.3 ps, which is more marked for pure methanol. The same behavior

was found in pure water [81], with this secondary maximum placed at shorter times (around 0.15 ps). $C(t)$ decays in a subpicosecond scale, and the first zero of the VACFs, which indicates the mean collision time of alcohol molecules, increases with the addition of alcohol to the mixture in all cases until the value of pure alcohols (around 0.21 ps for ethanol and 0.28 ps for methanol due to the "cage effect") is reached. Moreover, at the same amount of alcohol, the mean collision time is somewhat longer in mixtures with [HMIM][PF_6] than that in mixtures with [HMIM][Cl] since alcoholmolecules seem to be homogeneously placed in the structure of the chlorinated IL [132] and alcohol motion in bulk cavities of mixtures with solvophobic ILs is more similar to that in pure alcohols. Collision times manifest the same trend as in our previous studies of IL + water mixtures [81]. On the other hand, correlations are rapidly and monotonically weakened in all the studied systems, so within 0.6 ps correlations are no longer present for alcohol molecules. Furthermore, there is no evidence of long-time tails in these mixtures. Finally, the oscillatory behavior of the VACFs found in [HMIM][Cl] + water mixtures [81], which indicates a "rattling" motion of the molecules inside the cages formed by their heavier neighbors and is related to the diffusive regime in MSD [64], is not registered in mixtures of this chlorinated IL with alcohols.

2.3.5. Conclusions

We performed MD simulations for mixtures of three imidazolium-based ILs, [HMIM][PF_6], [HMIM][BF_4], and [HMIM][Cl], with methanol and ethanol, and we investigated several dynamical properties of the system. Specifically, we analyzed the effect of the anion hydrophobicity degree, of the length of the molecular chain of the alcohol, and of alcohol concentration on the evolution of the dynamics of the mixtures. Furthermore, we analyzed self-diffusion coefficients of the species present in the mixtures, MSDs (with an additional study of both ballistic and diffusive regimes), and VACFs of alcohol molecules.

Self-diffusion coefficients were computed from the slopes of the center-of-mass MSDs of the corresponding molecule, using data between 200 and 1800 ps. To check the accuracy of the force field employed we computed the self-diffusion coefficients of both ions in pure ILs and of pure alcohols and compared them with previously reported values. Our self-diffusion coefficients for pure liquids were found to be in good agreement with the experimental and computational values available in the literature, and self-

Figure 2.32 Concentration dependence of the VACFs of ethanol molecules in mixtures with (a) [HMIM][PF_6], (b) [HMIM][BF_4], and (c) [HMIM][Cl].

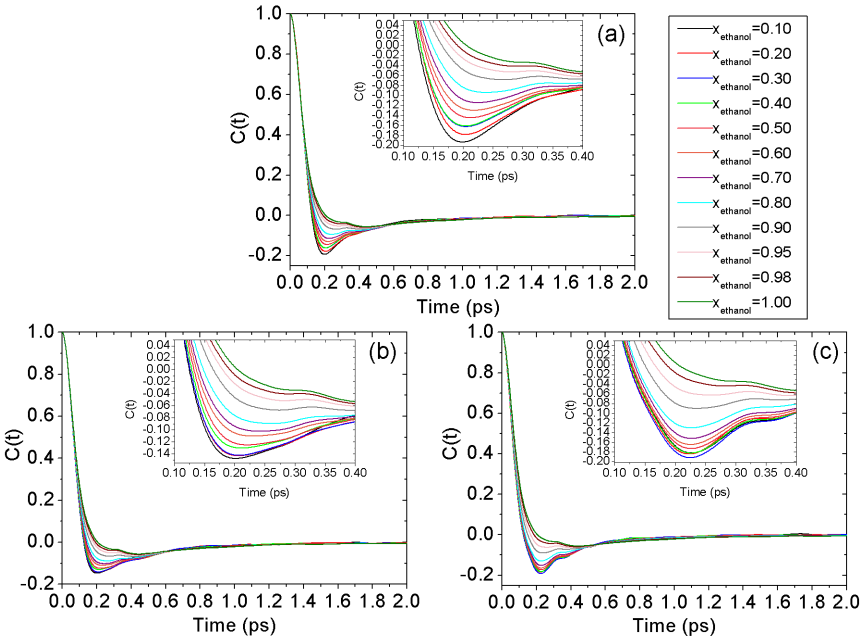

diffusivities of the ions were around 2 orders of magnitude smaller than those of pure alcohols or pure water at room temperature. Moreover, cations have a faster diffusion than their counterions, in spite of being heavier and larger. In mixtures with both alcohols, self-diffusion coefficients increase with increasing concentrations of alcohol, and two different regimes can be observed for this magnitude: (i) at high IL concentrations self- diffusion coefficients of alcohol molecules increase very slowly, which is associated to a possible glassy state of the system, and (ii) at low IL concentrations self-diffusion coefficients of alcohol molecules show a rapid increase with the amount of alcohol, which is related to percolation of alcohol regions (especially in mixtures with [HMIM][PF_6]), thus breaking the IL polar network. Faster diffusion was observed for PF_6^- than for the halogen anion in mixtures with both alcohols due to the higher hydrophobicity degree of hexafluorophosphate and the stronger interactions between alcohol molecules and chloride.

The analysis of the MSDs of these liquids and their mixtures confirms that the dynamics of these systems is very slow and complex. From the repres-

Figure 2.33 Concentration dependence of the VACFs of methanol in mixtures with (a) [HMIM][PF_6], (b) [HMIM][BF_4], and (c) [HMIM][Cl].

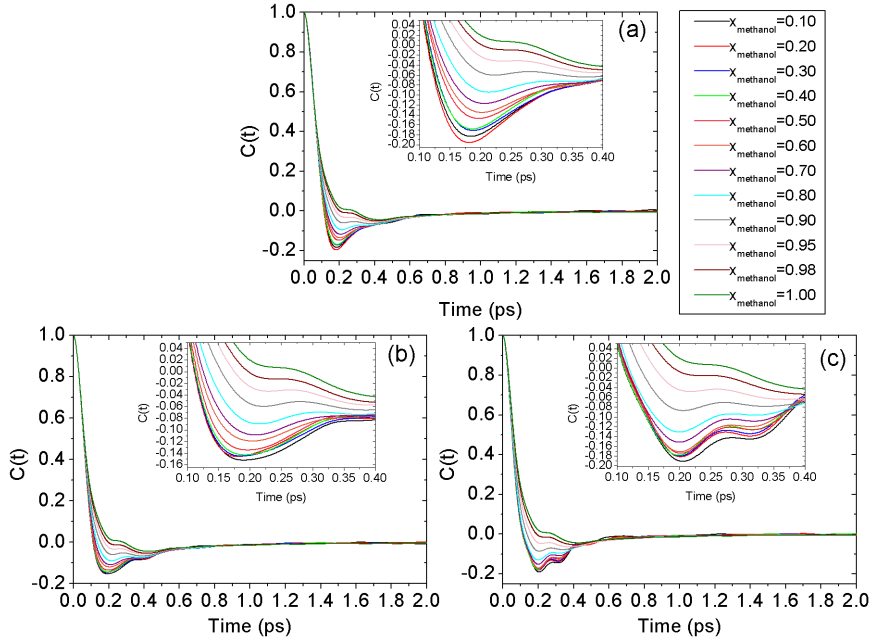

entations of the MSDs of the center-of-mass of the alcohols we observed three different time scales. At very short times the ballistic motion is characterized by the quadratic dependence of the MSD with the time, while at long times (after the alcohol molecules have undergone many collisions in the bulk) the behavior becomes diffusive and the dependence of MSD with time becomes linear. The subdiffusive regime observed at intermediate times within a time scale of several thousands of picosecondss is associated with the slow structural relaxation of the studied mixtures, and this non-Markovian dynamics exhibits a power-law dependence of the MSD with time with an exponent smaller than unity. This intermediate plateau was found to be narrower as the concentration of alcohol increases, until the faster dynamics of pure alcohols is reached. Moreover, the diffusive regime is reached at larger times in mixtures with the chlorinated IL since the motion of alcohol molecules is more similar to that in pure alcohol when the highly solvophobic hexafluorophosphate is present in the mixture.

Finally, the analysis of the VACFs of alcohol molecules revealed that the

correlations are rapidly and monotonically weakened in all cases and that the mean collision time increases with the addition of alcohol to the mixture. These collision times were shown to be longer for the more hydrophobic ILs, as determined by the clusterization degree of alcohols in mixtures with these ILs, which shows the dominant role of the anion on the dynamical properties of IL + solvent mixtures.

2.4. MD Simulations of the Formation of Stable Clusters in Mixtures of Alkaline Salts and Imidazolium-Based Ionic Liquids.

As previously mentioned, among the multiple applications of ILs, one of the most relevant is as electrolytes in electrochemical devices. Current knowledge of the microscopic physical properties of mixtures of ILs with salts is still very scarce, which limits the applicability of these solvents in electrochemical devices. In order to improve the use of ILs in these devices, bulk physical properties of salt-doped ILs require further analysis, specifically solvation of salt ions in these dense ionic environments.

In this work we carried out MD simulations to determine the structural and dynamical properties of ILs based on the $[Bmim]^+$ cation combined with three different anions ($[PF_6]^-$, $[BF_4]^-$ and $[NTf_2]^-$), mixed with lithium and sodium salts that share their anions with the IL [228]. Interestingly enough, we found that salt cations are strongly coordinated with the anions of the mixtures and that they adopt two possible conformations within the first solvation shell. As a result, they form long-lived aggregates that act as stable kinetic entities, which was not only confirmed by means of structural analysis, but also with studying the single-particle dynamics.

In addition, we reported values of ionic conductivity for this type of mixtures from the self-diffusion coefficients. However, the obtained data were slightly underestimated when compared to the experimental ones, which is due to the need of including polarization effects.

2.4.1. Paper IV: MD Simulations of the Formation of Stable Clusters in Mixtures of Alkaline Salts and Imidazolium-Based Ionic Liquids; *J. Phys. Chem. B 117 (2013) 3207-3220.*

Trinidad Méndez-Morales,[1] Jesús Carrete,[1] Silvia Bouzón-Capelo,[1] Martín Pérez-Rodríguez,[2] Óscar Cabeza,[3] Luis J. Gallego[1] and Luis M. Varela[1]

Structural and dynamical properties of room-temperature ionic liquids containing the cation 1-butyl-3-methylimidazolium ($[BMIM]^+$) and three different anions (hexafluorophosphate, $[PF_6]^-$, tetrafluoroborate, $[BF_4]^-$ and bis(trifluoromethylsulfonyl)imide, $[NTf_2]^-$) doped with several molar fractions of lithium salts with a common anion at 298.15 K and 1 atm were investigated by means of molecular dynamics simulations. The effect of the size of the salt cation was also analyzed by comparing these results with those for mixtures of $[BMIM][PF_6]$ with $NaPF_6$. Lithium/sodium solvation and ionic mobilities were analyzed via the study of radial distribution functions, coordination numbers, cage autocorrelation functions, mean square displacements (including the analysis of both ballistic and diffusive regimes), self-diffusion coefficients of all the ionic species, velocity and current autocorrelation functions, and ionic conductivity in all the ionic liquid/salt systems. We found that lithium and sodium cations are strongly coordinated in two different positions with the anion present in the mixture. Moreover, $[Li]^+$ and $[Na]^+$ cations were found to form bonded-like, long-lived aggregates with the anions in their first solvation shell, which act as very stable kinetic entities within which a marked rattling motion of salt ions takes place. With very long MD simulation runs, this phenomenon is proved to be on the basis of the decrease of self-diffusion coefficients and ionic conductivities previously reported in experimental and computational results.

[1] *Grupo de Nanomateriais e Materia Branda, Departamento de Física da Materia Condensada, Universidade de Santiago de Compostela, Campus Vida s/n E-15782, Santiago de Compostela, Spain*

[2] *Departamento de Física Aplicada, Universidade de Vigo, Lagoas-Marcosende s/n E-36310, Vigo, Spain*

[3] *Facultade de Ciencias, Universidade da Coruña, Campus A Zapateira s/n E-15008, A Coruña, Spain*

2.4.2. Introduction

Room-temperature ionic liquids (ILs), that is, a class of organic salts whose melting points are usually below 100 °C, have attracted considerable attention recently due to their unique and favorable properties such as low vapor pressure, high thermal and electrochemical stability, low viscosity, high ionic conductivity, inflammability, and ability to dissolve an enormous range of organic and inorganic materials [36, 133, 229]. These properties make them very attractive "green" candidates for replacing conventional organic solvents in a variety of industrial applications [84, 134, 135] and contribute to their increasing use in various fields of chemistry: synthesis, catalysis, lubrication, thermal separation processes, purification methods and electrochemical applications [3, 12, 185].

Regarding to electrochemical studies, the use of ILs as a new class of liquid electrolytes in lithium batteries have focused the attention of many research groups due to their nonvolatile and noncombustible natures, and it is now under investigation worldwide [230–247]. Although ILs are formed solely by ions (generally, a large organic cation, such as those based on imidazolium, pyridinium, pyrrolidinium, ammonium or phosphonium and an inorganic anion, such as $[PF_6]^-$, $[BF_4]^-$, $[NTf_2]^-$, etc.[179]), their use in battery electrolytes entails the addition of a lithium salt to the IL since they are not electroactive [238]. However, there is a lack of information on the solubility of lithium salts in ILs, above all, regarding the mixtures of imidazolium-based ILs with lithium salts, and only a few works presented a detailed study of the solubility of several inorganic salts in ILs up to now [242, 248–251].

With the aim of providing useful salt/IL systems that give good performance and of improving the application of ILs in lithium battery electrolytes, a detailed picture of the structural and ion transport properties of lithium salt-doped ILs is of essential importance, since they affect properties of the electrolyte (e.g., conductivity) that play a fundamental role in the performance of lithium batteries. However, the lithium cation ($[Li]^+$) solvation process and its transport mechanism in these mixtures have not been analyzed very extensively either in experimental studies or, even, by computational simulations.

In one of the experimental studies that have been published to date, Hayamizu *et al.* [252] measured, by using the pulsed-gradient spin-echo NMR (PGSE-NMR) method, the self-diffusion coefficients of each ion in samples of 1-ethyl-3-methylimidazolium tetrafluoroborate ([EMIM][BF_4]) with $LiBF_4$.

They also studied the ionic conductivity, viscosity, and thermal properties up to a salt concentration of 1.5 M at various temperatures, and indicated that both the ionic conductivity and the ion self-diffusion coefficients decreased with increasing $LiBF_4$ concentration, as well as that the ions form associated structures and diffuse under the influence of the counterions in the salt/IL systems. A similar behaviour for the self-diffusion coefficients was reported by Duluard *et al.* [253] in 2008, who analyzed the Raman spectra of 1-butyl-3-methylimidazolium bis(trifluoromethylsulfonyl)imide ([BMIM][NTf_2]) doped with $LiNTf_2$ for salt molar fractions $x < 0.4$. Moreover, they observed that lithium solvation is essentially due to two $[NTf_2]^-$ anions forming $[Li(NTf_2)_2]^-$ anionic clusters. This result, also obtained by Lassègues *et al.* [239], was fully confirmed by Umebayashi *et al.* [254] by Raman spectroscopy and DFT calculations of the solvation structure of the lithium ion in 1-ethyl-3-methylimidazolium bis(trifluoromethylsulfonyl)imide ([EMIM][NTf_2]) and N-butyl-N-methylpyrrolidinium bis(trifluoromethylsulfonyl)imide ([BMPy][NTf_2]). Also in 2008, Monteiro *et al.* [255] determined thermal properties, density, viscosity, ionic conductivity, and self-diffusion coefficients of mixtures of ([BMIM][NTf_2]) with $LiNTf_2$ at several temperatures. Their Raman spectroscopy studies indicated the formation of at least two different types of aggregates, $[BMIM]^+$ with $[NTf_2]^-$ (which they called the "weak" ones), and $[Li]^+$ with $[NTf_2]^-$ (the "strong" ones). In addition, they performed molecular dynamics (MD) simulations and showed that the average number of $[NTf_2]^-$ anions around a given $[Li]^+$ changes with salt concentration, causing a change of the structure of the mixture and provoking a reduction of diffusion coefficients of all species in the IL/salt system.

As it is usually very complicated to experimentally achieve a detailed knowledge of the behaviour of lithium salt-doped ILs at the molecular level, MD simulations are an essential tool for exploring the interplay between dynamical properties and local structures in this kind of systems. One example would be the study reported by Borodin *et al.* [256], in which they performed MD simulations of N-methyl-N-propylpyrrolidinium bis(trifluoromethylsulfonyl)imide ([MPPY][NTf_2]) and N,N-dimethyl- pyrrolidinium bis(trifluoromethylsulfonyl)imide ([MMPY][NTf_2]) doped with 0.25 molar fraction of $LiNTf_2$ at 303 – 500 K. They found that $[Li]^+$ cations are coordinated on average by four oxygen atoms with each oxygen atom being contributed by a different $[NTf_2]^-$ anion, that is, the formation of $[Li(NTf_2)_4]^{3-}$, and even a lithium aggregation in which two $[Li]^+$ are strongly coordinated by sharing

up to three $[NTf_2]^-$ anions was observed at lower temperatures. Additionally, in a recent computational work, Niu *et al.* [257] performed MD simulations of 1-ethyl-2,3-dimethylimidazolium hexafluorophosphate ([EMIM][PF_6]) mixed with different molar ratios of $LiPF_6$ at 523.15 K and 1 bar. Their structural analysis showed that $[Li]^+$ cations are strongly coordinated by the fluorine atom of the $[PF_6]^-$ anion, and the number of hexafluorophosphates in the first solvation layer of the lithium cation is about four, and increases slightly with increasing the salt concentration. Moreover, they reported a two-dimensional radial-angular distribution study of $[Li^+]$-P distance and Li-P-F′ angle, in which they found that the $[Li]^+$-$[PF_6]^-$ complex tends to form the C_{2v} conformation (forming Li-P-F′ an angle of around 45°) at low salt concentration, with C_{4v} conformation (forming Li-P-F′ an angle of 0°) predominating at higher salt concentration. However, some controversy around the lifetime of these aggregates at room temperature still exists in some computational works, and the existence of long-lived stable lithium-induced anionic clusters was attributed to deficient equilibration [256]. To shed some light on this question, we report very long simulation runs to ensure the stabilization of the systems and an exhaustive study of the formation, stability, and influence on transport properties of this kind of clusters.

In this work, we present a comparison among three ILs from the imidazolium family in mixtures with lithium salts with the same anion. These ILs have the same cation: 1-butyl-3-methylimidazolium ($[BMIM]^+$), the anions being hexafluorophosphate, $[PF_6]^-$, tetrafluoroborate, $[BF_4]^-$, and bis (trifluoromethylsulfonyl)imide, $[NTf_2]^-$, chosen by electrochemical interest. The self-diffusion coefficients of each ionic species in the binary IL/salt system were analyzed as a function of salt concentration, as well as density, radial distribution functions, coordination numbers, cage autocorrelation functions, mean square displacements, ballistic and diffusive regimes, velocity and current autocorrelation functions, and ionic conductivity with the intent of providing an insight for understanding the structural and ion transport properties of salt-doped ILs. In addition, to our knowledge, this is the first time that the effects of the size of the cation are analyzed, reporting a brief comparison between the effects of lithium and sodium cations in mixtures of this kind of salts with [BMIM][PF_6].

The remainder of this paper is organized as follows: In the following section, we provide a detailed description of the computational procedure employed in this study. Next, we present and discuss the obtained results, and in

the final section, we summarize our main conclusions.

2.4.3. Simulation details

All simulations for pure [BMIM][BF_4], [BMIM][PF_6] and [BMIM][NTf_2], as well as their mixtures with the corresponding lithium/sodium salts ($LiBF_4$, $LiPF_6$/$NaPF_6$, and $LiNTf_2$, respectively) were performed using the Gromacs 4.5.4 package [104]. The thermodynamic state investigated was $T = 298.15$ K and $P = 1$ atm, and the salt molar percentages considered in all the systems were $\%_{salt}$={0, 1, 5, 10, 15, 25 and 40}, because, even though there are hardly any experimental studies concerning the solubility of lithium salts in ILs (and none related to sodium salts), some previous works have investigated mixtures of imidazolium-based ILs with lithium salts up to a salt mole fraction of $x_{salt} = 0.50$ (see ref.[240] and references therein). The initial configurations for $\%_{salt} = 1, 5$ and 10 were obtained by randomly inserting, respectively, 4950, 950 and 450 ionic pairs of IL in a cubic box in order to have enough salt to yield statistically significant trajectories, whereas for the rest of the molar percentages, we considered 300 ionic pairs. The number of lithium/sodium salt molecules was calculated for each situation by considering each ionic pair as a single unit in the calculation of mole fractions.

We employed the OPLS-AA force field in order to carry out the parameterization of the ions. This all-atom version of the OPLS force field, in which every hydrogen atom bonded to carbon is modelled explicitly, was developed by Jorgensen [153] for different organic liquids. The functional form of the OPLS force field is described by

$$\begin{aligned} E = & \sum_i K_{b,i}\left[r_i - r_{0,i}\right]^2 + \sum_i K_{b,i}\left[\theta_i - \theta_{0,i}\right]^2 + \\ & + \sum_i \left[\frac{1}{2}V_{1,i}(1+\cos(\varphi_i)) + \frac{1}{2}V_{2,i}(1+\cos(2\varphi_i)) + \right. \\ & \left. + \frac{1}{2}V_{3,i}(1+\cos(3\varphi_i)) + \frac{1}{2}V_{4,i}(1+\cos(4\varphi_i))\right] + \\ & + \sum_i \sum_{j<i} \left\{ \frac{1}{4\pi\varepsilon_0}\frac{q_i q_j e^2}{r_{ij}} + 4\varepsilon_{ij}\left[\left(\frac{\sigma_{ij}}{r_{ij}}\right)^{12} - \left(\frac{\sigma_{ij}}{r_{ij}}\right)^{6}\right]\right\}, \end{aligned} \tag{2.13}$$

which includes intramolecular interactions, such as bond stretching, angle bending, dihedral torsion, and van der Waals and Coulombic interactions. The

parameters employed in eq.(2.13) are the force constants K, the nominal values r_0 and θ_0, the Fourier coefficients V, and the partial atomic charges q fixed on each atom center. σ_{ij} and ε_{ij} represent the Lennard-Jones radii and potential well depths, respectively, which are obtained from parameters for each type of atom by using geometric combination rules $\epsilon_{ij} = \sqrt{\epsilon_{ii}\epsilon_{jj}}$ and $\sigma_{ij} = \sqrt{\sigma_{ii}\sigma_{jj}}$. The imidazolium cation was modelled by using the all-atom representation of the CH_2 and CH_3 groups in the alkyl chain, as well as that of the methyl group attached to the imidazolium ring, while lithium and sodium cations were modelled by a single site of charge +1. As for the anions, $[PF_6]^-$ was modelled as a set of seven sites with partial charges of 1.34 for the phosphorus atom and −0.39 for the fluorine atoms [154]. $[BF_4]^-$ was modelled as a set of 5 sites with partial charges of 1.176 for the boron atom and −0.544 for the fluorine atoms [155], and $[NTf_2]^-$ was modelled as a set of 15 sites whose partial charges were reported in a previous article by Canongia-Lopes and Pádua [258]. Long-range electrostatic interactions were treated by using the particle-mesh ewald (PME) [77] method with a grid spacing of 12 nm and cubic interpolation. A cut-off distance of 1.1 nm was used for Lennard-Jones interactions, and a neighbor searching was made up to this same distance from the central ion and was updated every five simulation steps. The linear constraint solver (LINCS) algorithm [159, 160] with a fourth-order expansion of the constraint coupling matrix was used to hold the bonds rigid, and long range dispersion corrections were used for both energy and pressure.

Initial configurations were relaxed for 10^6 steps using a conjugated gradients algorithm in order to remove bad contacts resulting from the initial random configuration of ions. The maximum step size and the tolerance were set to 0.01 nm and 0.1 kJ/nm · mol, respectively. For each molar percentage of salt, the system was equilibrated for 10 ns in the isothermal-isobaric (NpT) ensemble. The results of an additional 10 ns long simulation in the isothermal-isobaric ensemble were then used for the analysis of the structure of the mixtures. The time step of the simulations was 2 fs. The temperature was controlled by using the V-rescale thermostat [161]. Cations and anions were separated in two (or three) baths with temperature coupling constants of 0.1 ps. The pressure control was set by using the Parrinello-Rahman barostat [162] with a reference pressure of 1 atm, an isothermal compressibility of $4.5 \cdot 10^{-5}$ bar^{-1}, and a relaxation time of 0.1 ps. Moreover, we performed 10 ns long simulations in the NVE ensemble in order to remove the characteristic times of both the thermostat and the barostat, and whose starting point was taken from the

equilibrating runs in the isothermal-isobaric ensemble for analyzing some of the dynamical properties of the mixtures, such as mean square displacement, velocity and current autocorrelation functions, and self-diffusion coefficients. The energy was kept constant by using a combination of PME and a switch function for the direct-space part (PME-switch), making a search of neighbors with an automated update frequency, and increasing the number of iterations to correct for rotational lengthening in LINCS.

Each of these simulations provided us a sequence of configurations, that is, positions and instantaneous velocities of all atoms of the mixtures, which was analyzed to obtain structural and dynamical information about the aforementioned systems.

2.4.4. Results and discussion

Of all physical properties of interest of ILs, density is the most reliably and unambiguously determined. The values obtained from our simulations for pure ILs were $\rho_{[BMIM][PF_6]}$ = (1336.7 ± 6.1) kg/m^3, $\rho_{[BMIM][BF_4]}$ = (1180.0 ± 5.0) kg/m^3 and $\rho_{[BMIM][NTf_2]}$ = (1495.9 ± 5.4) kg/m^3, which yielded a maximum deviation from available experimental results (1370 kg/m^3, 1120 kg/m^3 and 1430 kg/m^3, respectively) [36, 147, 259] of 4.6%, allowing us to be reasonably confident in our simulation model. Additionally, Figure 2.34 shows the concentration dependence of density for mixtures of [BMIM][PF_6], [BMIM][BF_4] and [BMIM][NTf_2] with the corresponding lithium or sodium salt up to a molar percentage of $\%_{salt}$ = 40 at 298.15 K. It can be seen that the addition of lithium salt increases the density of the mixture by about 5% at $\%_{salt}$ = 25 when compared with pure ILs, in agreement with values previously reported by Borodin *et al.* [256], and about 10% at the highest molar percentage. The density of [BMIM][PF_6] doped with $NaPF_6$ is included with the aim of comparing the effect of sodium cation with that of lithium in the density. As expected, replacing the lithium cation with sodium leads to an increase in the density for the same amount of salt, since lithium hexafluorophosphate is less dense than sodium hexafluorophosphate. Thus, at $\%_{salt}$ = 25, an increase in the density of the mixture with sodium salt by about 8% with respect to that of the pure IL can be seen, this being increase nearly 15% at the highest amount of sodium salt.

To study the microstructure of the mixtures and gain further insight at the molecular level into the kind of aggregates that can be formed in these systems

Figure 2.34 Simulated densities of [BMIM][PF_6] (black dots), [BMIM][BF_4] (red dots), and [BMIM][NTf_2] (blue dots) mixed with lithium salts with a common anion as a function of the lithium salt concentration. Density of [BMIM][PF_6] doped with $NaPF_6$ (green dots) is also included with the purpose of comparison. Moreover, experimental densities of the pure ILs (squares) have been included as a reference point.

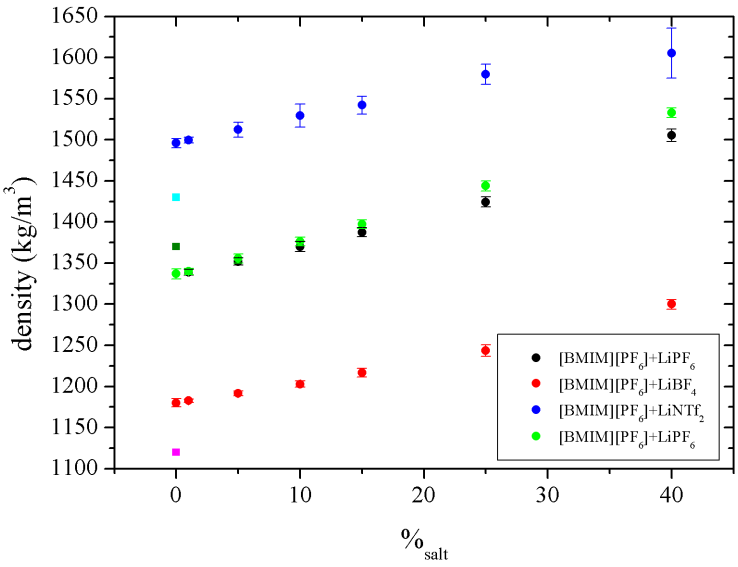

with the addition of lithium salt, we calculated radial distribution functions (RDFs)

$$g(r) = \frac{1}{\rho N}\langle \sum_{ij} \delta(r - r_{ij})\rangle \tag{2.14}$$

where N is the number of particles in the system, ρ stands for its number density, i and j run over all the particles, and brackets indicate the ensemble average. It must be noted that, in the RDFs that involve the imidazolium cation, only the five atoms in the imidazole ring were considered in the calculations, and all RDFs presented in this paper were calculated using the center of mass of the molecules.

The lithium salt concentration dependence of lithium-anion RDFs is shown in Figure 2.35, in which we can observe that lithium molecules are strongly coordinated with the anions in all three systems, as indicated by the height

Figure 2.35 Salt molar percentage dependence of lithium-anion RDFs for mixtures of lithium salts with (a) [BMIM][PF_6], (c) [BMIM][BF_4], and (d) [BMIM][NTf_2] at 298.15 K and 1 atm. Sodium-anion RDFs for [BMIM][PF_6] mixed with $NaPF_6$ are also included in (b) with the purpose of comparison. For clarity, only a few of all the analyzed molar percentages are shown.

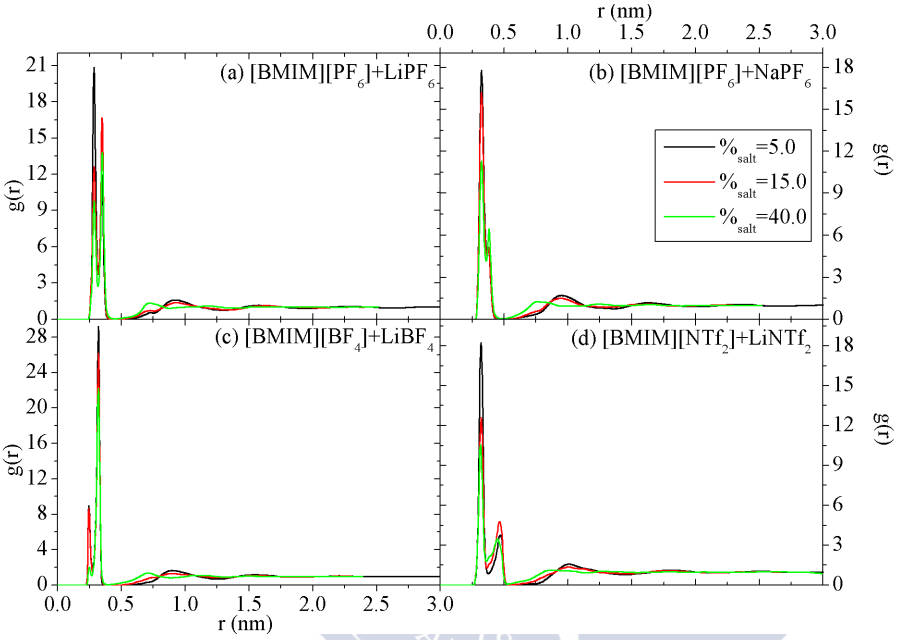

of their peaks. A comparison with sodium-anion RDFs for [BMIM][PF_6] mixed with $NaPF_6$ is also shown. For clarity, only a few of all the analyzed molar percentages are shown. Concerning lithium salt mixtures, if we consider that the end of the first solvation layer is placed at the position of the deepest minimum (0.4, 0.35, and 0.5 nm for [BMIM][PF_6], [BMIM][BF_4], and [BMIM][NTf_2], respectively), a double peak can be seen within this first solvation shell in all the studied mixtures, showing that several anions coordinate with the ($[Li]^+$) cations, in agreement with previous results reported by Niu *et al.* [257] for [EMIM][PF_6] mixed with $LiPF_6$ at 523.15 K. In mixtures in which $[PF_6]^-$ or $[NTf_2]^-$ anions are present, the first peak is sharper than the second one, whereas mixtures with [BMIM][BF_4] show the opposite behaviour. In addition, both peaks decrease when lithium salt is added to the mixture. If we take a look at each system separately, Figure 2.35.(a), which represents lithium-anion RDFs of [BMIM][PF_6] doped with $LiPF_6$, exhibits the first peak

around 0.28 nm and the second one at 0.34 nm. Those peaks correspond to the lithium cation placed between two fluorine atoms of the hexafluorophosphate anion (forming $[Li]^+$-$[P]^-$-$[F]^-$, an angle of around 45°) or next to one of the fluorines (forming $[Li]^+$-$[P]^-$-$[F]^-$, an angle of 0°), as represented in Figure 2.36.(a) and (b), respectively. These distances are in excellent agreement with those reported by Niu *et al.* [257] in their two-dimensional radial-angular distribution study. Moreover, they found that C_{4v} conformation, which coincides with the second peak, becomes more important at higher salt concentrations, this result being consistent with the fact that, when the amount of salt present in the mixture is high, the height of the second peak becomes greater than that of the first one and, taking into account that the width of the peaks is approximately constant, height can be considered as a direct measure of the number of species in each position. On the other hand, we did not find any evidence of a tridendate coordination (C_{3v}) of lithium cations by $[PF_6]^-$, which was reported to be the most stable structure in gas phase by Xuan *et al.* [260]. In this conformation, lithium is close to three fluorine atoms forming $[F]^-$-$[Li]^+$-$[F']^-$, an angle of around 73.6°, and it is placed 0.24 nm away from the central phosphorus. Figure 2.35.(c) shows that the first peak of lithium-anion RDFs of mixtures of [BMIM][BF_4] with $LiBF_4$ is located around 0.23 nm and the second one at 0.32 nm. This behaviour is similar to the one found in mixtures of [BMIM][PF_6], since the first peak corresponds to a conformation in which the lithium cation gets close to the boron atom approaching from between two of the fluorine atoms (a bidendate structure), and the second peak is consistent with a lithium cation forming an angle of 0° with a fluorine and the central boron (a monodendate mode of coordination). This second conformation is more important at all salt concentrations, as shown by the evolution of the heights of both peaks. However, in the study reported by Francisco and Williams [261] by employing ab initio quantum-chemical methods, a bidendate C_{2v} structure was predicted to be the most stable and a monodendate C_{4v} conformation was regarded as very unlikely, both structures giving $[B]^-$-$[Li]^+$ distances in good agreement with the ones showed in Figure 2.35.(c). A tridendate C_{3v} structure with a $[B]^-$-$[Li]^+$ distance of 0.21 nm and an intermediate stability was not found in our mixtures. Finally, Figure 2.35.(d) corresponds to [BMIM][NTf_2] doped with $LiNTf_2$, and it illustrates a first peak situated around 0.32 nm and a second one at 0.45 nm. This RDF is very similar to that of the lithium cation and the nitrogen atom of the anion. Therefore, it can be deduced that lithium cations are correlated to nitrogen

Figure 2.36 Representation of the two possible conformations of the lithium cation around a $[PF_6]^-$ anion in mixtures of [BMIM][PF_6] with $LiPF_6$.

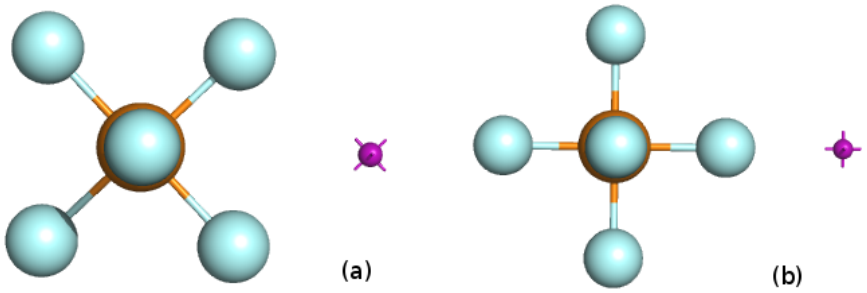

and oxygen atoms of the anion due to their negative partial charges, since this conformation is consistent with the positions of both observed peaks. The first peak reveals a conformation in which the lithium cation is placed close to the nitrogen in an intermediate position between both sulfur atoms. The second peak is due to all the possible orientations of $[Li]^+$ around the four oxygens of the anion. This picture is in good agreement with the one reported by Borodin *et al.* [256] in their study of [MMPY][NTf_2] mixed with $LiNTf_2$. The RDFs of [BMIM][PF_6] mixed with $NaPF_6$ included in Figure 2.35.(b) show, as for the mixture with lithium salt, a double peak within the first solvation layer of central sodium cation. However, in this case, both peaks are located at slightly larger distances that those of lithium-anion RDFs, 0.32 nm and 0.38 nm, respectively, due to the larger size of sodium ion. Moreover, the first peak is higher than the second one for all the studied percentages of sodium salt, showing that a conformation in which $[Na]^+$ cations are placed between two fluorine atoms of the $[PF_6]^-$ anion is always predominant in this kind of mixtures.

Packing effects on the structural conformation are shown by the evolution of the height of the two first peaks, and they can be more clearly seen in Figure 2.37, in which we show the concentration dependence of the relation between the height of the first peak and that of the second one for the lithium/sodium-anion RDFs of all the studied mixtures. As we can observe, mixtures of [BMIM][BF_4] with $LiBF_4$ are the only systems whose second peak is higher than the first one for all the analyzed molar percentages of lithium salt. On the other hand, in those mixtures of [BMIM][NTf_2] and [BMIM][PF_6]

Figure 2.37 Salt molar percentage dependence of the relation between the height of the first two peaks for the lithium/sodium-anion RDFs of all the studied mixtures.

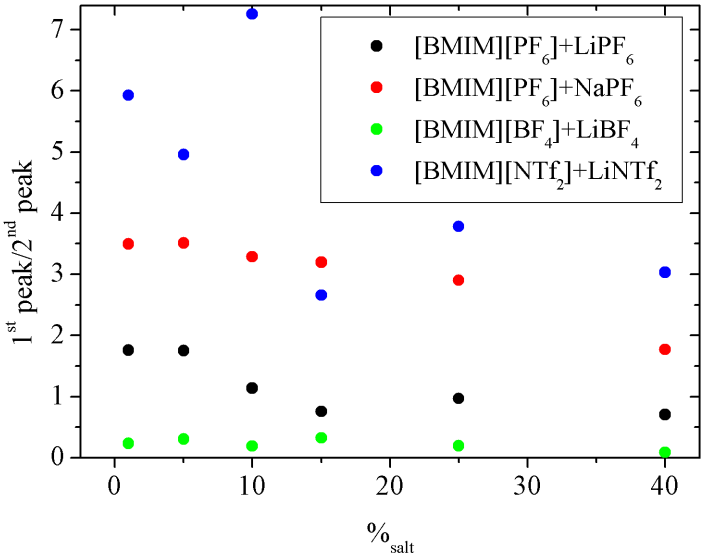

with $LiNTf_2$ and $NaPF_6$, respectively, the first peak is always higher than the second one, decreasing the difference between them as the amount of salt increases. Finally, [BMIM][PF_6] mixed with $LiPF_6$ is the only system that shows an inversion in the height of the first two peaks with the addition of lithium salt to the mixture, since, for less than a 15% of salt, the relation between them is greater than 1 and, at higher molar percentages of salt the relation becomes smaller than 1.

The lithium salt concentration dependence of lithium-cation RDFs for all the studied IL/salt mixtures, as well as a comparison with sodium-cation RDFs for [BMIM][PF_6] mixed with $NaPF_6$ is included as part of the Supporting Information for this paper. Regarding lithium salt mixtures, in systems with [BMIM][NTf_2] the first peak is a little bit displaced to higher distances than in those mixtures in which $[PF_6]^-$ or $[BF_4]^-$ anions are present, as expected due to the greater size of the $[NTf_2]^-$ anion and, therefore, of the first solvation layer. Moreover, the fact that the first peak height is lower than those of the anion-lithium RDFs and that the RDFs are quickly smoothed out implies that there

is no aggregation of imidazolium cations around the lithium ions, as expected from the electrostatic interactions between cations and anions. It can be also observed that replacing lithium cations with sodium ions does not lead to a significant change in this RDFs, the most remarkable and somehow expected variation being a slightly higher first peak in the mixture with sodium salt, but with this first peak placed approximately at the same distance as the one obtained in the system doped with lithium salt.

All the studied systems exhibit an exclusion of anions after the first solvation shell, in which a layer of lithiums can be found, as we can observe looking at the first peaks in lithium-lithium RDFs, also included as Supporting Information, placed at intermediate distances between those of lithium-cation RDFs and those of lithium-anion ones. This figure also includes a comparison with sodium-sodium RDFs for [BMIM][PF_6] mixed with $NaPF_6$. Thus, from the analysis of the RDFs, we can conclude that lithium/sodium cations are surrounded by a first solvation layer of anions (with which they are strongly coordinated), followed by a second shell of lithium/sodium ions and a third layer of imidazolium cations, resembling a pseudolattice structure according to the structural model on the basis of Bahe-Varela theory [117, 118, 262]. This conformation can indeed be observed in a snapshot included in Figure 2.38.(a) of a few molecules in the final configuration in the simulation box of a 40% [BMIM][PF_6]/$LiPF_6$ mixture.

The above conclusions can be reinforced by evaluating the coordination numbers of ions in the mixtures. The most common way for analyzing coordination numbers in the literature is by numerical integration of the function $4\pi r^2 \rho g(r)$ up to the first minimum (being ρ the numerical density of the ionic species surrounding a lithium cation) and $g(r)$ the corresponding RDFs plotted in Figure 2.35, as well as in cation-lithium and lithium-lithium RDFs, which indicates the end of the corresponding solvation layer. The coordination number of the anions, lithium ions, and imidazolium cations in the first, second and third coordination shell, respectively, of the $[Li]^+$ cation are shown in Table 2.4 for all the studied mixtures. In addition, coordination numbers corresponding to mixtures of [BMIM][PF_6] with $NaPF_6$ are included, and they seem to be compatible with those of lithium ions.

Regarding the number of anions coordinating a $[Li]^+$ cation, it can be seen that $[BF_4]^-$ ions provide the highest value, which is approximately 3.3. In the case of $[PF_6]^-$, the value is around 3, which is in good agreement with the results reported by Niu *et al.* [257] In both cases, the coordination numbers

Table 2.4 Coordination numbers of imidazolium cations (left), anions (center), and lithium ions (right) around a lithium cation in mixtures of [BMIM][PF_6], [BMIM][BF_4], and [BMIM][NTf_2] and lithium salts with a common anion. Coordination numbers of imidazolium cations (left), anions (center), and sodium ions (right) around a sodium cation of [BMIM][PF_6] mixed with $NaPF_6$ are also included with the purpose of comparison.

	[BMIM][PF_6] + [$LiPF_6$]		
$\%_{salt}$	$n_{[Li]^+-[BMIM]^+}$	$n_{[Li]^+-[PF_6]^-}$	$n_{[Li]^+-[Li]^+}$
5.0	8.20	2.87	0.15
10.0	8.16	2.86	0.23
15.0	7.94	2.90	0.41
25.0	7.41	2.88	0.59
40.0	6.89	2.91	1.00
	[BMIM][PF_6] + [$NaPF_6$]		
$\%_{salt}$	$n_{[Na]^+-[BMIM]^+}$	$n_{[Na]^+-[PF_6]^-}$	$n_{[Na]^+-[Na]^+}$
5.0	8.28	2.67	0.13
10.0	8.45	2.70	0.19
15.0	8.03	2.72	0.29
25.0	7.52	2.69	0.53
40.0	6.56	2.75	1.06
	[BMIM][BF_4] + [$LiBF_4$]		
$\%_{salt}$	$n_{[Li]^+-[BMIM]^+}$	$n_{[Li]^+-[BF_4]^-}$	$n_{[Li]^+-[Li]^+}$
5.0	9.10	3.24	0.10
10.0	8.94	3.24	0.31
15.0	8.69	3.29	0.38
25.0	8.48	3.29	0.71
40.0	7.53	3.35	1.27
	[BMIM][NTf_2] + [$LiNTf_2$]		
$\%_{salt}$	$n_{[Li]^+-[BMIM]^+}$	$n_{[Li]^+-[NTf_2]^-}$	$n_{[Li]^+-[Li]^+}$
5.0	6.55	1.91	0.04
10.0	6.12	1.84	0.13
15.0	6.39	1.96	0.26
25.0	5.49	1.90	0.42
40.0	4.47	1.71	0.59

Figure 2.38 (a) Snapshot of a few molecules of the final configuration of a 40% [BMIM][PF_6]/$LiPF_6$ mixture, in which we can observe a central lithium cation (red) surrounded by a first layer of $[PF_6]^-$ anions, a second shell of lithium ions (violet), and a further layer of imidazolium cations. (b) Snapshot of two $[NTf_2]^-$ anions and one lithium cation of the final configuration of a mixture of [BMIM][NTf_2] and a 40% of $LiNTf_2$, in which we can observe that each anion provides two oxygen atoms (red) to the first coordination shell of the lithium cation (violet).

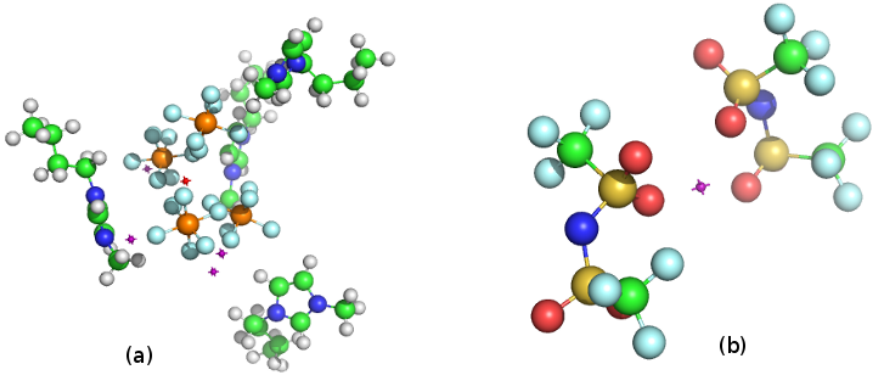

slightly increase with increasing the amount of salt in the system. For the biggest anion, $[NTf_2]^-$, the coordination number reaches a value of approximately 2, which reasonably agrees with previously reported data published by Borodin *et al.* [256] They found that $[Li]^+$ cations are surrounded by nearly 4 oxygen atoms of the $[NTf_2]^-$ anion, so that our results suggest a configuration in which a single $[NTf_2]^-$ anion provides two oxygen atoms to the first coordination layer of a given lithium ion. This conformation can be observed in a snapshot included in Figure 2.38(b) of two anions around a lithium cation in the final configuration in the simulation box of [BMIM][NTf_2] mixed with a 40% of $LiNTf_2$. It must be noted that Borodin *et al.* reported a probability for this conformation of less than 5%, whereas Duluard *et al.* [253] and Lassègues *et al.* [239, 240] proposed a structure as the one that our MD simulations show of $[Li(NTf_2)_2]^-$ clusters in which the lithium is tetrahedrally coordinated to four oxygen atoms of two different anions and, as they indicated, theoretical studies suggest the formation of this bidendate structure [263, 264]. As expected, the number of $[NTf_2]^-$ anions coordinated with a lithium cation is smaller than that of hexafluorophosphate or tetrafluoroborate, due to the

greater size of the former. In addition, in Table 2.4, we can observe that the coordination numbers of imidazolium cations around a lithium atom are approximately 8 for mixtures with [BMIM][PF_6] and [BMIM][BF_4] and nearly 6 for those with [BMIM][NTf_2]. Although both cations are not strongly coordinated (as one can see in the corresponding RDF in Supporting information) due to the electrostatic repulsion between them, the coordination number was expected to be greater than that of any of the anions, since imidazolium cations are located in the third solvation layer of lithium ions and due to its larger radius, this third solvation shell can accommodate a greater number of molecules than the first one. Finally, as indicated in Table 2.4, the number of $[Li]^+$ cations placed within the second solvation layer of lithium ions increases with lithium salt concentration in all the studied systems. The highest value, 1.3, was found in mixtures of [BMIM][BF_4] at a $\%_{salt} = 40$ of salt, whereas mixtures of [BMIM][NTf_2] provided the lowest $[Li]^+$-$[Li]^+$ coordination number (0.6) at that same amount of salt. These results are in good agreement with the ones reported by Borodin *et al.* [256], whose simulations shown that each $[Li]^+$ cation has other 0.7−0.8 lithium molecules in the second solvation layer at a salt molar percentage of $\%_{salt} = 25$ in mixtures of [MMPY][NTf_2] with $LiNTf_2$. All previous comments about mixtures of [BMIM][PF_6] with $LiPF_6$ could be also extended to those with $NaPF_6$, since all the coordination numbers included in Table 2.4 for both cations of the salt are very similar to each other and there is no remarkable effect due to the different size of these ions.

To sum up, the most relevant structural features arising from our simulations are probably those concerning the position of $[Li]^+$ ions around anions, and the probable formation of bonded-like structures that could diffuse as stable kinetic entities, with all the implications this could have in what transport properties are concerned. Obviously, this hypothesis can only be tested analyzing the dynamics of $[Li]^+$ cations and anions in the bulk, what we do in the following.

Single-particle dynamics in these mixtures can be analyzed by means of the study of the center-of-mass velocity autocorrelation functions (VACFs) of their different components. The normalized VACF is calculated as

$$C(t) = \frac{\langle \vec{v}(t) \cdot \vec{v}(0) \rangle}{\langle \vec{v}(0) \cdot \vec{v}(0) \rangle} \tag{2.15}$$

where $\vec{v}(t)$ is the velocity of the center-of-mass of the molecule at time t and the brackets indicate the ensemble average. To the best of our knowledge,

Figure 2.39 Concentration dependence of lithium cations VACF in mixtures with [BMIM][PF_6] (a), [BMIM][BF_4] (c), and [BMIM][NTf_2] (d). The insets show the evolution of the collision time with the amount of salt. Sodium VACFs in mixtures of [BMIM][PF_6] with $NaPF_6$ are also included in (b) with the purpose of comparison.

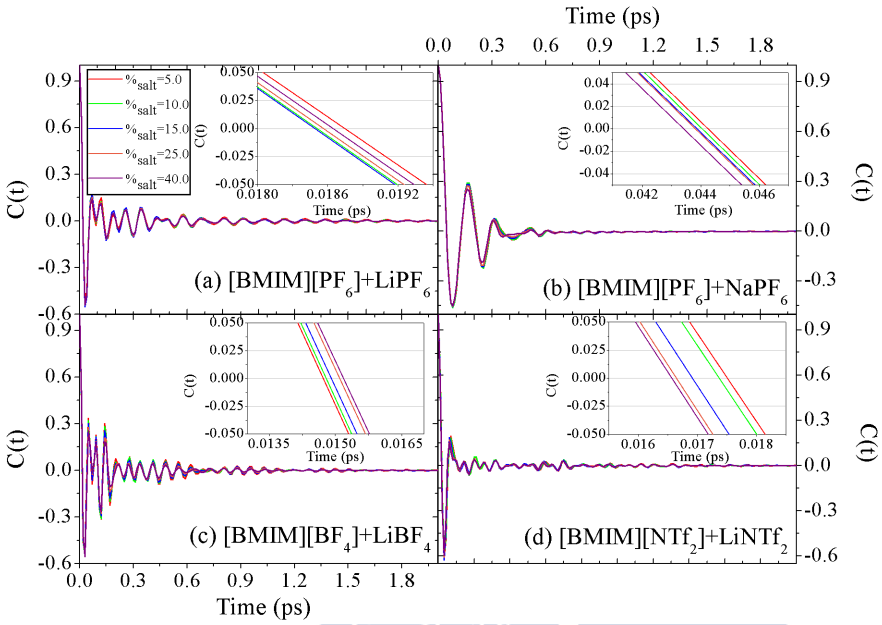

this is the first time that computational results are reported for this quantities in mixtures of ILs with lithium/sodium salts. In Figure 2.39 the concentration dependence of dimensionless VACFs of lithium cations are shown for mixtures with [BMIM][PF_6] (a), [BMIM][BF_4] (c), and [BMIM][NTf_2] (d). This figure also includes a comparison with sodium VACFs for [BMIM][PF_6] mixed with $NaPF_6$. The insets were included in order to allow one to distinguish the evolution of the collision time, indicated by the first zero of the function, with the addition of salt to the system.

As one can see, the mean collision time shows a different trend depending on the anion that is present in the mixture. First, in cases in which hexafluorophosphate is the common anion (Figure 2.39.(a)) the mean collision time increases with increasing salt concentration, except for the lowest molar percentage, for which the first zero of the function takes place at longer times. Moreover, those systems with tetrafluoroborate (Figure 2.39.(c)) exhibit an in-

creasing mean collision time as lithium salt is added to the mixture. However, the observed tendency in mixtures with bis(trifluoromethylsulfonyl)imide (Figure 2.39.(d)) is exactly the opposite, since the first zero of the VACFs appears at lower times when the amount of salt increases. In addition, it must be added that, for the same amount of lithium salt, the mean collision time is somewhat longer in mixtures with [BMIM][PF_6] (around 0.0187 ps) and lower in those with [BMIM][BF_4] (around 0.015 ps), probably due to the stronger interactions between $[Li]^+$ and $[BF_4]^-$ seen in the structural analysis; the systems with [BMIM][NTf_2] being in an intermediate position (0.017 ps approximately). On the other hand, all the VACFs of lithium cation show clear oscillations after the first collision, and this oscillatory behaviour is registered up to around 1.5 ps, indicating a rattling motion of lithium ions in the "cage" of their nearest neighbors, in agreement with previous studies of lithium ions [240, 265]. As expected, this rattling motion is more markedly observed the lighter the anion, probably due to the effect of the different mass ratios between imidazolium cation and anion, since lighter anions suffer more intense oscillations in their VACFs in the presence of the same cation [266, 267], and this has an influence on lithium oscillations. In addition, a weakening of the caging effect with increasing salt concentration can be observed is mixtures with $[BF_4]^-$ anions. Moreover, the oscillations of the lithium VACFs are more rapidly weakened in this system, since the greater number of collisions of the lighter ions cancels out the correlations sooner. No evidence of long-time tails was detected in any of these mixtures. Regarding the VACFs of sodium cation, we can observe that the rattling motion of sodium ions is much less pronounced than that of lithium ions in mixtures with [BMIM][PF_6], these oscillations being completely damped after 0.8 ps, as expected due to the greater mass of sodium ions. In addition, in mixtures of [BMIM][PF_6] with sodium salts the first zero of the function takes place at times around twice longer (0.044 ps approximately) than in mixtures with lithium salts, and the evolution of this mean collision time with the addition of sodium salt to the mixture exhibits the opposite trend of that observed for lithium salt, showing a decrease with increasing sodium salt concentration.

In addition, single-particle dynamics of the ions and the influence of the formation of aggregates on these properties were studied by analyzing, among others, the mean square displacement (MSD), defined as

$$MSD = \langle \Delta|\vec{r}(t)|^2 \rangle = \frac{1}{N} \langle \sum_{i=1}^{N} |\vec{r}_i(t) - \vec{r}_i(0)|^2 \rangle \quad (2.16)$$

where $\vec{r}(t)$ is the location of the center of mass of ion i at time t, the sum extends over all the ions present in the mixture and brackets indicate the ensemble average. In the Supporting information, we include an illustration (Figure 2.44) of the behaviour of MSDs of imidazolium cation, anion, and lithium, respectively, with increasing salt concentration in mixtures of [BMIM][PF_6]/$LiPF_6$ (a)-(d)-(g), [BMIM][BF_4]/$LiBF_4$ (b)-(e)-(h), and [BMIM][NTf_2]/$LiNTf_2$ (c)-(f)-(i). The results for the ions included in the systems are similar to each other, with a faster diffusion of the anions at very short times (when the expected inertial behaviour takes place), and after the appearance of a crossing point at intermediate times, the MSD of the $[BMIM]^+$ cation becomes higher than that of the anion, showing a faster diffusion of the imidazolium cation at long times. After around 3 ns, the three ionic species diffuse approximately at the same rate, showing that the diffusion of these ions is correlated and that they do not move separately. Furthermore, all these three figures show that both MSDs and their slopes of all the ions decrease with increasing lithium salt concentration. We can also observe that, even though the cation is always the same, its MSD varies depending on the anion, a faster diffusion corresponds to mixtures in which $[NTf_2]^-$ is present and a slower dynamics to those with hexafluorophosphate. Moreover, $[NTf_2]^-$ anion diffuses faster than $[PF_6]^-$ and $[BF_4]^-$, both exhibing a similar dynamics (although faster for tetrafluoroborate), despite its greater size. Finally, the motion of lithium cation decreases in most of the studied concentrations following the trend [NTf_2]>[BF_4]>[PF_6].

In the linear representation of the MSDs, it seems that the dynamics reaches a diffusive regime after a few picoseconds, since then MSDs appear to have a linear dependence with time. However, the log-log plots of those figures, included as Supporting information, prove that the situation is somehow more complex, and we can observe three different time scale behaviours. These three different regimes can be characterized by means of the dependence of the MSD with time, which can be measured as

$$\langle \Delta|\vec{r}(t)|^2 \rangle \propto t^{\beta} \quad (2.17)$$

where β describes the type of motion of the molecules of the system. The slow dynamics at intermediate times of ILs is well known and, because of this

reason, it is of fundamental importance to ensure that the ions of the ILs have reached a diffusive behavior during the simulation in order to get the correct values of long-time magnitudes, since trajectories that appear to be in the linear diffusive regime are often still subdiffusive [189]. First, the behaviour of the ions at short times is ballistic, so that $\beta \simeq 2$. At the longest times, the molecules of the system exhibit linear diffusive motion after the molecules have experienced many collisions, and this Gaussian diffusion implies $\beta = 1$. Finally, at intermediate times a subdiffusive plateau, already reported for pure ILs, characteristic of glass formers in the supercooled region, is observed [128, 268]. For this non-Gaussian dynamics during the intermediate stage, related to long cage escaping time of the ions, $\beta < 1$. The log-log plots of the MSDs of lithium cations represented in graphics included in Supporting information show that the two transitions between the three regimes take place at similar times in all the studied systems.

To obtain a more detailed microscopic description of the single-particle dynamics of these systems, the translational diffusion coefficients can be analyzed, since this magnitude is particularly amenable for calculation with MD simulations. The self-diffusion coefficient of the ionic species i can be obtained from the long-time limit of the MSD by the well-known Einstein equation [60, 223]

$$D_i^{MSD} = \frac{1}{6} \lim_{t \to \infty} \frac{d}{dt} \langle [\vec{r}_i(t) - \vec{r}_i(0)]^2 \rangle \tag{2.18}$$

This equation is valid only at long simulation times, when the MSD shows a linear dependence with time and a truly diffusive regime is reached, since too short MD trajectories usually provide wrongly estimated self-diffusion coefficients [216]. Particularly, in this work, we made a least-square fit of the data between 1000 ps and 9000 ps in order to apply eq.2.18.

As a validation of the accuracy of the employed force field in what transport properties are concerned, an additional testing of the dynamical and transport properties of our model can be made by calculating the self-diffusion coefficients of pure ILs and contrasting them with available experimental and computational data. For this purpose, Table 2.5 shows the simulated self-diffusion coefficients of cation and anion in pure ILs obtained by using Einstein equation (2.18), including their respective uncertainties, directly provided by the Gromacs package.

As can be seen, the self-diffusion coefficients calculated from MSDs are in

Table 2.5 Self-diffusion coefficients (in 10^{-12} m^2/s) of cation and anion in pure ILs obtained by using Einstein equation (2.18).

IL	D_{cation}^{MSD}	D_{anion}^{MSD}
[BMIM][PF_6]	1.07 ± 0.49	0.310 ± 0.021
[BMIM][BF_4]	4.32 ± 0.63	1.82 ± 0.86
[BMIM][NTf_2]	5.86 ± 0.14	4.44 ± 0.91
IL	$D_{cation}^{MSD-exp}$	$D_{anion}^{MSD-exp}$
[BMIM][PF_6]	7 [26] / 8 [198] / 6.9 [269]	5 [26] / 5.2 [269]
[BMIM][BF_4]	15 [26] / 16 [198] / 14.5 [269]	15 [26] / 13.4 [269]
[BMIM][NTf_2]	25 [26] / 32 [198] / 27.5 [269]	20 [26] / 21.8 [269]

the order of 10^{-12} m^2/s, and they underestimate the experimental values reported in literature for pure ILs [26, 198] by a factor of 4-5, which could suggest that our simulations were not long enough to let the system reach the diffusive regime and the slope of the MSD (from where the self-diffusion coefficient is estimated) is still too low. Actually, Borodin *et al.* [256] indicated that $[Li]^+$ motion is still subdiffusive up to 33 ns at temperatures close to room temperature. However, we performed 40 ns–long simulations of pure [BMIM][PF_6] in order to check the influence of the simulation times and we noticed no significant effect on the self-diffusion coefficients of both ionic species. In view of the obtained results, we must point out that, although the structure of the mixtures is reasonably predicted, the single-particle dynamics seems to be quite slow. This could certainly be improved using a polarizable model, as it has been discussed by Borodin *et al.* in previous studies [269, 270].

Moreover, although cations and anions MSDs were found to exhibit similar behaviour for each IL, this route of calculation provided larger values for the cation than for the anion in all cases, despite their larger volumes and masses, an observation that shows that the diffusion of the ions is correlated, as it has been reported in previous studies [26–28, 266]. Furthermore, self-diffusion coefficients of both cation and anion were expected to follow the trend [NTf_2]>[BF_4]>[PF_6] [26], in agreement with our results.

The dependence on lithium salt molar percentage of the self-diffusion coefficients calculated from MSDs of $[BMIM]^+$, anions, and $[Li]^+$ are shown in Figure 2.40 in plots (a), (b), and (c), respectively. In addition, self-diffusion coefficients obtained from the slope of MSDs of imidazolium cation, hexafluorophosphate and sodium in systems with $NaPF_6$ doping [BMIM][PF_6] are included. In agreement with previous studies of mixtures of ILs with lithium

Figure 2.40 Concentration dependence of the self-diffusion coefficients of cation (a), anions (b), and lithium (c), calculated by using Einstein equation (2.18). Self-diffusion coefficients of imidazolium cation (a), hexafluorophosphate (b), and sodium (c) obtained from MSDs for [BMIM][PF_6] doped with $NaPF_6$ are also included with the aim of comparison.

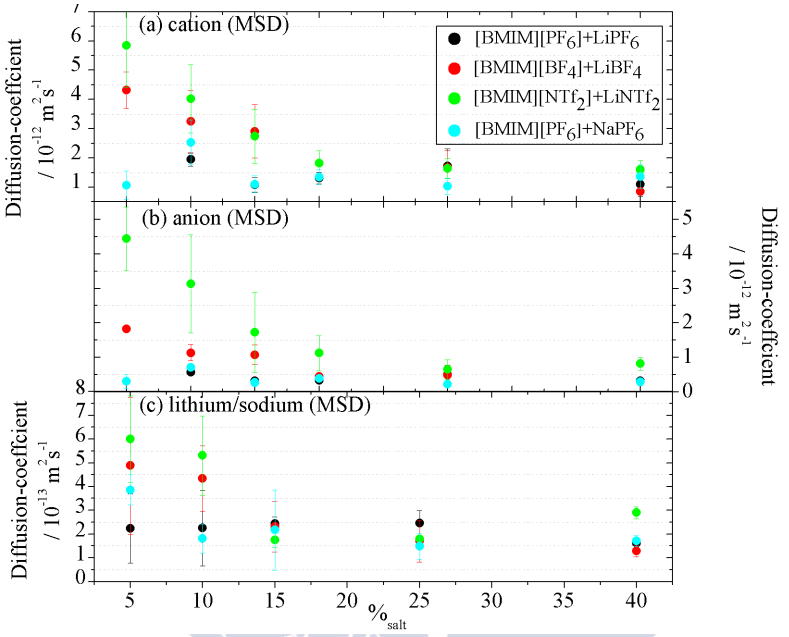

salts [238, 246, 252, 253, 255, 257], the motion of the ions is sensitive to the lithium salt concentration and, in binary systems, the increase in the amount of salt causes a slight decrease of the self-diffusion coefficients of all the ions, although in mixtures in which hexafluorophosphate anion is present, this trend is not as clear as in those mixtures with the other two anions. Moreover, it can be seen that the smallest ion, $[Li]^+$, is always the slowest species, with the imidazolium cation being the fastest and the anions occupying intermediate positions, as reported in the literature [252, 253, 255, 257]. This slower motion of the lightest ionic species was also found in mixtures of ILs with aluminium salts [271], and it was reported that their greater equivalent surface charge density reduces drastically the mobility of these ions and forces them to remain in almost fixed equilibrium positions. On the other hand, self-diffusion coefficients for lithium cation was found to be around one order of magnitude lower than expected, since, as for cations and anions, lithium coefficients are

also in the order of 10^{-11} – 10^{-12} m^2/s, but with lower coefficients [252, 253, 255]. It can be observed that self-diffusion coefficients of imidazolium cation, hexafluorophosphate, and sodium in the [BMIM][PF_6]/$NaPF_6$ systems are very close to those of the lithium salt mixtures at the same amount of salt, but slightly lower in the case of sodium ion, probably due to the effect of the different size of $[Na]^+$ cation. From the Stokes-Einstein equation

$$D_i = \frac{k_B T}{c\pi\eta r_i} \tag{2.19}$$

where T is the temperature of the mixture, c is a constant, η is the viscosity of the system, and r_i is the effective hydrodynamic radius of molecule i. From this relation, we could conclude that the greater the size of the ion, the slower it is. However, as we said for the self-diffusion coefficients obtained from the MSD curves, this is not the trend obtained in previous experimental studies. The existence of small clusters involving $[Li]^+$/$[Na]^+$ cations and anions is strongly suggested from our structural analysis, as it has also been observed in previous publications [239, 256, 257, 272]. Thus, we conclude that both lithium and sodium form kinetic entities with its surrounding anions, thus, reducing their mobilities. For example, Duluard *et al.* [253] estimated the diffussion coefficients of the free $[NTf_2]^-$ anions and of those involved in anionic $[Li(NTf_2)_2]^-$ clusters, and they also found that the value of the latter was similar to that of the lithium cation. The first solvation shell of the lithium/sodium ions is expected to be dynamically broken and formed [256, 257], with a transport mechanism in which lithium/sodium moves from one anion to another, but with a quite low hopping rate (of $[Li]^+$/$[Na]^+$ cation) and strong aggregation. Hence, our study of VACFs and MSDs suggests a picture in which lithium ions are moving inside the cages formed by their nearest neighbours suffering many collisions with the anions around them before reaching a subdiffusive motion, since the first collision of lithium cations takes place at much shorter times than that of the end of the ballistic region (around 0.017 ps and 1 ps, respectively). This is also confirmed by the strong correlation of the velocity of $[Li]^+$ cations with their initial velocity, as indicated by the long-lived oscillations showed in the VACFs, and in agreement with the effect of the mass ratio between the lighter lithium and the heavier anions in an elastic collision between them. This is not the behaviour found in mixtures with water [81] or alcohols [174], for which collision and ballistic times were very similar to each other. Water molecules seem to have a few collisions with other water mo-

lecules surrounding them before reaching the subdiffusive regime, whereas alcohol molecules have more similar masses to their coordinating anions so their VACFs do not show marked rattling motion regions. Once again, these deeds suggest the formation of stable kinetic aggregates induced by lithium cations.

To obtain additional insight of the dynamics of lithium and sodium cations and their coordinating anions, we analyzed the lifetime of these structures by calculating a cage autocorrelation function (CaACF) defined as [256, 257]

$$P(t) = \frac{\langle H_{ij}(t)H_{ij}(0)\rangle}{\langle H_{ij}(0)H_{ij}(0)\rangle} \tag{2.20}$$

where $H_{ij}(t)$ takes the value 1 if $[Li]^+/[Na]^+$ cations, i, and the center of mass of their surrounding anions, j, are closer than the position of the first minimum of the lithium/sodium-anion RDFs at time t, and zero, otherwise. The brackets $\langle\rangle$ indicate the average over all time origins. In Figure 2.41, the concentration dependence of CaACFs of the anionic clusters formed by lithium cations and anions in their first coordination shell is shown for mixtures of lithium salt with [BMIM][PF_6] (a), [BMIM][BF_4] (c), and [BMIM][NTf_2] (d). This figure also includes a comparison with CaACFs of the complexes present in [BMIM][PF_6] mixed with $NaPF_6$.

It can be observed that the decay of the CaACFs in mixtures with the lowest concentrations is slower than in those with the highest amount of salt, showing that the increasing of lithium salt in the mixture leads to the formation of less rigid structures, which is due to the fact that each lithium added to the mixture needs 2 − 3 coordinated anions. This tendency is compatible with the fact that the ionic mobility decreases with the amount of salt in the mixture, since a slower motion of the whole aggregate, which seems to be the entity that reaches the diffusive regime, does not imply a longer stability of that cluster. It can be also noted that the stability of the complexes in those mixtures of [BMIM][PF_6] with $LiPF_6$ is less sensitive to salt amount variations than in the rest of the systems, since the curves of CaCAFs are more similar to each other. The most remarkable aspect seen in Figure 2.41 is the strong memory effect and the very large association-dissociation characteristic times of $[Li(Anion)_n]^{n-1}$ aggregates, which is shown by the slight decay of all the CaACFs (after 10 ns none of the CaACFs decayed more than 5%). Borodin *et al.* [256] found a similar result for [MPPY][NTf_2] and [MMPY][NTf_2] doped with 0.25 molar fraction of $LiNTf_2$ at 303 − 333 K, but they attributed this res-

Figure 2.41 Concentration dependence of CaACFs of anions within the first solvation layer of lithium cations in mixtures with [BMIM][PF_6] (a), [BMIM][BF_4] (c), and [BMIM][NTf_2] (d). CaACFs of [PF_6]$^-$ anions coordinating sodium cations in mixtures of [BMIM][PF_6] with $NaPF_6$ are also included in (b) with the purpose of comparison.

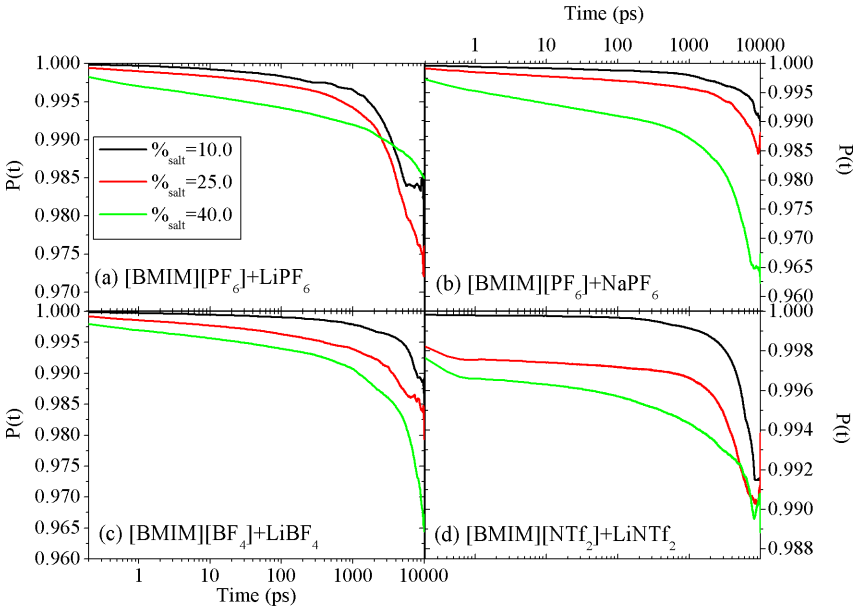

ult to the fact that their systems were not well-equilibrated. However, we must point out that we ensured the equilibration of our mixtures by performing two 50 ns long simulations, one in the NVE ensemble and the other one in the NpT ensemble, both also giving a decay of less than 5%. In addition, we further proved the resilience of these structures, verifying that the anions surrounding a given $[Li]^+$ in every time frame of the simulation run are always the same. Residence times of tens and even hundreds of nanoseconds of lithium ions inside the cages formed by their nearest neighbours were previously reported by Borodin *et al.* [273] in simulations of amorphous dilithium ethylene dicarbonate (Li_2EDC) and lithium methyl carbonate (LiMC) at temperatures from 393 to 600 K. On the other hand, the relatively fast decay of $P(t)$ found by Niu *et al.* [257] in [EMIM][PF_6] mixed with $LiPF_6$ can be due to the high temperature at which they performed the runs, 523.15 K, which is consistent with the results reported by Borodin *et al.* [256] at 393 K and shows the great effect of

the temperature on this magnitude. All previous comments can be referred to those mixtures of [BMIM][PF_6] with $NaPF_6$, since CaACF of systems with sodium salt do not show significative differences compared to the ones with lithium beyond a slightly slower decay.

From this analysis, we conclude that the first solvation shell of lithium/sodium cations is very stable, leading to the formation of strong and long-lived $[Li(Anion)_n]^{n-1}$ anionic clusters. Thus, even though, in our single-particle dynamics analysis, the results from MSDs and VACFs seemed to be somewhat contradictory, it has been shown that they lead to a picture in which $[Li]^+$ and $[Na]^+$ diffuse altogether with their surrounding anions as a stable kinetic entity; meanwhile, they suffer a rattling motion inside those clusters, in agreement with several previously reported experimental studies [238, 240, 252, 253].

Further information about the dynamics of the system can be obtained by studying another interesting magnitude, the current autocorrelation function (CACF), which can be calculated from NVE simulations as

$$J(t) = \frac{\langle \vec{j}(t) \cdot \vec{j}(0) \rangle}{\langle \vec{j}(0) \cdot \vec{j}(0) \rangle} \tag{2.21}$$

where the electrical current, $\vec{j}(t)$, is given by

$$\vec{j}(t) = \sum_{i=1}^{N} q_i \vec{v}_i(t) \tag{2.22}$$

and q_i represents the charge of ion i and $\vec{v}_i$ stands for the velocity of the center of mass of that ion. The CACF can be also defined as the sum of two contributions, the self and the cross-term [128, 274]

$$J(t) = C(t) + \Delta(t) \tag{2.23}$$

the self-term, $C(t)$, being the total VACF of the system and the cross-term, $\Delta(t)$, the deviation from the ideal Nernst-Einstein relation [61]

$$\sigma_{NE} = \frac{e^2}{V k_B T} \sum_{i=1}^{N} n_i D_i \tag{2.24}$$

where e is the electron charge, V is the volume of the system, T stands for the temperature, n_i represents the total number of ions of species i and D_i its self-diffusion coefficient. If the overall effect of cross-correlations was negligible, the normalized velocity and current autocorrelation functions would be

expected to coincide. This is the assumption made in eq. (2.24), and therefore, the decisive part missing in this relation are the cross-correlations of the single particle velocities, that is, $\langle \vec{v}_i(t) \cdot \vec{v}_j(t) \rangle$ (for $i \neq j$), of which a pair of ions with opposite charges would contribute to diffusion, but not to conductivity, leading to a significant decrease of this magnitude.

The evolution for a few molar percentages of lithium salts of the normalized total VACFs (red), the normalized CACFs (green) and the difference between them, $\Delta(t)$ (blue), are included in the Supporting information file (Figure 2.46), in order to analyze the relevance of cross-correlations in [BMIM][PF_6]/$LiPF_6$ (a)-(e)-(i), [BMIM][PF_6]/$NaPF_6$ (b)-(f)-(j), [BMIM][BF_4]/$LiBF_4$ (c)-(g)-(k); and [BMIM][NTf_2]/$LiNTf_2$ (d)-(h)-(l) mixtures. The importance of the correlations among ions can be clearly observed in the difference between the total VACFs and the CACFs registered, above all, at short times. The x-intercept and decay times for the CACFs are shorter than those of the VACFs, providing a negative value of the $\Delta(t)$ terms for all the studied molar percentages, which shows that neutral pairs of ions of opposite charge tend to diffuse together and do not contribute to charge transport [128, 274, 275]. In addition, in all the systems $\Delta(t)$ reaches positive values, which indicates that the correlation between ions with charges of the same sign can also have significant effects. In our case, both effects nearly cancel each other and cross-correlations can be considered as negligible, leading to a good agreement of the conductivity calculated by employing the Nernst-Einstein equation (2.24) and that obtained by means of Green-Kubo relation

$$\sigma_{GK} = \frac{1}{3k_B TV} \int_0^\infty \langle \vec{j}(t) \cdot \vec{j}(0) \rangle dt \tag{2.25}$$

In Table 2.6, we include the ionic conductivities obtained from Nernst-Einstein equation (2.24) using self-diffusion coefficients calculated by employing MSDs reported in Figure 2.40 for the three pure ILs and their mixtures with lithium salts. It must be noted that, due to the fact that $[Li]^+$ cations are coordinated with the same anions for very long times, each lithium can be considered as neutralized by one of the anions in its solvation shell, and because of this reason, we do not consider the contribution of these neutral pairs to the Nernst-Einstein relation in order to calculate the ionic conductivity. The results of the ionic conductivity for the pure systems are only slightly underestimated by a factor of 3 for pure [BMIM][BF_4] and [BMIM][NTf_2], since the expected values were about 3.5 mS/cm and 3.9 mS/cm, respect-

Table 2.6 Ionic conductivity (in *mS/cm*) of pure ILs ([BMIM][PF_6], [BMIM][BF_4], and [BMIM][NTf_2]) and their mixtures with lithium salts with a common anion obtained from Nernst-Einstein equation (2.24) using self-diffusion coefficients calculated by employing MSDs reported in Figure 2.40.

[BMIM][PF_6]	+	[$LiPF_6$]
$\%_{salt}$		σ_{NE}^{MSD}
0.0		0.242
5.0		0.197
10.0		0.114
15.0		0.112
25.0		0.162
40.0		0.206
[BMIM][BF_4]	+	[$LiBF_4$]
$\%_{salt}$		σ_{NE}^{MSD}
0.0		1.200
5.0		0.849
10.0		0.760
15.0		0.340
25.0		0.389
40.0		0.195
[BMIM][NTf_2]	+	[$LiNTf_2$]
$\%_{salt}$		σ_{NE}^{MSD}
0.0		1.372
5.0		0.933
10.0		0.567
15.0		0.363
25.0		0.207
40.0		0.177

ively [36, 276]. In the case of pure [BMIM][PF_6], the experimental conductivity is approximately 1.5 mS/cm, which leads to an underestimation of our simulated value by around a factor of 6 [36, 277]. These underestimations of the ionic conductivities are associated to the smaller values of the self-diffusion coefficients of MSDs, but the trend of the conductivity [BMIM][NTf_2]>[BMIM][BF_4]>[BMIM][PF_6] was obtained. On the other hand, it was found that the Nernst-Einstein ionic conductivity calculated by using self-diffusion coefficients from MSDs decreases with increasing the amount of salt added to mixtures, which was already reported in some previous studies [230, 252], and it is the expected trend for mixtures of ILs with lithium salts

with a common anion [248], since the increase in the viscosity with increasing salt concentration leads to a lower mobility of the carrier ions. However, the decrease obtained is not as pronounced as the one reported by Monteiro *et al.* [255], since they found an ionic conductivity of 0.06 mS/cm in mixtures of [BMIM][NTf_2] with a 40% of $LiNTf_2$ at room temperature. In addition, mixtures with lithium hexafluorophosphate show an unexpected increase in the conductivity at the higher amounts of salt related to the behaviour of the self-diffusion coefficients in these mixtures, for which we have not seen a clear decrease with increasing lithium salt concentration. These fluctuations of the electrical conductivity could be associated to concentration fluctuations in a metastable supersaturated phase, but this possibility demands further analysis.

2.4.5. Conclusions

We performed MD simulations of three imidazolium-based ILs, [BMIM][PF_6], [BMIM][BF_4], and [BMIM][NTf_2], mixed with lithium salts with a common anion, and we investigated several structural and dynamical properties of the systems at $T = 298.15$ K and $P = 1$ atm. We also included mixtures of [BMIM][PF_6] with $NaPF_6$ with the purpose of comparison, in order to observe the effect of the size of the monoatomic cation in the analyzed properties. Particularly, lithium/sodium solvation and ionic mobilities were studied via the analysis of radial distribution functions, coordination numbers, mean square displacements, cage autocorrelation functions, self-diffusion coefficients of all the ionic species, velocity and current autocorrelation functions, and ionic conductivity in all the ionic liquid/salt systems.

With the aim of checking the accuracy of the employed force field, we calculated the densities of the three pure ILs and compared them to experimental data. Our simulated densities shown a maximum deviation from available experimental values of 4.6%. Additionally, the densities of the mixtures were found to decrease with increasing lithium salt concentration, in good agreement with the experimental results available in the literature.

The analysis of the RDFs of the mixtures showed that lithium/sodium cations are surrounded by a first solvation layer of anions (with which they have stronger correlations), followed by a second shell of lithium/sodium molecules and a third layer of imidazolium cations. In the three systems, the first solvation layer of $[Li]^+/[Na]^+$ is occupied by anions in two different

possible conformations that are sensitive to the amount of salt present in the mixture, as shown by the presence and the evolution of the two sharp peaks in the lithium/sodium-anion RDFs. The study of the coordination numbers provided a central $[Li]^+$ cation surrounded by about 3, 3.3 and 2 anions for mixtures with hexafluorophosphate, tetrafluoroborate and bis(trifluoromethylsulfonyl)imide, respectively, this value being slightly increased for increasing lithium salt concentration. Moreover, the $[Na]^+$ cation was found to have nearly three hexafluorophosphates around it. All these facts suggest the formation of $[Li/Na(Anion)_n]^{n-1}$ stable kinetic entities, which was further confirmed by means of the analysis of lithium and sodium single-particle dynamics.

VACFs of lithium and sodium cations were also reported, and they revealed an oscillatory behaviour up to around 1.5 ps and 0.8 ps, respectively, indicating a remarkable rattling motion of lithium and sodium ions in the "cage" of their nearest neighbors. This rattling motion was more markedly observed for mixtures with tetrafluoroborate anions, and an enhancement of the caging effect with decreasing salt concentration can also be seen is this system. In addition, the analysis of the salt cation CaCAF proved this structure to be extraordinary resilient, since it was seen to survive during tens of nanoseconds, providing a further confirmation of the occurrence and stability of $[Li/Na(Anion)_n]^{n-1}$ clusters in the bulk mixture that can be considered to act as real kinetic entities. On the other hand, the self-diffusion coefficients were calculated from the Einstein relation, predicting a decrease of the mobility of all the ionic species with increasing salt concentration, in agreement with previously reported experimental results and as a possible consecuence of the formation of the clusters. However, although the self-diffusion coefficients obtained from the slope of MSDs provided a trend of the ionic motion of $[BMIM]^+ > [anion]^- > [Li]^+$, they were slightly underestimated for our analyzed simulation times. The analysis of CACFs and cross-correlations showed that effects of correlations between ions with charges of the same and opposite sign cancel each other, causing a negligible contribution of cross-correlations to the Nernst-Einstein equation. Thus, the ionic conductivity at room temperature was reported for lithium/sodium salts mixed with imidazolium-based ILs for the first time up to our knowledge, using the Nernst-Einstein relation combined with the self-diffusion coefficients from the slope of the MSDs. This method provided slightly underestimated values of the ionic conductivity, and it showed that this magnitude decreases with increasing lithium salt concen-

Figure 2.42 Salt molar percentage dependence of lithium-cation RDFs for mixtures of lithium salts with (a) [BMIM][PF_6], (c) [BMIM][BF_4] and (d) [BMIM][NTf_2] at 298.15 K and 1 atm. Sodium-cation RDFs for [BMIM][PF_6] mixed with $NaPF_6$ are also included in (b) with the purpose of comparison.

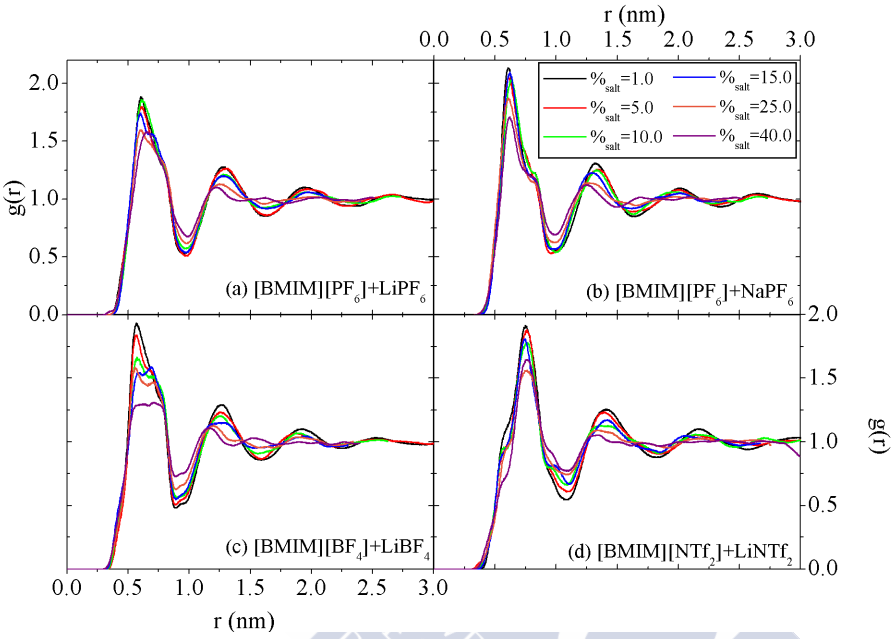

trations, in accordance to experimental observations and in line with the experimental fact that an increase in viscosity slows down the ionic mobility of the components of the mixture.

In summary, all the presently reported structural and dynamic evidences can only be understood if long-lived, stable $[Li/Na(Anion)_n]^{n-1}$ clusters are formed in the bulk solution, in which the salt cation is diffusing in a bonded-like state with the anions of its first coordination shell giving rise to stable kinetic entities whose lifetimes spans over tens of nanoseconds.

2.4.6. Supporting Information

Figures equivalent to Figure 2.35, for cation-lithium and lithium-lithium RDFs, time dependence of the MSDs and their log-log plot, and total velocity and current autocorrelation functions and the cross-terms.

Figure 2.43 Salt molar percentage dependence of lithium-lithium RDFs for mixtures of lithium salts with (a) [BMIM][PF_6], (c) [BMIM][BF_4] and (d) [BMIM][NTf_2] at 298.15 K and 1 atm. Sodium-sodium RDFs for [BMIM][PF_6] mixed with $NaPF_6$ are also included in (b) with the purpose of comparison.

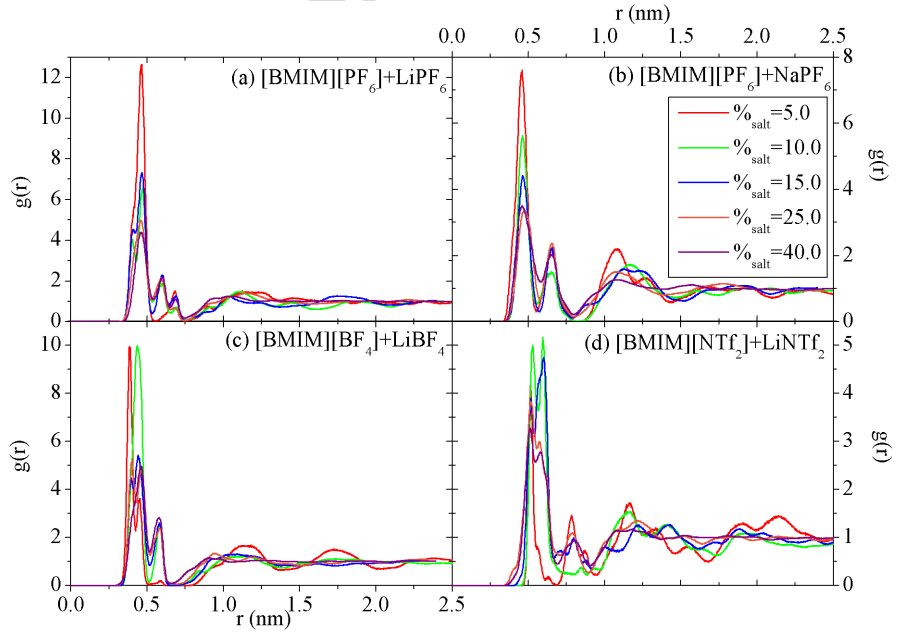

Figure 2.44 Time dependence of the MSDs of (a)-(b)-(c) imidazolium cation, (d)-(e)-(f) anion and (g)-(h)-(i) lithium in mixtures of [BMIM][PF_6] with $LiPF_6$, [BMIM][BF_4] with $LiBF_4$ and [BMIM][NTf_2] with $LiNTf_2$ for all the studied concentrations.

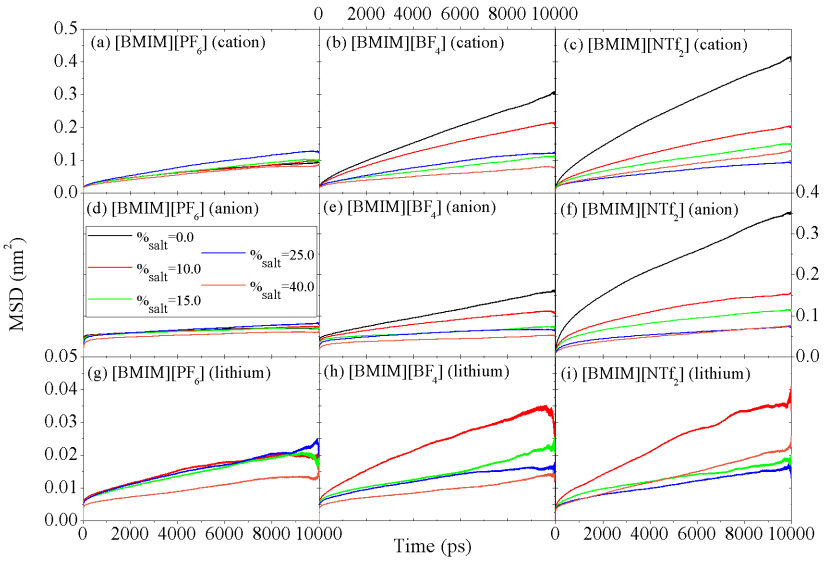

Figure 2.45 Log-log plots of the MSDs.

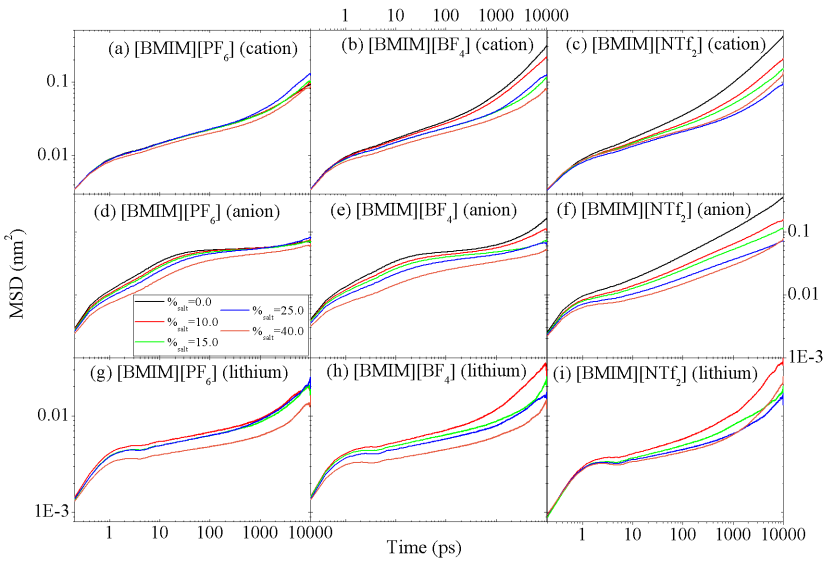

Figure 2.46 Concentration dependence of the total VACFs (red), CACFs (green) and the cross-terms, $\Delta(t)$ (blue), for [BMIM][PF_6] (a)-(e)-(i), [BMIM][BF_4] (c)-(g)-(k) and [BMIM][NTf_2] (d)-(h)-(l) mixed with lithium salt and [BMIM][PF_6] (b)-(f)-(j) mixed with sodium salt, at 298.15 K and 1 atm.

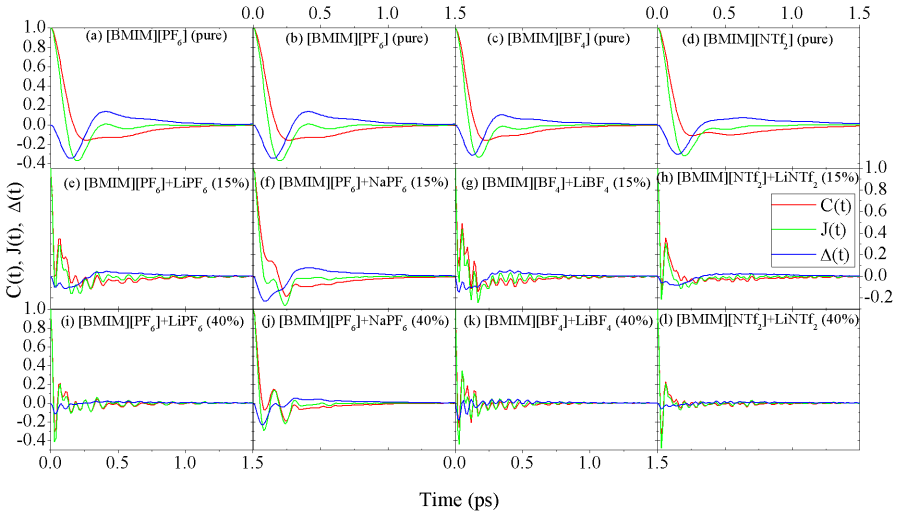

2.5. Solvation of Lithium Salts in Protic Ionic Liquids: A Molecular Dynamics Study.

In order to expand the studies carried out in 2.4 and explore solvation of lithium salts in PILs in order to use them as electrolytes in lithium batteries, we performed the first computational work in which the solvation mechanisms of ions of electrochemical interest in bulk mixtures with PILs are analyzed.

In this work we employed MD simulations to investigate the structural features of solutions of lithium nitrate in the PIL *par excellence*, EAN [278]. The obtained results of density, radial distribution functions, hydrogen bonds, spatial distribution functions and coordination numbers revealed a similar behaviour to that found in 2.4. The well-known formation of polar and apolar domains in bulk is slightly disrupted by the addition of the lithium salt, the result being the dispersion of lithium cations in the polar nanoregions of the mixture, with the consequent transference of $[NO_3]^-$ anions to the inner regions of these polar nanodomains due to the strong interaction between lithium cations and nitrate anions. The polar areas of the mixture show some kind of pseudolattice structure in which anions and $[Li]^+$ cations form solid-like structures until saturation.

2.5.1. Paper V: Solvation of Lithium Salts in Protic Ionic Liquids: A Molecular Dynamics Study; *J. Phys. Chem. B 118 (2014) 761-770.*

Trinidad Méndez-Morales,[1] Jesús Carrete,[1,2] Óscar Cabeza,[3] Olga Russina,[4] Alessandro Triolo,[5] Luis J. Gallego[1] and Luis M. Varela[1]

The structure of solutions of lithium nitrate in a protic ionic liquid with a common anion, ethylammonium nitrate, at room temperature is investigated by means of molecular dynamics simulations. Several structural properties, such as density, radial distribution functions, hydrogen bonds, spatial distribution functions and coordination numbers, are analyzed in order to get a picture of the solvation of lithium cations in this hydrogen-bonded, amphiphilically nanostructured environment. The results reveal that the ionic liquid mainly retains its structure upon salt addition, the interaction between the ammonium group of the cation and the nitrate anion being only slightly perturbed by the addition of the salt. Lithium cations are solvated by embedding them in the polar nanodomains of the solution formed by the anions, where they coordinate with the latter in a solid-like fashion reminiscent of a pseudolattice structure. Furthermore, it is shown that the average coordination number of $[Li]^+$ with the anions is 4, nitrate coordinating $[Li]^+$ in both monodentate and bidentate ways, and that in the second coordination layer both ethylammonium cations and other lithiums are also found. Additionally, the rattling motion of lithium ions inside the cages formed by their neighbouring anions, indicative of the so-called caging effect, is confirmed by the analysis of the $[Li]^+$ velocity autocorrelation functions. The overall picture indicates that the solvation of $[Li]^+$ cations in this amphiphilically nanostructured environment takes place by means of a sort of inhomogeneous nanostructural solvation, which we could refer to as nanostructured solvation, and which could be a universal solvation mechanism in ionic liquids.

[1]*Grupo de Nanomateriais e Materia Branda, Departamento de Física da Materia Condensada, Universidade de Santiago de Compostela, Campus Vida s/n E-15782, Santiago de Compostela, Spain*

[2]*LITEN, CEA-Grenoble, 17 Rue des Martyrs, BP166, F-38054, Grenoble, Cedex 9, France*

[3]*Facultade de Ciencias, Universidade da Coruña, Campus A Zapateira s/n E-15008, A Coruña, Spain*

[4]*Dipartimento di Chimica, Università di Roma, 'La Sapienza', P. le Aldo Moro 5, I-00185 Roma, Italy*

[5]*Istituto di Struttura della Materia, Consiglio Nazionale delle Ricerche, Area della Ricerca di Tor Vergata, Via del Fosso del Cavaliere 100, I-00133 Roma, Italy*

2.5.2. Introduction

Ionic liquids (ILs) are a new class of low-melting-point solvents consisting entirely of ions that have been extensively studied in recent years for both fundamental and technological reasons. This increasing research interest is mainly due to their "tunable" properties such as negligible vapour pressure, wide temperature stability range, good conductivity or low viscosity [36, 42, 279], that contribute to their reputation as "green solvents" and make them very attractive candidates for many applications [3, 84, 133, 135, 185, 236].

An interesting subset of ILs are protic ionic liquids (PILs), which are formed through proton transfer from a Brønsted acid to a Brønsted base [280–282]. The proton transfer gives rise to the presence of proton-donor and proton-acceptor sites and leads to the formation of a hydrogen-bond network in bulk PILs that mimics the three-dimensional hydrogen bond network of water [51, 183]. These key features confer PILs a unique set of properties (such as higher conductivities and fluidities) that distinguish them from aprotic ionic liquids (AILs) and provide them with a huge potential in electrochemical applications such as electrolytes for fuel cells, solar cells or double-layer capacitors [272, 283–286]. In addition, PILs have been identified as being able to act as self-assembly media and a help in the analysis of these aggregation processes [52, 287–292].

This kind of systems is known since 1914, when ethylammonium nitrate (EAN) was described by Walden as an IL with a melting point of 287.6 K [1], thus becoming not only the earliest discovered IL but also the PIL on which most research has been has focused up to now. However, even though the importance of PILs has increased and several experimental [41, 50, 280, 282, 290, 291, 293–297] and, to a much lesser extent, computational [292, 298–304] studies concerning their properties and behavior have been reported over the last few years, PILs have not received as much attention as AILs. In particular, the field of ILs in lithium-battery research has been completely focused on the use of AILs as an alternative to conventional electrolytes (see Ref.[228] and the references cited therein), and to our knowledge, the only study on the possible use of PILs as electrolytes in lithium batteries has very recently been reported by Menne *et al.* [305]. In their work, the conductivity and the electrochemical stability of a solution containing triethylammonium bis(tetrafluoromethylsulfonyl)amide ($Et_3NHTFSI$) and a lithium salt with a common anion, LiTFSI, were investigated, concluding that it is possible to successfully

design lithium batteries that show capabilities comparable to those of AILs-based devices by using PILs-based electrolytes.

Taking into account the fact that, while keeping the same beneficial aspects, the cost and difficulty of synthesizing PILs are usually lower than that of AILs, the introduction of PILs as electrolytes in lithium batteries would be a good option in terms of safety, manufacturing cost, and performance. Hence, it is of fundamental importance to further understand the structure of these PILs at the molecular level, which crucially determines the solvation mechanisms of ions of electrochemical interest in order to improve their performance in this kind of applications. As far as we know, contrary to what happens for their aprotic counterparts [81, 228] there is a virtually complete lack of reported results about solvation of molecular or ionic species in PILs, an essential step for almost any successful application. In this regard, computational simulations are crucial in order to overcome the limitations of experimental research and get a complete molecular-level description of dynamical and structural properties of PILs and their solutions with salts.

With the aim of providing some insight into the structure of PILs and their solutions with salts, specifically into the solvation mechanisms of lithium in these systems, in this contribution, we carried out a series of room temperature molecular dynamics (MD) simulations of solutions in the most studied PIL, EAN, of a lithium salt with common anion, lithium nitrate, $LiNO_3$. Our results give information about the salt concentration dependence of several properties of the system such as density, radial distribution functions, coordination numbers, spatial distribution functions, hydrogen bonds, and velocity autocorrelation functions, in order to shed some light on the peculiarities of the solvation mechanism of lithium in salt-doped amphiphilically nanostructured PILs, specifically on the effect of added lithium cations on the well-known dense hydrogen-bonded network of the PIL.

The structure of the rest of the paper is as follows. The essential technical details of the computational method used in this paper are described in Sec.2.5.3, where we also give information on the preliminary experimental measurements we performed on the systems investigated. Our results are presented and discussed in Sec.2.5.4, and in Sec.2.5.5, we summarize our main conclusions.

2.5.3. Experimental and computational details

2.5.3.1. Density measurements

EAN was purchased from IOLITEC with purity degree of > 97%, and it was used as received. $LiNO_3$ (> 99%) was a Merck product and it was used as received. Density was continuously and automatically measured at 298.15 K using a DSA 5000 Anton Paar density and sound velocity analyzer. This apparatus is equipped with a latest-generation vibrating tube for density measurements with a resolution of $\pm 10^{-6}$ g cm^{-3}. Temperature was controlled to within $\pm 10^{-3}$ K by means of a Peltier module. The density meter was calibrated with dry air and distilled water at known pressure and temperature.

2.5.3.2. Simulation details

MD simulations of pure EAN and its solutions with $LiNO_3$ at $T = 298.15$ K and $P = 1$ atm were carried out using the Gromacs 4.5.4 package [70]. With regard to the parametrization of the ions, the OPLS-AA force field, which is an all-atom version of the OPLS force field that models every hydrogen atom bonded to carbon explicitly, was used [153]. Intramolecular interactions such as bond stretching, angle bending, dihedral torsion, as well as van der Waals and Coulomb interactions, are described by the functional form

$$\begin{aligned} E = & \sum_i K_{b,i}\left[r_i - r_{0,i}\right]^2 + \sum_i K_{b,i}\left[\theta_i - \theta_{0,i}\right]^2 + \\ & + \sum_i \left[\frac{1}{2}V_{1,i}(1+\cos(\varphi_i)) + \frac{1}{2}V_{2,i}(1+\cos(2\varphi_i)) + \right. \\ & \left. + \frac{1}{2}V_{3,i}(1+\cos(3\varphi_i)) + \frac{1}{2}V_{4,i}(1+\cos(4\varphi_i))\right] + \\ & + \sum_i \sum_{j<i} \left\{ \frac{1}{4\pi\varepsilon_0}\frac{q_i q_j e^2}{r_{ij}} + 4\varepsilon_{ij}\left[\left(\frac{\sigma_{ij}}{r_{ij}}\right)^{12} - \left(\frac{\sigma_{ij}}{r_{ij}}\right)^{6}\right]\right\} \end{aligned} \tag{2.26}$$

The parameters employed in eq. (2.26) are the force constants K, the nominal values r_0 and θ_0, the Fourier coefficients V, and the partial atomic charges q fixed on each atom center. σ_{ij} and ε_{ij} represent the Lennard-Jones (LJ) radii and potential well depths, respectively, which are obtained from parameters for each type of atom by using the geometric combination rules $\epsilon_{ij} = \sqrt{\epsilon_{ii}\epsilon_{jj}}$ and $\sigma_{ij} = \sqrt{\sigma_{ii}\sigma_{jj}}$. The ethylammonium cation was modelled by using the LJ

parameters previously reported by Umebayashi *et al.* [301], while its partial charges were evaluated by Choe *et al.* [306] using the 6-31G** method. Lithium cations were modelled as single sites of charge +1, and their LJ parameters were directly taken from Gromacs database. On the other hand, each nitrate anion was parameterized as a set of seven sites, three of them heavy and the other four virtual. A heavy site carries no charge, but is associated with 1/3 of the total mass of the ion and placed so as to yield the right tensor of inertia. In contrast, virtual sites are massless but have partial charges of $q_N = +0.794$ for the nitrogen atom and $q_O = -0.598$ for the oxygen atoms [154], whose LJ parameters are, respectively, $\sigma_N = 3.496 \cdot 10^{-1}$ nm, $\varepsilon_N = 7.1128 \cdot 10^{-1}$ kJ/mol, $\sigma_O = 3.175 \cdot 10^{-1}$ nm, and $\varepsilon_O = 8.7864 \cdot 10^{-1}$ kJ/mol; and were fitted in order to reproduce the experimental density of the pure IL. Long-range electrostatic interactions were treated by using the particle-mesh Ewald (PME) [77] method with a grid spacing of 12 nm, the typical cutoff of 1.1 nm and cubic interpolation. A cut-off distance of 1.1 nm was used for LJ interactions, and a neighbour searching was made up to this same distance from the central ion and was updated every five simulation steps. The linear constraint solver (LINCS) algorithm [159, 160] with a fourth-order expansion of the constraint coupling matrix was used to hold the bonds rigid, and long-range dispersion corrections were used for both energy and pressure.

The salt molar percentages simulated covered the whole range of concentrations up to saturation and some metastable concentrations above this point, and they were $\%_{salt}$={0, 5, 10, 15, 20 and 25}, since our experiments revealed that the solubility limit for $LiNO_3$ in EAN is $\%_{salt} = 18.5$ (2.1 mol $\cdot$ kg^{-1}). The initial configurations for $\%_{salt} = 5$ and 10 were obtained by randomly inserting, respectively, 1000 and 450 ionic pairs of IL in a cubic box in order to have enough salt to yield statistically significant trajectories, whereas for the rest of the molar percentages we considered 300 ionic pairs. The number of lithium salt molecules was calculated for each situation by considering each ionic pair as a single unit in the calculation of mole fractions.

Initial configurations were relaxed for 10^6 steps using a conjugate-gradient algorithm in order to remove bad contacts resulting from the initial random configuration of ions. The maximum step size and the tolerance were set to 0.01 nm and 0.1 kJ/nm $\cdot$ mol, respectively. For each molar percentage of salt, the system was equilibrated for 20 ns in the isothermal-isobaric (NpT) ensemble applying periodic boundary conditions. Then, the results of an additional 10 ns long simulation in the isothermal-isobaric ensemble were used for

the analysis of the structure of the solutions. The time step of the simulations was 2 fs. The temperature was controlled by using the V-rescale thermostat [161]. Cations and anions were separated in two (or three) baths with temperature coupling constants of 0.1 ps. Pressure control was effected by using the Parrinello-Rahman barostat [162] with a reference pressure of 1 atm, an isothermal compressibility of $4.5 \cdot 10^{-5}$ bar^{-1}, and a relaxation time of 0.1 ps.

Each of these simulations provided us a sequence of configurations, *i.e.*, positions and instantaneous velocities of all atoms of the solutions, which was analyzed to obtain information about the aforementioned systems.

2.5.4. Results and discussion

Because of the reliability of its experimental determination, density is usually considered as one of the most suitable properties to analyze the validity of the force field employed in a MD simulation. A direct comparison between computational and experimental results allows the accuracy of the MD simulations to represent the behaviour of a given system to be estimated. To perform such a test, the concentration dependence of the density of $LiNO_3$ solutions in EAN was measured, and the results are shown in Figure 2.47 together with the MD simulations results. It can be seen there that, adjusting the parameters of the force field, the predicted density for the pure IL (1206.2 kg/m^3) shows excellent agreement (less than 0.003% of deviation) with the experimental result (1206.235 kg/m^3), and the value for EAN+$LiNO_3$ does not exceed 1.5% (for the highest percentages). These results allow us to be reasonably confident in the accuracy of our force field to reproduce the structural properties and the solvation mechanism of ions in this PIL. Certainly, the usage of polarizable force fields would lead to improved predictions of thermodynamic properties [307] and they are essential for calculating transport coefficients. However, non-polarizable force fields are conventionally used for analyzing equilibrium structure predictions [39, 93], an option that we follow in this paper. We can also observe a linear increase in the density with increasing salt concentration in the system, a behavior previously reported for the density of lithium salt solutions in AILs [228].

On the other hand, it is well-known that EAN develops a strong network of hydrogen bonds that gives rise to solvophobic effects increasing the van der Waals attractions. The latter, together with the electrostatic interactions, lead to the formation of nanoscopic polar (of nitrate anion and ammonium group)

Figure 2.47 Simulated (black) and experimental (red) densities at $T = 298.15$ K of EAN mixed with a lithium salt with the same anion as a function of the lithium salt concentration.

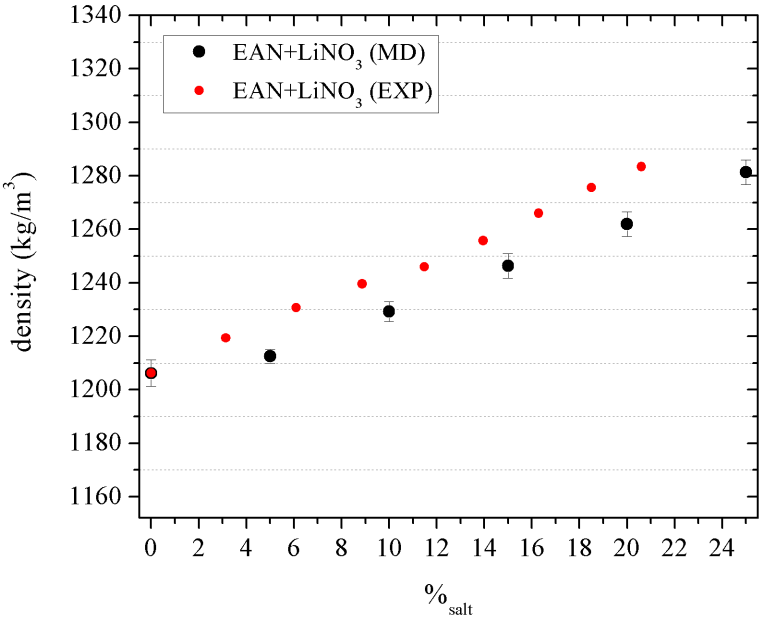

and apolar domains (of methylene and methyl groups) in the bulk that have a great impact in the properties of the liquid. Surely, as in aqueous environment (see, e.g., Marcus' excellent review about the influence of ions in water structure and the role of hydrogen bond in the hydration of ions [308]), this feature also has a significant influence on the solvation process of ions when a salt is added to the PIL. In order to gain further insight into the accommodation of $[Li]^+$ in the two networks, it is interesting to obtain radial distribution function (RDF)

$$g(r) = \frac{1}{\rho N}\langle \sum_{ij} \delta(r - r_{ij})\rangle \tag{2.27}$$

where N is the number of particles in the system, ρ stands for its number density, i and j run over all the particles, and brackets indicate the ensemble average. It must be noted that, in the RDFs that involve the ethylammonium cation, only the four atoms in the ammonium or methyl groups

Figure 2.48 Concentration dependence of anion-ammonium group (a), anion-methyl group (b), and hydrogen-oxygen (of ammonium group and nitrate, respectively) (c) RDFs for $LiNO_3$ solutions in EAN at $T = 298.15$ K and $p = 1$ atm. RDFs involving anions and cations were calculated using the center of mass of the nitrate and that of the ammonium/methyl groups, respectively, whereas the RDF regarding hydrogen-oxygen was computed by averaging the atomic RDFs.

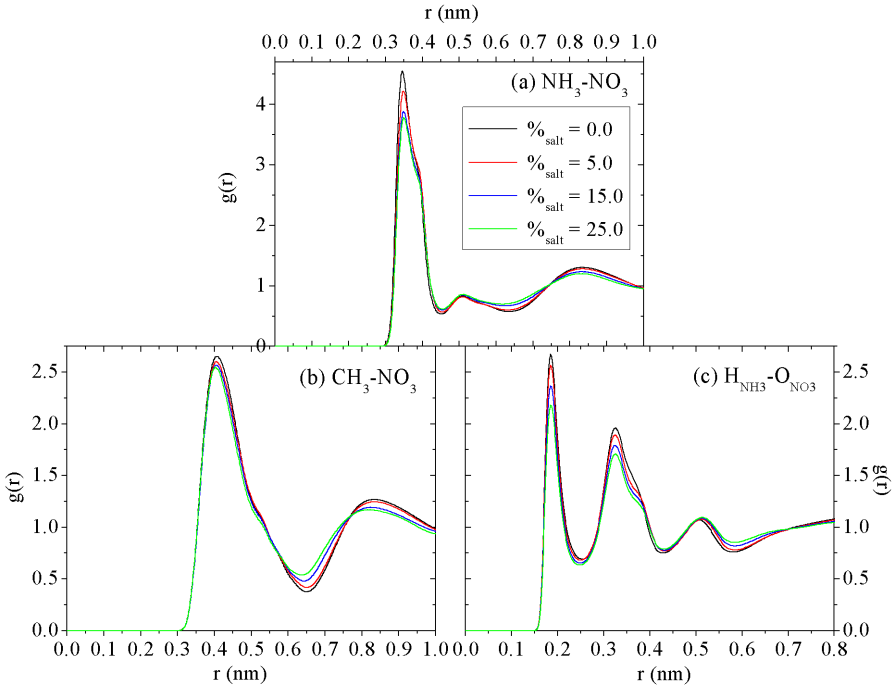

were considered in the calculations, and all RDFs presented in this paper were calculated using the center of mass of the molecules, except that of hydrogen-oxygen (of ammonium group and nitrate, respectively), for which an average of the atomic RDFs was calculated.

The evolution of several RDFs with the addition of lithium salt to the system is shown in Figure 2.48, in which we can see anion-ammonium group (a), anion-methyl group (b), and hydrogen-oxygen (of ammonium group and nitrate, respectively) (c) RDFs. The most salient feature of this figure is the notable resilience of the structure of EAN to salt addition. Only the heights of the peaks are slightly changed as concentration increases, and no relative shift of their positions is detected. This seems to indicate that no significant

effect is exerted by the salt cations in the structure of the liquid beyond some gradual transference of $[NO_3]^-$ to the interior of the polar regions from the $[NH_3]^+$ neighbourhood. This effect could be even smaller than in aqueous environments, where the influence of the ions in water structure beyond the first hydration shell is still an open question [308, 309]. Moreover, Figure 2.48.a provides us with information about the behaviour of the polar network, since the peak intensity gives us an idea of the number of molecules surrounding a given species. In this case, we can observe that the first peak is placed at around 0.35 nm, whereas that of the anion-methyl group RDF (Figure 2.48.b) is located at 0.41 nm. In addition, this first peak shown in Figure 2.48.a is almost twice the height of the one in Figure 2.48.b, which indicates that, as expected, the $[NH_3]^+$ tends to approach the $[NO_3]^-$ at closer distances and with a stronger coordination than the methyl group of the tail. It can also be seen that, in both cases, the height of the peaks decreases as we add lithium salt to the mixture. This effect is more clear in the $[NH_3]^+$-$[NO_3]^-$ RDFs, which can be indicative of the lithium placing itself in the polar areas of the bulk and destroying gradually the network of hydrogen bonds as it induces the transference of $[NO_3]^-$ to the inner regions of the polar nanodomains upon solvation. This is indicative that $[Li]^+$ has a similar effect in the hydrogen-bonded network of the solvent as in aqueous environment, a behaviour that will be further discussed below in the analysis of the RDFs involving lithium ion and that of the evolution of hydrogen bonds with the addition of salt. Moreover, in Figure 2.48.c, the first maximum reveals that the distance between the hydrogens of the ammonium group of the cation and the oxygens of the nitrate anion (both groups taking part in the formation of the hydrogen bonds) is around 0.18 nm, which is similar to the ones reported by Bodo *et al.* [299] both from their quantum structures and from a 2 ns classical dynamics simulation (between 0.17 nm and 0.19 nm), and by Zahn *et al.* [302] (0.18 nm) in a similar system, but considerably different from the values reported in Refs.[292], [304] and [310] (between 0.24 nm and 0.26 nm).

It is also worth discussing the concentration dependence of the RDFs involving $[Li]^+$, which are shown in Figure 2.49 for lithium-anion (a), lithium-ammonium group (b), and lithium-lithium (c) correlations. This figure suggests a much stronger coordination of lithiums with the $[NO_3]^-$ than with the other two species, not only indicated by the height of the first peaks, but also due to the fact that anions are placed at shorter distances from a central lithium. In this sense, it is worth mentioning that our MD simulations

Figure 2.49 Concentration dependence of lithium-anion (a), lithium-ammonium group (b), and lithium-lithium (c) RDFs for EAN mixed with $LiNO_3$ at T = 298.15 K and p = 1 atm. RDFs involving anions and cations were calculated using the center of mass of the nitrate and that of the ammonium group, respectively.

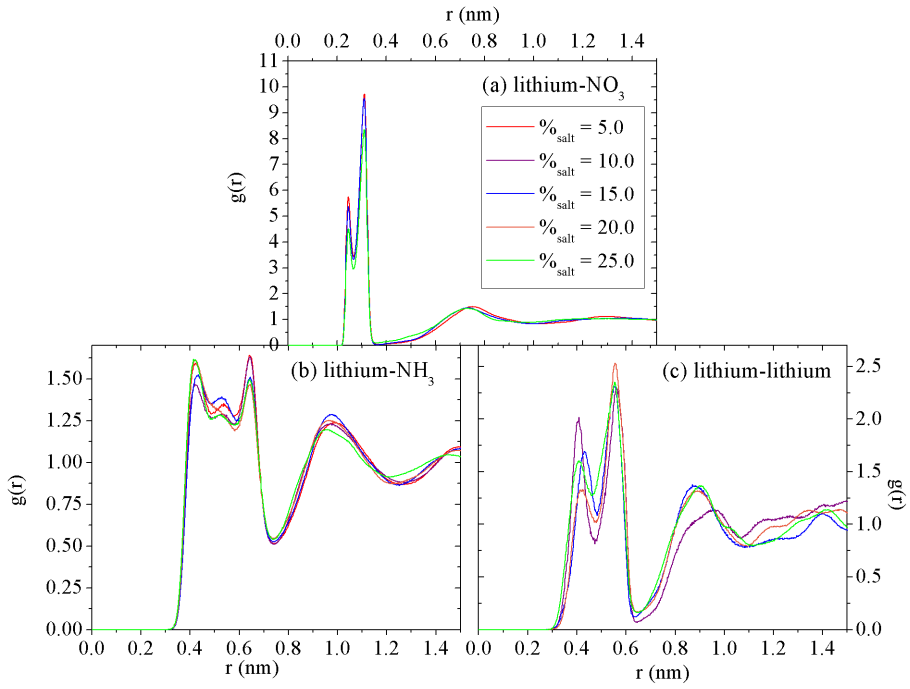

provide a density of lithium cations around nitrates in the polar regions of about 4.34 $[Li]^+/nm^3$, while that in the IL neighbourhood of the cation alkyl groups is only 0.36 $[Li]^+/nm^3$, an order of magnitude lower, proving that an overwhelming majority of $[Li]^+$ is placed in the polar domains of the IL, in agreement with some very recently reported results for AILs [311]. Figure 2.49.a also exhibits a double peak within what we can consider the first solvation shell. The first peak is placed at around 0.24 nm, and it is always lower than the second one, which is located at 0.31 nm, approximately. This is indicative of the lithium ion having two different conformations around the nitrate anion (corresponding to nitrate coordinating lithium cations in monodentate or bidentate ways, as it will be confirmed below by the analysis of the spatial distribution functions), and the one at longer distances being relatively more

Figure 2.50 Snapshots of the simulation box of a solution of $LiNO_3$ in EAN at a concentration of 25% of lithium salt at $T = 298.15$ K and $p = 1$ atm. The snapshots of the whole system (a), nitrate anions and ammonium groups of the cation (red) with lithiums (blue) (b) and apolar region of the ethylammonium cation (green) with lithiums (blue) (c) are presented. The relative size of lithium cations has been increased for the purpose of clarity.

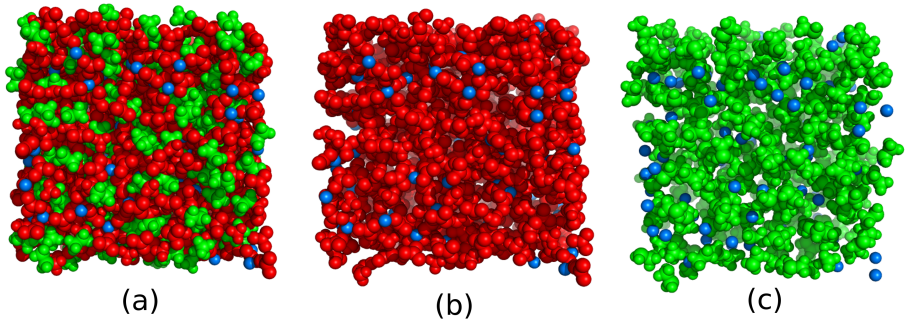

abundant at all the analyzed solution concentrations. In addition, the evolution of these two peaks shows a clear decrease as we increase the amount of salt in the system. It can also be noted that the distributions reported in Figure 2.49 somehow remind that of the calcite-type structure characteristic of a crystal of lithium nitrate [312, 313], and not that of molten lithium nitrate, since the latter does not exhibit the double peak in the lithium-anion RDF [314]. It is also noteworthy that in Figure 2.49.c we observe the existence of a somewhat inhomogeneous distribution of lithium inside the polar domains, showing (i) a low-r region where $[Li]^+$ is notably structured, followed by (ii) a (pseudo)exclusion zone where (almost) no $[Li]^+$ is found, and (iii) the virtual absence of long-ranged order (essentially random oscillations around 1 at long distances). This same $[Li]^+$ organization was previously reported in solutions of lithium salts in AILs [228].

Thus, the study of the RDFs reveals that $[NO_3]^-$ interacts more significantly with the ammonium group than with the methyl group of the ethylammonium cation, whereas $[Li]^+$ is surrounded by a first solvation layer of nitrate anions in two possible conformations, followed by a second layer composed of both lithium and ethylammonium cations (but with the lithiums always placed slightly closer to the central $[Li]^+$ than to the IL cations). These features support the image of $[Li]^+$ embedded in the polar nanodomains made up by the anions in a solid-like pseudolattice structure [118], avoiding contacts with the

Figure 2.51 Concentration dependence of the average number of ethylammonium-nitrate hydrogen bonds per molecule for solutions of $LiNO_3$ in EAN (see text).

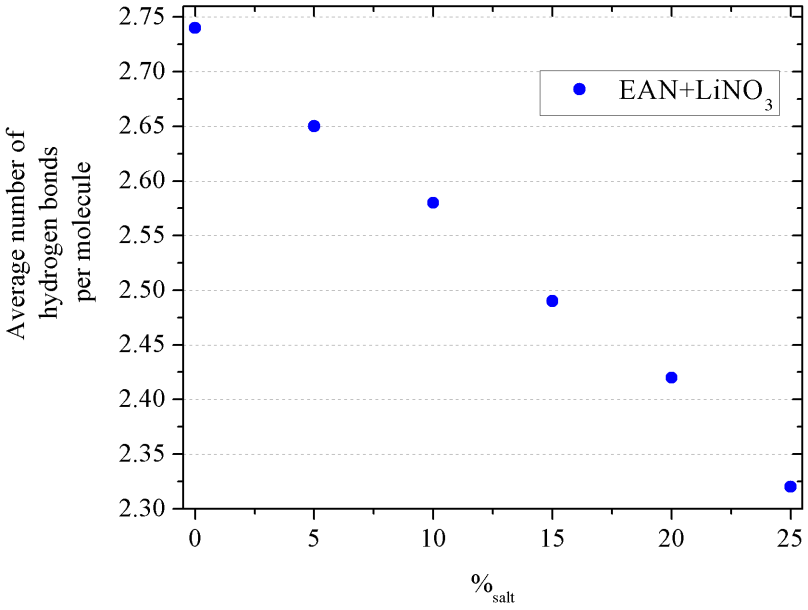

hydrophobic moieties of the IL. Thermodynamically, this is expectable, since the enthalpy of formation of $LiNO_3$ is -483.10 kJ mol^{-1} while its solvation enthalpy in ethanol (as representative of the solvation in an organic liquid with two carbon atoms in the chain) is a mere 19.45 kJ mol^{-1}, so energetically it is very favourable that $[Li]^+$ is in the polar domains. Such a distribution is expected mainly due to the electrostatic and hydrogen bonding interactions, as well as to the different sizes of the three species, and it is strongly supported with the snapshots of the simulation box shown in Figure 2.50, where both the polar (red) (b) and the apolar (green) (c) regions of the PIL together with the lithium cations (blue) are distinguished. These three snapshots confirm not only the formation of the polar and apolar domains but also that lithium cations are mainly located in the polar regions of the solutions, which has a great influence on the well-known network of hydrogen bonds formed in this kind of systems.

Further evidence of the lithium placing itself in the polar domains of the system is apparent from the analysis of the evolution of the hydrogen bond network between ethylammonium cations and nitrate anions upon salt addition, which is shown in Figure 2.51. The average number of hydrogen bonds per molecule is calculated normalizing the total number of hydrogen bonds by the number of ions except $[Li]^+$ in order to analyze the specific effect of this cation on the network of hydrogen bonds. In this kind of systems, hydrogen bonds take place between the ammonium hydrogen atoms (donors) and the oxygen atoms of the nitrate (acceptors), resulting in the well-known three-dimensional network of hydrogen bonds [51]. The calculated average number of hydrogen bonds per molecule found in pure EAN is 2.74, quite similar to the experimental value of 3 reported by Fumino and Ludwig [51], and in contrast to 4 in water environment. In this case, our criterion for defining a hydrogen bond is exclusively geometric. As reported in previous works [132] and according to the criterion implemented in Gromacs, two molecules are considered H-bonded if the distance between the donor and the acceptor is smaller than 0.35 nm and the angle of the donor-hydrogen-acceptor is less than 30°. As can be seen in Figure 2.51, a decrease in the average number of hydrogen bonds per ion with increasing salt concentration is registered, indicating that lithium cations are breaking the IL network of hydrogen bonds. $[Li]^+$ is a small cation with a high charge density that interacts more strongly with $[NO_3]^-$ than $[EA]^+$, attracting the IL anions to the interior of the polar nanodomains in the bulk system and breaking consequently the $[EA]^+ \ldots [NO_3]^-$ hydrogen bonds. As it is well known [315, 316], this behaviour of $[Li]^+$ cations is also registered in aqueous solutions, where it also breaks the hydrogen bond network despite being normally (and, unfortunately, according to Soper and Weckström [316]) considered a kosmotrope or structure-maker.

A three-dimensional picture of the local molecular structure in the bulk can be obtained from the spatial distribution function (SDF), understood here as the angular dependence of the probability of finding a molecule of species *j* at a chosen distance from a molecule of species *i*. The heat maps included in Figure 2.52 represent the angular distribution of lithium cations (a) and (b), cations (c) and anions (d) at a given distance from a central $[NO_3]^-$ for the solution with a 15% of salt. In these cases, the chosen distances correspond to the maximum of the first (and also the second in the case of lithium) peak of the corresponding RDFs. It must be noted that the different sizes of the central nitrate anion give us an idea of the distances of the first maximum. The two

Figure 2.52 SDFs of the three species (lithium (a) and (b), nitrogen in the ammonium group of the cation (c), and nitrogen in the anion (d)) around nitrates with the distance fixed at the first (or second) maximum of the corresponding RDF: (a) first peak in Figure 2.49.a (0.24 nm), (b) second peak in Figure 2.49.a (0.31 nm), (c) first peak in Figure 2.48.a (0.35 nm), and (d) first peak in anion-anion RDF (0.49 nm). All the SDFs were calculated for the solution with a 15% of lithium salt.

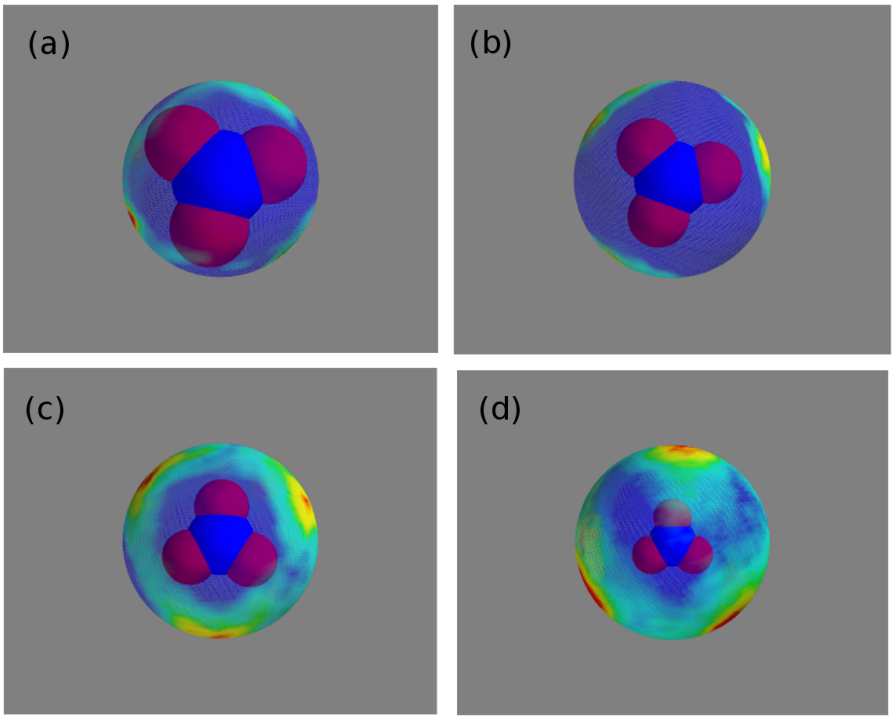

possible conformations of $[Li]^+$ surrounding a central $[NO_3]^-$ mentioned above when discussing the RDFs are also clearly seen in Figures 2.52.a and 2.52.b. There we can observe that at the shorter distance nitrate coordinates lithium cations in a bidentate way, with lithium cations being preferentially found in the bisectrix of the angle formed by two oxygens and the central nitrogen of the anions, while at the distance of the second peak lithium cations are facing the nitrate oxygens, so nitrate coordinates lithium in a monodentate fashion. Additionally, Figure 2.52.c shows that the nitrogen of the $[NH_3]^+$ is also preferentially occupying the same bisectrix as $[Li]^+$ in the first peak within their first coordination shell around nitrates. This spatial distribution is in good agree-

Figure 2.53 Coordination numbers of lithium cations (black squares), nitrate anions (red circles), and ethylammonium cations (blue triangles) around a lithium cation in solutions of EAN with $LiNO_3$. Number of anions surrounding an ethylammonium cation (green triangles) and viceversa (pink triangles) are also included.

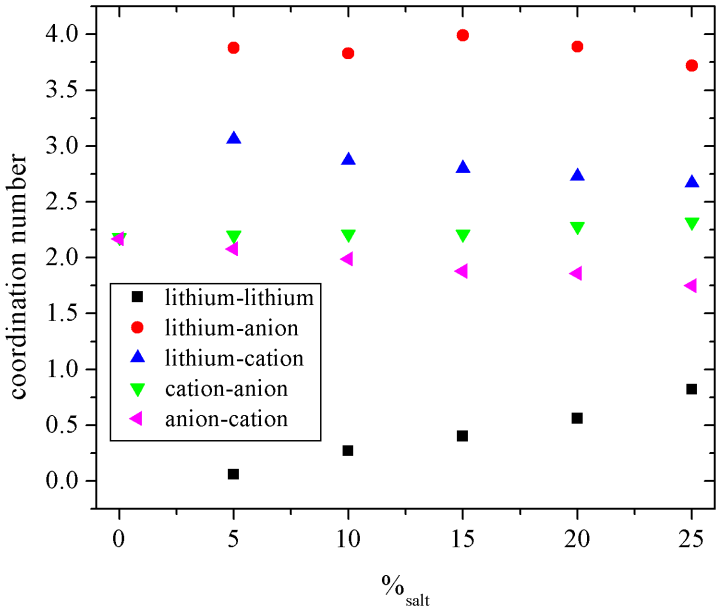

ment with the one previously reported by Hayes *et al.* in their studies of pure EAN [310] and its solutions with water [303], and those published by Song *et al.* [292] This competitive behaviour probably explains the fact that the second conformation of lithium cations is different from the first one, since these regions of the space are shared with the ethylammonium cations. Finally, the ordering of the nitrate anions around ions of this same species seen in Figure 2.52d shows that $[NO_3]^-$ is mainly arranged in a line with the oxygens of the central nitrate.

Another interesting feature that can be analyzed is the evolution of the coordination numbers of the different species in solution as salt concentration increases. For that, we calculated the different coordination numbers by means of the numerical integration of the function $4\pi r^2 \rho g(r)$ up to the first minimum

of the corresponding RDF (with ρ being the numerical density of the ionic species surrounding a central molecule and $g(r)$ the corresponding RDFs plotted in Figures 2.48.a and 2.49), which indicates the end of the corresponding solvation layer. The corresponding results are shown in Figure 2.53. The coordination numbers of the different species around a central lithium indicate that, on average, a $[Li]^+$ is surrounded by around four anions that form its first coordination shell and, approximately, three ethylammonium cations and less than one lithium ion in the second one. However, one must recall that the density of $[Li]^+$ is much lower in the apolar domains of the IL, as mentioned above. Moreover, whereas the number of anions and cations solvating a given $[Li]^+$ is almost the same over the whole miscibility range, the coordination number of $[Li]^+$ cations with themselves increases with the amount of salt in the system, suggesting the formation of some kind inhomogenous structures of $[Li]^+$ in the polar nanodomains as the salt concentration increases, which could finally lead to the formation of crystallization nuclei. On the other hand, it can be seen that, in pure EAN, the number of nitrate anions coordinating an IL cation and viceversa is 2.2 and, as expected, this coordination number increases or decreases, respectively, due to the addition of common anions as we add salt to the mixture. This value is slightly lower than the ones reported by Hayes *et al.* [310] and Song *et al.* [292] of 2.98 and 2.76, respectively.

All these structural features somehow resemble the behavior of lithium cations and IL anions observed in solutions of lithium salts in AILs in a previous work [228], in which we reported the formation of stable and long-lived aggregates that involve one lithium and those anions on its first solvation shell. In order to test whether these cages formed by the nearest neighbours of the lithium cations are also found in this type of ILs or not, we analyzed the single-particle dynamics of these solutions by means of the study of the center-of-mass velocity autocorrelation functions (VACFs) of $[Li]^+$ cations. The normalized VACF is calculated as

$$C(t) = \frac{\langle \vec{v}(t) \cdot \vec{v}(0) \rangle}{\langle \vec{v}(0) \cdot \vec{v}(0) \rangle} \tag{2.28}$$

where $\vec{v}(t)$ is the velocity of the center-of-mass of the molecule at time t and the brackets indicate the ensemble average. In Figure 2.54, the concentration dependence of dimensionless VACFs of lithium cations in the solutions with EAN is shown. The inset was included with the aim of allowing us to distinguish the evolution of the collision time, indicated by the first zero of

the function, with the addition of [$LiNO_3$] to the system. As can be seen, this property shows a clear oscillatory behaviour after the first collision, and these oscillations are completely damped out after 0.3 ps. This indicates that lithium ions exhibit a rattling motion in the "cages" formed by their nearest nitrate anions, in agreement with previous studies of solutions with AILs, and that this ion reverses its relative direction of motion within its solvation shell during the lifetime of the nitrate shell for the relevant residence times [228]. Furthermore, the caging effect is slightly weakened as the salt concentration in the system increases, while the mean collision time increases with the amount of salt (except for the mixture of 15%, probably due to uncertainties of the simulation associated to the low number of frames in the trajectories for these short times). This could be associated to the scarcity of $[NO_3]^-$ to build up cages as $[Li]^+$ concentration increases, since each lithium cation is coordinated with four nitrates as we have seen.

2.5.5. Conclusions

We performed MD simulations of a PIL, EAN, mixed with $LiNO_3$ at room temperature. In order to gain further insight into the structure of this kind of systems, several properties such as density, radial distribution functions, hydrogen bonds, spatial distribution functions, coordination numbers, and velocity autocorrelation functions have been reported.

The observed properties show that, in neat EAN, nitrate anions interact preferentially with the ammonium group of the cations, as expected from the electrostatic, van der Waals, and hydrogen bonding interactions leading to the formation of polar and apolar nanodomains. We also found that the addition of the alkali salt leads to very limited disruption of the structure of the PIL solvent, the main effect of the salt addition being the transference of nitrate anions to the inner regions of the polar nanodomains where lithium cations are mainly placed. Due to their strong interaction with nitrate anions, these small, high-charge-density cations are dispersed in the polar environments of the PIL and give rise to the gradual disruption of the PIL network of hydrogen bonds upon solvation, clusterizing anions in their neighbourhood. Some sort of inhomogeneous nucleation of $[Li]^+$ in the polar domains seems to develop, since $[Li]^+$-$[Li]^+$ coordination numbers increase with increasing salt concentration. It has been seen that the interaction of lithium cations with nitrate anions leads to a solid-like short-ranged order in the polar regions reminiscent of pseudolat-

Figure 2.54 Concentration dependence of lithium cations VACFs in solutions with EAN. The inset shows the evolution of the collision time with the amount of lithium salt. The statistical uncertainties of $C(t)$ in the time interval of the inset are expected to be less than 10^{-4}.

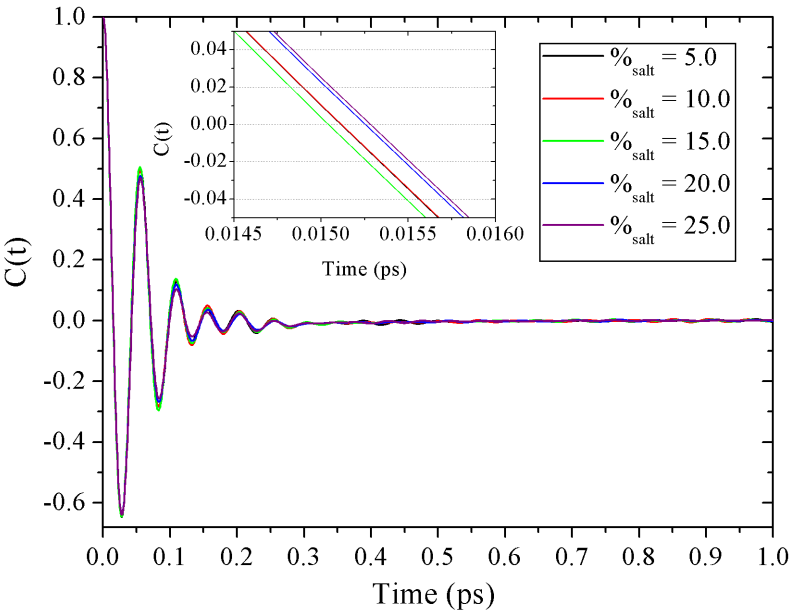

tice structures, in which lithium cations are surrounded by an average of four anions in two different conformations, corresponding to nitrates coordinating lithium cations in either monodentate or bidentate ways. The analysis of the lithium VACFs confirms the existence of a remarkable rattling motion of lithiums inside the cages formed by their heavier anionic neighbours.

In conclusion, all the available evidence supports that the solvation of $[Li]^+$ cations in PILs takes place by means of an inhomogeneous nanostructural mechanism, which could be named nanostructured solvation, embedding the $[Li]^+$ cations in the polar domains of the amphiphilically nanostructured PIL where solid-like $[Li]^+$-$[NO_3]^-$ structures progressively evolve until saturation, where they act as crystallization nuclei. This could possibly be a universal type of ion solvation in ILs, but more work is needed to prove this hypothesis. A systematic study of the solvation mechanism of ions in PILs is now in progress.

2.6. Nanostructure of Mixtures of Protic Ionic Liquids and Lithium Salts: Effect of Alkyl Chain Length.

With the aim of further improving our knowledge of solvations of salts in PILs with an eye on its use as electrolytes in lithium batteries, we expanded the analysis initiated in 2.5 and considered the influence of the chain length of the alkylammonium cation on the structural properties. On this occasion we did not opt for performing a single-particle dynamics analysis because of the need of using a polarizable force field when the dynamical properties are involved in the study. Further work in this direction is in progress in our research group.

Thus, in this work we employed MD simulations trying to shed light on the bulk structure of mixtures of propylammonium nitrate (PAN) and butylammonium nitrate (BAN) with a salt with a common anion, lithium nitrate [317]. In this case, we found a nanostructuration of the bulk in which the longer the alkyl chain length the better defined are the polar and apolar domains. The increase in the size of both domains with increasing the alkyl chain length of the alkylammonium cations or with the amount of salt in the mixture was not only suggested by the simulations, but also confirmed by means of experimental techniques. Additionally, lithium cations were found to heterogeneously accommodate into the polar area of the IL and progressively erode the hydrogen bond network. However, this effect becomes more pronounced for those PILs with longer alkylammonium cations due to their lower degree of hydrogen bonding.

In summary, salt ions are nanostructuredly solvated on the polar nanoregions of the bulk IL mixtures where they form solid-like pseudolattice structures.

2.6.1. Paper VI: Nanostructure of Mixtures of Protic Ionic Liquids and Lithium Salts: Effect of Alkyl Chain Length; *Phys. Chem. Chem. Phys. 17 (2015) 5298-5307.*

Trinidad Méndez-Morales,[1] Jesús Carrete,[1,2] Julio R. Rodríguez,[1] Óscar Cabeza,[3] Luis J. Gallego,[1] Olga Russina[4] and Luis M. Varela[1]

The bulk structure of mixtures of two protic ionic liquids, propylammonium nitrate and butylammonium nitrate, with a salt with a common anion, is analyzed at room temperature by means of small angle X-ray scattering and classical molecular dynamics simulations. The study of several structural properties, such as density, radial distribution functions, spatial distribution functions, hydrogen bonds, coordination numbers and velocity autocorrelation functions, demonstrates that increasing the alkyl chain length of the alkylammonium cation results in more segregated, better defined polar and apolar domains, the latter having a larger size. This increase, ascribed to the erosion of the H-bond network in the ionic liquid polar regions as salt is added, is confirmed by means of small angle X-ray scattering measurements, which show a clear linear increase of the characteristic spatial sizes of the studied protic ionic liquids with salt concentration, similar to that previously reported for ethylammonium nitrate (J. Phys. Chem. B 2014, 118, 761-770). In addition, larger ionic liquid cations lead to a lower degree of hydrogen bonding and to more sparsely packed three-dimensional structures, which are more easily perturbed by the addition of lithium salts.

2.6.2. Introduction

Ionic liquids (ILs) are salts composed exclusively of cations and anions that are poorly coordinated, which leads to them being in a liquid state below 100 °C and even at room temperature. Due to their unique array of physicochemical properties (high thermal stability, high ionic conductivity, negligible vapor pressure, large electrochemical window and ability to solvate a wide range of organic and inorganic materials) [36, 279, 318] and their numerous

[1]*Grupo de Nanomateriais e Materia Branda, Departamento de Física da Materia Condensada, Universidade de Santiago de Compostela, Campus Vida s/n E-15782, Santiago de Compostela, Spain*
[2]*CEA-Grenoble, 17 Rue des Martyrs, Grenoble 38054, France*
[3]*Facultade de Ciencias, Universidade da Coruña, Campus A Zapateira s/n E-15008, A Coruña, Spain*
[4]*Department of Chemistry, Sapienza University, P. le Aldo Moro 5 Roma, IT 00185, Italy*

potential applications (as lubricants, fuel additives and electrolytes, in separation processes, heat storage, synthesis and catalysis, among others) [6, 30, 319, 320], great research efforts have been conducted towards better understanding them over the last few decades.

A subset of ILs is that of protic ionic liquids (PILs), first discovered in 1914, when Walden [1] reported the description of ethylammonium nitrate (EAN) and classified it as an IL whose melting point is 287.6 K. These ILs are formed by proton transfer from a Brønsted acid to a Brønsted base [280–282]. The existence of this exchangeable proton is the main difference between PILs and aprotic ionic liquids (AILs) and gives rise to an extended hydrogen bond network, which not only resembles the three-dimensional hydrogen bond network of water [51, 183], but it is also responsible for their special set of properties and their highly ordered structures [280, 282, 288].

The number of articles studying the properties of PILs is not comparable to those on AILs (amongst which it is worth mentioning the firt computational, work performed by Canongia-Lopes and Pádua [39], that reported the formation of segregated domains), but relevant contributions have already been reported that shed some light on their peculiar behavior [288, 291, 293–296, 321]. For example, Greaves *et al.* [280, 282] published several thermal and physicochemical properties of a series of PILs, including glass transition, melting point, boiling point, density, refractive index, viscosity, ionic conductivity, and air-liquid surface tension. In another experimental work, Atkin and Warr investigated the bulk structure of EAN and propylammonium nitrate (PAN) by using small-angle neutron scattering (SANS) [41]. They reported the existence of a L_3-sponge-like bulk structure of polar and non-polar domains, these nanoscale heterogeneities being favoured by the solvophobic interactions between alkyl groups, as well as by the electrostatic and hydrogen bonding attractions between the ammonium cation and nitrate anion. This same sponge-like structure in bulk PAN was also reported by Hayes *et al.* [297] using empirical potential structure refinement (EPSR). The resultant amphiphilic PAN nanostructure is more pronounced and with a larger non-polar domain size than that observed in EAN due to the extra methylene unit. Besides, Kennedy and Drummond observed the formation of large aggregates of the constituent ions in several PILs by employing electrospray ionization mass spectrometry (ESI-MS) [290]. They showed that the $C_8A_7^+$ species (C = cation, A = Anion) was the most abundant and that the formation and size of clusters was dependent on the nature of the anion and cation. This nanostructure is known to occur

in imidazolium-based ILs with alkyl chains > C_4, whereas chains as short as C_2 are enough to induce nanostructuring of primary ammonium based PILs [41]. Moreover, the spatial dimension of the nanodomains in ILs is known to be controlled by the length of the alkyl chains in their constituents. In a recent article we reported a systematic study of the effect of the cationic chain length and the degree of hydrogen bonding on several equilibrium and transport properties of EAN, PAN and butylammonium nitrate (BAN) by means of several experimental techniques [50]. All our observations reflected the lower hydrogen bonding degree of the PILs with the longer chains, which is due to to enhanced hydrophobic interactions with the cationic chain length of the PILs.

Concerning solutions in PILs, the first contributions on their structure have just been reported by Hayes *et al.* [322] and by some of us [323] using, respectively, neutron (WANS) and X-ray scattering (WAXS), combined with reverse Monte Carlo simulation. In them, salt cations are clearly seen to be dissolved into the polar domains of the IL bulk. Upon this solvation process, IL nanosegregation of the PILs persists, only slightly influenced by the salt addition, and crystalline-like organizations are adopted by the added salt in the polar nanocavities of the amphphilic IL [323].

Although many physicochemical properties of PILs are now better characterized, it must be said that we are still far from having a complete molecular understanding of dynamical and structural properties of PILs. In this regard, computational simulations are crucial in order to overcome the limitations of experimental research and to get a systematic understanding of the interaction mechanisms between the ions. However, the number of works using computational methods is still very limited [297–300, 303, 304] and, to our knowledge, only a few publications based on molecular dynamics (MD) simulations have been reported so far [278, 292, 301, 302]. In one of the MD studies that have been published to the date, Umebayashi *et al.* [301] analyzed the liquid structure of EAN and found that $[NO_3]^-$ anions significantly interact not only with the ammonium group but also with the alkyl chain of the cations. Their simulations also supported relatively short alkyl chain aggregation as proposed by Atkin and Warr [41]. In addition, Zahn *et al.* [302] performed *ab initio* MD simulations of the PIL monomethylammonium nitrate (MMAN) to investigate its dynamics. Their results exhibited a fast fluctuating hydrogen bond network in which, on average, one hydrogen bond acceptor and one donor site in each ion pair remain free. The structural heterogeneity of EAN, PAN and BAN was also studied by Song *et al.* [292]. They found the formation of a distorted NH···O

hydrogen bonded network structure regardless of the alkyl chain length, in which nitrate anions usually bond to the charged ammonium headgroup of the cation, and the uncharged alkyl chains aggregate with each other. Finally, we recently reported the first (to our knowledge) MD study of the structure of mixtures of a PIL with an inorganic salt, specifically lithium nitrate with EAN [278], and we found that Li^+ cations placed themselves in the polar domains of the amphiphilically nanostructured PIL, forming solid-like aggregates with the anions in the bulk.

Focusing on the role of ILs as electrolytes for lithium and lithium-ion batteries, most of the studies have been devoted to the analysis of AILs, whereas only Menne *et al.* [305, 324] have considered PILs as being a good and cheaper alternative to conventional electrolytes. As it is well-known, obtaining information at the molecular level about the structure and solvation process of these liquids is of fundamental importance for a further understanding of their properties and, thus, improving their performance in these types of applications. In order to provide an insight into the behavior of this kind of ILs, we carried out a series of MD simulations of several PILs and their mixtures with alkaline salts.

Continuing with our previous studies [50, 278, 323], and trying to further understand the structural features of salt solvation in PILs, in this work we present an experimental and computational room-temperature study of the structure of mixtures of lithium nitrate with three members of the most studied family of PILs, alkylammonium nitrates: EAN [278], PAN and BAN. To access structural information we performed small angle X-ray scattering (SAXS) to investigate the influence of the added salt and the alkyl chain length on the nanostructuring of the ILs, and computationally examined the evolution of the radial distribution functions, spatial distribution functions, coordination numbers, degrees of hydrogen bonding and cage autocorrelation functions.

After this introduction we include a section describing the computational details of our study, which is followed by a discussion of the obtained results. Finally, we summarize our main conclusions.

2.6.3. Experimental and computational details

2.6.3.1. Chemical, density and small-angle X-ray scattering measurements

EAN was purchased from IOLITEC with a purity degree of > 97%, and it was used as received. $LiNO_3$ (> 99.9%) was a Merck product, and it was

used as received. Density was continuously and automatically measured at 298.15 K using a DSA 5000 Anton Paar density and sound velocity analyzer. This device is equipped with a latest-generation vibrating tube for density measurements with a resolution of $\pm 10^{-6}$ $g \cdot cm^{-3}$. Temperature was controlled to within $\pm 10^{-3}$ K by means of a Peltier module. The densimeter was calibrated with dry air and distilled water at known pressure and temperature.

SAXS measurements were conducted at the ID02 beamline at ESRF. The beamline makes use of an instrumental setup that covers the momentum range $Q = 1 - 11$ nm^{-1}. Measurements were performed at 298.15 K using a thermostated bath. The samples were kept inside a temperature-controlled flow-through cell with an internal diameter of 1.9 mm. The corresponding empty-cell contribution was subtracted.

2.6.3.2. Simulation details

MD simulations of pure PAN and BAN, whose schemes are shown in Fig. 2.55, as well as their mixtures with $LiNO_3$ at $T = 298.15$ K and $P = 1$ atm, were carried out using the Gromacs 4.5.4 package [70]. With regard to the parametrization of the ions, the OPLS-AA force field was used, which is an all-atom version of the OPLS force field that models every hydrogen atom bonded to carbon explicitly and whose details have reported in Ref.[153].

Propylammonium and butylammonium cations were built by adding the corresponding number of sites and maintaining the same charge of the alkyl chain as in EAN [278], and lithium cations were modelled by a single site of charge +1 whose Lennard-Jones parameters are $\sigma = 1.25992 \cdot 10^{-1}$ nm and $\varepsilon = 2.615 \cdot 10^{+1}$ kJ/mol. The rest of the details of the simulations have been reported elsewhere [278].

Due to the fact that our experimental measurements of the density showed that the solubility limits are $\%_{salt} = 18.0$ and $\%_{salt} = 15.4$ for PAN and BAN, respectively, the salt molar percentages simulated in all the systems ($\%_{salt}$={0, 5, 10, 15, 20 and 25}) covered the whole range of concentrations up to saturation and some metastable concentrations above this point. All the initial configurations were built by randomly inserting 300 ionic pairs of IL in a cubic box;, with the exception of the percentages $\%_{salt} = 5$ and 10, for which we considered 1000 and 450 ionic pairs with the aim of having enough salt to yield statistically significant trajectories. The number of lithium salt molecules was calculated for each situation by considering each ionic pair as a single unit in the calculation

Figure 2.55 The molecular structure of (a) nitrate anion, (b) ethylammonium cation, (c) propylammonium cation and (d) butylammonium cation. All of them were modeled using an all-atom representation.

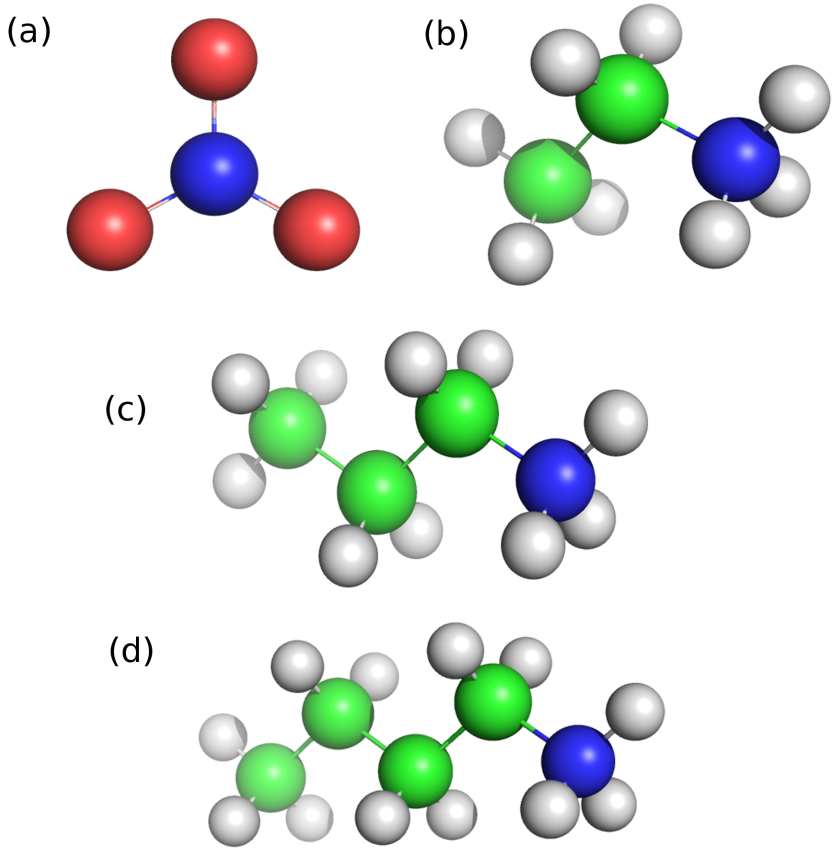

of mole fractions.

For each molar percentage of salt, the system was equilibrated for 20 ns in the isothermal-isobaric (NpT) ensemble applying periodic boundary conditions. We have employed 20 ns long simulations, a time long enough to ensure complete equilibration and sampling of relevant enough regions of the phase space. One must recall to this respect that the experimental bulk density of the IL and its mixtures is reached after 0.5 ns, and the correlation of the ion velocities are completely dumped out after 1 ns. Then, the results of an additional 10 ns–long simulation in the isothermal-isobaric ensemble were used for the analysis of the structure of the mixtures.

2.6.4. Results and discussion

SAXS data from binary mixtures of alkylammonium nitrates (PAN and BAN) and $LiNO_3$ at ambient conditions are shown in Fig. 2.56. Data for EAN-$LiNO_3$ mixtures in the same concentration range and conditions have been recently published by some of us [323].

Neat alkylammonium nitrates have been studied in the past using diffraction techniques. Here we concentrate on those studies referring to small angle X-ray/neutron scattering techniques. In 2008 Atkin *et al.* observed the existence of a low-Q feature in EAN and PAN [41], extending results [40] from some of us on AILs. Greaves and coworkers extended this investigation to longer members of the series up to pentylammonium nitrates [325] and similar results were obtained by Song and coworkers [292]. These structural features have been rationalised in terms of nanoscale segregated morphology in ILs as a consequence of their inherent amphiphilicity, which leads to a polar *vs.* apolar domains segregation. In several ILs, the characteristic size associated to this structural feature (that is estimated as given by $D \sim 2\pi/Q$, Q being the position of the low-Q peak) is found to depend linearly on the number of CH_2/CH_3 groups in the side alkyl tail and this is also the case for alkyl ammonium nitrates. SAXS data from EAN-$LiNO_3$ mixtures have been recently reported by us [323] together with a modelling of wide angle X-ray scattering data, while wide angle neutron scattering data from different isotopically-substituted mixtures were investigated by Atkin *et al.* [322].

The existence of low-Q peaks associated to structural features in the mixtures was also confirmed by means of MD simulations, as shown in Fig. 2.57, where MD SAXS calculations for a mixture of BAN with a 10% of lithium salt

are compared to the experimental observations. As can be observed in the inset, the agreement for this concentration is very good, and this is also the case for most of the studied concentrations, as shown in the inset.

In Fig. 2.58, we show the $LiNO_3$ concentration dependence of the characteristic scales in the three sets of mixtures. Together with the data obtained for PAN and BAN, we also report data from Ref.[323]. We note that the three sets of solutions show an approximately linear trend for D *vs.* $[Li]^+$ content. These data sets show that the characteristic spatial scales for the mesoscopic order in these mixtures fall in the range from 9 to 16 Å, with progressive increase of this size with increasing $[Li]^+$ content.

It is noteworthy that, at intermediate concentrations, EAN-$LiNO_3$ mixtures show deviations from such a linear trend, and D at 0.06 molar fraction (mf) in lithium salt is smaller than the value for neat EAN. At higher $[Li]^+$ content, however, D tends to grow and becomes larger than in neat EAN. This kind of behaviour explains the observation in a recent paper by Atkin *et al.*, where they reported experimental neutron scattering data for the case of 0.10 molar fraction in $[Li]^+$ salt, and noticed that, for that concentration, the low-Q peak position falls at larger Q values than for neat EAN. Our present X-ray data set somehow confirms that a concentration regime exists where the peak position shifts towards larger Q values (decrease in D values), but that this is followed by a concentration range where the peak shifts towards smaller Q values (increase in D values). It is also noteworthy that the same trend is not observed for the case of PAN and BAN mixtures with the lithium salt, as the peak position (characteristic spatial scale) progressively shifts downwards (upwards) upon lithium salt addition. Moreover, we notice that, even when the 0.055 mf data deviates by *ca.* 2%, the characteristic spatial sizes in the EAN-$LiNO_3$ mixtures follow a linear trend with a slope $dD/dx_{[Li]^+} = 5\text{Å} \cdot \text{mf}^{-1}$. This trend is also followed by the PAN and BAN mixtures with $LiNO_3$, in the dilute regime below $x_{[Li]^+} = 0.1$. This observation might imply subtle structural effects from the lithium addition on the sponge-like morphology in bulk alkylammonium nitrates.

Hence, our X-ray data suggest that the characteristic size of the mesoscopic correlations increases with salt addition. In order to get further understanding of this phenomenon, we performed MD simulations of the studied mixtures. As density is one of the properties most easily comparable with experimental data, it is worth making a comparison between computational and experimental density results, to estimate the validity of the force field employed in

our MD simulations and its accuracy in representing the behavior of a given system. Fig. 2.59 shows the salt concentration dependence of both experimental and simulated density for mixtures of EAN (which had been previously reported in Ref.[278]), PAN and BAN with $LiNO_3$. It can be seen there that the predicted densities of the systems involving PAN and BAN are in excellent agreement with the experimental values. In view of these results, we can be reasonably confident about the ability of our force field to reproduce the structural properties and the solvation process of these PILs. However, it must be taken into account that, since the force field employed is non-polarizable, we cannot obtain quantitatively accurate predictions for the dynamic properties of lithium ions (as we proved in Ref.[228]). It can be also seen that all the mixtures show the same linear increase with salt concentration previously reported for lithium salts in AILs and in EAN [228, 278]. In addition, the slope of the density is practically independent of the IL cation alkyl chain length. These features suggest that added salt ions are solvated into the polar nanoregions of the mixture, the density of which increases upon salt addition either by breaking hydrogen bonds in these regions and/or by forming clusters with the $[NO_3]^-$. Moreover, if we recall that the partial molar volume of a solute of molar mass M_2, $\bar{V}_2$, in an IL of density ρ_0 can be approximated for constant partial molar volume (*i.e.* when the partial molar volume and the apparent molar volume are equal) as

$$\bar{V}_2 \simeq \frac{1}{\rho_0}\left(M_2 - \frac{\partial \rho}{\partial c}\right) \tag{2.29}$$

where c is the molar concentration of the salt, we can easily conclude that, as the chain length of the cation IL increases, the partial (equiv. apparent) molar volume of the salt increases. This can be seen as an indicative of an enhanced influence of the addition of salt on the thermodynamic properties of the systems, the longer the IL cation alkyl chain length is.

These features can be also observed in Fig. 2.60, in which we analyze the concentration dependence of the well-known hydrogen bond network between nitrate anions and alkylammonium cations. For this purpose, we calculated the evolution of the average number of hydrogen bonds per molecule by normalizing the number of H-bonds by the number of ions (excluding lithium cations), as explained in Ref.[278]. In addition, since the large organic parts of the molecules of these systems are not involved in hydrogen bonds, the fraction of hydrogen-bonded atoms is more informative about the relative

extent of hydrogen bonding. Accordingly, we included the analysis of the average number of hydrogen bonds per atom in the ionic pair in order to clarify the effect that the cationic chain length has on this property. The criteria considered in Gromacs for determining the presence of a hydrogen bond are purely geometrical; that is to say, the distance between aceptor and hydrogen must be lower than or equal to 0.35 nm, and the angle between acceptor-donor-hydrogen must be smaller than or equal to 30°. In this case, the three-dimensional network results from hydrogen bonding taking place between the oxygen atoms of all the nitrates that are present in the mixture (regarded as acceptors) and the hydrogen atoms of the ammonium head group of the cation (considered as donors). In Fig. 2.60.a we can observe a linear decrease in the average number of hydrogen bonds regardless of the alkylammonium cation chain length as the lithium salt concentration increases, which shows a gradual break up of the IL H-bond network due to the $[Li]^+$ cations placing themselves in the polar domains of the network. This is the same tendency previously reported for solutions of EAN with $LiNO_3$ [278]. Furthermore, Fig. 2.60.b evidences that the hydrogen bonding extent of the PILs is lower the longer the cation chain length, since the formation of a hydrogen bond is more difficult due to the larger size of the apolar domains and the greater distance between ions [50]. Interestingly, we can see in Fig. 2.60.a that the number of hydrogen bonds per molecule is practically the same for the various studied PILs, and, even more interestingly, the rate of change of this number with concentration is practically identical for the different ILs. This further reinforces the notion that changes on the hydrogen bond network with salt addition are confined to the polar nanoregions of the mixture, where a $[Li]^+$ electrostrictive ionic field forces reorientation of $[NO_3]^-$ anions, removing them from H-bonds with the $[XA]^+$ cations. However, when we come to analyze the number of hydrogen bonds per atom, we see that the average number of H-bonds per atom in the ionic pair decreases slightly faster for mixtures of PILs with shorter alkyl chains, since longer cations have more atoms that do not participate in a hydrogen bond. Nevertheless, it must be pointed out that, since mixtures of PILs with longer alkyl chains are hydrogen bonded to a lesser extent, H-bonds breakage is expected to have a deeper impact on the properties of the mixture the longer the alkyl chain length of the solvent cation is.

A strong segregation of polar and apolar domains in the mixtures can be clearly observed in Fig. 2.61, in which we show several snapshots of the simu-

lation box of 25% of $LiNO_3$ mixed with PAN and BAN. As we previously found in solutions of $LiNO_3$ in EAN [278], the vast majority of the $[Li]^+$ cations are located in the polar regions of the bulk, decreasing the interaction strength between nitrate anions and ammonium groups and gradually breaking the strong hydrogen bond network existing in bulk PILs. Moreover, these snapshots support the picture of larger apolar domains as the IL cation alkyl chain length increases, in agreement with the study of Hayes *et al.* [321].

Further evidence of lithium cations solvation in the bulk system and its influence on the IL network can be obtained by quantifying spatial structure through the analysis of the radial distribution function (RDF),

$$g_{ij}(r_{12}) = \frac{1}{\rho_i \rho_j} \sum_{i,j}^{N} \langle \delta(\vec{r}_1 - \vec{r}_i) \delta(\vec{r}_2 - \vec{r}_j) \rangle \tag{2.30}$$

where ρ is the number density, N stands for the number of particles in the system, i and j run over all the species, and brackets indicate the ensemble average. It must be clarified that for the calculations of the RDFs involving the alkylammonium cation, we only took into account the four atoms in the ammonium or methyl groups; all RDFs presented in this paper were calculated by considering the center of mass of the defined groups, except in the case of hydrogen-oxygen $g(r)$'s (of ammonium group and nitrate, respectively), for which an average of the atomic RDFs was calculated.

The lithium salt concentration dependences of the RDFs involving the ions of the PILs are presented in Fig. 2.62 and 2.63 for mixtures with PAN and BAN, respectively. In particular, these two figures show $g(r)$'s between (a) $[NO_3]^-$ anion-ammonium group of the IL cation, (b) $[NO_3]^-$ anion-methyl group of the IL cation, and (c) hydrogen-oxygen (of the ammonium group of the IL cation and the nitrate anion, respectively). In a similar way to that reported for EAN [278], the strongest coordination is found between $[NO_3]^-$ and $[NH_3]^+$. The strength of this interaction decreases in a more pronounced way than that between $[NO_3]^-$ and IL cation alkyl groups with the addition of lithium salt to the system, which once again indicates that lithium cations are accommodated into the polar domains of the bulk inducing a rupture of the H-bonds between IL ions in the nanoregion. Moreover, the position of the first peaks of the $g(r)$'s of the IL components does not vary as the concentration of lithium salt increases, which indicates that the structure of these liquids is not significantly changed by salt addition, except for its hydrogen bond extent in the polar nanoregions. However, increasing the length of the cation alkyl chain

does have an impact on the amphiphilic nanostructure of the bulk. Firstly, the height of the first peak in the RDF between nitrate anion and ammonium group (Fig. 2.62.a and 2.63.a in this paper, and Fig. 2.a in Ref.[278]) clearly increases upon increasing the cation alkyl chain, which is indicative of an increasing segregation of the fluid, giving rise to better defined polar domains of the PILs with alkyl chain length [321]. Additionally, the decrease of the height of the first peak in the $g(r)$ between the nitrate anion and the methyl group (Fig. 2.62.b and 2.63.b in this paper, and Fig. 2.b in Ref.[278]) reveals a reduction in the coordination between these two groups of atoms, which is due to the existence of larger and better defined apolar domains. This leads to a looser nanostructuration, more similar to a sponge, in the mixtures with longer alkyl chains. Finally, there are no substantial differences in the distance between the atoms that participate in the hydrogen bond (Fig. 2.62.c and 2.63.c and Fig. 2.c in Ref.[278]), and we obtained an average $O \ldots H$ distance of 0.18 nm, in agreement with the conclusions drawn by Bodo *et al.* [299]. However, the number of atoms at that distance decreases with the addition of salt, as reflected in the height of the peak of Fig. 2.63.c.

Fig. 2.64 and 2.65, which show the RDFs involving $[Li]^+$ cations and both ionic species of the PILs, provide us with further evidence regarding the location of lithium cations in the bulk mixtures. The greater height of the peaks of the RDFs between $[NO_3]^-$ anions and $[Li]^+$ and their positions at shorter distances show that lithiums are mainly coordinated with nitrate anions, as we found in mixtures with EAN [278]. It is also noteworthy that the interaction of lithium cations with both nitrate anions and the ammonium group of the IL cations increases as the degree of hydrogen bonding decreases (that is, as the alkyl chain length of the IL cation increases), which is compatible with lithium being constrained to lie in progressively more compact, denser polar nanoregions. In the case of PAN and BAN, the first solvation shell of lithium cations around nitrates is composed of a double peak (Fig. 2.64.a and 2.65.a) as in the case of EAN mixtures, which indicates that $[Li]^+$ cations can be found in two different conformations: bidendate (corresponding to the first peak) and monodendate (corresponding to the second peak). Although the monodendate conformation is the more abundant independently of the alkyl chain length of the IL cation, it seems that the relative abundance of this way of coordination becomes comparable to that of the bidendate conformation when increasing the length of the IL cation alkyl chain, since the heights of the peaks tend to become more similar. This is indicative of a compaction of the polar regions

as the alkyl chain length of the IL cation is increased, ascribed to a decrease in their volume fraction decrease *via* a "dilution effect".

Another interesting tool for shedding light on the bulk structure is the spatial distribution function (SDF), which provides useful information about the three-dimensional density distribution of atoms around a central molecule. In this case, the SDFs were determined by fixing a distance from the central molecule, which corresponds to the position of the first (and also second for calculations involving lithiums) maximum of the RDFs, and calculating the angular probability distribution of finding an atom at a specific point in the mixture. All the reported SDFs correspond to the different species around the nitrate anions, which are indeed plane molecules. The reference plane corresponds to the plane of the molecule itself, and all the nitrate anions have been rotated so that their planes are identically oriented before calculating the corresponding average angular probabilities. Thus, Fig. 2.66 shows the heat maps of the angular distribution of (a), (b), (e) and (f) lithium cations, (c) and (g) nitrogen in the $[NH_3]^+$ group of the IL cation and (d) and (h) nitrogen in the $[NO_3]^-$ anion at an specific distance from a central nitrate, for the mixtures of 15% of $LiNO_3$ with PAN (a-d) and BAN (e-h). The main observed effect of increasing the alkyl chain length of the IL cation is that, despite the better defined polar and apolar domains the longer the alkyl chains, the polar domains of PAN and BAN mixtures seem to be, on average, less ordered than those in EAN mixtures [278]. This is reflected in the much more diffuse heat maps of the distributions of lithium cations (a, b, e and f) around the nitrates, where we see that $[Li]^+$ are neither forced to be located in the bisectrix of the angle formed by two oxygens and the central nitrogen of the anions (bidendate conformation), nor facing the nitrate oxygens (monodendate conformation). Hence, these two conformations around a central $[NO_3]^-$ are less clearly observed than in mixtures with EAN [278]. A similar effect, although slightly less marked in the case of the nitrogen of the ammonium cation, is observed for both alkylammonium cations and nitrate anions surrounding a central $[NO_3]^-$. This increase of the orientational disorder in the nanoregions could be associated with the collapse of the directional hydrogen bond network inside the polar nanoregions.

The lithium salt concentration dependence of the coordination numbers of the ions in the mixtures is also an informative variable. The results of numerically integrating the function $4\pi r^2 \rho g(r)$ (where ρ is the numerical density of the molecules around an specific central ion, lithium in this case, and $g(r)$ is one of the RDFs plotted in Fig. 2.62.a, 2.63.a, 2.64 and 2.65) up to the end of the

first solvation shell (given by the first minimum of the corresponding RDFs) are shown in Fig. 2.67. In general, there are no significant differences between the coordination numbers in solutions of $LiNO_3$ in EAN, PAN and BAN, except for the fact that the number of alkylammonium cations solvating a given lithium slightly decreases with increasing the alkyl chain length, going from 3 in EAN to less than 2.5 in BAN. The reason why this change takes place is the increase of the thickness of the apolar domains with increasing IL alkyl chain length, as indicated by bulk liquid correlation length (determined from low Q Bragg peaks). Additionally, a slight decreasing of the coordination numbers of alkylammonium cations around a central $[Li]^+$ can be observed upon salt addition. This could be explained by an increase of the polar domains, since this kind of expansion would lead to fewer cations in a solvation shell with the same size. The swelling of the polar domains is due to the increase in the number of ions in these regions, ascribed to a decrease in the number of H-bonds. However, the observed increase in density would be associated with an increase in the ion densities in the polar regions, confirmed not only by an increase of $[NO_3]^-$ densities in the polar regions from 1.25 $[NO_3]^-/nm^3$ for pure PIL to 1.71 $[NO_3]^-/nm^3$ from a mixture with 20% of lithium salt, but also by a shift in the position of the first peak in the anion-anion RDFs as the amount of salt increases. We can also deduce an expansion of the apolar domains with the addition of lithium salt, which is suggested by a slight decrease of $[CH_3]$ densities in the apolar regions. On the other hand, in mixtures with PAN and BAN a central $[Li]^+$ is also surrounded by almost four $[NO_3]^-$ in its first coordination layer, and an average of nearly one lithium in its second solvation shell over the whole miscibility range, as we reported for EAN [278]. This is in agreement with neutron diffraction [297, 325, 326] and SAXS [323] experiments, which have shown that the underlying bulk nanostructure does not significantly undergo changes (and ion-ion correlations) as the IL alkyl chain length is increased.

In order to analyze the behaviour of lithium cations within their first coordination shell, we calculated the velocity autocorrelation functions (VACFs) of these ions, which are shown in Fig. 2.68. The normalized VACFs are determined as

$$C(t) = \frac{\langle \vec{v}(t) \cdot \vec{v}(0) \rangle}{\langle \vec{v}(0) \cdot \vec{v}(0) \rangle}, \tag{2.31}$$

where $\vec{v}(t)$ is the velocity of the center of mass of the molecule at time t

and the brackets indicate the ensemble average. We have performed high-frequency calculations (time step = 1 fs) and further verified that the results are not modified if we increase the saving frequency to 2 fs. The first thing we observe in the two panels of these figures is that the VACFs are almost identical for PAN and BAN mixtures, once again reflecting the relative independence of the solvation environment of lithium on the alkyl chain length of the IL cation, which can only be explained if the salt cation goes into the polar nanodomains of the mixture. Moreover, in exactly the same way as it was found in mixtures with EAN [278], this magnitude shows a clear oscillatory behavior that reveals that lithium cations experience a rattling motion inside the "cages" formed by their nearest neighbors, that is, the four nitrate anions that form their first coordination shell. Additionally, these oscillations are in all cases completely damped out after 0.3 ps. However, in mixtures of $LiNO_3$ with PAN and BAN we could not find clear trends in the collision times (indicated by the first zero of the VACF) with the amount of salt, but this is probably due to the uncertainties related to the low number of frames in the trajectories for these short times.

2.6.5. Conclusions

In the present paper, SAXS and MD simulations have been used with the aim of elucidating the bulk structure and the solvation process in mixtures of PAN and BAN with $LiNO_3$ at room temperature. For this purpose, we analyzed the influence of the amount of salt and of the alkyl chain length of the IL cation on several properties such as density, the radial distribution function, coordination numbers, the spatial distribution function, hydrogen bonds and velocity autocorrelation function.

Like we previously showed for mixtures with EAN in Ref.[278], the bulk of PAN and BAN is also nanostructured due to the electrostatic, van der Waals, hydrogen bonding and solvophobic interactions. As a result, charged groups (nitrate anions and cation head groups) interact to form polar domains, whereas alkyl groups tend to associate into apolar domains. This nanosegregation of PILs has a deep impact on the solvation of lithium salts, since their ions are forced to heterogeneously accommodate into the polar network of the ILs, coordinating mainly with the nitrate anions and giving rise to crystalline-like structures. In turn, lithium ions in the polar nanodomains progressively erode the hydrogen bond network of the PIL, decreasing

the extent of hydrogen bonding of the mixtures and inducing orientational disorder in their polar nanodomains. This effect is more pronounced for PILs whose cations have longer alkyl, chains due to the lower degree of hydrogen bonding among their constituents.

Figure 2.56 Small angle X-ray scattering data from binary mixtures of (a) propylammonium and (b) butylammonium nitrate-$LiNO_3$ at ambient conditions. The legend refers to lithium salt content expressed in molar fraction. Data have been vertically shifted for clarity purposes.

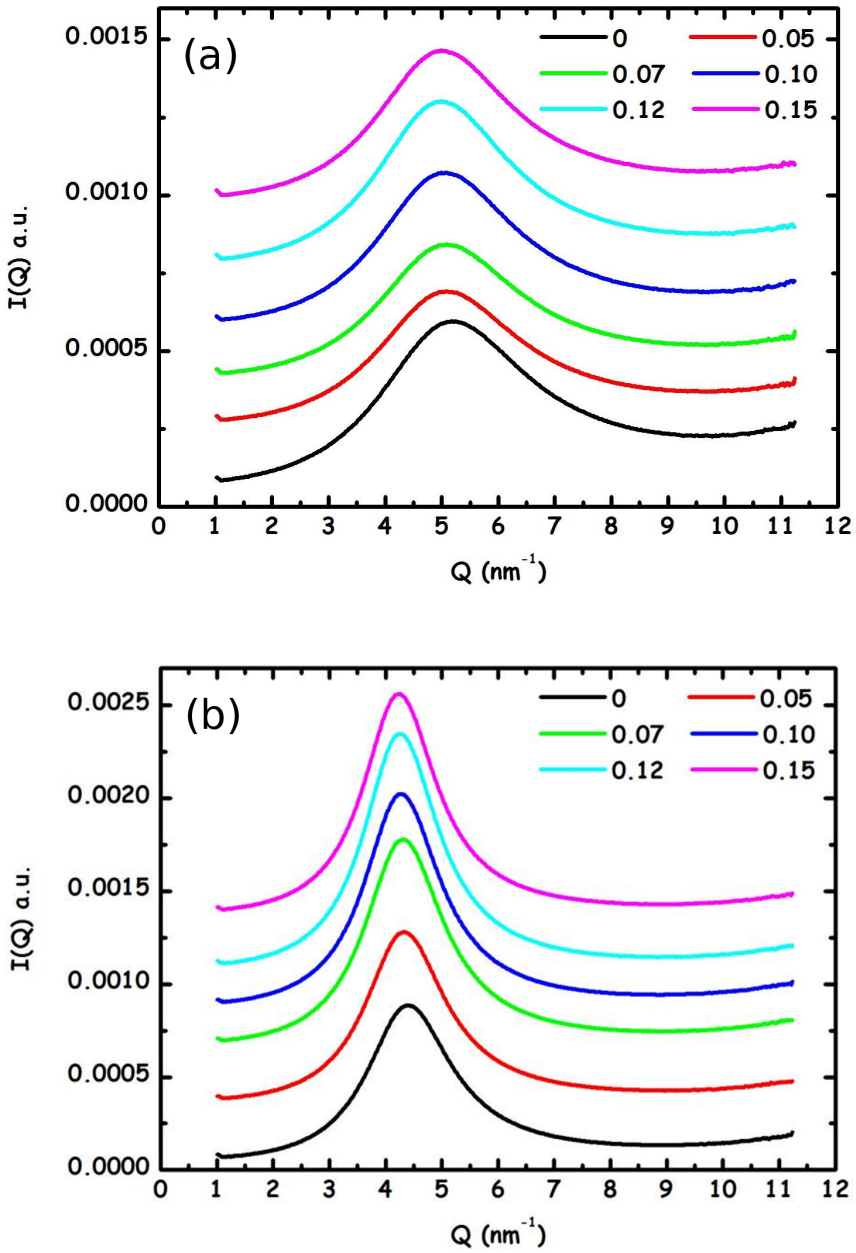

Figure 2.57 Small angle X-ray scattering data from MD simulations of BAN mixed with 10% of $LiNO_3$. The inset shows the experimental heights of the low-Q peaks *vs.* the corresponding MD predictions for the various studied concentrations of mixtures with PAN and BAN. The dashed line corresponds to perfect agreement.

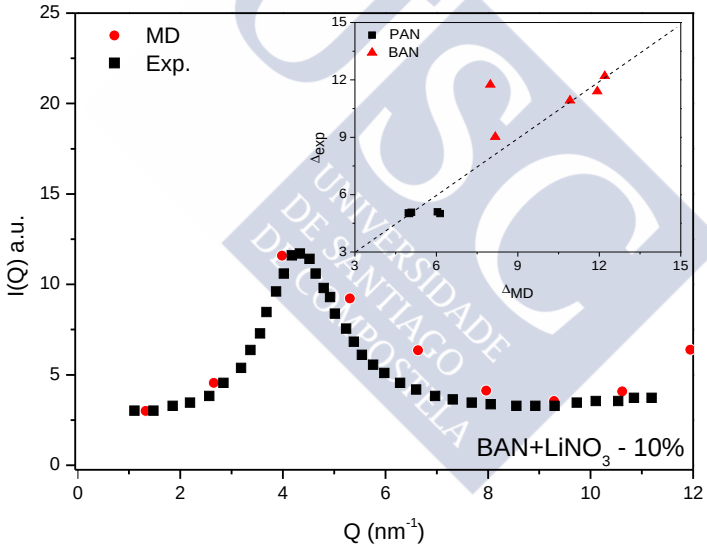

Figure 2.58 Characteristic spatial sizes (D) extracted from small angle X-ray scattering data from binary mixtures of ethyl-, propyl- and butyl-ammonium nitrate/$LiNO_3$ (EAN, PAN and BAN, respectively) at ambient conditions. The three lines are parallel, with the gradient obtained by a linear fitting to the EAN-$LiNO_3$ trend excluding the 0.055 molar fraction value.

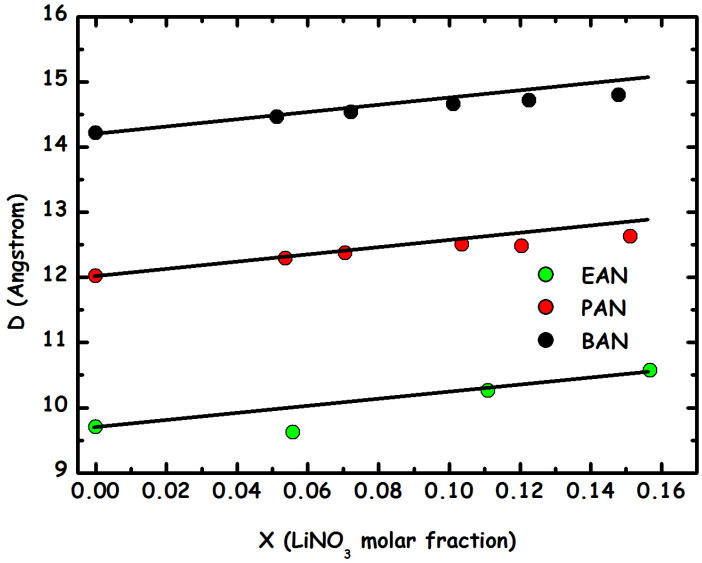

Figure 2.59 Simulated and experimental densities at $T = 298.15$ K of EAN (squares), PAN (dots) and BAN (triangles) mixed with lithium salts with a common anion as a function of the lithium salt concentration. Data for EAN were taken from Ref.[278].

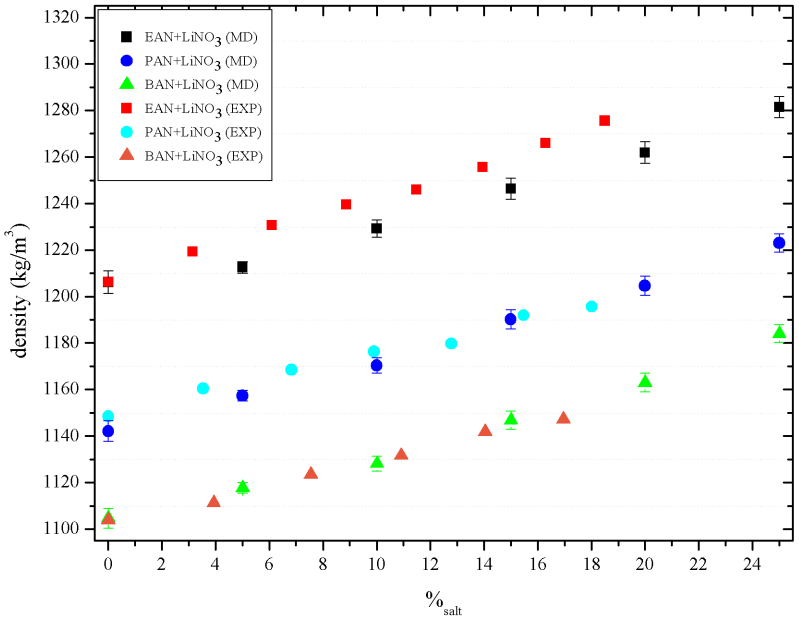

Figure 2.60 (a) Concentration dependence of the average number of hydrogen bonds per molecule for solutions of $LiNO_3$ with EAN (blue), PAN (red) and BAN (green). (b) Concentration dependence of the average number of hydrogen bonds per atom in the ionic pair for solutions of $LiNO_3$ in EAN (blue), PAN (red) and BAN (green). The lines are guides for the eye. Data for EAN were taken from Ref.[278].

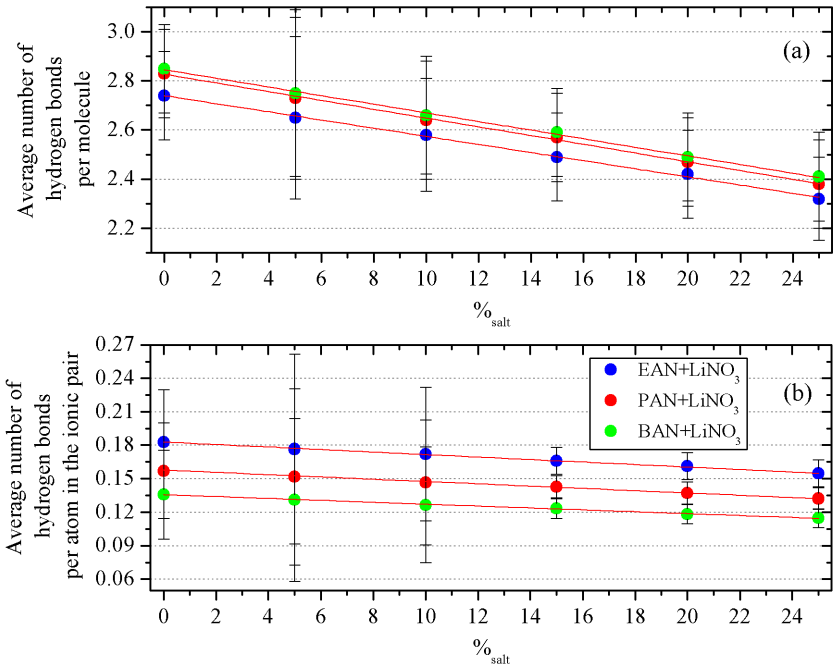

Figure 2.61 Snapshots of the simulation box of the mixtures of 25% of $LiNO_3$ with PAN (a-c) and BAN (d-f) at 298 K. The representations of the bulk structure include: (a) and (d) the whole system, (b) and (e) nitrate anions, ammonium group of the IL cation (polar domain - red) and lithiums (blue), (c) and (f) chain of the IL cation (apolar domain - green) and lithium ions (blue). The relative size of lithium has been exaggerated for clarity.

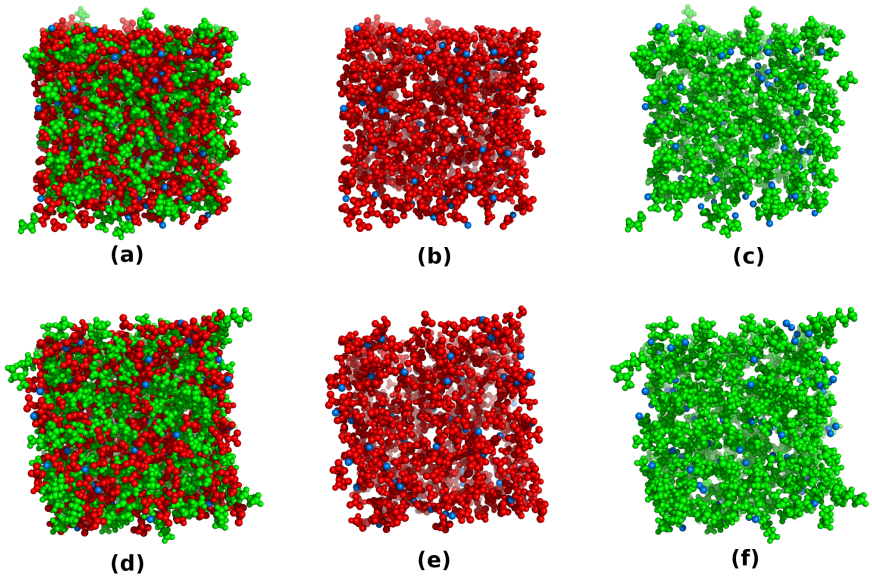

Figure 2.62 RDFs of (a) nitrate anion-ammonium group, (b) nitrate anion-methyl group and, (c) hydrogen-oxygen (of the ammonium group and the nitrate anion) as a function of the lithium salt concentration in solutions of $LiNO_3$ in PAN at 298.15 K.

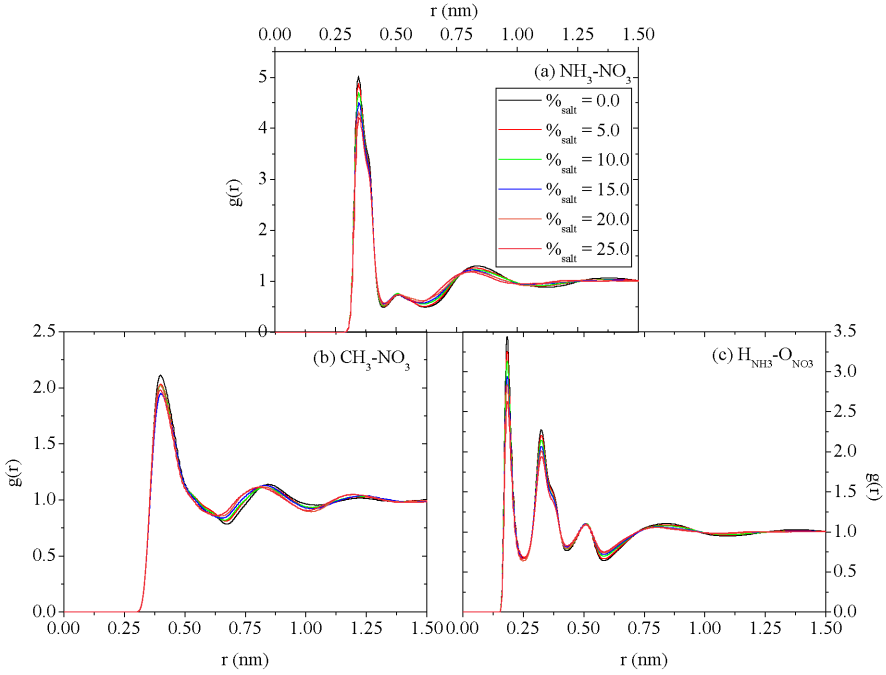

Figure 2.63 RDFs of (a) nitrate anion-ammonium group, (b) nitrate anion-methyl group and, (c) hydrogen-oxygen (of the ammonium group and the nitrate anion) as a function of the lithium salt concentration in solutions of $LiNO_3$ in BAN at 298.15 K.

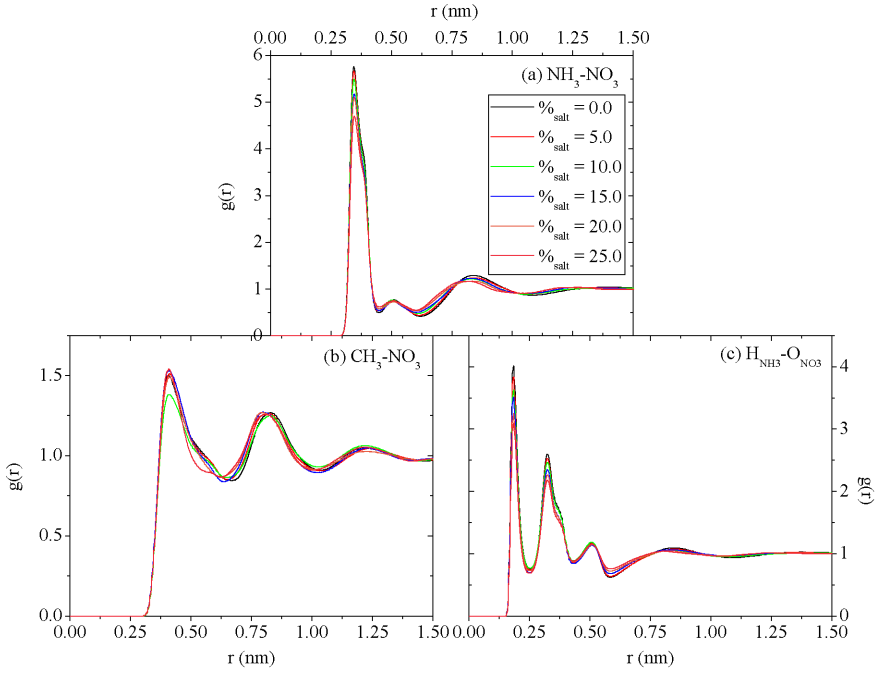

Figure 2.64 RDFs of (a) lithium-nitrate anion, (b) lithium-ammonium group and, (c) lithium-lithium as a function of the lithium salt concentration in solutions of $LiNO_3$ in PAN at 298.15 K.

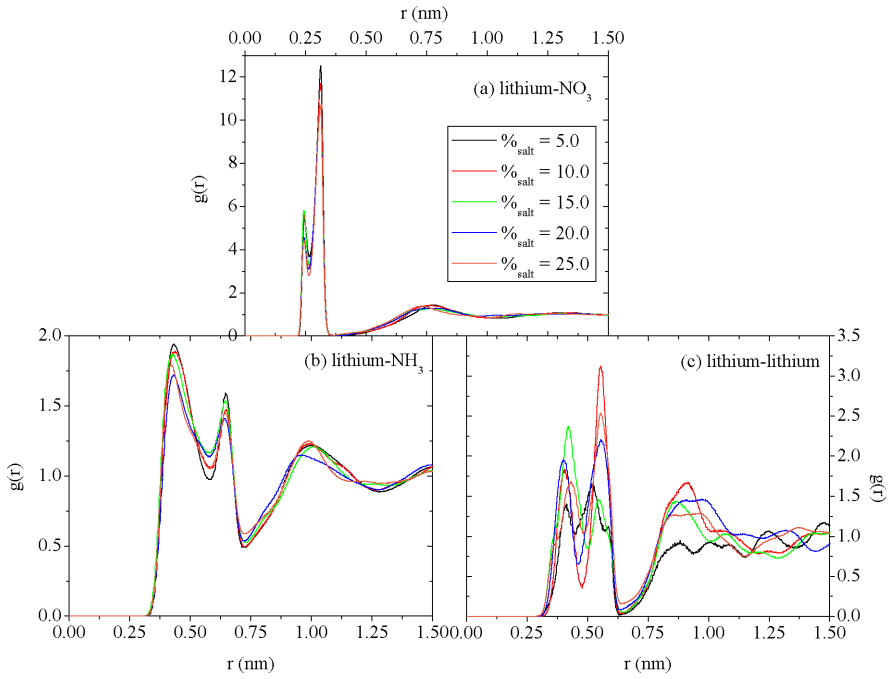

Figure 2.65 RDFs of (a) lithium-nitrate anion, (b) lithium-ammonium group and, (c) lithium-lithium as a function of the lithium salt concentration in solutions of $LiNO_3$ in BAN at 298.15 K.

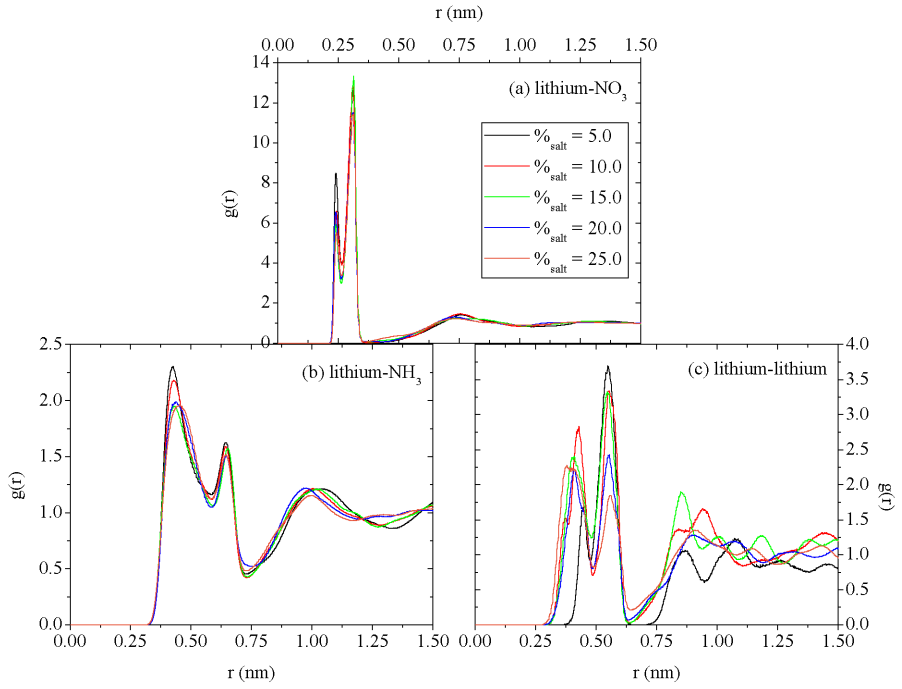

Figure 2.66 SDF plots of lithium first (a), (b), and second peaks, (e) and (f), nitrogen in the ammonium group of the alkylammonium cation (c) and (g), and nitrogen in the nitrate anion (d) and (h) as a function of the angular position around a central nitrate anion in mixtures of a 15% of $LiNO_3$ with PAN (a-d) and BAN (e-h). The distance at which SDFs were calculated corresponds to the first (or second in the case of lithium cations) maximum of the RDFs: (a) and (e) the first peak (0.24 nm) in Fig. 2.64.a and 2.65.a, respectively; (b) and (f) the second peak (0.31 nm) in Fig. 2.64.b and 2.65.b, respectively; (c) and (g) the first peak (0.34 nm) in Fig. 2.62.a and 2.63.a, respectively; (d) and (h) the first peak (0.50 nm) in anion-anion RDFs.

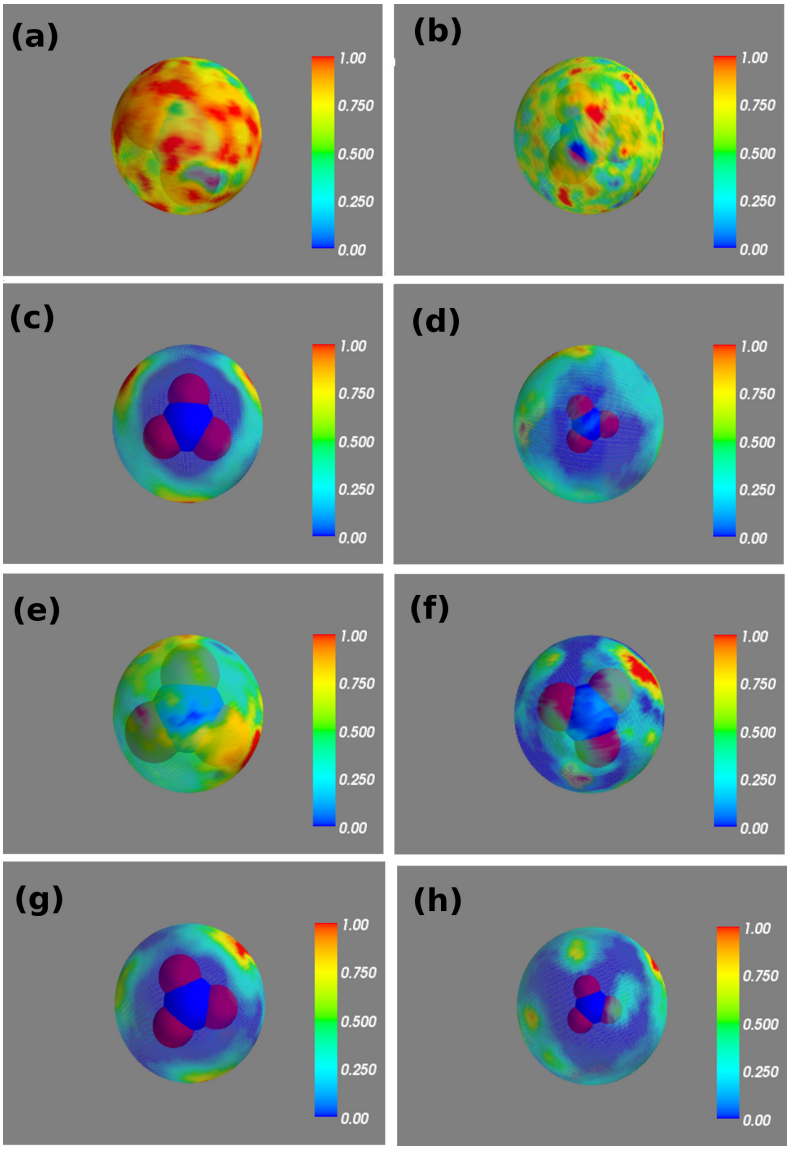

Figure 2.67 Concentration dependence of the coordination numbers of lithium cations (black squares-PAN, grey squares-BAN), nitrate anions (red circles-PAN, pink circles-BAN), and alkylammonium cations (dark blue pentagons-PAN, light blue pentagons-BAN) surrounding a central lithium cation in mixtures of PAN and BAN with $LiNO_3$. The number of nitrate anions around a central alkylammonium cation (dark green stars-PAN, light green stars-BAN) and *vice versa* (violet triangles-PAN, orange triangles-BAN) are also included.

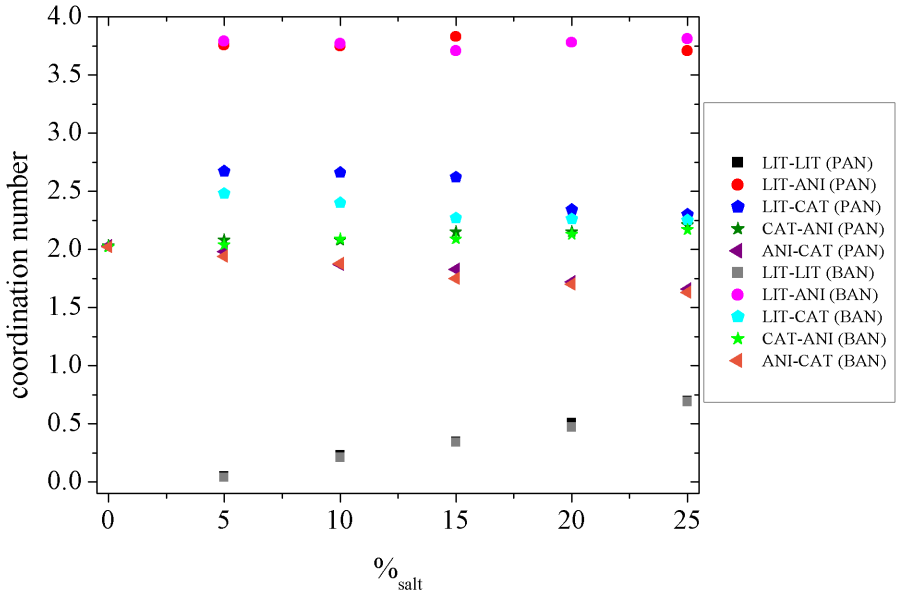

Figure 2.68 Evolution of the lithium cations VACFs with the amount of lithium salt in mixtures with (a) PAN and (b) BAN. The insets show the concentration dependence of the collision time.

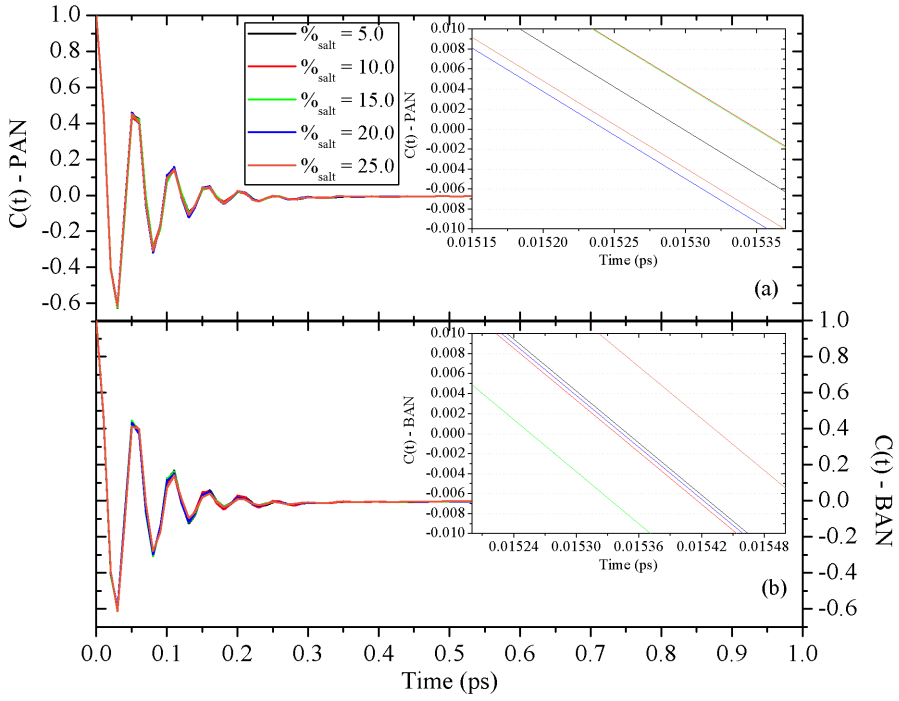

2.7. Molecular Dynamics Simulations of the Structure of the Graphene–Ionic Liquid/Alkali Salt Mixtures Interface.

In order to complete the research plan of this thesis, we analized the behaviour of inhomogeneous mixtures of ILs with alkali salts confined between two graphene walls. This is one of the first computational works that focus on IL doped with lithium salts near interfaces, since most of the simulations performed up to know had explored the electric double layer in ILs using probes.

To achieve this goal we carried out MD simulations of [Bmim][BF_4] mixed with lithium tetrafluoroborate ($LiBF_4$) and potassium tetrafluoroborate (KBF_4) between two charged and uncharged graphene walls [327]. The analysis of the structure revealed the formation of cation and anion layers in the proximities of the surface whose ion densities are greater than in the bulk. In addition, the average orientation of $[Bmim]^+$ cations was found to change from 36° with respect to the normal to larger angles the larger the charge of the walls. The free energy profiles provided us with very useful information concerning electrochemical applications, since large energy barriers associated to the ion layers in the electric double layer are predicted, and lithium and potassium cations seem to be able to reach the negative surface only for high amounts of salt.

Once again, we see that the addition of salt to the mixture has little effect on the distribution of the IL ions in the proximities of both charged and uncharged walls. The distribution of lithium and potassium cations is mainly determined by the formation of the ionic aggregates that salt cations form with the anions in their first solvation layer instead of by the electrode potential.

2.7.1. Paper VII: Molecular Dynamics Simulations of the Structure of the Graphene–Ionic Liquid/Alkali Salt Mixtures Interface; *Phys. Chem. Chem. Phys. 16 (2014) 13271-13278.*

Trinidad Méndez-Morales,[1] Jesús Carrete,[1,2] Martín Pérez-Rodríguez,[3] Óscar Cabeza,[4] Luis J. Gallego,[1] Ruth M. Lynden-Bell[5] and Luis M. Varela[1]

We performed molecular dynamics simulations of mixtures of 1-butyl-3-methylimidazolium tetrafluoroborate with lithium tetrafluorobate and potassium tetrafluorobate between two charged and uncharged graphene walls, in order to analyze the structure of the well-known formation of layers that takes place on liquids under confinement. For this purpose, we studied the molecular density profiles, free energy profiles for bringing lithium and potassium cations from the bulk mixture to the graphene wall and the orientational distributions of imidazolium rings within the first adsorbed layer as a function of salt concentration and electrode potential. The charge densities in the electrodes were chosen to be zero and ±1 e/nm^2, and the salt molar percentages were $\%_{salt}$=0, 10 and 25. We found that the layered structure extends up to 1 – 2 nm, where the bulk behaviour is recovered. In addition, whereas for the neutral surface the layers are composed of both ionic species, increasing the electrode potential, the structure changes to alternating cationic and anionic layers leading to an overcompensation of the charge of the previous layer. We also calculated the distribution of angles of imidazolium rings near neutral and charged graphene walls, finding a limited influence of the added salt. In addition, the average tilt of the imidazolium ring within the first layer goes from 36° with respect to a normal vector to the uncharged graphene wall to 62° in the presence of charged walls. The free energy profiles revealed that lithiums and potassiums are adsorbed on the negative surface only for the highest amount of salt, since the free energy barriers for approaching this electrode are considerably higher than k_BT.

[1]*Grupo de Nanomateriais e Materia Branda, Departamento de Física da Materia Condensada, Universidade de Santiago de Compostela, Campus Vida s/n E-15782, Santiago de Compostela, Spain*
[2]*CEA, DRT, 38054 Grenoble, France*
[3]Departamento de Física Aplicada, Universidade de Vigo, Lagoas-Marcosende s/n E-36310, Vigo, Spain
[4]*Facultade de Ciencias, Universidade da Coruña, Campus A Zapateira s/n E-15008, A Coruña, Spain*
[5]*University of Cambridge, University Chemical Laboratory, Lensfield Road, Cambridge, UK CB2 1EW*

2.7.2. Introduction

During the last decades there has been an increasing interest in room temperature ionic liquids (RTILs), salts composed entirely of ions with melting points below 100 °C, mainly due to their fascinating physical and chemical properties and their potential use in several fields. These key properties can be controlled with the appropiate selection of cations and anions, which contributes to their reputation as "green solvents" and makes them promising candidates for a great number of applications, ranging from biological uses, synthesis and catalysis, to lubrication or heat storage. In particular, they are known to show high ionic conductivity, low vapour pressure that makes them practically non-flammable and wide electrochemical window; which provide them with a huge potential in electrochemical applications such as supercapacitors, solar cells or lithium batteries, among others.

Regarding electrochemical devices, the choice of the electrolyte employed when producing a lithium battery is of crucial importance and the possibility of improving not only the efficiency, but also the safety of these devices by applying ILs as electrolytes, has led to a vast number of studies during the last few years [47, 234, 236, 241, 328–330]. Since ILs are practically non electroactive, any attempt to use them as electrolytes in lithium batteries requires mixing of the IL with a suitable lithium salt, resulting in a mixture of three or four ions. At this point, the main aspects that need particular attention for optimum battery operation are: firstly, a detailed picture of the solvation processes of lithium ions in the bulk IL and, secondly, the influence of these lithium salts on the well-known solvation layers formed at the electrode/IL interface. Although both aspects play a fundamental role in the performance of lithium batteries, they still remain as open questions and a deeper understanding is required.

Concerning lithium environment in bulk IL mixtures, very few publications have focused on the structural and dynamic properties of lithium salts doping aprotic ionic liquids (AILs) (see Ref.[228] and references cited therein) and, to our knowlegde, only two papers have been reported for protic ionic liquids (PILs) [278, 305].

On the other hand, due to the fact that understanding the influence of the nature of the IL ions, temperature and applied electrode potential on the properties of the electric double layer is of paramount importance for theoretical and practical purposes, as indicated in some influential experimental [331] and computational [69] results, much theoretical, computational and exper-

imental research devoted to this issue is needed. In spite of this, it must be said that even though great progress has been made towards a fundamental understanding of the behaviour of ILs at charged interfaces, this question has been much less extensively studied than bulk properties. In this case, the analysis of the differential capacitance (DC) as a function of the electrode potential has been regarded as a helpul source of information about the electric double layer behaviour and, up to now, many experimental [332–335] and computational [336–345] studies have reported bell-shaped or camel-shaped DC curves.

From the theoretical point of view, Kornyshev stressed [346] that the Gouy-Champman-Stern theory could not be applied to these dense ionic systems, in which the effects of ionic correlations and overscreening are important [347]. The author proposed a mean-field theory (MFT) to interpret the potential dependence of the double-layer capacitance at a planar metal/IL interface. However, last year Gebbie *et al.* [348] reported a controversial picture in which ILs would behave as dilute electrolyte solutions due to the existence of a very limited amount of unpaired ions in ILs. Their reported results for the force between colloidal particles immersed in bulk ILs was interpreted as showing that the screening of charged surfaces by ILs takes place through the formation of both bound (Stern) and diffuse electric double layers, where the latter is composed of effectively dissociated ions. Hence, the essentials of screening in ILs are still in need of more stable foundations.

In addition, the arrangement and the orientations of the ions at the IL/electrode interface, with a multiple layer organization at the surface, have been experimentally investigated by means of atomic force microscopy (AFM) [349–351], scanning tunneling microscope (STM) [350, 352, 353], a surface force apparatus (SFA) [354, 355], X-ray reflectivity [356] and X-ray spectroscopy studies [357]. By contrast, several groups concluded that some ILs do not show interfacial layering, but only a single ion layer of enhanced electron density [358–360].

Since the formation of the electric double layers is a highly complicated phenomena, experimental mesurements can be complemented by atomistic simulations in order to shed some light into the structure of the electrode/IL interface. In addition, due to their lower cost as compared to experimental research, computer simulations are an essential tool for performing systematic studies of ILs and designing new and improved materials. Thus, many groups have focused up to now on the interface behaviour of IL/solid systems from a computational perspective [361–367], molecular dynamics (MD) being the

most widely employed technique. For example, Pinilla *et al.* [368, 369] employed MD simulations to study the behaviour of 1,3-dimethylimidazolium chloride ([DMIM][Cl]) confined between two charged (± 0.12 $e \cdot nm^{-2}$) and neutral parallel walls. Their simulations revealed a clear structure of layers with a high-density peak at the proximities of the walls followed by weaker oscillations toward the bulk system, as well as a rearrangement of the ions with increasing field strength. In addition, they determined that cations at the interface tend to orient their rings tilted around 70° with respect to the surface. More recently, Lynden-Bell *et al.* [67, 68] investigated the properties of [DMIM][Cl] near charged graphene surfaces. They also reported the formation of several alternating layers of cations and anions with ion densities higher than in the bulk even at the non-charged electrode surface. Regarding the orientation of the ions, the authors found that, at the neutral electrode, the preferential orientation of the cations is parallel to the surface, whereas near the negative electrode some of them tend to be perpendicular to the surface. They concluded that the IL provides excellent electrostatic screening at distances longer than 1 – 2 nm.

In spite of the number of studies that have explored the electric double layer structure in ILs using probes, to our knowledge only one publication has been reported focusing on IL/lithium salt mixtures near interfaces. In this case, Smith *et al.* [370] performed atomistic MD simulations of a lithium iron phosphate ($LiFePO_4$) surface in contact with a mixture of 1-ethyl-3-methylimidazolium bis(fluorosulfonyl)amide ([EMIM][FSI]) with a 22.6% of lithium bis(fluorosulfonyl)amide (LiFSI). They observed a free energy barrier for bringing $[Li]^+$ cations from the bulk system to the surface of around 16 $kJ \cdot mol^{-1}$.

In this work we performed MD simulations of mixtures of 1-butyl-3-methylimidazolium tetrafluoroborate ([BMIM][BF_4]) (chosen by electrochemical interest and because its bulk properties had been analyzed previously [228]) with lithium tetrafluoroborate ($LiBF_4$) and potassium tetrafluoroborate (KBF_4) confined between two parallel graphene surfaces, with the aim of gaining some insight into the structure of IL/alkali salts electrolytes at the proximities of charged and neutral electrodes. Molecular density profiles, free energy profiles for bringing $[Li]^+$ and $[K]^+$ cations from the bulk mixture to the graphene wall and imidazolium orientational distributions within the first adsorbed layer were analyzed as a function of salt concentration and electrode potential.

The outline of this paper is as follows. In section 2.7.3, we provide a detailed account of the simulation method. In section 2.7.4, we present and discuss the results obtained and concluding remarks are offered in section 2.7.5.

2.7.3. Simulation details

We performed MD simulations of [BMIM][BF_4] doped with either $LiBF_4$ or KBF_4 enclosed between two flat graphene walls using Gromacs 4.5.4 package [70]. In order to avoid the system being "trapped" in a local minimum due to the well-known high viscosity of ILs, the temperature investigated was $T = 450$ K, and the molar percentages of salt considered in the mixtures were $\%_{salt} = 0$, 10 and 25. The number of lithium/potassium salt molecules was calculated for each situation by considering each ionic pair as a single unit in the calculation of mole fractions.

The fixed graphene walls had charges and a Lennard-Jones (LJ) center on each carbon seat and they were built with the help of the Visual Molecular Dynamics (VMD) package [78]. The charges on the carbon atoms of the graphene sheets were chosen to give wall charge densities of $+1\ e \cdot nm^{-2}$ and $-1\ e \cdot nm^{-2}$ in the left and right electrodes, respectively (and zero in the uncharged case). Their LJ parameters were $\sigma_C = 3.55 \cdot 10^{-1}$ nm and $\varepsilon_C = 2.9288 \cdot 10^{-1}\ kJ \cdot mol^{-1}$. The graphene sheets were placed parallel to the XY-plane in such a way that one electrode was kept at $Z = 0$ and the other one was located at positive values of Z at the distance needed to obtain the bulk density in the middle of the rectangular box used to emulate a semi-infinite slab geometry. All three coordinates of these carbon atoms were frozen at their initial values and the electrodes were held rigid with a carbon bond length of $l_{CC} = 0.142$ nm. Periodic boundary conditions were applied in all directions and the graphene electrodes were considered as periodic molecules in order to couple to themselves through the periodic boundary conditions. A slab of vacuum was left outside the confining sheets for avoiding artificial influence from periodic images, as shown in Fig. 2.69.

We employed the OPLS-AA force field in order to carry out the parametrization of the ions. This all-atom version of the OPLS force field, in which every hydrogen atom bonded to carbon is modeled explicitly, was developed by Jorgensen [153] for different organic liquids. The functional form of the OPLS force field takes the standard form

Figure 2.69 Schematic representation of the simulation box for the pure IL along the Z direction. The liquid is confined between two walls separated 10.48 nm, and whose sides measure 4.2 nm. The system is periodically repeated every 16 nm in the Z direction.

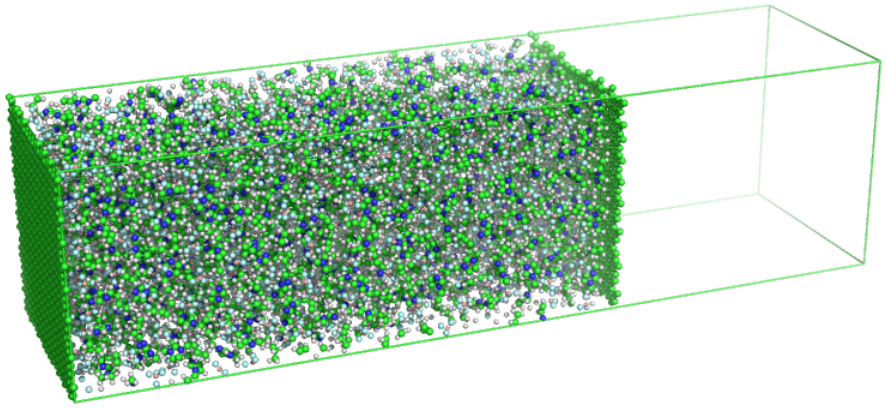

$$
\begin{aligned}
E = &\sum_i K_{b,i}\left[r_i - r_{0,i}\right]^2 + \sum_i K_{b,i}\left[\theta_i - \theta_{0,i}\right]^2 + \\
&+ \sum_i \left[\frac{1}{2}V_{1,i}(1+\cos(\varphi_i)) + \frac{1}{2}V_{2,i}(1+\cos(2\varphi_i)) + \right. \\
&\left. + \frac{1}{2}V_{3,i}(1+\cos(3\varphi_i)) + \frac{1}{2}V_{4,i}(1+\cos(4\varphi_i))\right] + \\
&+ \sum_i \sum_{j<i} \left\{ \frac{1}{4\pi\varepsilon_0}\frac{q_i q_j e^2}{r_{ij}} + 4\varepsilon_{ij}\left[\left(\frac{\sigma_{ij}}{r_{ij}}\right)^{12} - \left(\frac{\sigma_{ij}}{r_{ij}}\right)^{6}\right]\right\},
\end{aligned}
\tag{2.32}
$$

which includes intramolecular interactions such as bond stretching, angle bending, dihedral torsion, as well as van der Waals and Coulombic interactions. The parameters employed in eqn (2.32) are the force constants K, the nominal values r_0 and θ_0, the Fourier coefficients V, and the partial atomic charges q fixed on each atom center. σ_{ij} and ε_{ij} represent the LJ radii and potential well depths, respectively, which are obtained from parameters for each type of atom by using geometric combination rules $\epsilon_{ij} = \sqrt{\epsilon_{ii}\epsilon_{jj}}$ and $\sigma_{ij} = \sqrt{\sigma_{ii}\sigma_{jj}}$. The imidazolium cation was modeled by using the all-atom representation of the CH_2 and CH_3 groups in the alkyl chain, as well as that of the methyl group attached to the imidazolium ring, and its parameters were assigned according

to the values reported by Sambasivarao and Acevedo [154]; while lithium and potassium cations were modeled by a single site of charge +1 and LJ parameters taken directly from Gromacs database. As for the anion, $[BF_4]^-$ was modelled as a set of 5 sites with partial charges of +1.776 for the boron atom and −0.544 for the fluorine atoms [155]. The electronic polarizability for both the graphene walls and the electrolyte was not taken into account in our study, since even though polarizability has been found to have a deep impact on dynamic properties of ILs, Yan *et al.* [371] showed that the major structural properties of the IL/vacuum interface for both polarizable and non polarizable models were similar. Long-range electrostatic interactions were treated by using the Particle Mesh Ewald (PME) [77] method with a FFT grid spacing of 12 nm, a 1.1 nm cut-off distance for the real space sum and cubic interpolation; together with Yeh-Berkowitz corrections for our slab geometry [79, 80]. A cut-off radius of 1.1 nm was used for LJ interactions, and a neighbor updated for the nonbonded interactions was made up to this same distance from the central ion and was updated every ten simulation steps. The Linear Constraint Solver (LINCS) algorithm [159, 160] with a fourth-order expansion of the constraint coupling matrix was used to fix all the bond lengths.

Initial configurations were relaxed for 10^6 steps using a conjugate gradients algorithm in order to remove bad contacts resulting from the initial random configuration of ions. The maximum step size and the tolerance were set to 0.01 nm and 1 kJ/(nm · mol), respectively. For each molar percentage of salt, the system was heated during 100 ps from 450 K to 1000 K in the NVT ensemble,followed by a run of 100 ps; cooling it gradually to 450 K during further 100 ps. Following annealing, each mixture was equilibrated for 30 ns at 450 K and the resultant configurations were taken as the initial configurations for the production runs. The time step of the simulations was 2 fs. The temperature was controlled by using the V-rescale thermostat [161]. Cations and anions were separated in two (or three) baths with temperature coupling constants of 0.1 ps. The results of an additional 10 ns–long simulations in the NVT ensemble were used for obtaining structural information about the systems.

2.7.4. Results and discussion

In order to shed some light on the structure of the electric double layer at the interface between ILs-alkali salts mixtures and planar electrodes, Fig. 2.70 and 2.71 show, as a function of the distance from the surface, the number dens-

ity of $[BMIM]^+$ and $[BF_4]^-$ ions near positively (a), negatively (b) and neutrally (c) charged graphene walls for mixtures of [BMIM][BF_4] with $LiBF_4$ and KBF_4, respectively. For this calculations, the positions of the imidazolium cations and tetrafluoroborate anions were computed by considering the carbon atom between the two nitrogens of the imidazolium ring (C_2) and the boron atom (B_1), respectively. The density profiles for $[Li]^+$ and $[K]^+$ cations were not included since their heights are much lower than those of the ions of the IL, but the positions of their peaks can be inferred from the free energy profiles shown in Fig. 2.74 below. One remarkable feature shown in Fig. 2.70.c and 2.71.c is that, even in the absence of an applied field, the graphene surfaces have an effect on the structure of the liquid. The formation of layers near a neutral graphene wall can be clearly observed in both systems, in which the density of the mixture is much higher than in the bulk. These oscillations of the density in the interfacial area are progressively damped out until values for bulk mixtures are recovered at around 1.5 nm within three layers from the surface. Such layering behaviour has been reported previously in many computational studies [67, 68, 361–366, 368, 369]. In addition, the layers of the dense region are composed of both ionic species of the IL, $[BMIM]^+$ cations and $[BF_4]^-$ anions, with the presence of imidazoliums approaching slightly closer to the wall and a larger local density of the tetrafluoroborates, probably due to their smaller size. However, there are neither $[Li]^+$ nor $[K]^+$ cations in the first contact layer at any amount of salt (they are firstly located at 0.7 nm); thus, the concentration of adsorbed lithiums and potassiums is zero in contact with neutral graphene.

The highly inhomogeneous layering of the IL in the neighborhood of the graphene electrode is also observed for charged electrodes. Besides, the surface charge induces molecular reorganization. In comparison with the uncharged surface, the first layer slightly changes its position and moves towards the graphene wall, but its height considerably increases. Moreover, this first peak is composed only of cations in the proximities of the negatively charged electrode ($-1\ e \cdot nm^{-2}$) and, in the same way, composed only of anions in the vicinities of the positively charged surface ($+1\ e \cdot nm^{-2}$). For the latter, the local density is much higher than that of cations near the negative wall, since the first layer can accommodate more tetrafluoroborates due to their smaller size. However, it seems that they do not approach the electrode more than the imidazoliums do. As a result, there are neither adsorbed $[BMIM]^+$ cations on the positive wall nor $[BF_4]^-$ anions adsorbed on the negative surface, and it also results in positive and negative charge densities near the negative and

Figure 2.70 Number density (in nm^{-3}) for the $[BMIM]^+$, (C2), and $[BF_4]^-$, (B1), ions near positive (a), negative (b) and neutral (c) as a function of the distance to the graphene walls in mixtures of [BMIM][BF_4] with $LiBF_4$.

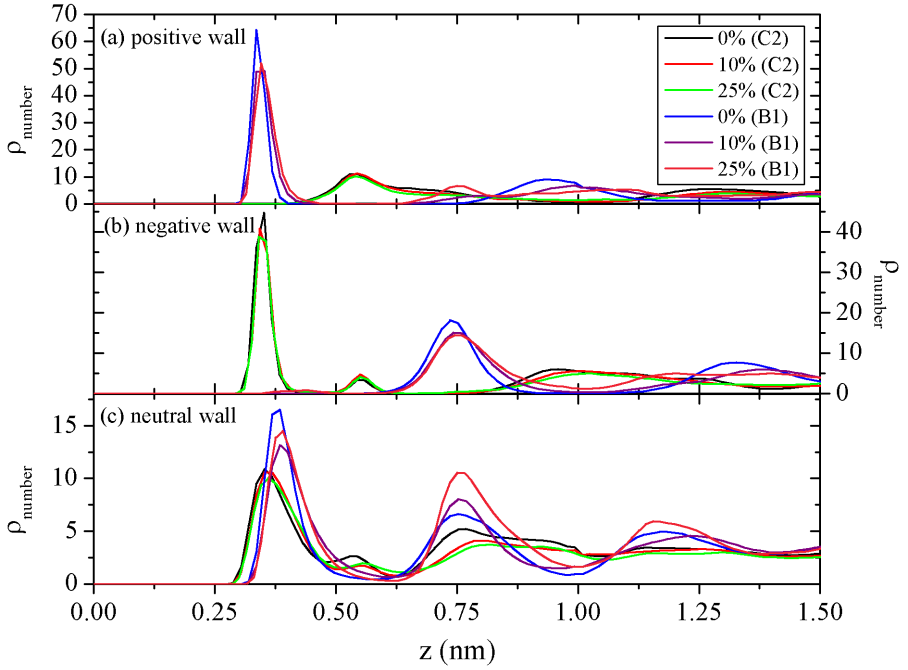

the positive electrode, respectively. This excess of positive/negative charge that overcompensates the electrode charge attracts ions of the opposite ionic species, giving place to the formation of a lower second peak of negative/positive density, respectively. Again, this second layer that overcompensates the charge on the first layer attracts another layer with opposite charge density and so on, until the bulk behavior is reached and all the oscillations are completely smoothed out. In this case, the alternating layers of cations and anions persist up to approximately 2.0 nm for both electrodes and the region where oscillations take place comprises 5 layers. It can be seen that the addition of salt has little effect on the $[BMIM]^+$ and $[BF_4]^-$ density profiles near both charged and uncharged electrodes. On the other hand, as can be seen in Fig. 2.74 below, near the positively charged surface (Fig. 2.70.a and 2.71.a) lithium and potassium cations are found at 0.47 and 0.49 nm respectively, between the first anionic layer and the second cationic layer, whereas the behaviour in the vi-

Figure 2.71 Number density (in nm^{-3}) for the $[BMIM]^+$, (C2), and $[BF_4]^-$, (B1), ions near positive (a), negative (b) and neutral (c) as a function of the distance to graphene walls in mixtures of $[BMIM][BF_4]$ with KBF_4.

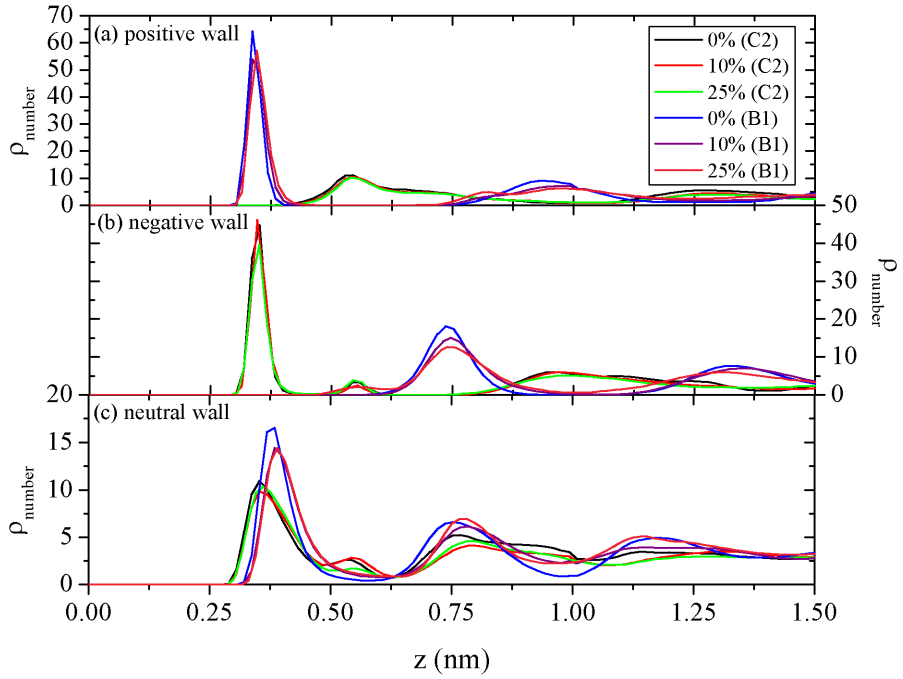

cinities of the negatively charged electrode (Fig. 2.70.b and 2.71.b) is slightly different. In this case, for the lowest concentration of salt, 10%, $[Li]^+$ and $[K]^+$ cations are located at around 0.9 nm in the third cationic layer. This shows that the formation of the previously reported anionic aggregates that lithium and potassium form with the anions in their first solvation shell [228, 278] is not avoided by the electrode potential or the presence of the surfaces, and it has the greatest impact on the organization of these cations. The picture slightly changes for the highest simulated amount of salt, 25%, for which both lithium and potassium cations approach the negative graphene surface up to 0.21 nm and 0.28 nm, respectively. Those distances are closer to the negative electrode than the first cationic layer, meaning that for lithium/potassium cations to be adsorbed on the graphene wall a considerable amount of salt must be added to the IL, which has a great importance for redox processes.

This behaviour can be clearly observed in Fig. 2.72, in which we show the

structure of the electric double layer near the negative graphene wall for mixtures of [BMIM][BF_4] with a 25% of $LiBF_4$ (left) and KBF_4 (right). It can be observed that, in both cases, the first layer consists of a dense layer of imidazolium cations that overcompensates the wall charge. This first layer is then followed by a second one of tetrafluorobate anions due to overcompensations of the charge in the previous layer. Even though the greatest amount of $[Li]^+$ and $[K]^+$ cations is found in the third cationic layer, some of them are able to approach the wall more closely than any other ionic species for this concentration of salt.

Taking all this information into account, we considered the orientations of imidazolium cations in the first layer of cations in order to know more details of the electric double layer in this kind of systems. The orientational structure of the ring can be analysed in terms of the angle θ between the vector normal to the walls (parallel to the Z-axis) and a vector normal to the imidazolium ring. In Fig. 2.73 we plot the probability distribution functions for the ring orientations as a function of $|\cos\theta|$. Note that positive and negative values of $\cos\theta$ are equally likely as the ring is flat and that a uniform distribution of orientations in space would give a flat distribution as a function of $\cos\theta$. Fig. 2.73 shows the distributions in the first layers of cations near (a) positively charged walls (up to 1.0 nm), (b) negatively charged walls (up to 0.45 nm) and (c) neutral walls (up to 0.65 nm). In addition, in Table 2.7 we include the average values of $\cos^2\theta$ for the $[BMIM]^+$ cations in the first cation layer near the walls. The results show that the average angle between normal to ring is of about 36 $^\circ$ with the normal vector to the neutral wall. Charging the walls results in a new average angle of 62 $^\circ$ between the ring of the cation and both positive and negative walls. These results are in good agreement with those reported by Baldelli near charged IL-metal interface from *SFG* spectra [359].

We observe in Fig. 2.73 that at uncharged electrodes the most probable configuration for imidazolium rings is to lie nearly flat on the surface, although there exist a continuous distribution of orientations extending even to orientations perpendicular to the wall. The influence of the added salt in this distribution is almost negligible for uncharged walls. However, charging the wall leads to new configurations for the rings. Near the positively charged wall, the most probable configuration of the $[BMIM]^+$ rings is that in which they are normal to the wall, but there is a broad range of orientations with the probability distribution decaying smoothly to include configurations in which the rings lie flat against the charged surface. In this case, added salt increases the

Figure 2.72 Snapshots of the structural organization of the ions near negatively charged graphene walls from simulations of [BMIM][BF_4] doped with a 25% of $LiBF_4$ (a) and a 25% KBF_4 (b). The relative size of lithium (dark pink) and potassium (violet) atoms has been exaggerated for the purpose of clarity. Colour coding for the rest of the atoms is as follows: green, carbons; dark blue, nitrogens; light blue, fluorines; and light pink, borons. Hydrogens have been removed for the purpose of clarity.

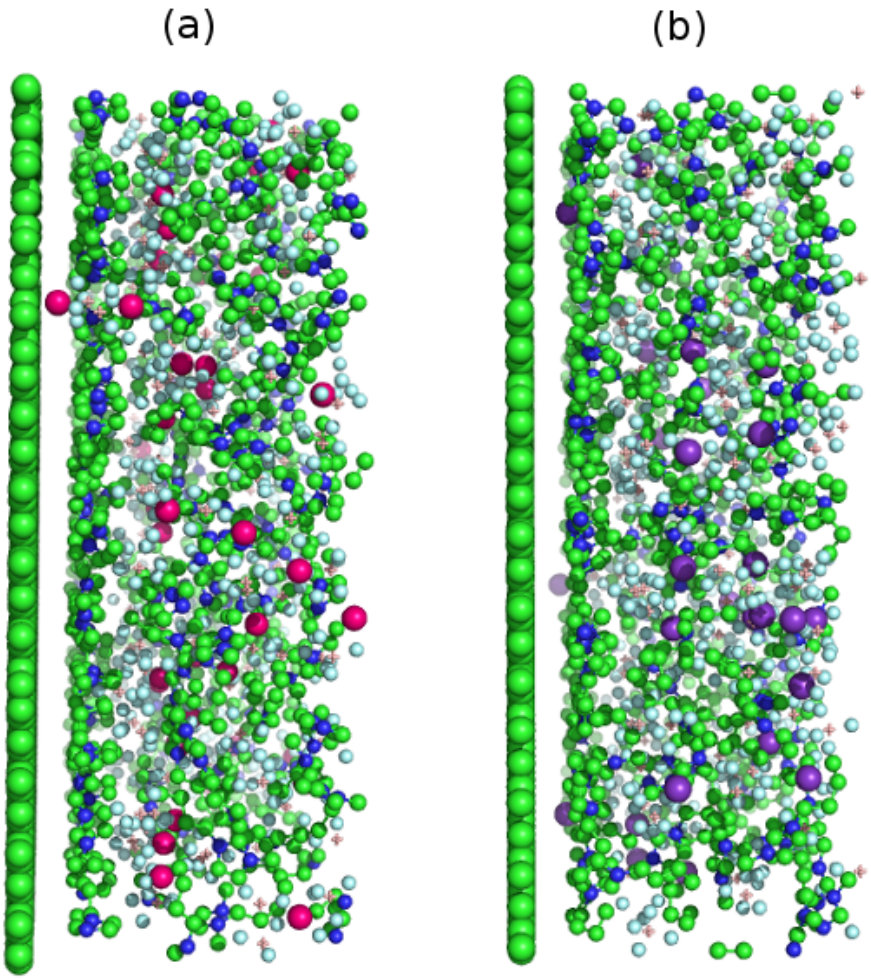

Figure 2.73 Probability distribution of $|\cos\theta|$ for the $[BMIM]^+$ cations in the first layer near positively (a), negatively (b) and neutrally (c) charged graphene walls for mixtures of [BMIM][BF_4] with $LiBF_4$ and KBF_4.

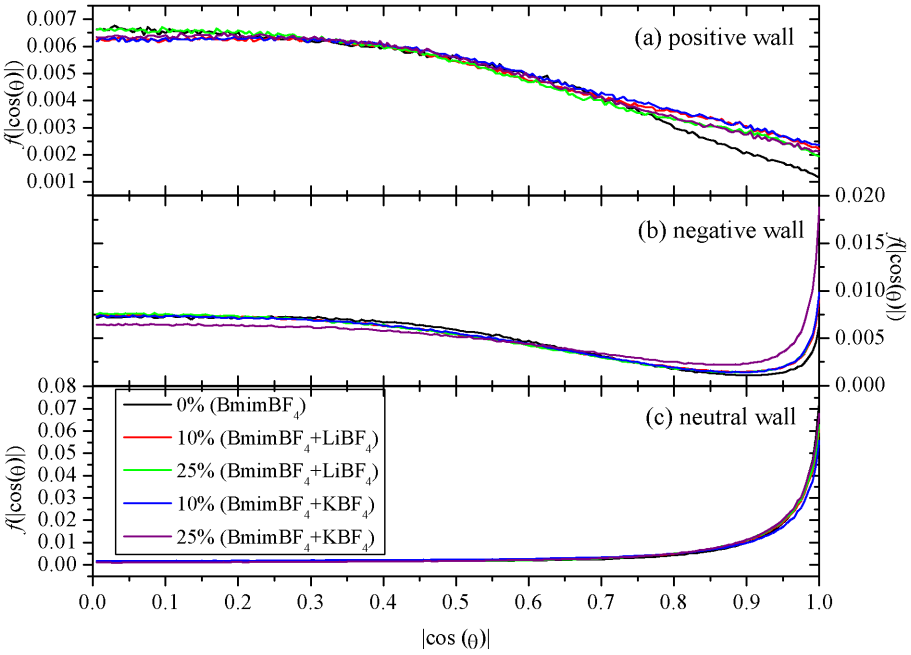

dispersion of the distribution function and chains laying flat to the charged electrode are more likely. On the other hand, near the negatively charged electrode, although a significant fraction of the rings lie flat on the surface, there is a large region of almost constant probability extending from 66° to 90°. Moreover, low-angle orientations are scarcely probable as indicated by the minima of $f(|\cos\theta|)$ near $|\cos\theta| = 0.9$. These minima are displaced towards higher angles with salt addition, and more ions are allowed to lie flat to the interface in these circumstances.

Finally, in Fig. 2.74 we determined the free energy profiles for bringing a lithium or potassium cation from the bulk to the graphene electrode by

$$A(z) = -kT \cdot \ln\left(\frac{\rho_{CI}(z)}{\rho_{CI}(bulk)}\right). \tag{2.33}$$

We can observe that these curves show oscillations due to the layering be-

Table 2.7 Average values of $\cos^2(\theta)$ for the $[BMIM]^+$ cations in the first layer of cations near positively (a), negatively (b) and neutrally (c) charged graphene walls for mixtures of $[BMIM][BF_4]$ with $LiBF_4$ and KBF_4.

	$< \cos^2\theta >$		
	neutral	+1 e/nm^2	−1 e/nm^2
0.0 %	0.68	0.24	0.20
10.0 %-$LiBF_4$	0.67	0.23	0.22
25.0 %-$LiBF_4$	0.69	0.26	0.22
10.0 %-KBF_4	0.62	0.26	0.21
25.0 %-KBF_4	0.72	0.25	0.28

haviour of the IL in the proximities of the wall. Additionally, the height of the barriers impeding the cations of the salt from approaching the walls generally decreases with the amount of salt in the mixtures. Independently of the electrode potential, the highest barriers are found for the lowest concentration of $[Li]^+$ cations, 10%, going from 12 kJ $\cdot$ mol^{-1} in the neutral wall to 25 kJ $\cdot$ mol^{-1} in the unfavourable positively charged wall. The values of the free energy barriers near the neutral wall are comparable to that obtained by Smith *et al.* [370] of around 16 kJ $\cdot$ mol^{-1} for LiFSI doping [EMIM][FSI]. Another remarkable feature is that, as we said previously, both $[Li]^+$ and $[K]^+$ cations can be adsorbed on the negative electrode only at high concentrations of salt due to the occurrence of very high free energy barriers at *ca.* 0.5 nm that they must overcome for getting to the wall. This is probably due to the dense layer of imidazolium cations that causes a very high energy barrier for the salt cations to approach the negative wall. We get a divergence partly due to the calculation procedure, so the physical barrier is expected to be very high compared to k_BT. Moreover, we can also observe in Fig. 2.74.b the differences in position and depth of the first minima associated with both cations, for potassium being deeper than for lithium, and the displacement of their barriers in Fig. 2.74.a, which are associated with their different radii.

2.7.5. Conclusions

Using MD simulations, we have analyzed the behaviour of mixtures of $[BMIM][BF_4]$ with $LiBF_4$ and KBF_4 confined between two parallel charged and uncharged graphene walls, in order to clarify the potential use of ILs as electrolytes in electrochemical devices. Although for the technical reasons described

Figure 2.74 Free energy profiles for lithium and potassium cations approaching graphene surfaces with positive (a), negative (b) and neutral (c) charge densities for mixtures of [BMIM][BF_4] with $LiBF_4$ and KBF_4.

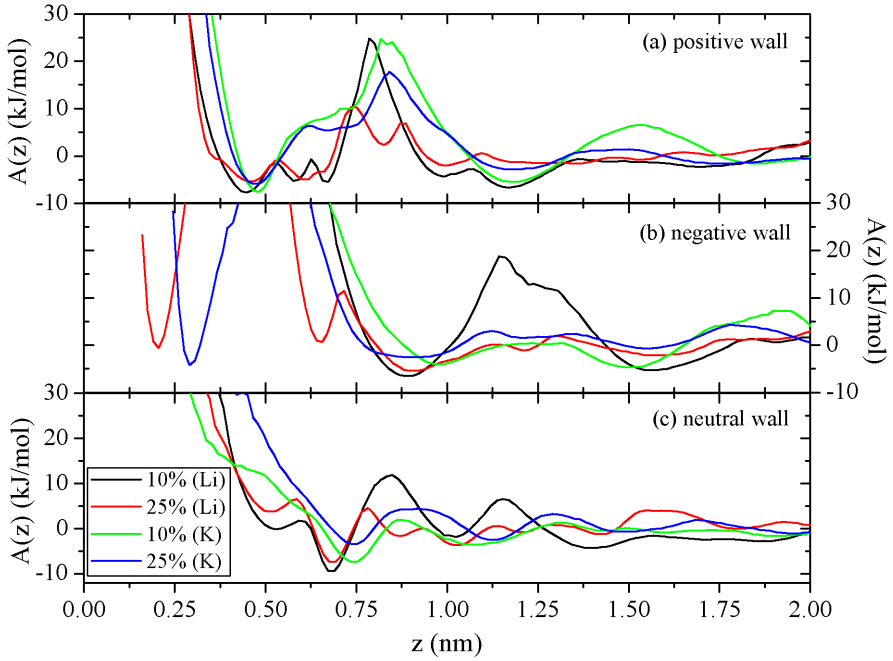

in the corresponding section the calculations in this paper were performed at 450 K, it is expected that our results will also be representative of the behaviour of the systems considered at somewhat lower temperatures. Accordingly, they can be useful for practical applications of those systems; for example, as supercapacitors or batteries.

Number density profiles in the Z direction show, even for the uncharged electrodes, the formation of a layered structure with ion densities higher than in the bulk in the proximities of the surface. This layers were found to be composed of both ionic species of the IL, with the imidazolium cations approximating slightly closer to the electrode. In addition, $[BMIM]^+$ rings within the first layer tend to be oriented in such a way that they form an average angle of around 36° with the wall and, in this case, there are no lithium or potassium cations absorbed on the walls.

As the electrode potential increases, a systematic rearrangement of the ions,

in which tetrafluorobate anions segregate toward the positive electrode and away from the negative wall and imidazolium cations show the opposite behaviour, takes place. In neutral graphene interface, $[BMIM]^+$ cations orient with an average angle of 36° with respect to the normal vector to the surface, and upon charging they tend to be preferentially oriented in a more perpendicular fashion, forming an average angle of 62° with both the positive and the negative electrode due to the high density of cations screening the negatively charged electrode and the first layer of cations in the positively charged one. Once again, we see the formation of layers near the electrode when the electrode is charged. These layers are formed mainly by cations near the negative electrode and anions near the positive electrode. Oscillations of charge were clearly observed to a depth of 2 nm. Moreover, the fact that we observe the same average angles in the first layer of cations with the negative and the positive electrode shows that the charge of the positive electrode is overcompensated by the layer of anions. This is the result of a delicate balance between screening and packing. We also observed that only for a salt concentration of 25% were $[Li]^+$ and $[K]^+$ able to reach on the negatively charged electrode, but the free energy barriers for these cations approaching the negative wall are considerably higher than $20K_BT$.

References

1. Walden, P. *Bull. Russian Acad. Sci.* **1800,** 405–422 (1914).
2. Wasserscheid, P. & Keim, M. *Angew. Chem. Int. Ed. Engl.* **39,** 3772–3789 (2000).
3. Welton, T. *Chem. Rev.* **99,** 2071–2084 (1999).
6. MacFarlane, D. R., Forsyth, M., Howlett, P. C., Pringle, J. M., Sun, J., Annat, G., Neil, W. & Izdorodina, E. *Acc. Chem. Res.* **40,** 1165–1173 (2007).
10. Ye, C., Liu, W., Chen, Y. & Yu, L. *Chem. Commun.* **2001,** 2244–2245 (2001).
12. Han, X. & Armstrong, D. W. *Acc. Chem. Res.* **40,** 1079–1086 (2007).
16. Carmichael, A. J. & Seddon, K. R. *J. Phys. Org. Chem.* **13,** 591–595 (2000).
22. Wilkes, J. S. & Zaworotko, M. J. *J. Chem. Soc., Chem. Commun.* **1992,** 965–967 (1992).
26. Tokuda, H., Hayamizu, K., Ishii, K., Susan, M. A. B. H. & Watanabe, M. *J. Phys. Chem. B* **108,** 16593–16600 (2004).
27. Tokuda, H., Hayamizu, K., Ishii, K., Susan, M. A. B. H. & Watanabe, M. *J. Phys. Chem. B* **109,** 6103–6110 (2005).
28. Tokuda, H., Ishii, K., Susan, M. A. B. H., Tsuzuki, S., Hayamizu, K. & Watanabe, M. *J. Phys. Chem. B* **110,** 2833–2839 (2006).
30. Wilkes, J. S. *J. Mol. Catal. A: Chem.* **214,** 11–17 (2004).
36. Wasserscheid, P. & Welton, T. *Ionic liquids in synthesis* (Wiley Online Library, 2003).
39. Canongia-Lopes, J. N. & Pádua, A. A. H. *J. Phys. Chem. B* **110,** 3330–3335 (2006).
40. Triolo, A., Russina, O., Bleif, H.-J. & Di Cola, E. *J. Phys. Chem. B* **111,** 4641–4644 (2007).
41. Atkin, R. & Warr, G. G. *J. Phys. Chem. B* **112,** 4164–4166 (2008).
42. Freemantle, M. *An Introduction to Ionic Liquids* (RSC Publishing, 2009).
47. Galiński, M., Lewandowski, A. & Stepniak, I. *Electrochim. Acta* **51,** 5567–5580 (2006).
50. Capelo, S. B., Méndez-Morales, T., Carrete, J., Lago, E. L., Vila, J., Rodríguez, O. C. J. R., Turmine, M. & Varela, L. M. *J. Phys. Chem. B* **116,** 11302–11312 (2012).

51. K. Fumino, A. W. & Ludwig, R. *Angew. Chem. Int. Ed.* **48,** 3184–3186 (2009).

52. Fernández-Castro, B., Méndez-Morales, T., Carrete, J., Fazer, E., Cabeza, O., Rodríguez, J. R., Turmine, M. & Varela, L. M. *J. Phys. Chem. B* **115,** 8145–8154 (2011).

60. Frenkel, D. & Smit, B. *Understanding molecular simulation: From algorithms to applications* (Academic Press: New York., 1996).

61. Hansen, J. P. & McDonald, I. R. *Theory of simple liquids* (Academic press: Oxford, 1986).

63. Urahata, S. M. & Ribeiro, M. C. C. *J. Chem. Phys.* **120,** 1855–1863 (2004).

64. Urahata, S. M. & Ribeiro, M. C. C. *J. Chem. Phys.* **122,** 024511(1)–024511(9) (2005).

65. Hanke, C. G. & Lynden-Bell, R. M. *J. Phys. Chem. B* **107,** 10873–10878 (2003).

66. Jahangiri, S., Taghikhani, M., Behnejad, H. & Ahmadi, S. J. *Mol. Phys.* **106,** 1015–1023 (2008).

67. Lynden-Bell, R. M., Frolov, A. I. & Fedorov, M. V. *Phys. Chem. Chem. Phys.* **14,** 2693–2701 (2012).

68. Fedorov, M. V. & Lynden-Bell, R. M. *Phys. Chem. Chem. Phys.* **14,** 2552–2556 (2012).

69. Merlet, C., Rotenberg, B., Madden, P. A., Taberna, P.-L., Simon, P., Gogotsi, Y. & Salanne, M. *Nat. Mater.* **11,** 306–310 (2012).

70. Spoel, D. V. D., Lindahl, E., Hess, B., Buuren, A. R. V., Apol, E., Meulenhoff, P. J., Tieleman, D. P., Sijbers, A. L. T. M., Feenstra, K. A., Drunen, R. V. & Berendsen, H. J. C. *Gromacs User Manual version 4.0* (http://www.Gromacs.org, 2005).

71. Hess, B., Kutzner, C., Spoel, D. V. D. & Lindahl, E. *J. Chem. Theory Comput.* **4,** 435–447 (2008).

74. Scott, W. R. P., Hünenberger, P. H., Tironi, I. G., Mark, A. E., Billeter, S. R., Fennen, J., Torda, A. E., Huber, T., Krüger, P. & Gunsteren, W. F. V. *J. Phys. Chem. A* **103,** 3596–3607 (1999).

75. Jorgensen, W. L., Maxwell, D. S. & Tirado-Rives, J. *J. Am. Chem. Soc.* **118,** 11225–11236 (1996).

77. Darden, T., York, D. & Pedersen, L. *J. Chem. Phys.* **98,** 10089–10094 (1993).

78. Humphrey, W., Dalke, A. & Schulten, K. *J. Mol. Graphics* **14,** 33–38 (1996).

79. Yeh, I. & Berkowitz, M. L. *J. Chem. Phys.* **111,** 3155–3162 (1999).

80. Yeh, I. & Berkowitz, M. L. *J. Chem. Phys.* **112,** 10491–10495 (2000).

81. Méndez-Morales, T., Carrete, J., Cabeza, O., Gallego, L. J. & Varela, L. M. *J. Phys. Chem. B* **115,** 6995–7008 (2011).

82. Wilkes, J. S. *Green Chem.* **4,** 73–80 (2002).

83. Hagiwara, R. & Ito, Y. *J. Fluorine Chem.* **105,** 221–227 (2000).

84. Earle, M. J. & Seddon, K. R. *Pure Appl. Chem.* **72,** 1391–1398 (2000).

85. Earle, M. J., Esperança, J. M. S. S., Gilea, M. A., Canongia-Lopes, J. N., Rebelo, L. P. N., Magee, J. W., Seddon, K. R. & Widegren, J. A. *Nature (London, U.K.)* **439,** 831–834 (2006).

86. Wakai, C., Oleinikova, A., Ott, M. & Weingärtner, H. *J. Phys. Chem. B* **109,** 17028–17030 (2005).

87. Carrete, J., García, M., Rodríguez, J., Cabeza, O. & Varela, L. *Fluid Phase Equilib.* **301,** 118–122 (2011).

88. Cuadrado-Prado, S., Domínguez-Pérez, M., Rilo, E., García-Garabal, S., Segade, L. & C. Franjo, O. C. *Fluid Phase Equilib.* **278,** 36–40 (2009).

89. Bowers, J., Butts, C. P., Martin, P. J., Vergara-Gutierrez, M. C. & Heenan, R. K. *Langmuir* **20,** 2191–2198 (2004).

90. Malham, I. B., Letellier, P. & Turmine, M. *J. Phys. Chem. B* **110,** 14212–14214 (2006).

91. Firestone, M. A., Dzielawa, J. A., Zapol, P., Curtiss, L. A., Seifert, S. & Dietz, M. L. *Langmuir* **18,** 7258–7260 (2002).

92. Antonietti, M., Kuang, D., Smarsly, B. & Zhou, Y. *Angew. Chem. Int. Ed.* **43,** 4988–4992 (2004).

93. Jiang, W., Wang, Y. & Voth, G. A. *J. Phys. Chem. B* **111,** 4812–4818 (2007).

94. Kelkar, M. S., Shi, W. & Maginn, E. J. *Ind. Eng. Chem. Res.* **47,** 9115–9126 (2008).

95. Canongia-Lopes, J. N., Costa-Gomes, M. F. & Pádua, A. A. H. *J. Phys. Chem. B* **110,** 16816–16818 (2006).

96. Spickermann, C., Thar, J., Lehmann, S. B. C., Zahn, S., Hunger, J., Buchner, R., Hunt, P. A., Welton, T., & Kirchner, B. *J. Chem. Phys.* **129,** 104505(1)–104505(13) (2008).

97. Porter, A. R., Liem, S. Y. & Popelier, P. L. A. *Phys. Chem. Chem. Phys.* **10,** 4240–4248 (2008).

98. Feng, S. & Voth, G. A. *Fluid Phase Equilib.* **294,** 148–156 (2010).

99. Chevrot, G., Schurhammer, R. & Wipff, G. *Phys. Chem. Chem. Phys.* **8,** 4166–4174 (2006).

100. Inoue, G., Shimoyama, Y., Su, F., Takada, S., Iwai, Y. & Arai, Y. *J. Chem. Eng. Data* **52,** 98–101 (2007).

101. Freire, M. G., Santosa, L. M. N. B. F., Fernandes, A. M., Coutinho, J. A. & Marrucho, I. M. *Fluid Phase Equilib.* **261,** 449–454 (2007).

102. Wong, D. S. H., Chen, J. P., Chang, J. M. & Chou, C. H. *Fluid Phase Equilib.* **194–197,** 1089–1095 (2002).

103. Margulis, C. J., Stern, H. A. & Berne, B. J. *J. Phys. Chem. B* **106,** 12017–12021 (2002).

104. Spoel, D. V. D., Lindahl, E., Hess, B., Buuren, A. R. V., Apol, E., Meulenhoff, P. J., Tieleman, D. P., Sijbers, A. L. T. M., Feenstra, K. A., Drunen, R. V. & Berendsen, H. J. C. *Gromacs User Manual version 3.2* (http://www.Gromacs.org, 2005).

105. Bayly, C. I., Cieplak, P., Cornell, W. D. & Kollman, P. A. *J. Phys. Chem* **97,** 10269–10280 (1993).

106. Berendsen, H. J. C., Grigera, J. R. & Straatsma, T. P. *J. Phys. Chem.* **91,** 6269–6271 (1987).

107. Essmann, U., Perera, L., Berkowitz, M. L., Darden, T., Lee, H. & Pedersen, L. G. *J. Chem. Phys.* **103,** 8577–8593 (1995).

108. Jorgensen, W. L. & Madura, J. D. *J. Am. Chem. Soc.* **105,** 1407–1413 (1983).

109. Mahoney, M. W. & Jorgensen, W. L. *J. Chem. Phys.* **112,** 8910–8922 (2000).

110. Cornell, W. D., Cieplak, P., Bayly, C. I., Gould, I. R., Merz, K. M., Ferguson, D. M., Spellmeyer, D. C., Fox, T., Caldwell, J. W. & Kollman, P. A. *J. Am. Chem. Soc.* **117,** 5179–5197 (1995).

111. Zielkiewicz, J. *J. Chem. Phys.* **123,** 104205(1)–104205(6) (2005).

112. Klähn, M., Stuber, C., Seduraman, A. & Wu, P. *J. Phys. Chem. B* **114,** 2856–2868 (2010).

113. Head-Gordon, T. & Johnson, M. E. *Proc. Natl. Acad. Sci. U.S.A.* **103,** 7973–7977 (2006).

114. Berendsen, H. J. C., Postma, J. P. M., van Gunsteren, W. F., DiNola, A. & Haak, J. R. *J. Phys. Chem.* **81,** 3684–3690 (1984).

115. Morrow, T. I. & Maginn, E. J. *J. Phys. Chem. B* **106,** 12807–12813 (2002).

116. Bowron, D. T., D'Agostino, C., Gladden, L. F., Hardacre, C., Holbrey, J. D., Lagunas, M. C., McGregor, J., Mantle, M. D., Mullan, C. L. & Youngs, T. G. A. *J. Phys. Chem. B* **114,** 7760–7768 (2010).

117. Bahe, L. W. *J. Phys. Chem* **76,** 1062–1071 (1972).

118. Varela, L. M., Garcia, M., Sarmiento, F., Attwood, D. & Mosquera, V. *J. Chem. Phys.* **107,** 6415–6419 (1997).

119. Souto, J., Alemany, M. M. G. & Gallego, L. J. *Phys. Rev. B* **81,** 134201(1)–134201(15) (2010).

120. Alavi, S. & Thompson, D. L. *J. Chem. Phys.* **122,** 154704(1)–154715(12) (2005).

121. Liu, Z., Wu, X. & Wang, W. *Phys. Chem. Chem. Phys.* **8,** 1096–1104 (2006).

122. Liu, Z., Huang, S. & Wang, W. *J. Phys. Chem. B* **108,** 12978–12989 (2004).

123. Micaelo, N. M., Baptista, A. M. & Soares, C. M. *J. Phys. Chem. B* **110,** 14444–14451 (2006).

124. Hardacre, C., McMath, S. E. J., Nieuwenhuyzen, M., Bowron, D. T & Soper, A. K. *J. Phys.: Condens. Matter* **15,** S159–S166 (2003).

125. Köddermann, T., Wertz, C., Heintz, A. & Ludwig, R. *Angew. Chem. Int. Ed.* **45,** 3697–3702 (2006).

126. Raugei, S. & Klein, M. *J. Chem. Phys.* **116,** 196–202 (2002).

127. H. Ohtaki, T. R. *Chem. Rev.* **93,** 1157–1204 (1993).

128. Pópolo, M. G. D. & Voth, G. A. *J. Phys. Chem. B* **108,** 1744–1752 (2004).

129. Harsányi, I., Pusztai, L., Soetens, J. C. & Bopp, P. A. *J. Mol. Liq.* **129,** 80–85 (2006).

130. Sokol, M., Dawid, A., Dendzik, Z. & Gburski, Z. *J. Mol. Struct.* **704,** 341–345 (2004).

131. Chaumont, A., Schurhammer, R. & Wipff, G. *J. Phys. Chem. B* **109,** 18964–18973 (2005).

132. Méndez-Morales, T., Carrete, J., Cabeza, O., Gallego, L. J. & Varela, L. M. *J. Phys. Chem. B* **115,** 11170–11182 (2011).

133. Rogers, R. D. & Seddon, K. R. *Science* **302,** 792–793 (2003).

134. Rogers, R. D. & Seddon, K. R. *Ionic liquids as green solvents: progress and prospects* (American Chemical Society, 2003).

135. Rogers, R. D. & Seddon, K. R. *Ionic liquids: industrial applications for green chemistry* (American Chemical Society, 2002).

136. Cabeza, O., Segade, L., García-Garabal, S., Rilo, E., Domínguez-Pérez, M. & Varela, L. M. in *Ionic Liquids, Theory and Applications* 111–136 (InTech, 2011).

137. Pereiro, A. B. & Rodríguez, A. *J. Chem. Eng. Data* **52,** 1408–1412 (2007).

138. Sahandzhieva, K., Tuma, D., Breyer, S., Kamps, A. P. S. & Maurer, G. *J. Chem. Eng. Data* **51,** 1516–1525 (2006).

139. Crosthwaite, J. M., Aki, S. N. V. K., Maginn, E. J. & Brennecke, J. F. *J. Phys. Chem. B* **108,** 5113–5119 (2004).

140. Pereiro, A. B. & Rodríguez, A. *J. Chem. Thermodyn.* **39,** 978–989 (2007).

141. Domańska, U. & Marciniak, A. *J. Phys. Chem. B* **108,** 2376–2382 (2004).

142. Huo, Y., Xia, S. & Ma, P. *J. Chem. eng. Data* **52,** 2077–2082 (2007).

143. Gómez, E., González, B., Calvar, N., Tojo, E. & Domínguez, A. *J. Chem. Eng. Data* **51,** 2096–2102 (2006).

144. Pereiro, A. B., Tojo, E., Rodríguez, A., Canosa, J. & Tojo, J. *J. Chem. Thermodyn.* **38,** 651–661 (2006).

145. Stoppa, A., Hunger, J. & Buchner, R. *J. Chem. Eng. Data* **54,** 472–479 (2009).

146. Gómez, E., Calvar, N., Domínguez, I. & Domínguez, A. *Phys. Chem. Liq.* **44,** 409–417 (2006).

147. Rilo, E., Pico, J., García-Garabal, S., Varela, L. M. & Cabeza, O. *Fluid Phase Equilib.* **285,** 83–89 (2009).

148. Hanke, C. G., Atamas, N. A. & Lynden-Bell, R. M. *Green Chem.* **4,** 107–111 (2002).

149. Raabe, G. & Köhler, J. *J. Chem. Phys.* **129,** 144503(1)–144503(8) (2008).

150. Heintz, A., Ludwig, R. & Schmidt, E. *Phys. Chem. Chem. Phys.* **13,** 3268–3273 (2011).

151. Huddleston, J. G., Visser, A. E., Reichert, W. M., Willauer, H. D., Broker, G. A. & Rogers, R. D. *Green Chem.* **3,** 156–164 (2001).

152. Holbrey, J. D. & Seddon, K. R. *J. Chem. Soc., Dalton Trans.* 2133–2139 (1999).

153. Jorgensen, W. L. *J. Phys. Chem.* **90,** 1276–1284 (1986).

154. Sambasivarao, S. . V. & Acevedo, O. *J. Chem. Theory Comput.* **5,** 1038–1050 (2009).

155. Prado, C. E. R. & Freitas, L. C. G. *J. Mol. Struct. (Theochem.)* **847,** 93–100 (2007).

156. Canongia-Lopes, J. N., Deschamps, J. & Pádua, A. H. *J. Phys. Chem. B* **108,** 2038–2047 (2004).

157. Brenneman, C. M. & Wiberg, K. B. *J. Comp. Chem.* **11,** 361–373 (1990).

158. Frisch, M. J. *et al. Gaussian 94, Revision A.1* (Gaussian, Inc., Pittsburgh, PA, 1995).

159. Hess, B., Bekker, H., Berendsen, H. J. C. & Fraaije, J. G. E. M. *J. Comp. Chem.* **18,** 1463–1472 (1997).

160. Hess, B. *J. Chem. Theory Comp.* **4,** 116–122 (2007).

161. Bussi, G., Donadio, D. & Parrinello, M. *J. Chem. Phys.* **126,** 014101(1)–014101(7) (2007).

162. Parrinello, M. & Rahman, A. *J. Appl. Phys.* **52,** 7182–7190 (1981).

163. Gómez, E., González, B., Domínguez, A., Tojo, E. & Tojo, J. *J. Chem. Eng. Data* **51,** 696–701 (2006).

164. Gibson, H. M. & Wilding, N. B. *Phys. Rev. E* **73,** 061507(1)–061507(7) (2006).

165. Saiz, L., Padro, J. A. & Guardia, E. *J. Phys. Chem. B* **101,** 78–86 (1997).

166. Stuart, S. J. & Berne, B. J. *J. Phys. Chem.* **100,** 11934–11943 (1996).

167. McGreevy, R. L., Baranyai, A. & Ruff, I. *Phys. Chem. Liq.* **16,** 47–54 (1986).

168. Haughney, M., Ferrario, M. & McDonald, I. R. *J. Phys. Chem.* **91,** 4934–4940 (1987).

169. Yamaguchi, T., Hidaka, H. & Soper, A. K. *Mol. Phys.* **96,** 1159–1168 (1999).

170. Matsumoto, M. & Gubbins, K. E. *J. Chem. Phys.* **93,** 1981–1994 (1990).

171. J. H. Guo, A. A. J. E. R. C. S. H. A. H. S. Y. Luo & Nordgren, J. *Phys. Rev. Lett.* **89,** 137402(1)–137402(4) (2002).

172. Luzar, A. & Chandler, D. *Phys. Rev. Lett.* **76,** 928–931 (1996).

173. Stillinger, F. H. *Science* **209,** 451–457 (1980).

174. Méndez-Morales, T., Carrete, J., García, M., Cabeza, O., Gallego, L. J. & Varela, L. M. *J. Phys. Chem. B* **115,** 15322–15322 (2011).

175. Heintz, A. *J. Chem. Thermodyn.* **37,** 525–535 (2005).

176. Jr, A. A. F., King, L. A., Levisky, J. A. & Wilkes, J. S. *J. Phys. Chem.* **88,** 2609–2614 (1984).

177. Hussey, C. L. *Pure Appl. Chem.* **60,** 1763–1772 (1988).

178. Bonhôte, P., Dias, A. P., Papageorgiou, N., Kalyanasundaram, K. & Grätzel, M. *Inorg. Chem.* **35,** 1168–1178 (1996).

179. Holbrey, J. D. & Seddon, K. R. *Clean Prod. Proc.* **1,** 223–236 (1999).

180. Bates, E. D., Mayton, R. D., Ntai, I. & Jr, J. H. D. *J. Am. Chem. Soc.* **124,** 926–927 (2002).

181. Lu, W. *et al. Science* **297,** 983–987 (2002).

182. Liu, W., Ye, C., Gong, Q., Wang, H. & Wang, P. *Tribol. Lett.* **13,** 81–85 (2002).

183. Xu, W. & Angell, C. A. *Science* **302,** 422–425 (2003).

184. Seki, S., Kobayashi, Y., Miyashiro, H., Ohno, Y., Usami, A., Mita, Y., Kihira, N., Watanabe, M. & Terada, N. *Chem. Commun.* **2006,** 544–10230 (2006).

185. Anderson, J. L., Armstrong, D. W. & Wei, G. T. *Anal. Chem.* **78,** 2892–2902 (2006).

186. Fabregat-Santiago, F., Bisquert, J., Palomares, E., Otero, L., Kuang, D., Zakeeruddin, S. M. & Grätzel, M. *J. Phys. Chem. C* **111,** 6550–6560 (2007).

187. MacFarlane, D. R., Meakin, P., Sun, J., Amini, N. & Forsyth, M. *J. Phys. Chem. B* **103,** 4164–4170 (1999).

188. Sun, J., Forsyth, M. & MacFarlane, D. R. *J. Phys. Chem. B* **102,** 8858–8864 (1998).

189. Cadena, C., Zhao, Q., Snurr, R. & Maginn, E. J. *J. Phys. Chem. B* **110,** 2821–2832 (2006).

190. Wu, X., Liu, Z., Huang, S. & Wang, W. *Phys. Chem. Chem. Phys.* **7,** 2771–2779 (2005).

191. Price, W. S. *Concepts Magn. Reson.* **9,** 299–336 (1997).

192. Price, W. S. *Concepts Magn. Reson.* **10,** 197–237 (1998).

193. Marquardt, E., Grober, N. & Richter, J. *Opt. Eng.* **36,** 2857–2862 (1997).

194. Marquardt, E. & Richter, J. *Opt. Eng.* **37,** 1514–1519 (1998).

195. Umecky, T., Kanakubo, M. & Ikushima, Y. *Fluid Phase Equilib.* **228–229,** 329–333 (2005).

196. Every, H. A., Bishop, A. G., MacFarlane, D. R., Oradd, G. & Forsyth, M. *Phys. Chem. Chem. Phys.* **6,** 1758–1765 (2004).

197. Noda, A., Hayamizu, K. & Watanabe, M. *J. Phys. Chem. B* **105,** 4603–4610 (2001).

198. Jin, H., O'Hare, B., Dong, J., Arzhantsev, S., Baker, G. A., Wishart, J. F., Benesi, A. J. & Maroncelli, M. *J. Phys. Chem. B* **112,** 81–92 (2008).

199. Umecky, T., Kanakubo, M. & Ikushima, Y. *J. Mol. Liq.* **119,** 77–81 (2005).

200. Bara, J. E., Carlisle, T. K., Gabriel, C. J., Camper, D., Finotello, A., Gin, D. L. & Noble, R. D. *Ind. Eng. Chem. Res.* **48,** 2739–2751 (2009).

201. Morgan, D., Ferguson, L. & Scovazzo, P. *Ind. Eng. Chem. Res.* **44,** 4815–4823 (2005).

202. Shiflett, M. B. & Yokozeki, A. *Ind. Eng. Chem. Res.* **44,** 4453–4464 (2005).

203. Shiflett, M. B., Harmer, M. A., Junk, C. P. & Yokozeki, A. *Fluid Phase Equilib.* **242,** 220–232 (2006).

204. Iacob, C., Sangoro, J. R., Papadopoulos, P., Schubert, T., Naumov, S., Valiullin, R., Kärger, J. & Kremer, F. *Phys. Chem. Chem. Phys.* **12,** 13798–13803 (2010).

205. Lovell, C. S., Walker, A., Damion, R. A., Radhi, A., Tanner, S. F., Budtova, T. & Ries, M. E. *Biomacromol.* **11,** 2927–2935 (2010).

206. Sarraute, S., Gomes, M. F. C. & Pádua, A. A. H. *J. Chem. Eng. Data* **54,** 2389–2394 (2009).

207. Wong, C. L., Soriano, A. N. & Li, M. H. *Fluid Phase Equilib.* **271,** 43–52 (2008).

208. De Castro, C. A. N. *et al. Fluid Phase Equilib.* **294,** 157–179 (2010).

209. Menjoge, A., Dixon, J. N., Brennecke, J. F., Maginn, E. J. & Vasenkov, S. *J. Phys. Chem. B* **113,** 6353–6359 (2009).

210. Heintz, A., Lehmann, J. K., Schmidt, E. & Wandschneider, A. *J. Solution Chem.* **38,** 1079–1083 (2009).

211. Richter, J., Leuchter, A. & Grober, N. *J. Mol. Liq.* **103–104,** 359–370 (2003).

212. Su, W. C., Chou, C. H., Wong, D. S. H. & Li, M. H. *Fluid Phase Equilib.* **252,** 74–78 (2007).

213. Huang, X., Margulis, C. J., Li, Y. & Berne, B. J. *J. Am. Chem. Soc.* **127,** 17842–17851 (2005).

214. Hu, Z. & Margulis, C. J. *Proc. Natl. Acad. Sci. USA* **103,** 831–836 (2006).

215. Kelkar, M. S. & Maginn, E. J. *J. Phys. Chem. B* **111,** 4867–4876 (2007).

216. Liu, Z., Chen, T., Bell, A. & Smit, B. *J. Phys. Chem. B* **114,** 4572–4582 (2010).

217. Borodin, O. & Smith, G. D. *J. Phys. Chem. B* **110,** 11481–11490 (2006).

218. Margulis, C. J. *Mol. Phys.* **102,** 829–838 (2004).

219. Yan, T., Burnham, C. J., Pópolo, M. G. D. & Voth, G. A. *J. Phys. Chem. B* **108,** 11877–11881 (2004).

220. De Andrade, J., Böes, E. S. & Stassen, H. *J. Phys. Chem. B* **106,** 13344–13351 (2002).

221. Annapureddy, H. V. R., Hu, Z., Xia, J. & Margulis, C. J. *J. Phys. Chem. B* **112,** 1770–1776 (2008).

222. Liu, X., Vlugt, T. J. H. & Bardow, A. *J. Phys. Chem. B* **115,** 8506–8517 (2011).

223. Einstein, A. *Ann. Phys.* **17,** 549–560 (1905).

224. Karger, N., Vardag, T. & Lüdemann, H. D. *J. Chem. Phys.* **93,** 3437–3444 (1990).

225. Martí, J., Padró, J. A. & Guàrdia, E. *J. Mol. Liq.* **64,** 1–12 (1995).

226. Guevara-Carrion, G., Nieto-Draghi, C., Vrabec, J. & Hasse, H. *J. Phys. Chem. B* **112,** 16664–16674 (2008).

227. Stern, H. A., Rittner, F., Berne, B. J. & Friesner, R. A. *J. Chem. Phys.* **115,** 2237–2251 (2001).

228. Méndez-Morales, T., Carrete, J., Bouzón-Capelo, S., Pérez-Rodríguez, M., Cabeza, O., Gallego, L. J. & Varela, L. M. *J. Phys. Chem. B* **117,** 3207–3220 (2013).

229. Dupont, J., de Souza, R. F. & Suarez, P. A. Z. *Chem. Rev.* **102,** 3667–3692 (2002).

230. Garcia, B., Lavallée, S., Perron, G., Michot, C. & Armand, M. *Electrochim. Acta* **49,** 4583–4588 (2004).

231. Diaw, M., Chagnes, A., Carré, B., Willmann, P. & Lemordant, D. *J. Power Sources* **146,** 682–684 (2005).

232. Zhou, Q., Henderson, W. A., Appetecchi, G. B. & Passerini, S. *J. Phys. Chem. C* **114,** 6201–6204 (2010).

233. Lee, S. Y., Yong, H. H., Lee, Y. J., Kim, S. K. & Ahn, S. *Green Chem.* **109,** 13663–13667 (2005).

234. Markevich, E., Baranchugov, V. & Aurbach, D. *Electrochem. Commun.* **8,** 1331–1334 (2006).

235. Castriota, M., Caruso, T., Agostino, R. G., Cazzanelli, E., Henderson, W. A. & Passerini, S. *J. Phys. Chem. A* **109,** 92–96 (2005).

236. Borgel, V., Markevich, E., Aurbach, D., Semrau, G. & Schmidt, M. *J. Power Sources* **189,** 331–336 (2009).

237. Nicolau, B. G., Sturlaugson, A., Fruchey, K., Ribeiro, M. C. C. & Fayer, M. D. *J. Phys. Chem. B* **114,** 8350–8356 (2010).

238. Nicotera, I., Oliviero, C., Henderson, W. A., Appetecchi, G. B. & Passerini, S. *J. Phys. Chem. B* **109,** 22814–22819 (2005).

239. Lassègues, J., Grondin, J. & Talaga, D. *Phys. Chem. Chem. Phys.* **8,** 5629–5632 (2006).

240. Lassègues, J., Grondin, J., Aupetit, C. & Johansson, P. *J. Phys. Chem. A* **113,** 305–314 (2009).

241. Egashira, M., Todo, H., Yoshimoto, N., Morita, M. & Yamaki, J. *J. Power Sources* **174,** 560–564 (2007).

242. Henderson, W. A. & Passerini, S. *Chem. Mater.* **16,** 2881–2885 (2004).

243. Zhou, Q., Fitzgerald, K., Boyle, P. D. & Henderson, W. A. *Chem. Mater.* **22,** 1203–1208 (2010).

244. Xu, J., Yang, J., NuLi, Y., Wang, J. & Zhang, Z. *J. Power Sources* **160,** 621–626 (2006).

245. Seki, S., Kobayashi, Y., Miyashiro, H., Ohno, Y., Usami, A., Mita, Y., Kihira, N., Watanabe, M. & Terada, N. *J. Phys. Chem. B* **110,** 10228–10230 (2006).

246. Saito, Y., Umecky, T., Niwa, J., Sakai, T. & Maeda, S. *J. Phys. Chem. B* **111,** 11794–11802 (2007).

247. Sakaebe, H. & Matsumoto, H. *Electrochem. Commun.* **5,** 594–598 (2003).

248. Rosol, Z. P., German, N. J. & Gross, S. M. *Green Chem.* **11,** 1453–1457 (2009).

249. Pereiro, A. B., Araújo, J. M. M., Oliveira, F. S., Esperança, J. M. S. S., Lopes, J. N. C., Marrucho, I. M. & Rebelo, L. P. N. *J. Chem. Thermodyn.* **55,** 29–36 (2012).

250. Zhou, Q., Boyle, P. D., Malpezzi, L., Mele, A., Shin, J.-H., Passerini, S. & Henderson, W. A. *Chem. Mater.* **23,** 4331–4337 (2011).

251. Burba, C. M., Rocher, N. M., Frech, R. & Powell, D. R. *J. Phys. CHem. B* **112,** 2991–2995 (2008).

252. Hayamizu, K., Aihara, Y., Nakagawa, H. & Nukuda, T. *J. Phys. Chem. B* **108,** 19527–19532 (2004).

253. Duluard, S., Grondin, J., Bruneel, J., Pianet, I., Grélard, A., Campet, G., Delville, M. & Lassègues, J. *J. Raman Spectroscopy* **39,** 627–632 (2008).

254. Umebayashi, Y., Mitsugi, T., Fukuda, S., Fujimori, T., Fujii, K., Kanzaki, R., Takeuchi, M. & Ishiguro, S. *J. Phys. Chem. B* **111,** 13028–13032 (2007).

255. Monteiro, M. J., Bazito, F. F. C., Siqueira, L. J. A., Ribeiro, M. C. C. & Torresi, R. M. *J. Phys. Chem. B* **112,** 2102–2109 (2008).

256. Borodin, O., Smith, G. D. & Henderson, W. *J. Phys. Chem. B* **110,** 16879–16886 (2006).

257. Niu, S., Cao, Z., Li, S. & Yan, T. *J. Phys. Chem. B* **114,** 877–881 (2010).

258. Canongia-Lopes, J. N. & Pádua, A. A. H. *J. Phys. Chem. B* **108,** 16893–16898 (2004).

259. Pereiro, A. B., Legido, J. L. & Rodríguez, A. . *Chem. Thermodyn.* **39,** 1168–1175 (2007).

260. Xuan, X., Wang, J. & Wang, H. *Electrochim. Acta* **50,** 4196–4201 (2005).

261. Francisco, J. S. & Williams, I. H. *Am. Chem. Soc.* **94,** 8522–8529 (1990).

262. Varela, L. M., Carrete, J., García, M., Rodríguez, J. R., Gallego, L. J., Turmine, M. & Cabeza, O. in *Ionic liquids: theory, properties, new approaches* (ed Kokorin, A.) (InTech, 2011).

263. Arnaud, R., Benrabah, D. & Sanchez, J.-Y. *J. Phys. Chem.* **100,** 10882–10891 (1996).

264. Gejji, S. P., Suresh, C. H., Babu, K. & Gadre, S. R. *J. Phys. Chem. A* **103,** 7474–7480 (1999).

265. Zhang, Y., Alonso, P. R., Martinez-Limia, A., Scanlon, L. G. & Balbuena, P. B. *J. Phys. Chem. B* **108,** 4659–4668 (2004).

266. Kowsari, M. H., Alavi, S., Ashrafizaadeh, M. & Najafi, B. *J. Chem. Phys.* **129,** 224508(1)–224508(13) (2008).

267. Rey-Castro, C., Tormo, A. L. & Vega, L. F. *Fluid Phase Equilib.* **256,** 62–69 (2007).

268. Qian, J., Hentschke, R. & Heuer, A. *J. Chem. Phys.* **110,** 4514–4522 (1999).

269. Borodin, O. *J. Phys. Chem. B* **113,** 11463–11478 (2009).

270. Borodin, O. *Mater. Res. Soc. Proc.* **1082,** Q06–04 (2008).

271. Vila, J., Rilo, E., Segade, L., Cabeza & Varela, L. M. *Phys. Rev. E* **71,** 031201(1)–031201(8) (2005).

272. Angell, C. A., Byrne, N. & Belieres, J.-P. *Acc. Chem. Res.* **40,** 1228–1236 (2007).

273. Borodin, O., Smith, G. D. & Fan, P. *J. Phys. Chem. B* **110,** 22773–22779 (2006).

274. Kowsari, M. H., Alavi, S., Ashrafizaadeh, M. & Najafi, B. *J. Chem. Phys.* **130,** 014703(1)–014703(10) (2009).

275. Rey-Castro, C. & Vega, L. F. *J. Phys. Chem. B* **110,** 14426–14435 (2006).

276. Rilo, E., Vila, J., García, M., Varela, L. M. & Cabeza, O. *J. Chem. Eng. Data* **55,** 5156–5163 (2010).

277. Carda-Broch, S., Berthod, A. & Armstrong, D. W. *Anal. Bioanal. Chem.* **375,** 191–199 (2003).

278. Méndez-Morales, T., Carrete, J., Cabeza, O., Russina, O., Triolo, A., Gallego, L. J. & Varela, L. M. *J. Phys. Chem. B* **118,** 761–770 (2014).

279. Zhang, S., Sun, N., He, X., Lu, X. & Zhang, X. *J. Phys. Chem. Ref. Data* **35,** 1475–1517 (2006).

280. Greaves, T. L. & Drummond, C. J. *Chem. Rev.* **108,** 206–237 (2008).

281. M. Yoshizawa, W. X. & Angell, C. A. *J. Am. Chem. Soc.* **125,** 15411–15419 (2003).

282. Greaves, T. L., Weerawardena, A., andgre I. Krodkiewska, C. F. & Drummond, C. J. *J. Phys. Chem. B* **110,** 22479–22487 (2006).

283. Nakamoto, H. & Watanabe, M. *Chem. Commun.* 2539–2541 (2007).

284. Md. A. B. H. Susan, S. M. A. Noda & Watanabe, M. *Chem. Commun.* **2003,** 938–939 (2003).

285. Timperman, L., Skowron, P., Boisset, A., Galiano, H., Lemordant, D., Frackowiak, E., Beguinb, F. & Anouti, M. *Phys. Chem. Chem. Phys.* **14,** 8199–8207 (2012).

286. Anouti, M. & Timperman, L. *Phys. Chem. Chem. Phys.* **15,** 6539–6548 (2013).

287. Greaves, T. L., Weerawardena, A., Fong, C. & Drummond, C. J. *J. Phys. Chem. B* **111,** 4082–4088 (2007).

288. Greaves, T. L., Weerawardena, A., Krodkiewska, I. & Drummond, C. J. *Chem. Rev.* **112,** 896–905 (2008).

289. Atkin, R., Bobillier, S. M. C. & Warr, G. G. *J. Phys. Chem. B* **114,** 1350–1360 (2010).

290. Kennedy, D. F. & Drummond, C. J. *J. Phys. Chem. B* **113,** 5690–5693 (2009).

291. X. Wang, X. C. Q. Li & Li, Z. *Langmuir* **28,** 16547–16554 (2012).

292. Song, X., Hamano, H., Minofar, B., Kanzaki, R., Fujii, K., Kameda, Y., Kohara, S., Watanabe, M., Ishiguro, S. & Umebayashi, Y. *J. Phys. Chem. B* **116,** 2801–2813 (2012).

293. Alvarez, V. H., Dosil, N., Gonzalez-Cabaleiro, R., Mattedi, S., Martin-Pastor, M., Iglesias, M. & Navaza, J. M. *J. Chem. Eng. Data* **55,** 625–632 (2010).

294. Hunger, J., Sonnleitner, T., Liu, L., Buchner, R., Bonn, M. & Bakker, H. J. *J. Phys. Chem* **3,** 3034–3038 (2012).

295. Niga, P., Wakeham, D., Nelson, A., Warr, G. G., Rutland, M. & Atkin, R. *Langmuir* **26,** 8282–8288 (2010).

296. Zhao, C., Burrell, G., Torriero, A. A. J., Separovic, F., Dunlop, N. F., MacFarlane, D. R. & Bond, A. M. *J. Phys. Chem. B* **112,** 6923–6936 (2008).

297. Hayes, R., Imberti, S., Warr, G. G. & Atkin, R. *Phys. Chem. Chem. Phys.* **13,** 13544–13551 (2011).

298. Bodo, E., Postorino, P., Mangialardo, S., Piacente, G., Ramondo, F., Bosi, F., Ballirano, P. & Caminiti, R. *J. Phys. Chem. B* **115,** 13149–13161 (2011).

299. Bodo, E., Mangialardo, S., Ramondo, F., Ceccacci, F. & Postorino, P. *J. Phys. Chem. B* **116,** 13878–13888 (2012).

300. Markusson, H., Belieres, J.-P., Johansson, P., Angell, C. A. & Jacobsson, P. *J. Phys. Chem. A* **111,** 8717–8723 (2007).

301. Umebayashi, Y., Chung, W.-L., Mitsugi, T., Fukuda, S., Takeuchi, M., Fujii, K., Takamuku, T., Kanzaki, R. & Ishiguro, S. *J. Comput. Chem. Jpn.* **7,** 125–134 (2008).

302. Zahn, S., Thar, J. & Kirchner, B. *J. Chem. Phys.* **132,** 124506(1)–124506(13) (2010).

303. Hayes, R., Imberti, S., Warr, G. G. & Atkin, R. *Angew. Chem., Int. Ed.* **51,** 7468–7471 (2012).

304. Hayes, R., Imberti, S., Warr, G. G. & Atkin, R. *Angew. Chem., Int. Ed.* **52,** 4623–4627 (2013).

305. Menne, S., Pires, J., Anouti, M. & Balducci, A. *Electrochem. Commun.* **31,** 39–41 (2013).

306. Choe, J., Kim, K. & Chang, S. *Bull. Korean Chem. Soc.* **21,** 200–206 (2000).

307. Borodin, O. & Smith, G. D. *J. Phys. Chem. B* **113,** 1763–1776 (2009).

308. Marcus, Y. *Chem. Rev.* **109,** 1346–1370 (2009).

309. Nag, A., Chakraborty, D. & Chandra, A. *J. Chem. Sci.* **120,** 71–77 (2008).

310. Hayes, R., Imberti, S., Warr, G. G. & Atkin, R. *Phys. Chem. Chem. Phys.* **13,** 3237–3247 (2011).

311. Lawler, C. & Fayer, M. D. *J. Phys. Chem. B* **117,** 9768–9774 (2013).

312. Stromme, K. O. *Acta Chem. Scand.* **24,** 1479–1481 (1970).

313. Miller, R. E., Getty, R. R., Treuil, K. L. & Leroi, G. E. *J. Chem. Phys.* **51,** 1385–1389 (1969).

314. Adya, A. K., Neilson, G. W., Okada, I. & Okazaki, S. *Mol. Phys.* **79,** 1327–1350 (1993).

315. Mähler, J. & Persson, I. *Inorg. Chem.* **51,** 425–438 (2012).

316. Soper, A. K. & Weckström, K. *Biophys. Chem.* **124,** 180–191 (2006).

317. Méndez-Morales, T., Carrete, J., Rodríguez, J., Cabeza, O., Gallego, L. J., Russina, O. & Varela, L. M., – (2014).

318. Ohno, H. *Electrochemical aspects of Ionic Liquids* (John Wiley & Sons, Inc., 2005).

319. Plechkova, N. V. & Seddon, K. R. *Chem. Soc. Rev.* **37,** 123–150 (2008).

320. Zeng, Z., Phillips, B. S., Xiao, J.-C. & Shreeve, J. M. *Chem. Matter.* **20,** 12719–2726 (2008).

321. Hayes, R., Imberti, S., Warr, G. G. & Atkin, R. *J. Phys. Chem. C* **118,** 13998–14008 (2014).

322. Hayes, R., Bernard, S. A., Imberti, S., Warr, G. G. & Atkin, R. *J. Phys. Chem. C,* http://dx.doi.org/10.1021/jp506192d.

323. Russina, O., Caminiti, R., Méndez-Morales, T., Carrete, J., Cabeza, O., Gallego, L., Varela, L. & Triolo, A. *J. Mol. Liq.* http://dx.doi.org/10.1016/j.molliq.2014.08.007. ISSN: 0167-7322 (2014).

324. Menne, S., Vogl, T. & Balducci, A. *Phys. Chem. Chem. Phys.* **16,** 5485–5489 (2014).

325. Greaves, T. L., Kennedy, D. F., Mudie, S. T. & Drummond, C. J. *J. Phys. Chem. B* **114,** 10022–10031 (2010).

326. Hayes, R., Imberti, S., Warr, G. G. & Atkin, R. *Phys. Chem. Chem. Phys.* **13,** 3237–3247 (2011).

327. Méndez-Morales, T., Carrete, J., Pérez-Rodríguez, M., Cabeza, O., Gallego, L. J., Lynden-Bell, R. M. & Varela, L. M. *Phys. Chem. Chem. Phys.* **16,** 13271–13278 (2014).

328. Lewandowski, A. & Świderska Mocek, A. *J. Power Sources* **194,** 601–609 (2009).

329. Kuboki, T., Okuyama, T., Ohsaki, T. & Takami, N. *J. Power Sources* **26,** 766–769 (2005).

330. Sakaebe, H., Matsumoto, H. & Tatsumi, K. *Electrochim. Acta* **53,** 1048–1054 (2007).

331. Frackowiak, E. *Phys. Chem. Chem. Phys.* **9,** 1774–1785 (2007).

332. Islam, M. M., Alam, M. T., Okajima, T. & Ohsaka, T. *J. Phys. Chem. C* **113,** 3386–3389 (2009).

333. Lockett, V., Horne, M., Sedev, R., Rodopoulos, T. & Ralston, J. *Phys. Chem. Chem. Phys.* **12,** 12499–12512 (2010).

334. Drüschler, M., Borisenko, N., Wallauer, J., Winter, C., Huber, B., Endres, F. & Roling, B. *Phys. Chem. Chem. Phys.* **14,** 5090–5099 (2012).

335. Costa, R., Pereira, C. M. & Silva, F. *Phys. Chem. Chem. Phys.* **12,** 11125–11132 (2010).

336. Vatamanu, J., Borodin, O., Bedrov, D. & Smith, G. D. *J. Phys. Chem. C* **116,** 7940–7951 (2012).

337. Vatamanu, J., Cao, L., Borodin, O., Bedrov, D. & Smith, G. D. *J. Phys. Chem. Lett.* **2,** 2267–2272 (2011).

338. Merlet, C., Salanne, M., Rotenberg, B. & Madden, P. A. *J. Phys. Chem. C* **115,** 16613–16618 (2011).

339. Fedorov, M. V. & Kornyshev, A. A. *J. Phys. Chem. B* **112,** 11868–11872 (2008).

340. Fedorov, M. V., Georgi, N. & Kornyshev, A. A. *Electrochem. Commun.* **12,** 296–299 (2010).

341. Feng, G., Jiang, D. & Cummings, P. T. *J. Chem. Theory Comput.* **8,** 1058–1063 (2012).

342. Xing, L., Vatamanu, J., Smith, G. D. & Bedrov, D. *J. Phys. Chem. Lett.* **3,** 1124–1129 (2012).

343. Georgi, N., Kornyshev, A. A. & Fedorov, M. V. *J. Electroanal. Chem.* **649,** 261–267 (2010).

344. Fedorov, M. V. & Kornyshev, A. A. *Electrochim. Acta* **111,** 6835–6840 (2008).

345. Jiang, D., Jin, Z. & Wu, J. *Nano Lett.* **11,** 5373–5377 (2011).

346. Kornyshev, A. A. *J. Phys. Chem. B* **111,** 5545–5557 (2007).

347. Bazant, M. Z., Storey, B. D. & Kornyshev, A. A. *Phys. Rev. Lett.* **106,** 046102(1)–046102(4) (2011).

348. Gebbie, M. A., Valtiner, M., Banquy, X., Fox, E. T., Henderson, W. A. & Israelachvili, J. N. *PNAS* **110,** 9674–9679 (2013).

349. Atkin, R. & Warr, G. G. *J. Phys. Chem. C* **111,** 5162–5168 (2007).

350. Atkin, R., Abedin, S. Z. E., Hayes, R., Gaspatotto, L. H. S., Borisenko, N. & Endres, F. *J. Phys. Chem. C* **113,** 13266–13272 (2009).

351. Atkin, R., Borisenko, N., Drüschler, M., Abedin, S. Z. E., Endres, F., Hayes, R., Huber, B. & Roling, B. *Phys. Chem. Chem. Phys.* **13,** 6849–6857 (2011).

352. Wakeham, D., Hayes, R., Warr, G. G. & Atkin, R. *J. Phys. Chem. B* **113,** 5961–5966 (2009).

353. Endres, F., Hofft, O., Borisenko, N., Gasparotto, L. H., Prowald, A., Al-Salman, R., Carstens, T., Atkin, R., Bund, A. & Abedin, S. Z. E. *Phys. Chem. Chem. Phys.* **12,** 1724–1732 (2010).

354. Perkin, S., Crowhurst, L., Niedermeyer, H., Welton, T., Smitha, A. M. & Gosvami, N. N. *Chem. Commun.* **47,** 6572–6574 (2011).

355. Smith, A. M., Lovelock, K. R. J., Gosvami, N. N., Licence, P., Dolan, A., Welton, T. & Perkin, S. *J. Phys. Chem. Lett.* **4,** 378–382 (2013).

356. Mezger, M. *et al. Science* **322,** 424–428 (2008).

357. Cremer, T., Stark, M., Deyko, A., Steinruck, H.-P. & Maier, F. *Langmuir* **27,** 3662–3671 (2011).

358. Mezger, M., Schramm, S., Schröder, H., Reichert, H., Deutsch, M., Souza, E. J. D., Okasinski, J. S., Ocko, B. M., Honkimäki, V. & Dosch, H. *J. Chem. Phys.* **131,** 094701(1)–094701(9) (2009).

359. Baldelli, S. *Acc. Chem. Res.* **41,** 421–431 (2008).

360. Baldelli, S. *J. Phys. Chem. Lett.* **4,** 244–252 (2013).

361. Payal, R. S. & Balasubramanian, S. *Chem. Phys. Chem.* **13,** 1764–1771 (2012).

362. Kislenko, S. A., Samoylov, I. S. & Amirov, R. H. *Phys. Chem. Chem. Phys.* **11,** 5584–5590 (2009).

363. Wang, S., Li, S., Cao, Z. & Yan, T. *J. Phys. Chem. C* **114,** 990–995 (2010).

364. Dou, Q., Sha, M. L., Fu, H. Y. & Wu, G. Z. *J. Phys.: Condens. Matter* **23,** 175001(1)–175001(8) (2011).

365. Maolin, S., Fuchun, Z., Guozhong, W., Haiping, F., Chunlei, W., Shimou, C., Yi, Z. & Jun, H. *J. Chem. Phys.* **128,** 134504(1)–134504(7) (2008).

366. Feng, G., Zhang, J. S. & Qiao, R. *J. Phys. Chem. C* **113,** 4549–4559 (2009).

367. Sha, M., Wu, G., Dou, Q., Tang, Z. & Fang, H. *Langmuir* **26,** 12667–12672 (2010).

368. Pinilla, C., Pópolo, M. G. D., Lynden-Bell, R. M. & Kohanoff, J. *J. Phys. Chem. B* **109,** 17922–17927 (2005).

369. Pinilla, C., Pópolo, M. G. D., Kohanoff, J. & Lynden-Bell, R. M. *J. Phys. Chem. B* **111,** 4877–4884 (2007).

370. Smith, G. D., Borodin, O., Russo, S. P., Rees, R. J. & Hollenkamp, A. F. *Phys. Chem. Chem. Phys.* **11,** 9884–9897 (2009).

371. Yan, T., Li, S., Jiang, W., Gao, X., Xiang, B. & Voth, G. A. *J. Phys. Chem. B* **110,** 1800–1806 (2006).

USC
UNIVERSIDADE
DE SANTIAGO
DE COMPOSTELA

3 Conclusions

> Research is to see what everybody else has seen, and to think what nobody else has thought.
>
> ALBERT SZENT-GYORGYI

1. The interaction of aprotic ILs with molecular solvents such as water and alcohols has been analyzed using molecular dynamics simulations. The results revealed that water molecules tend to clusterize in the polar domains of the IL, the degree of clusterization being greater for the more hydrophobic anions. However, alcohol molecules do not form any kind of network and were found to be homogeneously distributed in the structure of the IL.

2. Single-particle dynamics of these mixtures has been also investigated. The study of velocity autocorrelation functions has shown a rattling motion of water molecules in the cavities formed by their heavier neighbours, whereas alcohol molecules do not experience any kind of oscillatory behaviour and diffuse much more easily than their water counterparts.

3. Neither water molecules nor alcohol ones are able to destroy the nanoseggregated structure of the ILs. Instead, they adapt to it and become solvated in the most favorable regions of the mixture, giving rise to a microscopic picture named nanostructured solvation.

4. In order to use ILs as electrolytes in electrochemical devices, the solvation processes of alkali salts when mixed with protic and aprotic ILs have been characterized. In both cases, the location of salt cations in the polar regions of the systems due to a strong correlation with the anions

has been predicted. The formation of stable kinetic entities composed of salt cations and the anions in their first coordination layer has been confirmed.

5. A gradual disruption of the well-known network of hydrogen bonds of the protic ILs with the addition of salt has been obtained. This effect has been found to be more pronounced for those protic ILs whose cations have longer alkyl chains, which is due to their lower degree of hydrogen bonding.

6. Salt cations fit to the IL structure being solvated in the polar nanoregions of the mixture and forming solid-like structures, which ultimately leads to phase separation. This also fits no the nanostructured solvation picture.

7. The study of mixtures of protic ILs with lithium and potassium salts confined between two parallel charged and uncharged graphene walls has been carried out in order to analyze the structure of the interfacial charge distribution for these mixtures. The formation of an overscreening induced layered structure at the interface with ion densities different from those in the bulk has been reported regardless the potential electrode.

8. A systematic rearrangement of the ions, in which anions are segregated towards the positive electrode and cations toward the negative one, as the charge of the walls increases, has been found. Both lithium and potassium cations have shown to be more influenced by the presence of anions in their first coordination shell when it comes to distribute themselves in the system than by the electrode potential. These cations adapt to the IL structure and they induce only very limited destructuring of the interfacial layers.

9. Very high energy barriers for the salt cations to approach the negative wall have been observed, due to which lithium and potassium cations can be adsorbed on the negative electrode only at high concentrations of salt.

List of Tables

List of Figures

USC
UNIVERSIDADE
DE SANTIAGO
DE COMPOSTELA

List of publications related to this thesis

- **Molecular dynamics simulation of the structure and dynamics of water-1-alkyl-3-methylimidazolium ionic liquid mixtures** Méndez-Morales, T., Carrete, J., Cabeza, O., Gallego, L. J. & Varela, L. M. *J. Phys. Chem. B* **115**, 6995 (2011).

- **Molecular dynamics simulations of the structural and thermodynamic properties of imidazolium-based ionic liquid mxtures**, Méndez-Morales, T., Carrete, J., Cabeza, O., Gallego, L. J. & Varela, L. M. *J. Phys. Chem. B* **115**, 1170 (2011).

- **Dynamical properties of alcohol + 1-hexyl-3-methylimidazolium ionic liquid mixtures: A computer simulation study**, Méndez-Morales, T., Carrete, J., García, M., Cabeza, O., Gallego, L. J. & Varela, L. M. *J. Phys. Chem. B* **115**, 15313 (2011).

- **MD Simulations of the Formation of Stable Clusters in Mixtures of Alkaline Salts and Imidazolium-Based Ionic Liquids**, Méndez-Morales, T., Carrete, J., Bouzón Capelo, S., Pérez-Rodríguez, M., Cabeza, O., Gallego, L. J. & Varela, L. M. *J. Phys. Chem. B* **117**, 3207 (2013).

- **Solvation of lithium salts in protic ionic liquids: a molecular dynamics study**, Méndez-Morales, T., Carrete, J., Cabeza, O., Russina, O., Triolo, A., Gallego, L. J. & Varela, L. M. *J. Phys. Chem. B* **118**, 761 (2014).

- **Nanostructure of mixtures of protic ionic liquids and lithium salts: effect of alkyl chain length**, Méndez-Morales, T., Carrete, J., Rodríguez, J. R., Cabeza, O., Gallego, L. J., Russina, O. & Varela, L. M. *Phys. Chem. Chem. Phys.* **17**, 5298 (2015).

- **Molecular dynamics simulations of the structure of the graphene–ionic liquid/alkali salt mixtures interface**, Méndez-Morales, T., Carrete, J.,

Pérez-Rodríguez, M., Cabeza, O., Gallego, L. J., Lynden-Bell, R. M. & Varela, L. M. *Phys. Chem. Chem. Phys.* **16**, 13271 (2014).

- **Surfactant Self-Assembly Nanostructures in Protic Ionic Liquids**, Fernández-Castro, B., Méndez-Morales, T., Carrete, J., Fazer, E., Cabeza, O., Rodríguez, J. R., Turmine, M. & Varela, L. M. *J. Phys. Chem. B* **115**, 8145 (2011).

- **Thermal Conductivity of Ionic Liquids: A Pseudolattice Approach**, Carrete, J., Méndez-Morales, T., García, M., Cabeza, O., Gallego, L. J. & Varela, L. M. *J. Phys. Chem. B* **116**, 1265 (2012).

- **Investigation of the local structure of mixtures of an ionic liquid with polar solvents through molecular dynamics: Cluster formation and angular distributions**, Carrete, J., Méndez-Morales, T., Cabeza, O., Lynden-Bell, R. M., Gallego, L. J. & Varela, L. M. *J. Phys. Chem. B* **116**, 5941 (2012).

- **Effect of temperature and cationic chain length on the physical properties of ammonium nitrate-based protic ionic liquids**, Bouzón Capelo, S., Méndez-Morales, T., Carrete, J., López Lago, E., Vila, J., Cabeza, O., Rodríguez, J. R., Turmine, M. & Varela, L. M. *J. Phys. Chem. B* **116**, 11302 (2012).

- **Physical properties of the gel phase of aqueous mixtures of the ionic liquid 1-ethyl-3-methylimidazolium octylsulfate: a new ionic rigid gel**, Cabeza, O., Vila, J., Rilo, E., Domínguez-Pérez, M., Otero-Cernadas, L., Méndez-Morales, T. & Varela, L. M. *J. Chem. Thermodynamics* **75**, 52 (2014).

- **Mixtures of protic ionic liquids and molecular cosolvents: A molecular dynamics simulation**, Docampo-Álvarez, B., Gómez-González, V., Méndez-Morales, T., Carrete, J., Rodríguez, J. R., Cabeza, O., Gallego, L. J. & Varela, L. M. *J. Chem. Phys.* **140**, 214502(1) (2014).

- **How does lithium nitrate dissolve in a protic ionic liquid?**, Russina, O., Caminiti, R., Méndez-Morales, T., Carrete, J., Cabeza, O., Gallego, L. J., Varela, L. M. & Triolo, A. *J. Mol. Liq.* **doi:10.1016/j.molliq.2014.08.007**, (2014).

- **2nd Iberian Meeting on Ionic Liquids. Book of Abstracts**, Varela, L. M., Cabeza, O., Carrete, J. & Méndez-Morales, T. *ISBN 987-84-9887-716-8* **205**, (2011).
- **Ionic Liquids in Separation Technology, 1st Edition. Chapter 1.5.** , Méndez-Morales, T. & Varela, L. M. *ISBN 978-04-4463-257-9*, (2014).

USC
UNIVERSIDADE
DE SANTIAGO
DE COMPOSTELA

Complete references

1. Walden, P. *Bull. Russian Acad. Sci.* **1800,** 405–422 (1914).
2. Wasserscheid, P. & Keim, M. *Angew. Chem. Int. Ed. Engl.* **39,** 3772–3789 (2000).
3. Welton, T. *Chem. Rev.* **99,** 2071–2084 (1999).
4. Hallett, J. P. & Welton, T. *Chem. Rev.* **111,** 3508–3576 (2011).
5. Yue, C., Fang, D., Liu, L. & Yi, T. *J. Mol. Liq.* **163,** 99–121 (2011).
6. MacFarlane, D. R., Forsyth, M., Howlett, P. C., Pringle, J. M., Sun, J., Annat, G., Neil, W. & Izdorodina, E. *Acc. Chem. Res.* **40,** 1165–1173 (2007).
7. Armand, M., Endres, F., MacFarlane, D. R., Ohno, H. & Scrosati, B. *Nat. Mat.* **8,** 621–629 (2009).
8. Valkenburg, M. E. V., Vaughn, R. L., Williams, M. & Wilkes, J. S. *Thermochim. Acta* **425,** 181–188 (2005).
9. Reddy, R. G., Zhang, Z., Arenas, M. F. & Blake, D. M. *High Temp. Mat. Proc.* **22,** 87–94 (2003).
10. Ye, C., Liu, W., Chen, Y. & Yu, L. *Chem. Commun.* **2001,** 2244–2245 (2001).
11. Bermúdez, M., Jiménez, A., Sanes, J. & Carrión, F. *Molecules* **14,** 2888–2908 (2009).
12. Han, X. & Armstrong, D. W. *Acc. Chem. Res.* **40,** 1079–1086 (2007).
13. Berthod, A., Ruiz-Angel, M. J. & Carda-Broch, S. *J. Chromatogr. A* **1184,** 6–18 (2008).
14. Hough, W. L., Smiglak, M., Rodríguez, H., Swatloski, R. P., Spear, S. K., Daly, D. T., Pernak, J., Grisel, J. E., Carliss, R. D., Soutullo, M. D., Davis, J. H. & Rogers, R. D. *New J. Chem.* **31,** 1429–1436 (2007).
15. Tadesse, H. & Luque, R. *Energy Environ. Sci.* **4,** 3913–3929 (2011).

16. Carmichael, A. J. & Seddon, K. R. *J. Phys. Org. Chem.* **13,** 591–595 (2000).
17. Hurley, F. H. & Wier, T. P. *J. Electrochem. Soc.* **98,** 207–212 (1951).
18. Scheffler, T. B., Hussey, C. L., Seddon, K. R., Kear, C. M. & Armitage, P. D. *Inorg. Chem.* **22,** 2099–2100 (1983).
19. Laher, T. M. & Hussey, C. L. *Inorg. Chem.* **22,** 3247–3251 (1983).
20. Scheffler, T. B. & Hussey, C. L. *Inorg. Chem.* **23,** 1926–1932 (1984).
21. Evans, D. F., Yamauchi, A. & Wei, G. J. *J. Phys. Chem.* **87,** 3537–3541 (1983).
22. Wilkes, J. S. & Zaworotko, M. J. *J. Chem. Soc., Chem. Commun.* **1992,** 965–967 (1992).
23. Dzyuba, S. V., Kollar, K. D. & Sabnis, S. S. *J. Chem. Educ.* **86,** 856–858 (2009).
24. Kim, D. J., Oh, K. H. & Park, J. K. *Green Chem.* **16,** 4098–4101 (2014).
25. Suarez, P. A. Z., Einloft, S., Dullius, J. E. L., de Souza, R. F. & Dupont, J. *J. Chim. Phys.* **95,** 1626–1639 (1998).
26. Tokuda, H., Hayamizu, K., Ishii, K., Susan, M. A. B. H. & Watanabe, M. *J. Phys. Chem. B* **108,** 16593–16600 (2004).
27. Tokuda, H., Hayamizu, K., Ishii, K., Susan, M. A. B. H. & Watanabe, M. *J. Phys. Chem. B* **109,** 6103–6110 (2005).
28. Tokuda, H., Ishii, K., Susan, M. A. B. H., Tsuzuki, S., Hayamizu, K. & Watanabe, M. *J. Phys. Chem. B* **110,** 2833–2839 (2006).
29. Marsh, K. N., Boxall, J. A. & Lichtenhaler, R. *Fluid Phase Equilib.* **10,** 93–98 (2004).
30. Wilkes, J. S. *J. Mol. Catal. A: Chem.* **214,** 11–17 (2004).
31. Olivier-Bourbigou, H. & Magna, L. *J. Mol. Catal. A: Chem.* **182–183,** 419–437 (2002).
32. Keskin, S., Kayrak-Talay, D., Akman, U. & Hortaçsu, O. *J. Sup. Fluids* **43,** 150–180 (2007).
33. Andreani, L. & Rocha, J. D. *Braz. J. Chem. Eng.* **29,** 1–13 (2012).
34. Ghandi, K. *Green and Sustainable Chemistry* **4,** 44–53 (2014).
35. Pandey, S. *Anal. Chim. Acta* **556,** 38–45 (2006).
36. Wasserscheid, P. & Welton, T. *Ionic liquids in synthesis* (Wiley Online Library, 2003).

37. Plechkova, N. V. & Seddon, K. R. in *Methods and Reagents for Green Chemistry* 103–130 (John Wiley & Sons, Inc., 2007).

38. Mohammad, A. & Inamuddin. *Green solvents II. Properties and applications of ionic liquids* (Springer, 2012).

39. Canongia-Lopes, J. N. & Pádua, A. A. H. *J. Phys. Chem. B* **110,** 3330–3335 (2006).

40. Triolo, A., Russina, O., Bleif, H.-J. & Di Cola, E. *J. Phys. Chem. B* **111,** 4641–4644 (2007).

41. Atkin, R. & Warr, G. G. *J. Phys. Chem. B* **112,** 4164–4166 (2008).

42. Freemantle, M. *An Introduction to Ionic Liquids* (RSC Publishing, 2009).

43. Sato, T., Maruo, T., Marukane, S. & Takagi, K. *J. Power Sources* **138,** 253–261 (2004).

44. Lee, J. S., Bae, J. Y., Lee, H., Quan, N. D. & Kim, H. S. *J. Ind. Eng. Chem.* **10,** 1086–1089 (2004).

45. Buzzeo, M. C., Evans, R. G. & Compton, R. G. *Chem. Phys. Chem.* **5,** 1106–1120 (2004).

46. Endres, F. & Abedin, S. Z. E. *Phys. Chem. Chem. Phys.* **8,** 2101–2116 (2006).

47. Galiński, M., Lewandowski, A. & Stepniak, I. *Electrochim. Acta* **51,** 5567–5580 (2006).

48. Cao, Y. & Mu, T. *Ind. Eng. Chem. Res.* **53,** 8651–8664 (2014).

49. Rocha, M. A. A., Ribeiro, F. M. S., Lobo-Ferreira, A. I. M. C., Coutinho, J. A. P. & Santos, L. M. N. B. F. *J. Mol. Liq.* **108,** 196–202 (2013).

50. Capelo, S. B., Méndez-Morales, T., Carrete, J., Lago, E. L., Vila, J., Rodríguez, O. C. J. R., Turmine, M. & Varela, L. M. *J. Phys. Chem. B* **116,** 11302–11312 (2012).

51. K. Fumino, A. W. & Ludwig, R. *Angew. Chem. Int. Ed.* **48,** 3184–3186 (2009).

52. Fernández-Castro, B., Méndez-Morales, T., Carrete, J., Fazer, E., Cabeza, O., Rodríguez, J. R., Turmine, M. & Varela, L. M. *J. Phys. Chem. B* **115,** 8145–8154 (2011).

53. Hunt, P. A. *Mol. Sim.* **32,** 1–10 (2006).

54. Bhargava, B. L., Balasubramanian, S. & Klein, M. L. *Chem. Commun.* 3339–3351 (2008).

55. Maginn, E. J. *J. Phys.: Condens. Matter* **21,** 373101(1)–373101(17) (2009).

56. Hanke, C. G., Price, S. L. & Lynden-Bell, R. M. *Mol. Phys.* **99,** 801–809 (2001).

57. Turner, E. A., Pye, C. C. & Singer, R. D. *J. Phys. Chem. A* **107,** 2277–2288 (2003).

58. Pópolo, M. G. D., Lynden-Bell, R. M. & Kohanoff, J. *J. Phys. Chem. B* **109,** 5895–5902 (2005).

59. Shah, J. K., Brennecke, J. F. & Maginn, E. J. *Green Chem.* **4,** 112–118 (2002).

60. Frenkel, D. & Smit, B. *Understanding molecular simulation: From algorithms to applications* (Academic Press: New York., 1996).

61. Hansen, J. P. & McDonald, I. R. *Theory of simple liquids* (Academic press: Oxford, 1986).

62. Allen, M. P. & Tildesley, D. J. *Computer Simulations of Liquids* (Oxford University Press, 1987).

63. Urahata, S. M. & Ribeiro, M. C. C. *J. Chem. Phys.* **120,** 1855–1863 (2004).

64. Urahata, S. M. & Ribeiro, M. C. C. *J. Chem. Phys.* **122,** 024511(1)–024511(9) (2005).

65. Hanke, C. G. & Lynden-Bell, R. M. *J. Phys. Chem. B* **107,** 10873–10878 (2003).

66. Jahangiri, S., Taghikhani, M., Behnejad, H. & Ahmadi, S. J. *Mol. Phys.* **106,** 1015–1023 (2008).

67. Lynden-Bell, R. M., Frolov, A. I. & Fedorov, M. V. *Phys. Chem. Chem. Phys.* **14,** 2693–2701 (2012).

68. Fedorov, M. V. & Lynden-Bell, R. M. *Phys. Chem. Chem. Phys.* **14,** 2552–2556 (2012).

69. Merlet, C., Rotenberg, B., Madden, P. A., Taberna, P.-L., Simon, P., Gogotsi, Y. & Salanne, M. *Nat. Mater.* **11,** 306–310 (2012).

70. Spoel, D. V. D., Lindahl, E., Hess, B., Buuren, A. R. V., Apol, E., Meulenhoff, P. J., Tieleman, D. P., Sijbers, A. L. T. M., Feenstra, K. A., Drunen, R. V. & Berendsen, H. J. C. *Gromacs User Manual version 4.0* (http://www.Gromacs.org, 2005).

71. Hess, B., Kutzner, C., Spoel, D. V. D. & Lindahl, E. *J. Chem. Theory Comput.* **4,** 435–447 (2008).

72. Swope, W. C., Andersen, H. C., Berens, P. H. & Wilson, K. R. *J. Chem. Phys.* **76,** 637–649 (1982).

73. Hockney, R. W., Goel, S. P. & Eastwood, J. W. *J. Comp. Phys.* **14** (1974).

74. Scott, W. R. P., Hünenberger, P. H., Tironi, I. G., Mark, A. E., Billeter, S. R., Fennen, J., Torda, A. E., Huber, T., Krüger, P. & Gunsteren, W. F. V. *J. Phys. Chem. A* **103,** 3596–3607 (1999).

75. Jorgensen, W. L., Maxwell, D. S. & Tirado-Rives, J. *J. Am. Chem. Soc.* **118,** 11225–11236 (1996).

76. Martínez, L., Andrade, R., Birgin, E. G. & Martínez, J. M. *J. Comput. Chem.* **30,** 2157–2164 (2009).

77. Darden, T., York, D. & Pedersen, L. *J. Chem. Phys.* **98,** 10089–10094 (1993).

78. Humphrey, W., Dalke, A. & Schulten, K. *J. Mol. Graphics* **14,** 33–38 (1996).

79. Yeh, I. & Berkowitz, M. L. *J. Chem. Phys.* **111,** 3155–3162 (1999).

80. Yeh, I. & Berkowitz, M. L. *J. Chem. Phys.* **112,** 10491–10495 (2000).

81. Méndez-Morales, T., Carrete, J., Cabeza, O., Gallego, L. J. & Varela, L. M. *J. Phys. Chem. B* **115,** 6995–7008 (2011).

82. Wilkes, J. S. *Green Chem.* **4,** 73–80 (2002).

83. Hagiwara, R. & Ito, Y. *J. Fluorine Chem.* **105,** 221–227 (2000).

84. Earle, M. J. & Seddon, K. R. *Pure Appl. Chem.* **72,** 1391–1398 (2000).

85. Earle, M. J., Esperança, J. M. S. S., Gilea, M. A., Canongia-Lopes, J. N., Rebelo, L. P. N., Magee, J. W., Seddon, K. R. & Widegren, J. A. *Nature (London, U.K.)* **439,** 831–834 (2006).

86. Wakai, C., Oleinikova, A., Ott, M. & Weingärtner, H. *J. Phys. Chem. B* **109,** 17028–17030 (2005).

87. Carrete, J., García, M., Rodríguez, J., Cabeza, O. & Varela, L. *Fluid Phase Equilib.* **301,** 118–122 (2011).

88. Cuadrado-Prado, S., Domínguez-Pérez, M., Rilo, E., García-Garabal, S., Segade, L. & C. Franjo, O. C. *Fluid Phase Equilib.* **278,** 36–40 (2009).

89. Bowers, J., Butts, C. P., Martin, P. J., Vergara-Gutierrez, M. C. & Heenan, R. K. *Langmuir* **20,** 2191–2198 (2004).

90. Malham, I. B., Letellier, P. & Turmine, M. *J. Phys. Chem. B* **110,** 14212–14214 (2006).

91. Firestone, M. A., Dzielawa, J. A., Zapol, P., Curtiss, L. A., Seifert, S. & Dietz, M. L. *Langmuir* **18,** 7258–7260 (2002).

92. Antonietti, M., Kuang, D., Smarsly, B. & Zhou, Y. *Angew. Chem. Int. Ed.* **43,** 4988–4992 (2004).

93. Jiang, W., Wang, Y. & Voth, G. A. *J. Phys. Chem. B* **111,** 4812–4818 (2007).

94. Kelkar, M. S., Shi, W. & Maginn, E. J. *Ind. Eng. Chem. Res.* **47,** 9115–9126 (2008).

95. Canongia-Lopes, J. N., Costa-Gomes, M. F. & Pádua, A. A. H. *J. Phys. Chem. B* **110,** 16816–16818 (2006).

96. Spickermann, C., Thar, J., Lehmann, S. B. C., Zahn, S., Hunger, J., Buchner, R., Hunt, P. A., Welton, T., & Kirchner, B. *J. Chem. Phys.* **129,** 104505(1)–104505(13) (2008).

97. Porter, A. R., Liem, S. Y. & Popelier, P. L. A. *Phys. Chem. Chem. Phys.* **10,** 4240–4248 (2008).

98. Feng, S. & Voth, G. A. *Fluid Phase Equilib.* **294,** 148–156 (2010).

99. Chevrot, G., Schurhammer, R. & Wipff, G. *Phys. Chem. Chem. Phys.* **8,** 4166–4174 (2006).

100. Inoue, G., Shimoyama, Y., Su, F., Takada, S., Iwai, Y. & Arai, Y. *J. Chem. Eng. Data* **52,** 98–101 (2007).

101. Freire, M. G., Santosa, L. M. N. B. F., Fernandes, A. M., Coutinho, J. A. & Marrucho, I. M. *Fluid Phase Equilib.* **261,** 449–454 (2007).

102. Wong, D. S. H., Chen, J. P., Chang, J. M. & Chou, C. H. *Fluid Phase Equilib.* **194–197,** 1089–1095 (2002).

103. Margulis, C. J., Stern, H. A. & Berne, B. J. *J. Phys. Chem. B* **106,** 12017–12021 (2002).

104. Spoel, D. V. D., Lindahl, E., Hess, B., Buuren, A. R. V., Apol, E., Meulenhoff, P. J., Tieleman, D. P., Sijbers, A. L. T. M., Feenstra, K. A., Drunen, R. V. & Berendsen, H. J. C. *Gromacs User Manual version 3.2* (http://www.Gromacs.org, 2005).

105. Bayly, C. I., Cieplak, P., Cornell, W. D. & Kollman, P. A. *J. Phys. Chem* **97,** 10269–10280 (1993).

106. Berendsen, H. J. C., Grigera, J. R. & Straatsma, T. P. *J. Phys. Chem.* **91,** 6269–6271 (1987).

107. Essmann, U., Perera, L., Berkowitz, M. L., Darden, T., Lee, H. & Pedersen, L. G. *J. Chem. Phys.* **103,** 8577–8593 (1995).

108. Jorgensen, W. L. & Madura, J. D. *J. Am. Chem. Soc.* **105,** 1407–1413 (1983).

109. Mahoney, M. W. & Jorgensen, W. L. *J. Chem. Phys.* **112,** 8910–8922 (2000).

110. Cornell, W. D., Cieplak, P., Bayly, C. I., Gould, I. R., Merz, K. M., Ferguson, D. M., Spellmeyer, D. C., Fox, T., Caldwell, J. W. & Kollman, P. A. *J. Am. Chem. Soc.* **117,** 5179–5197 (1995).

111. Zielkiewicz, J. *J. Chem. Phys.* **123,** 104205(1)–104205(6) (2005).

112. Klähn, M., Stuber, C., Seduraman, A. & Wu, P. *J. Phys. Chem. B* **114,** 2856–2868 (2010).

113. Head-Gordon, T. & Johnson, M. E. *Proc. Natl. Acad. Sci. U.S.A.* **103,** 7973–7977 (2006).

114. Berendsen, H. J. C., Postma, J. P. M., van Gunsteren, W. F., DiNola, A. & Haak, J. R. *J. Phys. Chem.* **81,** 3684–3690 (1984).

115. Morrow, T. I. & Maginn, E. J. *J. Phys. Chem. B* **106,** 12807–12813 (2002).

116. Bowron, D. T., D'Agostino, C., Gladden, L. F., Hardacre, C., Holbrey, J. D., Lagunas, M. C., McGregor, J., Mantle, M. D., Mullan, C. L. & Youngs, T. G. A. *J. Phys. Chem. B* **114,** 7760–7768 (2010).

117. Bahe, L. W. *J. Phys. Chem* **76,** 1062–1071 (1972).

118. Varela, L. M., Garcia, M., Sarmiento, F., Attwood, D. & Mosquera, V. *J. Chem. Phys.* **107,** 6415–6419 (1997).

119. Souto, J., Alemany, M. M. G. & Gallego, L. J. *Phys. Rev. B* **81,** 134201(1)–134201(15) (2010).

120. Alavi, S. & Thompson, D. L. *J. Chem. Phys.* **122,** 154704(1)–154715(12) (2005).

121. Liu, Z., Wu, X. & Wang, W. *Phys. Chem. Chem. Phys.* **8,** 1096–1104 (2006).

122. Liu, Z., Huang, S. & Wang, W. *J. Phys. Chem. B* **108,** 12978–12989 (2004).

123. Micaelo, N. M., Baptista, A. M. & Soares, C. M. *J. Phys. Chem. B* **110,** 14444–14451 (2006).

124. Hardacre, C., McMath, S. E. J., Nieuwenhuyzen, M., Bowron, D. T & Soper, A. K. *J. Phys.: Condens. Matter* **15,** S159–S166 (2003).

125. Köddermann, T., Wertz, C., Heintz, A. & Ludwig, R. *Angew. Chem. Int. Ed.* **45,** 3697–3702 (2006).

126. Raugei, S. & Klein, M. *J. Chem. Phys.* **116,** 196–202 (2002).

127. H. Ohtaki, T. R. *Chem. Rev.* **93,** 1157–1204 (1993).

128. Pópolo, M. G. D. & Voth, G. A. *J. Phys. Chem. B* **108,** 1744–1752 (2004).

129. Harsányi, I., Pusztai, L., Soetens, J. C. & Bopp, P. A. *J. Mol. Liq.* **129,** 80–85 (2006).

130. Sokol, M., Dawid, A., Dendzik, Z. & Gburski, Z. *J. Mol. Struct.* **704,** 341–345 (2004).

131. Chaumont, A., Schurhammer, R. & Wipff, G. *J. Phys. Chem. B* **109,** 18964–18973 (2005).

132. Méndez-Morales, T., Carrete, J., Cabeza, O., Gallego, L. J. & Varela, L. M. *J. Phys. Chem. B* **115,** 11170–11182 (2011).

133. Rogers, R. D. & Seddon, K. R. *Science* **302,** 792–793 (2003).

134. Rogers, R. D. & Seddon, K. R. *Ionic liquids as green solvents: progress and prospects* (American Chemical Society, 2003).

135. Rogers, R. D. & Seddon, K. R. *Ionic liquids: industrial applications for green chemistry* (American Chemical Society, 2002).

136. Cabeza, O., Segade, L., García-Garabal, S., Rilo, E., Domínguez-Pérez, M. & Varela, L. M. in *Ionic Liquids, Theory and Applications* 111–136 (InTech, 2011).

137. Pereiro, A. B. & Rodríguez, A. *J. Chem. Eng. Data* **52,** 1408–1412 (2007).

138. Sahandzhieva, K., Tuma, D., Breyer, S., Kamps, A. P. S. & Maurer, G. *J. Chem. Eng. Data* **51,** 1516–1525 (2006).

139. Crosthwaite, J. M., Aki, S. N. V. K., Maginn, E. J. & Brennecke, J. F. *J. Phys. Chem. B* **108,** 5113–5119 (2004).

140. Pereiro, A. B. & Rodríguez, A. *J. Chem. Thermodyn.* **39,** 978–989 (2007).

141. Domańska, U. & Marciniak, A. *J. Phys. Chem. B* **108,** 2376–2382 (2004).

142. Huo, Y., Xia, S. & Ma, P. *J. Chem. eng. Data* **52,** 2077–2082 (2007).

143. Gómez, E., González, B., Calvar, N., Tojo, E. & Domínguez, A. *J. Chem. Eng. Data* **51,** 2096–2102 (2006).

144. Pereiro, A. B., Tojo, E., Rodríguez, A., Canosa, J. & Tojo, J. *J. Chem. Thermodyn.* **38,** 651–661 (2006).

145. Stoppa, A., Hunger, J. & Buchner, R. *J. Chem. Eng. Data* **54,** 472–479 (2009).

146. Gómez, E., Calvar, N., Domínguez, I. & Domínguez, A. *Phys. Chem. Liq.* **44,** 409–417 (2006).

147. Rilo, E., Pico, J., García-Garabal, S., Varela, L. M. & Cabeza, O. *Fluid Phase Equilib.* **285,** 83–89 (2009).

148. Hanke, C. G., Atamas, N. A. & Lynden-Bell, R. M. *Green Chem.* **4,** 107–111 (2002).

149. Raabe, G. & Köhler, J. *J. Chem. Phys.* **129,** 144503(1)–144503(8) (2008).

150. Heintz, A., Ludwig, R. & Schmidt, E. *Phys. Chem. Chem. Phys.* **13,** 3268–3273 (2011).

151. Huddleston, J. G., Visser, A. E., Reichert, W. M., Willauer, H. D., Broker, G. A. & Rogers, R. D. *Green Chem.* **3,** 156–164 (2001).

152. Holbrey, J. D. & Seddon, K. R. *J. Chem. Soc., Dalton Trans.* 2133–2139 (1999).

153. Jorgensen, W. L. *J. Phys. Chem.* **90,** 1276–1284 (1986).

154. Sambasivarao, S. . V. & Acevedo, O. *J. Chem. Theory Comput.* **5,** 1038–1050 (2009).

155. Prado, C. E. R. & Freitas, L. C. G. *J. Mol. Struct. (Theochem.)* **847,** 93–100 (2007).

156. Canongia-Lopes, J. N., Deschamps, J. & Pádua, A. H. *J. Phys. Chem. B* **108,** 2038–2047 (2004).

157. Brenneman, C. M. & Wiberg, K. B. *J. Comp. Chem.* **11,** 361–373 (1990).

158. Frisch, M. J. *et al. Gaussian 94, Revision A.1* (Gaussian, Inc., Pittsburgh, PA, 1995).

159. Hess, B., Bekker, H., Berendsen, H. J. C. & Fraaije, J. G. E. M. *J. Comp. Chem.* **18,** 1463–1472 (1997).

160. Hess, B. *J. Chem. Theory Comp.* **4,** 116–122 (2007).

161. Bussi, G., Donadio, D. & Parrinello, M. *J. Chem. Phys.* **126,** 014101(1)–014101(7) (2007).

162. Parrinello, M. & Rahman, A. *J. Appl. Phys.* **52,** 7182–7190 (1981).

163. Gómez, E., González, B., Domínguez, A., Tojo, E. & Tojo, J. *J. Chem. Eng. Data* **51,** 696–701 (2006).

164. Gibson, H. M. & Wilding, N. B. *Phys. Rev. E* **73,** 061507(1)–061507(7) (2006).

165. Saiz, L., Padro, J. A. & Guardia, E. *J. Phys. Chem. B* **101,** 78–86 (1997).

166. Stuart, S. J. & Berne, B. J. *J. Phys. Chem.* **100,** 11934–11943 (1996).

167. McGreevy, R. L., Baranyai, A. & Ruff, I. *Phys. Chem. Liq.* **16,** 47–54 (1986).

168. Haughney, M., Ferrario, M. & McDonald, I. R. *J. Phys. Chem.* **91,** 4934–4940 (1987).

169. Yamaguchi, T., Hidaka, H. & Soper, A. K. *Mol. Phys.* **96,** 1159–1168 (1999).

170. Matsumoto, M. & Gubbins, K. E. *J. Chem. Phys.* **93,** 1981–1994 (1990).

171. J. H. Guo, A. A. J. E. R. C. S. H. A. H. S. Y. Luo & Nordgren, J. *Phys. Rev. Lett.* **89,** 137402(1)–137402(4) (2002).

172. Luzar, A. & Chandler, D. *Phys. Rev. Lett.* **76,** 928–931 (1996).

173. Stillinger, F. H. *Science* **209,** 451–457 (1980).

174. Méndez-Morales, T., Carrete, J., García, M., Cabeza, O., Gallego, L. J. & Varela, L. M. *J. Phys. Chem. B* **115,** 15322–15322 (2011).

175. Heintz, A. *J. Chem. Thermodyn.* **37,** 525–535 (2005).

176. Jr, A. A. F., King, L. A., Levisky, J. A. & Wilkes, J. S. *J. Phys. Chem.* **88,** 2609–2614 (1984).

177. Hussey, C. L. *Pure Appl. Chem.* **60,** 1763–1772 (1988).

178. Bonhôte, P., Dias, A. P., Papageorgiou, N., Kalyanasundaram, K. & Grätzel, M. *Inorg. Chem.* **35,** 1168–1178 (1996).

179. Holbrey, J. D. & Seddon, K. R. *Clean Prod. Proc.* **1,** 223–236 (1999).

180. Bates, E. D., Mayton, R. D., Ntai, I. & Jr, J. H. D. *J. Am. Chem. Soc.* **124,** 926–927 (2002).

181. Lu, W. *et al. Science* **297,** 983–987 (2002).

182. Liu, W., Ye, C., Gong, Q., Wang, H. & Wang, P. *Tribol. Lett.* **13,** 81–85 (2002).

183. Xu, W. & Angell, C. A. *Science* **302,** 422–425 (2003).

184. Seki, S., Kobayashi, Y., Miyashiro, H., Ohno, Y., Usami, A., Mita, Y., Kihira, N., Watanabe, M. & Terada, N. *Chem. Commun.* **2006,** 544–10230 (2006).

185. Anderson, J. L., Armstrong, D. W. & Wei, G. T. *Anal. Chem.* **78,** 2892–2902 (2006).

186. Fabregat-Santiago, F., Bisquert, J., Palomares, E., Otero, L., Kuang, D., Zakeeruddin, S. M. & Grätzel, M. *J. Phys. Chem. C* **111,** 6550–6560 (2007).

187. MacFarlane, D. R., Meakin, P., Sun, J., Amini, N. & Forsyth, M. *J. Phys. Chem. B* **103,** 4164–4170 (1999).

188. Sun, J., Forsyth, M. & MacFarlane, D. R. *J. Phys. Chem. B* **102,** 8858–8864 (1998).

189. Cadena, C., Zhao, Q., Snurr, R. & Maginn, E. J. *J. Phys. Chem. B* **110,** 2821–2832 (2006).

190. Wu, X., Liu, Z., Huang, S. & Wang, W. *Phys. Chem. Chem. Phys.* **7,** 2771–2779 (2005).

191. Price, W. S. *Concepts Magn. Reson.* **9,** 299–336 (1997).

192. Price, W. S. *Concepts Magn. Reson.* **10,** 197–237 (1998).

193. Marquardt, E., Grober, N. & Richter, J. *Opt. Eng.* **36,** 2857–2862 (1997).

194. Marquardt, E. & Richter, J. *Opt. Eng.* **37,** 1514–1519 (1998).

195. Umecky, T., Kanakubo, M. & Ikushima, Y. *Fluid Phase Equilib.* **228–229,** 329–333 (2005).

196. Every, H. A., Bishop, A. G., MacFarlane, D. R., Oradd, G. & Forsyth, M. *Phys. Chem. Chem. Phys.* **6,** 1758–1765 (2004).

197. Noda, A., Hayamizu, K. & Watanabe, M. *J. Phys. Chem. B* **105,** 4603–4610 (2001).

198. Jin, H., O'Hare, B., Dong, J., Arzhantsev, S., Baker, G. A., Wishart, J. F., Benesi, A. J. & Maroncelli, M. *J. Phys. Chem. B* **112,** 81–92 (2008).

199. Umecky, T., Kanakubo, M. & Ikushima, Y. *J. Mol. Liq.* **119,** 77–81 (2005).

200. Bara, J. E., Carlisle, T. K., Gabriel, C. J., Camper, D., Finotello, A., Gin, D. L. & Noble, R. D. *Ind. Eng. Chem. Res.* **48,** 2739–2751 (2009).

201. Morgan, D., Ferguson, L. & Scovazzo, P. *Ind. Eng. Chem. Res.* **44,** 4815–4823 (2005).

202. Shiflett, M. B. & Yokozeki, A. *Ind. Eng. Chem. Res.* **44,** 4453–4464 (2005).

203. Shiflett, M. B., Harmer, M. A., Junk, C. P. & Yokozeki, A. *Fluid Phase Equilib.* **242,** 220–232 (2006).

204. Iacob, C., Sangoro, J. R., Papadopoulos, P., Schubert, T., Naumov, S., Valiullin, R., Kärger, J. & Kremer, F. *Phys. Chem. Chem. Phys.* **12,** 13798–13803 (2010).

205. Lovell, C. S., Walker, A., Damion, R. A., Radhi, A., Tanner, S. F., Budtova, T. & Ries, M. E. *Biomacromol.* **11,** 2927–2935 (2010).

206. Sarraute, S., Gomes, M. F. C. & Pádua, A. A. H. *J. Chem. Eng. Data* **54,** 2389–2394 (2009).

207. Wong, C. L., Soriano, A. N. & Li, M. H. *Fluid Phase Equilib.* **271,** 43–52 (2008).

208. De Castro, C. A. N. *et al. Fluid Phase Equilib.* **294,** 157–179 (2010).

209. Menjoge, A., Dixon, J. N., Brennecke, J. F., Maginn, E. J. & Vasenkov, S. *J. Phys. Chem. B* **113,** 6353–6359 (2009).

210. Heintz, A., Lehmann, J. K., Schmidt, E. & Wandschneider, A. *J. Solution Chem.* **38,** 1079–1083 (2009).

211. Richter, J., Leuchter, A. & Grober, N. *J. Mol. Liq.* **103–104,** 359–370 (2003).

212. Su, W. C., Chou, C. H., Wong, D. S. H. & Li, M. H. *Fluid Phase Equilib.* **252,** 74–78 (2007).

213. Huang, X., Margulis, C. J., Li, Y. & Berne, B. J. *J. Am. Chem. Soc.* **127,** 17842–17851 (2005).

214. Hu, Z. & Margulis, C. J. *Proc. Natl. Acad. Sci. USA* **103,** 831–836 (2006).

215. Kelkar, M. S. & Maginn, E. J. *J. Phys. Chem. B* **111,** 4867–4876 (2007).

216. Liu, Z., Chen, T., Bell, A. & Smit, B. *J. Phys. Chem. B* **114,** 4572–4582 (2010).

217. Borodin, O. & Smith, G. D. *J. Phys. Chem. B* **110,** 11481–11490 (2006).

218. Margulis, C. J. *Mol. Phys.* **102,** 829–838 (2004).

219. Yan, T., Burnham, C. J., Pópolo, M. G. D. & Voth, G. A. *J. Phys. Chem. B* **108,** 11877–11881 (2004).

220. De Andrade, J., Böes, E. S. & Stassen, H. *J. Phys. Chem. B* **106,** 13344–13351 (2002).

221. Annapureddy, H. V. R., Hu, Z., Xia, J. & Margulis, C. J. *J. Phys. Chem. B* **112,** 1770–1776 (2008).

222. Liu, X., Vlugt, T. J. H. & Bardow, A. *J. Phys. Chem. B* **115,** 8506–8517 (2011).

223. Einstein, A. *Ann. Phys.* **17,** 549–560 (1905).

224. Karger, N., Vardag, T. & Lüdemann, H. D. *J. Chem. Phys.* **93,** 3437–3444 (1990).

225. Martí, J., Padró, J. A. & Guàrdia, E. *J. Mol. Liq.* **64,** 1–12 (1995).

226. Guevara-Carrion, G., Nieto-Draghi, C., Vrabec, J. & Hasse, H. *J. Phys. Chem. B* **112,** 16664–16674 (2008).

227. Stern, H. A., Rittner, F., Berne, B. J. & Friesner, R. A. *J. Chem. Phys.* **115,** 2237–2251 (2001).

228. Méndez-Morales, T., Carrete, J., Bouzón-Capelo, S., Pérez-Rodríguez, M., Cabeza, O., Gallego, L. J. & Varela, L. M. *J. Phys. Chem. B* **117,** 3207–3220 (2013).

229. Dupont, J., de Souza, R. F. & Suarez, P. A. Z. *Chem. Rev.* **102,** 3667–3692 (2002).

230. Garcia, B., Lavallée, S., Perron, G., Michot, C. & Armand, M. *Electrochim. Acta* **49,** 4583–4588 (2004).

231. Diaw, M., Chagnes, A., Carré, B., Willmann, P. & Lemordant, D. *J. Power Sources* **146,** 682–684 (2005).

232. Zhou, Q., Henderson, W. A., Appetecchi, G. B. & Passerini, S. *J. Phys. Chem. C* **114,** 6201–6204 (2010).

233. Lee, S. Y., Yong, H. H., Lee, Y. J., Kim, S. K. & Ahn, S. *Green Chem.* **109,** 13663–13667 (2005).

234. Markevich, E., Baranchugov, V. & Aurbach, D. *Electrochem. Commun.* **8,** 1331–1334 (2006).

235. Castriota, M., Caruso, T., Agostino, R. G., Cazzanelli, E., Henderson, W. A. & Passerini, S. *J. Phys. Chem. A* **109,** 92–96 (2005).

236. Borgel, V., Markevich, E., Aurbach, D., Semrau, G. & Schmidt, M. *J. Power Sources* **189,** 331–336 (2009).

237. Nicolau, B. G., Sturlaugson, A., Fruchey, K., Ribeiro, M. C. C. & Fayer, M. D. *J. Phys. Chem. B* **114,** 8350–8356 (2010).

238. Nicotera, I., Oliviero, C., Henderson, W. A., Appetecchi, G. B. & Passerini, S. *J. Phys. Chem. B* **109,** 22814–22819 (2005).

239. Lassègues, J., Grondin, J. & Talaga, D. *Phys. Chem. Chem. Phys.* **8,** 5629–5632 (2006).

240. Lassègues, J., Grondin, J., Aupetit, C. & Johansson, P. *J. Phys. Chem. A* **113,** 305–314 (2009).

241. Egashira, M., Todo, H., Yoshimoto, N., Morita, M. & Yamaki, J. *J. Power Sources* **174,** 560–564 (2007).

242. Henderson, W. A. & Passerini, S. *Chem. Mater.* **16,** 2881–2885 (2004).

243. Zhou, Q., Fitzgerald, K., Boyle, P. D. & Henderson, W. A. *Chem. Mater.* **22,** 1203–1208 (2010).

244. Xu, J., Yang, J., NuLi, Y., Wang, J. & Zhang, Z. *J. Power Sources* **160,** 621–626 (2006).

245. Seki, S., Kobayashi, Y., Miyashiro, H., Ohno, Y., Usami, A., Mita, Y., Kihira, N., Watanabe, M. & Terada, N. *J. Phys. Chem. B* **110,** 10228–10230 (2006).

246. Saito, Y., Umecky, T., Niwa, J., Sakai, T. & Maeda, S. *J. Phys. Chem. B* **111,** 11794–11802 (2007).

247. Sakaebe, H. & Matsumoto, H. *Electrochem. Commun.* **5,** 594–598 (2003).

248. Rosol, Z. P., German, N. J. & Gross, S. M. *Green Chem.* **11,** 1453–1457 (2009).

249. Pereiro, A. B., Araújo, J. M. M., Oliveira, F. S., Esperança, J. M. S. S., Lopes, J. N. C., Marrucho, I. M. & Rebelo, L. P. N. *J. Chem. Thermodyn.* **55,** 29–36 (2012).

250. Zhou, Q., Boyle, P. D., Malpezzi, L., Mele, A., Shin, J.-H., Passerini, S. & Henderson, W. A. *Chem. Mater.* **23,** 4331–4337 (2011).

251. Burba, C. M., Rocher, N. M., Frech, R. & Powell, D. R. *J. Phys. CHem. B* **112,** 2991–2995 (2008).

252. Hayamizu, K., Aihara, Y., Nakagawa, H. & Nukuda, T. *J. Phys. Chem. B* **108,** 19527–19532 (2004).

253. Duluard, S., Grondin, J., Bruneel, J., Pianet, I., Grélard, A., Campet, G., Delville, M. & Lassègues, J. *J. Raman Spectroscopy* **39,** 627–632 (2008).

254. Umebayashi, Y., Mitsugi, T., Fukuda, S., Fujimori, T., Fujii, K., Kanzaki, R., Takeuchi, M. & Ishiguro, S. *J. Phys. Chem. B* **111,** 13028–13032 (2007).

255. Monteiro, M. J., Bazito, F. F. C., Siqueira, L. J. A., Ribeiro, M. C. C. & Torresi, R. M. *J. Phys. Chem. B* **112,** 2102–2109 (2008).

256. Borodin, O., Smith, G. D. & Henderson, W. *J. Phys. Chem. B* **110,** 16879–16886 (2006).

257. Niu, S., Cao, Z., Li, S. & Yan, T. *J. Phys. Chem. B* **114,** 877–881 (2010).

258. Canongia-Lopes, J. N. & Pádua, A. A. H. *J. Phys. Chem. B* **108,** 16893–16898 (2004).

259. Pereiro, A. B., Legido, J. L. & Rodríguez, A. . *Chem. Thermodyn.* **39,** 1168–1175 (2007).

260. Xuan, X., Wang, J. & Wang, H. *Electrochim. Acta* **50,** 4196–4201 (2005).

261. Francisco, J. S. & Williams, I. H. *Am. Chem. Soc.* **94,** 8522–8529 (1990).

262. Varela, L. M., Carrete, J., García, M., Rodríguez, J. R., Gallego, L. J., Turmine, M. & Cabeza, O. in *Ionic liquids: theory, properties, new approaches* (ed Kokorin, A.) (InTech, 2011).

263. Arnaud, R., Benrabah, D. & Sanchez, J.-Y. *J. Phys. Chem.* **100,** 10882–10891 (1996).

264. Gejji, S. P., Suresh, C. H., Babu, K. & Gadre, S. R. *J. Phys. Chem. A* **103,** 7474–7480 (1999).

265. Zhang, Y., Alonso, P. R., Martinez-Limia, A., Scanlon, L. G. & Balbuena, P. B. *J. Phys. Chem. B* **108,** 4659–4668 (2004).

266. Kowsari, M. H., Alavi, S., Ashrafizaadeh, M. & Najafi, B. *J. Chem. Phys.* **129,** 224508(1)–224508(13) (2008).

267. Rey-Castro, C., Tormo, A. L. & Vega, L. F. *Fluid Phase Equilib.* **256,** 62–69 (2007).

268. Qian, J., Hentschke, R. & Heuer, A. *J. Chem. Phys.* **110,** 4514–4522 (1999).

269. Borodin, O. *J. Phys. Chem. B* **113,** 11463–11478 (2009).

270. Borodin, O. *Mater. Res. Soc. Proc.* **1082,** Q06–04 (2008).

271. Vila, J., Rilo, E., Segade, L., Cabeza & Varela, L. M. *Phys. Rev. E* **71,** 031201(1)–031201(8) (2005).

272. Angell, C. A., Byrne, N. & Belieres, J.-P. *Acc. Chem. Res.* **40,** 1228–1236 (2007).

273. Borodin, O., Smith, G. D. & Fan, P. *J. Phys. Chem. B* **110,** 22773–22779 (2006).

274. Kowsari, M. H., Alavi, S., Ashrafizaadeh, M. & Najafi, B. *J. Chem. Phys.* **130,** 014703(1)–014703(10) (2009).

275. Rey-Castro, C. & Vega, L. F. *J. Phys. Chem. B* **110,** 14426–14435 (2006).

276. Rilo, E., Vila, J., García, M., Varela, L. M. & Cabeza, O. *J. Chem. Eng. Data* **55,** 5156–5163 (2010).

277. Carda-Broch, S., Berthod, A. & Armstrong, D. W. *Anal. Bioanal. Chem.* **375,** 191–199 (2003).

278. Méndez-Morales, T., Carrete, J., Cabeza, O., Russina, O., Triolo, A., Gallego, L. J. & Varela, L. M. *J. Phys. Chem. B* **118,** 761–770 (2014).

279. Zhang, S., Sun, N., He, X., Lu, X. & Zhang, X. *J. Phys. Chem. Ref. Data* **35,** 1475–1517 (2006).

280. Greaves, T. L. & Drummond, C. J. *Chem. Rev.* **108,** 206–237 (2008).

281. M. Yoshizawa, W. X. & Angell, C. A. *J. Am. Chem. Soc.* **125,** 15411–15419 (2003).

282. Greaves, T. L., Weerawardena, A., andgre I. Krodkiewska, C. F. & Drummond, C. J. *J. Phys. Chem. B* **110,** 22479–22487 (2006).

283. Nakamoto, H. & Watanabe, M. *Chem. Commun.* 2539–2541 (2007).

284. Md. A. B. H. Susan, S. M. A. Noda & Watanabe, M. *Chem. Commun.* **2003,** 938–939 (2003).

285. Timperman, L., Skowron, P., Boisset, A., Galiano, H., Lemordant, D., Frackowiak, E., Beguinb, F. & Anouti, M. *Phys. Chem. Chem. Phys.* **14,** 8199–8207 (2012).

286. Anouti, M. & Timperman, L. *Phys. Chem. Chem. Phys.* **15,** 6539–6548 (2013).

287. Greaves, T. L., Weerawardena, A., Fong, C. & Drummond, C. J. *J. Phys. Chem. B* **111,** 4082–4088 (2007).

288. Greaves, T. L., Weerawardena, A., Krodkiewska, I. & Drummond, C. J. *Chem. Rev.* **112,** 896–905 (2008).

289. Atkin, R., Bobillier, S. M. C. & Warr, G. G. *J. Phys. Chem. B* **114,** 1350–1360 (2010).

290. Kennedy, D. F. & Drummond, C. J. *J. Phys. Chem. B* **113,** 5690–5693 (2009).

291. X. Wang, X. C. Q. Li & Li, Z. *Langmuir* **28,** 16547–16554 (2012).

292. Song, X., Hamano, H., Minofar, B., Kanzaki, R., Fujii, K., Kameda, Y., Kohara, S., Watanabe, M., Ishiguro, S. & Umebayashi, Y. *J. Phys. Chem. B* **116,** 2801–2813 (2012).

293. Alvarez, V. H., Dosil, N., Gonzalez-Cabaleiro, R., Mattedi, S., Martin-Pastor, M., Iglesias, M. & Navaza, J. M. *J. Chem. Eng. Data* **55,** 625–632 (2010).

294. Hunger, J., Sonnleitner, T., Liu, L., Buchner, R., Bonn, M. & Bakker, H. J. *J. Phys. Chem* **3,** 3034–3038 (2012).

295. Niga, P., Wakeham, D., Nelson, A., Warr, G. G., Rutland, M. & Atkin, R. *Langmuir* **26,** 8282–8288 (2010).

296. Zhao, C., Burrell, G., Torriero, A. A. J., Separovic, F., Dunlop, N. F., MacFarlane, D. R. & Bond, A. M. *J. Phys. Chem. B* **112,** 6923–6936 (2008).

297. Hayes, R., Imberti, S., Warr, G. G. & Atkin, R. *Phys. Chem. Chem. Phys.* **13,** 13544–13551 (2011).

298. Bodo, E., Postorino, P., Mangialardo, S., Piacente, G., Ramondo, F., Bosi, F., Ballirano, P. & Caminiti, R. *J. Phys. Chem. B* **115,** 13149–13161 (2011).

299. Bodo, E., Mangialardo, S., Ramondo, F., Ceccacci, F. & Postorino, P. *J. Phys. Chem. B* **116,** 13878–13888 (2012).

300. Markusson, H., Belieres, J.-P., Johansson, P., Angell, C. A. & Jacobsson, P. *J. Phys. Chem. A* **111,** 8717–8723 (2007).

301. Umebayashi, Y., Chung, W.-L., Mitsugi, T., Fukuda, S., Takeuchi, M., Fujii, K., Takamuku, T., Kanzaki, R. & Ishiguro, S. *J. Comput. Chem. Jpn.* **7,** 125–134 (2008).

302. Zahn, S., Thar, J. & Kirchner, B. *J. Chem. Phys.* **132,** 124506(1)–124506(13) (2010).

303. Hayes, R., Imberti, S., Warr, G. G. & Atkin, R. *Angew. Chem., Int. Ed.* **51,** 7468–7471 (2012).

304. Hayes, R., Imberti, S., Warr, G. G. & Atkin, R. *Angew. Chem., Int. Ed.* **52,** 4623–4627 (2013).

305. Menne, S., Pires, J., Anouti, M. & Balducci, A. *Electrochem. Commun.* **31,** 39–41 (2013).

306. Choe, J., Kim, K. & Chang, S. *Bull. Korean Chem. Soc.* **21,** 200–206 (2000).

307. Borodin, O. & Smith, G. D. *J. Phys. Chem. B* **113,** 1763–1776 (2009).

308. Marcus, Y. *Chem. Rev.* **109,** 1346–1370 (2009).

309. Nag, A., Chakraborty, D. & Chandra, A. *J. Chem. Sci.* **120,** 71–77 (2008).

310. Hayes, R., Imberti, S., Warr, G. G. & Atkin, R. *Phys. Chem. Chem. Phys.* **13,** 3237–3247 (2011).

311. Lawler, C. & Fayer, M. D. *J. Phys. Chem. B* **117,** 9768–9774 (2013).

312. Stromme, K. O. *Acta Chem. Scand.* **24,** 1479–1481 (1970).

313. Miller, R. E., Getty, R. R., Treuil, K. L. & Leroi, G. E. *J. Chem. Phys.* **51,** 1385–1389 (1969).

314. Adya, A. K., Neilson, G. W., Okada, I. & Okazaki, S. *Mol. Phys.* **79,** 1327–1350 (1993).

315. Mähler, J. & Persson, I. *Inorg. Chem.* **51,** 425–438 (2012).

316. Soper, A. K. & Weckström, K. *Biophys. Chem.* **124,** 180–191 (2006).

317. Méndez-Morales, T., Carrete, J., Rodríguez, J., Cabeza, O., Gallego, L. J., Russina, O. & Varela, L. M., – (2014).

318. Ohno, H. *Electrochemical aspects of Ionic Liquids* (John Wiley & Sons, Inc., 2005).

319. Plechkova, N. V. & Seddon, K. R. *Chem. Soc. Rev.* **37,** 123–150 (2008).

320. Zeng, Z., Phillips, B. S., Xiao, J.-C. & Shreeve, J. M. *Chem. Matter.* **20,** 12719–2726 (2008).

321. Hayes, R., Imberti, S., Warr, G. G. & Atkin, R. *J. Phys. Chem. C* **118,** 13998–14008 (2014).

322. Hayes, R., Bernard, S. A., Imberti, S., Warr, G. G. & Atkin, R. *J. Phys. Chem. C,* http://dx.doi.org/10.1021/jp506192d.

323. Russina, O., Caminiti, R., Méndez-Morales, T., Carrete, J., Cabeza, O., Gallego, L., Varela, L. & Triolo, A. *J. Mol. Liq.* http://dx.doi.org/10.1016/j.molliq.2014.08.007. ISSN: 0167-7322 (2014).

324. Menne, S., Vogl, T. & Balducci, A. *Phys. Chem. Chem. Phys.* **16,** 5485–5489 (2014).

325. Greaves, T. L., Kennedy, D. F., Mudie, S. T. & Drummond, C. J. *J. Phys. Chem. B* **114,** 10022–10031 (2010).

326. Hayes, R., Imberti, S., Warr, G. G. & Atkin, R. *Phys. Chem. Chem. Phys.* **13,** 3237–3247 (2011).

327. Méndez-Morales, T., Carrete, J., Pérez-Rodríguez, M., Cabeza, O., Gallego, L. J., Lynden-Bell, R. M. & Varela, L. M. *Phys. Chem. Chem. Phys.* **16,** 13271–13278 (2014).

328. Lewandowski, A. & Świderska Mocek, A. *J. Power Sources* **194,** 601–609 (2009).

329. Kuboki, T., Okuyama, T., Ohsaki, T. & Takami, N. *J. Power Sources* **26,** 766–769 (2005).

330. Sakaebe, H., Matsumoto, H. & Tatsumi, K. *Electrochim. Acta* **53,** 1048–1054 (2007).

331. Frackowiak, E. *Phys. Chem. Chem. Phys.* **9,** 1774–1785 (2007).

332. Islam, M. M., Alam, M. T., Okajima, T. & Ohsaka, T. *J. Phys. Chem. C* **113,** 3386–3389 (2009).

333. Lockett, V., Horne, M., Sedev, R., Rodopoulos, T. & Ralston, J. *Phys. Chem. Chem. Phys.* **12,** 12499–12512 (2010).

334. Drüschler, M., Borisenko, N., Wallauer, J., Winter, C., Huber, B., Endres, F. & Roling, B. *Phys. Chem. Chem. Phys.* **14,** 5090–5099 (2012).

335. Costa, R., Pereira, C. M. & Silva, F. *Phys. Chem. Chem. Phys.* **12,** 11125–11132 (2010).

336. Vatamanu, J., Borodin, O., Bedrov, D. & Smith, G. D. *J. Phys. Chem. C* **116,** 7940–7951 (2012).

337. Vatamanu, J., Cao, L., Borodin, O., Bedrov, D. & Smith, G. D. *J. Phys. Chem. Lett.* **2,** 2267–2272 (2011).

338. Merlet, C., Salanne, M., Rotenberg, B. & Madden, P. A. *J. Phys. Chem. C* **115,** 16613–16618 (2011).

339. Fedorov, M. V. & Kornyshev, A. A. *J. Phys. Chem. B* **112,** 11868–11872 (2008).

340. Fedorov, M. V., Georgi, N. & Kornyshev, A. A. *Electrochem. Commun.* **12,** 296–299 (2010).

341. Feng, G., Jiang, D. & Cummings, P. T. *J. Chem. Theory Comput.* **8,** 1058–1063 (2012).

342. Xing, L., Vatamanu, J., Smith, G. D. & Bedrov, D. *J. Phys. Chem. Lett.* **3,** 1124–1129 (2012).

343. Georgi, N., Kornyshev, A. A. & Fedorov, M. V. *J. Electroanal. Chem.* **649,** 261–267 (2010).

344. Fedorov, M. V. & Kornyshev, A. A. *Electrochim. Acta* **111,** 6835–6840 (2008).

345. Jiang, D., Jin, Z. & Wu, J. *Nano Lett.* **11,** 5373–5377 (2011).

346. Kornyshev, A. A. *J. Phys. Chem. B* **111,** 5545–5557 (2007).

347. Bazant, M. Z., Storey, B. D. & Kornyshev, A. A. *Phys. Rev. Lett.* **106,** 046102(1)–046102(4) (2011).

348. Gebbie, M. A., Valtiner, M., Banquy, X., Fox, E. T., Henderson, W. A. & Israelachvili, J. N. *PNAS* **110,** 9674–9679 (2013).

349. Atkin, R. & Warr, G. G. *J. Phys. Chem. C* **111,** 5162–5168 (2007).

350. Atkin, R., Abedin, S. Z. E., Hayes, R., Gaspatotto, L. H. S., Borisenko, N. & Endres, F. *J. Phys. Chem. C* **113,** 13266–13272 (2009).

351. Atkin, R., Borisenko, N., Drüschler, M., Abedin, S. Z. E., Endres, F., Hayes, R., Huber, B. & Roling, B. *Phys. Chem. Chem. Phys.* **13,** 6849–6857 (2011).

352. Wakeham, D., Hayes, R., Warr, G. G. & Atkin, R. *J. Phys. Chem. B* **113,** 5961–5966 (2009).

353. Endres, F., Hofft, O., Borisenko, N., Gasparotto, L. H., Prowald, A., Al-Salman, R., Carstens, T., Atkin, R., Bund, A. & Abedin, S. Z. E. *Phys. Chem. Chem. Phys.* **12,** 1724–1732 (2010).

354. Perkin, S., Crowhurst, L., Niedermeyer, H., Welton, T., Smitha, A. M. & Gosvami, N. N. *Chem. Commun.* **47,** 6572–6574 (2011).

355. Smith, A. M., Lovelock, K. R. J., Gosvami, N. N., Licence, P., Dolan, A., Welton, T. & Perkin, S. *J. Phys. Chem. Lett.* **4,** 378–382 (2013).

356. Mezger, M. *et al. Science* **322,** 424–428 (2008).

357. Cremer, T., Stark, M., Deyko, A., Steinruck, H.-P. & Maier, F. *Langmuir* **27,** 3662–3671 (2011).

358. Mezger, M., Schramm, S., Schröder, H., Reichert, H., Deutsch, M., Souza, E. J. D., Okasinski, J. S., Ocko, B. M., Honkimäki, V. & Dosch, H. *J. Chem. Phys.* **131,** 094701(1)–094701(9) (2009).

359. Baldelli, S. *Acc. Chem. Res.* **41,** 421–431 (2008).

360. Baldelli, S. *J. Phys. Chem. Lett.* **4,** 244–252 (2013).

361. Payal, R. S. & Balasubramanian, S. *Chem. Phys. Chem.* **13,** 1764–1771 (2012).

362. Kislenko, S. A., Samoylov, I. S. & Amirov, R. H. *Phys. Chem. Chem. Phys.* **11,** 5584–5590 (2009).

363. Wang, S., Li, S., Cao, Z. & Yan, T. *J. Phys. Chem. C* **114,** 990–995 (2010).

364. Dou, Q., Sha, M. L., Fu, H. Y. & Wu, G. Z. *J. Phys.: Condens. Matter* **23,** 175001(1)–175001(8) (2011).

365. Maolin, S., Fuchun, Z., Guozhong, W., Haiping, F., Chunlei, W., Shimou, C., Yi, Z. & Jun, H. *J. Chem. Phys.* **128,** 134504(1)–134504(7) (2008).

366. Feng, G., Zhang, J. S. & Qiao, R. *J. Phys. Chem. C* **113,** 4549–4559 (2009).

367. Sha, M., Wu, G., Dou, Q., Tang, Z. & Fang, H. *Langmuir* **26,** 12667–12672 (2010).

368. Pinilla, C., Pópolo, M. G. D., Lynden-Bell, R. M. & Kohanoff, J. *J. Phys. Chem. B* **109,** 17922–17927 (2005).

369. Pinilla, C., Pópolo, M. G. D., Kohanoff, J. & Lynden-Bell, R. M. *J. Phys. Chem. B* **111,** 4877–4884 (2007).

370. Smith, G. D., Borodin, O., Russo, S. P., Rees, R. J. & Hollenkamp, A. F. *Phys. Chem. Chem. Phys.* **11,** 9884–9897 (2009).

371. Yan, T., Li, S., Jiang, W., Gao, X., Xiang, B. & Voth, G. A. *J. Phys. Chem. B* **110,** 1800–1806 (2006).